

# Central Stellar Discs as Tracers of Galaxy Assembly

---

HUGO RICARDO BASTOS MARTINS LEDO

---

Thesis submitted to the University of Hertfordshire in partial  
fulfilment of the requirements for the degree of Doctor of Philosophy.

· March 2015 ·

## Abstract

In this thesis we explored the use of nuclear stellar discs as tracers of the merging history of early-type galaxies. These small structures, just a few tens to a few hundreds of parsecs across, are a common but poorly studied feature of early-type galaxies. They are formed during or shortly after merging events due to the infall of gas, which settles in a disc and leads to the formation of new stars. Initial simulations showed that they should not survive a following major merger and could, therefore, be used to trace the epoch when their host galaxies experienced their last major merger event. We produced the first census of nuclear discs and established that their incidence is 20%, fairly independent of the host-galaxy mass or galactic environment. Furthermore, we have more than doubled the sample of nuclear discs with known photometric properties, finding that they give a hint of possessing different characteristics from those of large, galactic discs.

Using these nuclear discs as clocks for the assembly history of galaxies requires dating their stellar populations. By combining the use of integral-field spectroscopy with the *a priori* knowledge of the relative bulge- and disc-light contribution to the observed spectra, as determined by a photometric disc-bulge decomposition, we have shown that it is possible to reduce the degeneracies that affect the study of two superimposed populations and thus that the age of stellar discs can be measured more precisely. To illustrate our method, we present VLT-VIMOS data for NGC 4458, a low-mass slowly rotating early-type galaxy with a disc that we found to be at least 5-6 Gyr old. The presence of such an old central disc in such a small, slowly-rotating and, mostly likely, round galaxy is particularly puzzling and presents a challenge to existing models.

Disc fragility is central to our studies and we have expanded the limited initial simulations to study it in more detail. By means of N-body simulations, we have reproduced the final stages of a galaxy encounter by exposing a nuclear disc rotating in the gravitational potential of its host bulge and central supermassive black hole to the impact of a secondary massive black hole. We explored not only major mergers (1:1 mass ratio), but also large minor mergers (1:5 and 1:10), across a variety of collision angles, and assessed the survival of the disc, as perceived by current observational limits, both for photometry and spectroscopy. As expected, the discs do not survive a major merger whereas it is in general possible to detect their presence after a 1:5 or 1:10 encounter, in particular when looking at kinematic signatures with spectroscopy.

This thesis has demonstrated that nuclear discs constitute both a common and accurate tool for constraining the assembling history of nearby early-type galaxies. The advent of more sensitive integral-field spectrographs, such as MUSE, will make measuring the stellar age of nuclear discs not only more precise, but also more economical in terms of telescope time. This will allow embarking on a more systematic age dating campaign for nuclear stellar discs across a wider range of type, mass and galactic environments for their host galaxies. Combining such a census with a larger set of numerical simulations aimed at calibrating better the range of merger event that would erase any photometric or kinematic signature of a nuclear disc, should finally allow us to put firm constraints on the merging history of early-type galaxies.

# Contents

<b>Acknowledgments</b>	<b>iv</b>
	<b>Page</b>
<b>1 Introduction</b>	<b>1</b>
1.1 Lost in a sea of galaxies . . . . .	1
1.2 Galaxy evolution . . . . .	4
1.3 Mergers and elliptical galaxies . . . . .	8
1.4 Nuclear stellar discs . . . . .	10
1.5 Thesis aims and outlook . . . . .	10
References . . . . .	12
<b>2 A census of nuclear stellar discs in early-type galaxies</b>	<b>17</b>
2.1 Introduction . . . . .	17
2.2 Sample selection and data mining . . . . .	22
2.2.1 Selection and acquisition . . . . .	22
2.2.2 Sample properties . . . . .	22
2.2.3 Inclination . . . . .	23
2.3 Analysis . . . . .	23
2.3.1 Disc identification process . . . . .	23
2.3.2 Disc-bulge decomposition . . . . .	28
2.3.3 Disc size estimates . . . . .	28
2.4 Results . . . . .	30
2.4.1 The census . . . . .	30

2.4.2	Properties of the decomposed discs . . . . .	32
2.5	Conclusions . . . . .	34
	References . . . . .	36
2.6	Appendix A: Nuclear stellar discs . . . . .	39
2.6.1	Properties of the galaxies with discs . . . . .	39
2.6.2	NSD structure maps, ellipticity and $a_4$ profiles . . . . .	44
2.7	Appendix B: Disc decomposition . . . . .	55
<b>3</b>	<b>Nuclear discs as clocks for the assembly history of early-type galaxies: the case of NGC 4458</b>	<b>62</b>
3.1	Introduction . . . . .	62
3.2	VIMOS observations and data reduction . . . . .	66
3.2.1	Observations . . . . .	66
3.2.2	Data reduction . . . . .	66
3.3	Analysis . . . . .	70
3.3.1	Nuclear disc and bulge decomposition . . . . .	70
3.3.2	HST to VIMOS matching . . . . .	71
3.3.3	Bulge spectrum analysis . . . . .	74
3.3.4	Nuclear stellar population analysis . . . . .	74
3.4	Discussion . . . . .	80
3.4.1	Future outlook . . . . .	82
	References . . . . .	86
3.5	Appendix C: Comparison between VIMOS and SAURON . . . . .	90
<b>4</b>	<b>On the fragility of nuclear stellar discs against galaxy mergers</b>	<b>93</b>
4.1	. . . . .	93
4.2	Simulation thought and design . . . . .	94
4.2.1	Simulation set-up . . . . .	95
4.2.2	Colliding bulge . . . . .	95

4.2.3	Technical aspects . . . . .	98
4.3	Simulation analysis . . . . .	102
4.3.1	Stellar surface brightness and velocity maps . . . . .	102
4.3.2	Kinometry . . . . .	102
4.3.3	Disc kinematic signature . . . . .	104
4.4	Assessment of disc survival . . . . .	106
4.4.1	Photometric assessment . . . . .	107
4.4.2	Spectroscopic assessment . . . . .	110
4.4.3	Impact of softening . . . . .	115
4.5	Discussion . . . . .	117
	References . . . . .	119
4.6	Appendix D: Maps and kinometry . . . . .	123
4.7	Appendix E: Maps and kinometry for softened BHs . . . . .	134
<b>5</b>	<b>Conclusions and future work</b>	<b>139</b>
5.1	Conclusions . . . . .	139
5.2	Aims for the future and opportunities . . . . .	142
	References . . . . .	145

# List of Figures

1.1	Hubble's tuning fork . . . . .	2
1.2	Kinematic morphology - density relation from ATLAS <sup>3D</sup> . . . . .	2
1.3	Location of the galaxies surrounding us . . . . .	3
1.4	Cosmic Microwave Background radiation . . . . .	4
1.5	Millennium simulation . . . . .	5
1.6	Star formation histories . . . . .	6
1.7	Star formation and mass assembly . . . . .	7
1.8	Luminosity profiles . . . . .	9
2.1	Nuclear Stellar Disc fragility . . . . .	19
2.2	Prediction from semi-analytical models . . . . .	20
2.3	No Nuclear Stellar Disc visual detection . . . . .	25
2.4	Nuclear Stellar Disc detection . . . . .	26
2.5	ESO 507-027 disc-bulge decomposition . . . . .	29
2.6	Disc size estimates . . . . .	30
2.7	Discs $\mu_0^c - h$ diagram. . . . .	33
2.8	ESO 352-057, ESO 378-020, ESO 507-027 and IC 0875 . . . . .	44
2.9	NGC 0584, NGC 1023, NGC 1129, NGC 1351, NGC 1381 and NGC 1426	45
2.10	NGC 1427, NGC 1439, NGC 2549, NGC 2685, NGC 2787 and NGC 2865	46
2.11	NGC 3115, NGC 3156, NGC 3377, NGC 3384, NGC 3385 and NGC 3610	47
2.12	NGC 3613, NGC 3706, NGC 3818, NGC 3900, NGC 3945 and NGC 4026	48
2.13	NGC 4128, NGC 4270, NGC 4318, NGC 4342, NGC 4352 and NGC 4458	49
2.14	NGC 4473, NGC 4474, NGC 4478, NGC 4483, NGC 4515 and NGC 4528	50

2.15	NGC 4546, NGC 4570, NGC 4621, NGC 4623, NGC 4660 and NGC 4742	51
2.16	NGC 4762, NGC 4866, NGC 5076, NGC 5252, NGC 5308 and NGC 5854	52
2.17	NGC 7173, NGC 7176, NGC 7562, NGC 7585, NGC 7619 and NGC 7785	53
2.18	PGC 013343, PGC 036465, PGC 044815, UGC 01003 and UGC 03426	54
2.19	Scorza and Bender decomposition of ESO 352-057 and ESO 378-020	55
2.20	Scorza and Bender decomposition of ESO 507-027 and IC 0875	56
2.21	Scorza and Bender decomposition of NGC 0584 and NGC 3385	57
2.22	Scorza and Bender decomposition of NGC 3610 and NGC 4128	58
2.23	Scorza and Bender decomposition of NGC 4474 and NGC 4621	59
2.24	Scorza and Bender decomposition of NGC 4660 and NGC 5308	60
3.1	Simulations showing the accuracy in recovering the age of a 7-Gyr-old disc population that is embedded in a 13-Gyr-old bulge population	65
3.2	Tracing galaxy centre coordinates	67
3.3	Central 5" VIMOS spectrum of NGC 4458	69
3.4	Disc-bulge decomposition of the nuclear regions of NGC 4458	71
3.5	Matching HST to VIMOS	73
3.6	Disc age determination	76
3.7	Differences between models	77
3.8	Final age estimate	79
3.9	Local $h_3-V/\sigma$ relation for the KDC of NGC 4458 compared to that observed for all such structures in the ATLAS <sup>3D</sup> survey	83
3.10	Comparison between SAURON and VIMOS stellar kinematic measurements for the central regions of NGC 4458	91
4.1	1:5 BH separations	101
4.2	Simulation initial conditions	103
4.3	Kinometry for initial conditions	105
4.4	Final 1:1	108

4.5	Final 1:5 . . . . .	109
4.6	Final 1:10 . . . . .	109
4.7	Disc detection: $a_4$ . . . . .	112
4.8	Disc detection: $V$ . . . . .	113
4.9	Disc detection: $k_5/k_1$ . . . . .	114
4.10	Effect of softening . . . . .	116
4.11	Final 1:1, $i_{\text{BH}} = 0^\circ$ . . . . .	124
4.12	Final 1:1, $i_{\text{BH}} = 30^\circ$ . . . . .	124
4.13	Final 1:1, $i_{\text{BH}} = 60^\circ$ . . . . .	125
4.14	Final 1:1, $i_{\text{BH}} = 90^\circ$ . . . . .	125
4.15	Final 1:1, $i_{\text{BH}} = 120^\circ$ . . . . .	126
4.16	Final 1:1, $i_{\text{BH}} = 150^\circ$ . . . . .	126
4.17	Final 1:1, $i_{\text{BH}} = 180^\circ$ . . . . .	127
4.18	Final 1:5, $i_{\text{BH}} = 0^\circ$ . . . . .	127
4.19	Final 1:5, $i_{\text{BH}} = 30^\circ$ . . . . .	128
4.20	Final 1:5, $i_{\text{BH}} = 60^\circ$ . . . . .	128
4.21	Final 1:5, $i_{\text{BH}} = 90^\circ$ . . . . .	129
4.22	Final 1:5, $i_{\text{BH}} = 120^\circ$ . . . . .	129
4.23	Final 1:5, $i_{\text{BH}} = 150^\circ$ . . . . .	130
4.24	Final 1:5, $i_{\text{BH}} = 180^\circ$ . . . . .	130
4.25	Final 1:10, $i_{\text{BH}} = 0^\circ$ . . . . .	131
4.26	Final 1:10, $i_{\text{BH}} = 30^\circ$ . . . . .	131
4.27	Final 1:10, $i_{\text{BH}} = 60^\circ$ . . . . .	132
4.28	Final 1:10, $i_{\text{BH}} = 90^\circ$ . . . . .	132
4.29	Final 1:10, $i_{\text{BH}} = 120^\circ$ . . . . .	133
4.30	Final 1:10, $i_{\text{BH}} = 150^\circ$ . . . . .	133
4.31	Final 1:10, $i_{\text{BH}} = 180^\circ$ . . . . .	134
4.32	Final 1:5, $i_{\text{BH}} = 0^\circ$ . . . . .	135

4.33	Final 1:5, softening 2 $i_{\text{BH}} = 0^\circ$ . . . . .	135
4.34	Final 1:5, softening 3.5 $i_{\text{BH}} = 0^\circ$ . . . . .	136
4.35	Final 1:5, softening 6.25 $i_{\text{BH}} = 0^\circ$ . . . . .	136
4.36	Final 1:5, $i_{\text{BH}} = 90^\circ$ . . . . .	137
4.37	Final 1:5, softening 2 $i_{\text{BH}} = 90^\circ$ . . . . .	137
4.38	Final 1:5, softening 3.5 $i_{\text{BH}} = 90^\circ$ . . . . .	138
4.39	Final 1:5, softening 6.25 $i_{\text{BH}} = 90^\circ$ . . . . .	138

# List of Tables

2.1	Galaxy ellipticity and $a_4$ comparison . . . . .	27
2.2	Nuclear Stellar Disc incidence per galaxy type . . . . .	31
2.3	NSD incidence per B-band magnitude . . . . .	32
2.4	NSD incidence as function of environment . . . . .	32
2.5	Galaxies where discs were found and some of their properties. . . . .	40
2.6	Continuation of properties table . . . . .	41
2.7	Continuation of properties table . . . . .	42
2.8	Continuation of properties table . . . . .	43
2.9	Properties of the decomposed discs . . . . .	61
3.1	NGC 4458 observations . . . . .	66
3.2	Properties of the decomposed disc . . . . .	72
4.1	Set of simulations . . . . .	96
4.2	Softened simulations . . . . .	97
4.3	Disc detection fractions . . . . .	111

# Acknowledgments/Agradecimentos

*Para os meus pais, com muito amor.*

*Rakastan sinua, Marjaana.*

*A special thank you to my supervisors, Marc and Elias, for having guided me throughout these years and to the collaborators who have made this work possible.*

*Finally, a word of appreciation to all those colleagues who were present during these last years, for their support.*



---

# CHAPTER 1: INTRODUCTION

---

## 1.1 Lost in a sea of galaxies

Less than a century ago we were still trying to make sense of our own position inside the Milky Way and questioning if we were part of a unique structure or if the observed “spiral nebulae” were other worlds just like our own (debate by Shapley and Curtis, 1921). We now know our galaxy is just one among billions of others. An extrapolation of what has been observed in the Hubble eXtreme Deep Field, a combination of all the observations taken for the last 10 years with the Advanced Camera and the Wide Field Camera 3 on the Hubble Space Telescope (Illingworth *et al.*, 2013), estimates the existence of more than 175 billion galaxies. And not only can we see our closest companions, but we have detected galaxies up to 13.2 billion light-years away (Zheng *et al.*, 2012).

As it often happens with new discoveries, galaxies were grouped into classes, according to apparent morphological characteristics. This process led to the construction known as Hubble’s tuning fork (Hubble, 1936), which can be seen in Figure 1.1. Although limited in its construction, it is the basis of a system still referred to nowadays. It has undergone several expansions and improvements over time (e.g. de Vaucouleurs, 1959; Sandage, 1961; Buta, 2013), mostly to accommodate more morphological parameters and further distinguish galaxies from one another. More recently though, this representation has been experiencing modifications that are intrinsically connected to physical properties of the galaxies being displayed. Already in 1996, Kormendy and Bender proposed that elliptical galaxies should be ordered not by apparent flattening, but according to the shape of their isophotes. The development of Integral Field Units allowed the ATLAS<sup>3D</sup> team to go a step further and propose a comb-shaped diagram based on the kinematics of the galaxies and on a distinction between slow and fast rotators, as seen in Fig. 1.2 (Cappellari *et al.*, 2011). Although with different motivation, this diagram is reminiscent of van den Bergh (1976) who had already included the S0 galaxies in a sequence parallel to the spirals.

And how are these galaxies distributed around us? Large surveys have allowed us to visualise the present structure of the Universe, with filamentary and nodal concentrations of galaxies delimiting large voids, as can be seen in Fig. 1.3, from the Sloan Digital Sky Survey (York *et al.*, 2000). This is immensely different from the Universe’s infancy as portrayed by the Cosmic Microwave Background, the earliest image we have of what now surrounds us (Fig. 1.4), showing regions of different

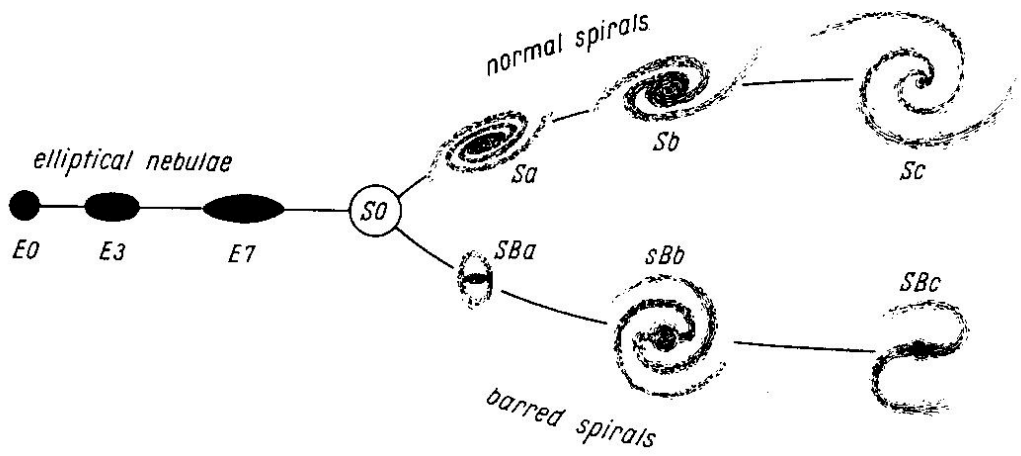


Fig. 1.1: Hubble's tuning fork based on the apparent morphology of the galaxies (Hubble, 1936).

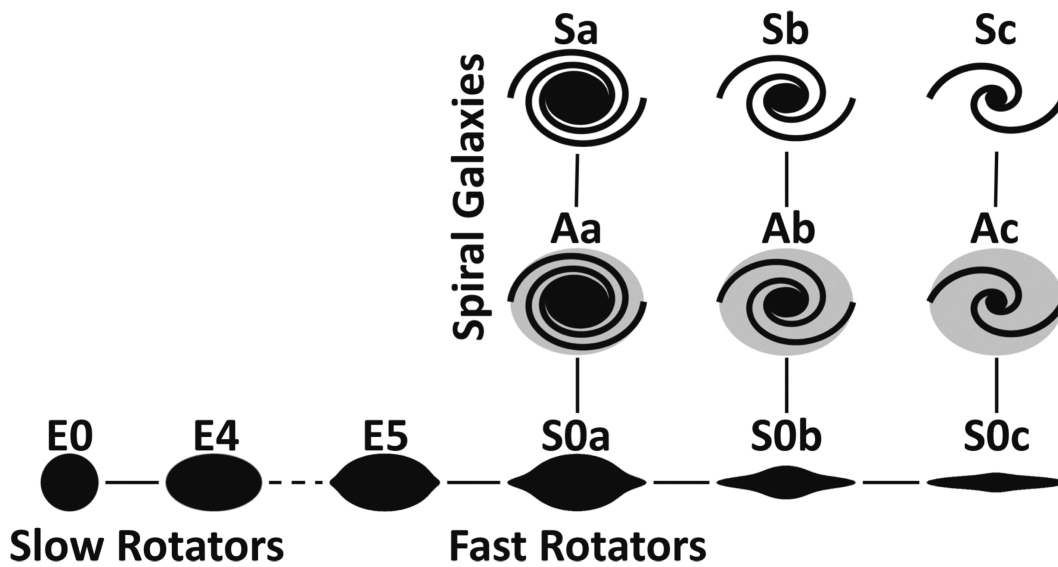


Fig. 1.2: Kinematic morphology - density relation from ATLAS<sup>3D</sup> (Cappellari *et al.*, 2011).

temperatures, which corresponded to the density fluctuations that gave rise to the structures we see today.

We are not as lost in this immense sea of galaxies as in a not so distant past, but it is a very demanding task to understand this evolution and transformation that from a very smooth state, with density perturbations smaller than 1 part in 100 thousand, created the variety of objects in the present universe, from stars to galaxies.

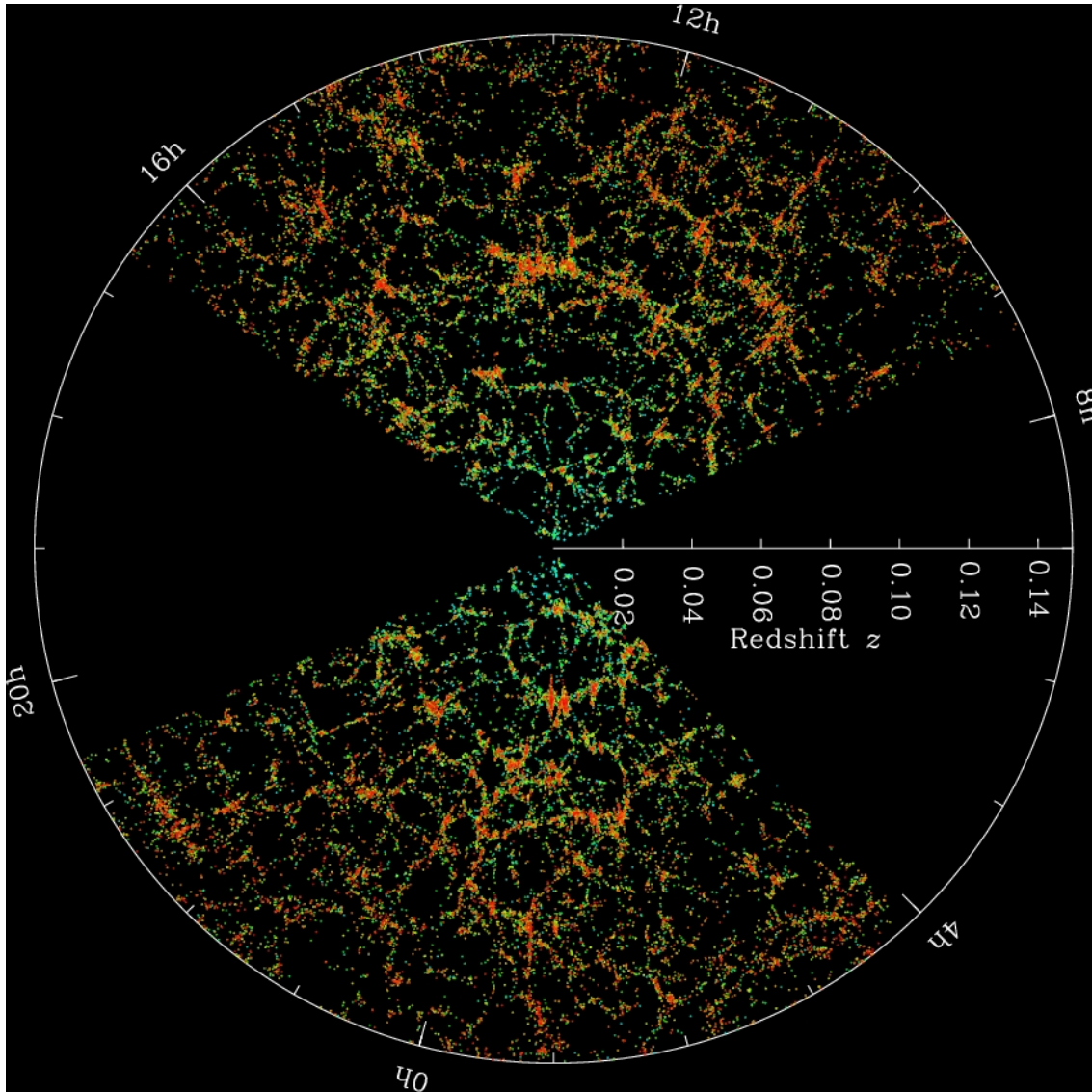


Fig. 1.3: Location of the galaxies surrounding us, from the Sloan Digital Sky Survey (Image by Michael Blandon SDSS, 2014), showing areas of high density forming clusters and walls that surround voids.

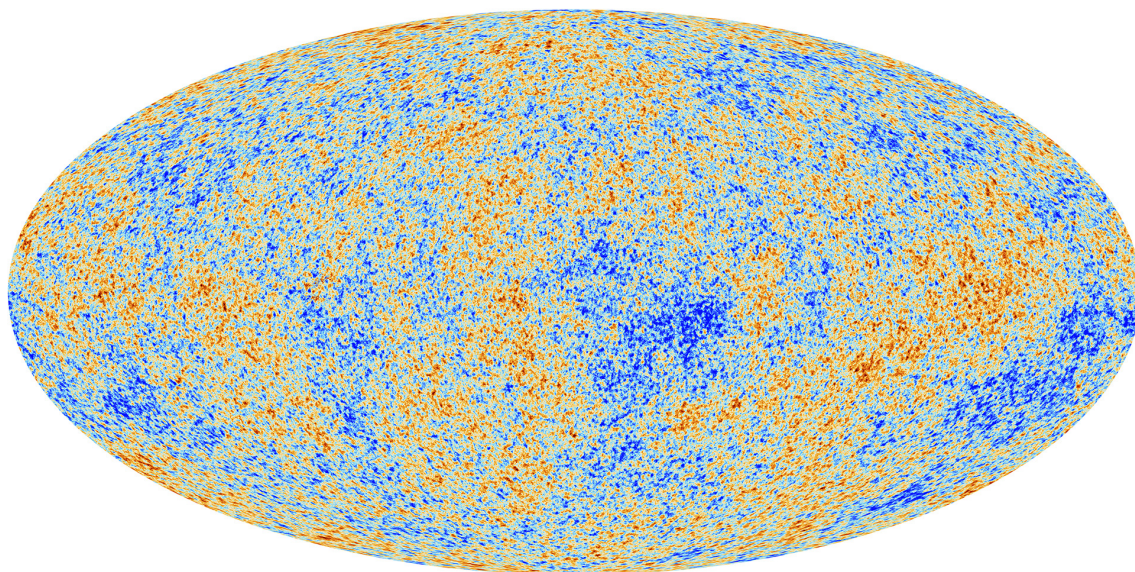


Fig. 1.4: Cosmic Microwave Background radiation taken by Planck satellite (ESA, 2013).

## 1.2 Galaxy evolution

The first attempts to explain galaxy evolution envisaged a single-event formation known as monolithic collapse in which primordial clouds of gas formed all the galaxies. Theoretical motivation for this theory was provided by Eggen *et al.* (1962) and, later supported by some observational evidence (e.g. Searle and Zinn, 1978). Simulations (Larson, 1974) also showed that this model could explain observable properties of spherical galaxies. More massive galaxies would have formed earlier and the different galaxy types would have come from different star formation and gas accretion rates. When the star formation occurred faster than the gas infall, it would create an elliptical galaxy, otherwise gas would settle first in a disc and form a spiral galaxy. It was also possible for galaxies initially formed as ellipticals to later accrete gas into a disc and become spirals. This basic model appeared to explain current morphologies, however, there is overwhelming evidence that galaxies do not just evolve passively. It started to become apparent that galaxies were not independent and isolated systems, but interacted with each other and even merged. This led to a different model of galaxy formation being proposed, that of a hierarchical formation whereby small proto-galaxies form from initial density perturbations and then grow not only by means of star formation but also by merging with other systems. This now preferred model is in better agreement with the fact that galaxies interact, the evolution of the different types with time and the results from  $\Lambda$ CDM models such as the Millennium simulation (Springel *et al.*, 2005). Although in this

particular simulation what is being followed is the behaviour of just the dark matter (DM), we should assume that baryons follow it. It is not yet feasible to include at the same time baryonic physics to deal with the physics of the interstellar medium, such as shocks, star formation, supernova feedback, metal enrichment and mixing, Active Galactic Nuclei, *etc.*, although Halo Abundance Matching techniques (e.g. Kravtsov *et al.*, 2004; Behroozi *et al.*, 2010; Trujillo-Gomez *et al.*, 2011) are proving to solve the problem of relating observed galaxies to simulated DM halos. Looking at Fig. 1.5 we can see the similarities between the Millennium simulation and the observational results from SDSS.

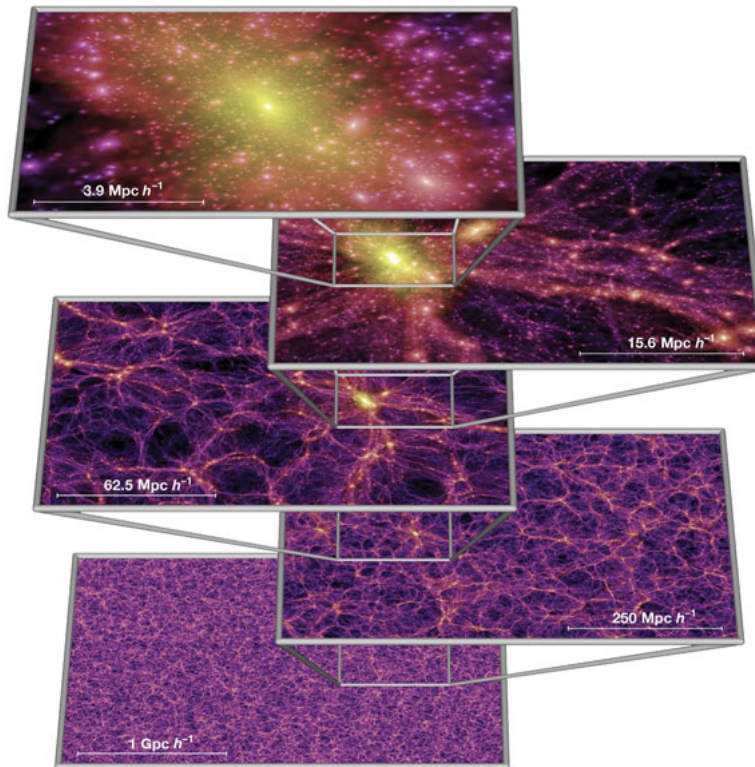


Fig. 1.5: In this figure from Springel *et al.* (2005) we can see the the results from the Millennium simulation, depicting the dark matter density. Each slice, with a thickness of  $15h^{-1}$  Mpc, is a four-times zoom of the previous one and is centred on a cluster.

When looking at how galaxies evolve we also need to explore the balance between star formation from the available gas which can be replenished via cold gas accretion (e.g. Kereš *et al.*, 2005; Brooks *et al.*, 2009), and Supernova (SN) and Active Galactic Nucleus (AGN) feedback which release energy into the intergalactic medium and can quench star formation (Kaviraj *et al.*, 2007) not only by heating up the gas and preventing it from collapsing and forming stars but also by expelling gas from the galaxies, in particular in lower mass galaxies. Tracing the star formation history has become less of a problem in recent years. Works such as from Thomas *et al.* (2005) show us how star formation evolved through time. They show that star formation

histories of early-type galaxies depend on galaxy mass and environment. Galaxies in high density environments had most of their star formation from  $2 \lesssim z \lesssim 5$  whereas those in low density environments formed galaxies at later epochs ( $1 \lesssim z \lesssim 2$ ) as seen in Fig. 1.6.

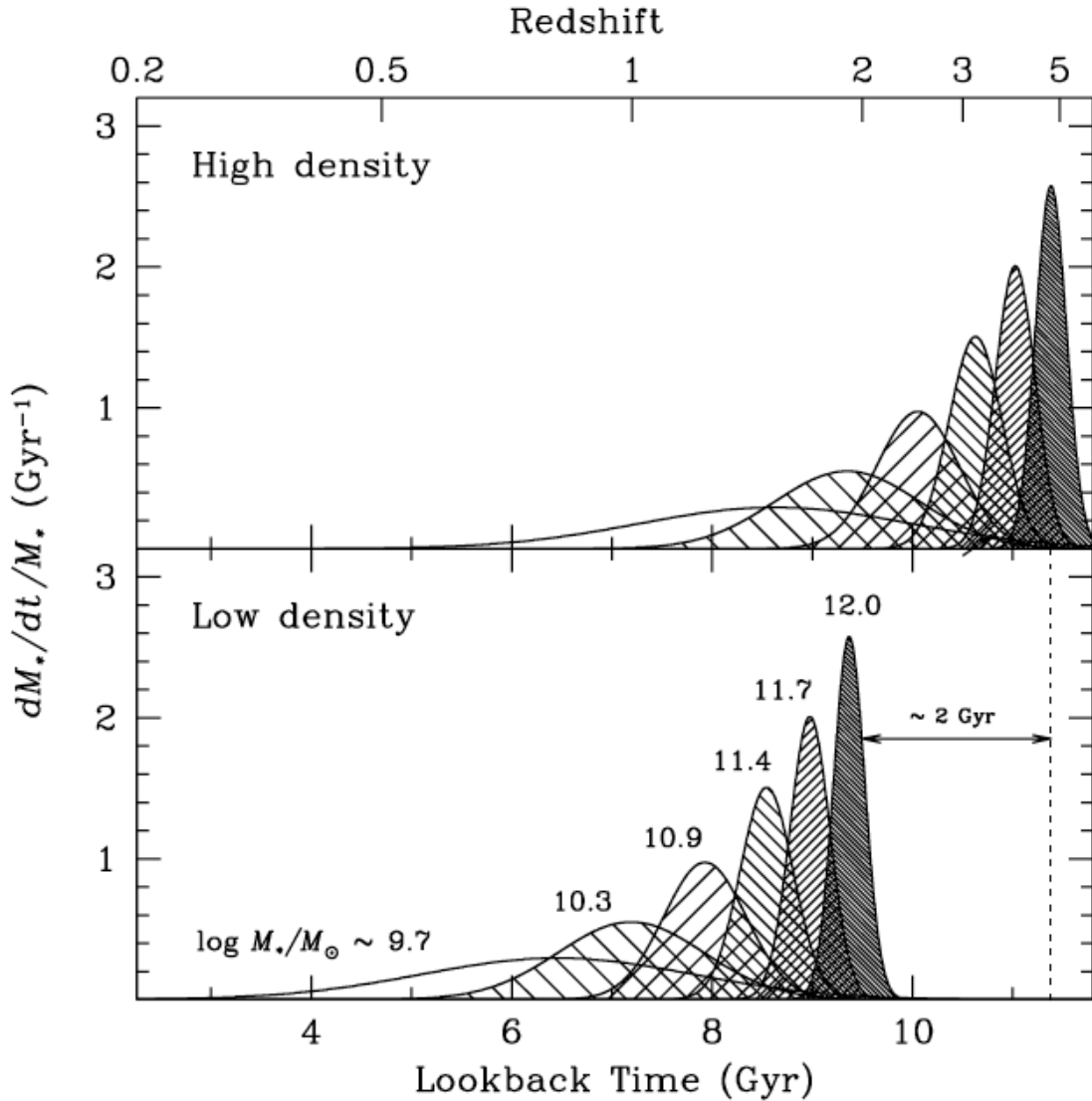


Fig. 1.6: Figure from Thomas *et al.* (2005) showing the star formation histories of early-type galaxies as a function of mass and environment density.

But where were those stars formed? In the galaxy they currently occupy or an earlier progenitor? What so far has proven to be more difficult is to draw a picture of mass assembly throughout time. Several methods were developed looking either for galaxies in the process of growing through merging (such as galaxy pairs, Kitzbichler and White, 2008) or for those that have already undergone merging events and display morphological relics from those encounters (polar rings, kinematically de-

coupled cores, *etc.*). We can also look at how the most massive galaxies evolve through cosmic time (e.g. Trujillo, 2013). This will be a consequence not only of star formation (which we can trace), but also of mass assembly. And these two aspects are not always related. During mergers where gas is available (the so called “wet mergers”), star formation will be increased, although not as much as previously thought. Kaviraj *et al.* (2013) have shown that for the case of major mergers (the only ones which can be detected at high  $z$ ), the merging process is only responsible for up to 27% per cent of the galaxy’s star formation.

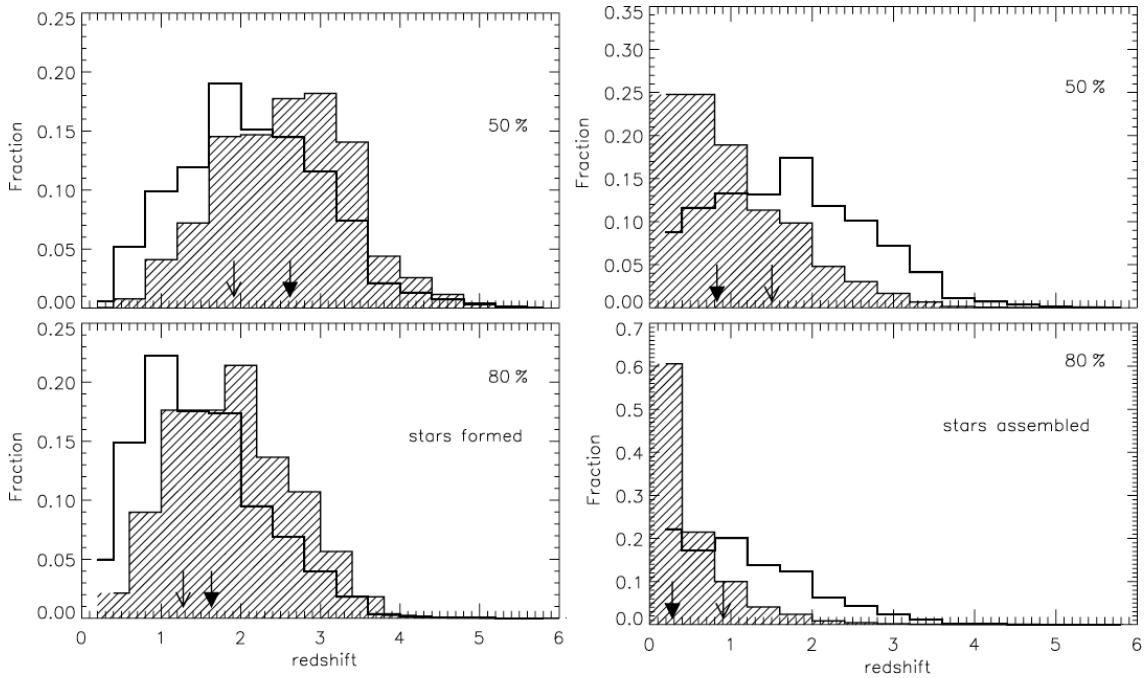


Fig. 1.7: Figure from De Lucia *et al.* (2006) showing results from the Millennium simulation. The shaded histogram corresponds to massive ellipticals ( $M > 10^{11} M_{\odot}$ ) and the open histogram, to those with mass larger than  $4 \times 10^9 M_{\odot}$ . The upper panel shows at which epoch those galaxies have formed 50% of their stars, whereas the bottom panel shows the formation of 80% of the stars. The arrows indicate the medians (thick for shaded and thin for open). We can see that more massive galaxies have formed their stars at earlier epochs consistent with the results from Thomas *et al.* (2005). In the panels on the right, we are looking at assembly epochs. What they show us is that the more massive galaxies, which have formed their stars earlier, have actually assembled later.

Also evident is that not only the overall structure of the Universe has changed, but also its building blocks. When zooming in and looking at individual galaxies, we notice they have evolved through time. The present morphologies and associated classifications do not seem to describe as well what is seen at early epochs. Are different types related to each other? Can they evolve from one type to another?

## 1.3 Mergers and elliptical galaxies

We have seen that a crucial method for galaxy growth and evolution has been the merging of several systems into a new one. This can occur between galaxies of very different mass where  $M_{*a} \leq 1/5 M_{*b}$  and we call these “minor mergers” (There is no consensus on the definition of minor merger. We adopted the 1:5 mass ratio as its upper limit, below the “major merger” threshold of 1:4 proposed by some authors (e.g. López-Sanjuan *et al.*, 2012; Bundy *et al.*, 2009; Maller *et al.*, 2006). These are more frequent (we see multiple evidence of minor mergers having occurred in the formation process in our own Milky Way) and do not lead to morphological changes. When the galaxies have similar masses we have what are called “major mergers”. These are thought to be the origin of elliptical galaxies. Toomre (1977) suggested that when similar mass disc galaxies merge, the resulting galaxy could be an elliptical. This was later demonstrated in numerical simulations by, for example, Farouki and Shapiro (1982).

Elliptical galaxies were, for many years, seen as uninteresting. They were thought to be old systems with little or no star formation, evolving passively, simple to describe and understand, a fairly homogeneous population (not like the spirals), with a  $r^{1/4}$  profile and following tight relations such as the Faber-Jackson relation (Faber and Jackson, 1976), linking their luminosity  $L$  and the central stellar velocity dispersion  $\sigma$ , of the form  $L \propto \sigma^\gamma$ , later recognised as a projection of the “Fundamental plane” relation (Djorgovski and Davis, 1987) between three parameters, the half-light radius  $r_e$ , and the mean surface brightness  $I_e$  and velocity dispersion  $\sigma_e$  inside that radius of the form

$$r_e \propto \sigma^{1.4 \pm 0.15} I_e^{-0.9 \pm 0.1}, \quad (1.1)$$

It is becoming apparent though that these massive stellar systems are fundamental to understanding mass assembly and that, maybe due to the past lack of interest in them, not much is known about their formation and evolution.

It has been noted (Kormendy *et al.*, 2009) that, despite their uniformity, early-type galaxies (ETG) present a dichotomy. Giant ellipticals are rounder, triaxial systems, supported not by rotation, but by an anisotropic velocity distribution of their stars. Bertola and Capaccioli (1975) noticed that, contrary to what was expected, the rotation of these luminous ETGs was too slow to be the cause of their flattening. These galaxies also present a cuspy core, where there is missing light if we extrapolate a Sérsic profile (Sersic, 1968) from the main body to the inner parts of the galaxy (see Figure 1.8). Sérsic profiles are functions of the form  $\log I(r) \propto r^{1/n}$

which have been shown to describe well the majority of ellipticals (Kormendy *et al.*, 2009). They arose from a generalisation (Caon *et al.*, 1993) of a previous law by de Vaucouleurs (1948), where  $n = 4$ . The formation of these central shallow cusps may have been caused by BH scouring after dry mergers, which have dominated the more recent history of these galaxies. When analysing the shape of the isophotes, they present a box-shaped deviation from ellipses.

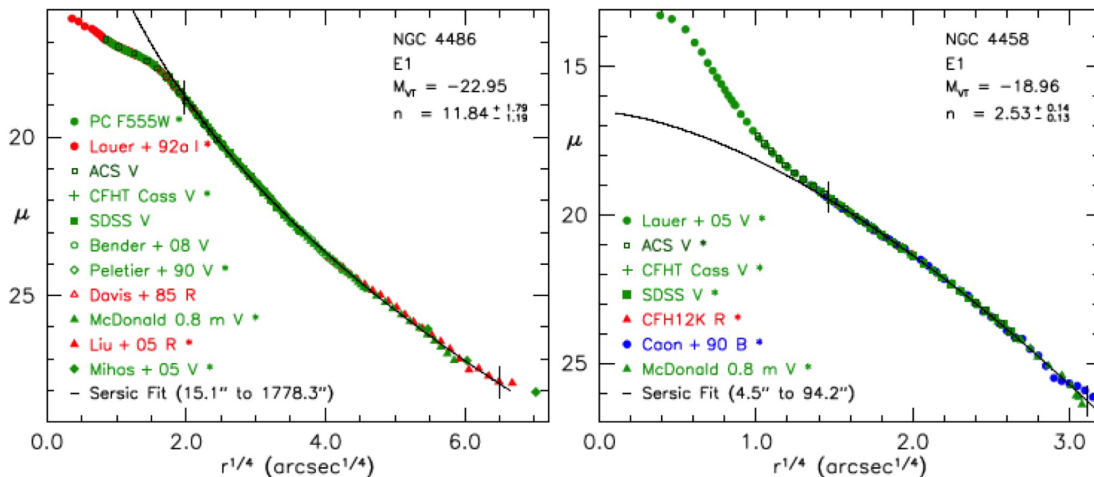


Fig. 1.8: This figure (Kormendy, 2009) shows the differences in profiles from core elliptical galaxies with missing light (left panel) and coreless (or power-law) ETGs (right panel). The solid line presents a Sérsic fit to the outer parts of the galaxies, between the vertical lines, extrapolated to the centre. We can see that the observations represented by coloured symbols show less and more light than the expected for the core and power-law galaxies, respectively.

Normal ETGs, on the other hand, usually show rotation, a flatter shape and a deviation in the luminosity profile in the opposite direction, presenting extra light which can correspond to discy isophotes. This extra light component has an exponential profile associated to discs. Why the difference then? The idea is that during wet mergers, the gas infall and following star formation have prevented the BH scouring. These gas-rich mergers are also consistent with the modest observed  $\alpha$ -enhancement. These  $\alpha$  elements (such as Mg, O, Ne, Si...) are released into the interstellar medium by Type II supernovae, being related to short star formation episodes. However, more extended periods of star formation such as those caused by multiple wet mergers, cause the decrease of the initial  $[\alpha/\text{Fe}]$  abundance ratios (e.g. de La Rosa *et al.*, 2011).

Besides this dichotomy, we can also see that present-day ETGs have different properties from those at earlier epoch. They have evolved in mass, size and density. Higher redshift ellipticals ( $z \sim 2 - 3$ ) are considerably more compact objects (Oogi and Habe, 2013). Their size growth seems to be the result of a series of minor

mergers, being dry mergers the preferred method, since less energy is dissipated due to the presence of gas.

It appears then that early-type galaxies are central to the study of galaxy evolution and that it is of paramount importance to be able to trace and distinguish episodes of mass increase and size growth, the former mainly due to star formation episodes and major mergers and the latter caused by minor mergers, especially dry ones. To do so is not a trivial task and we need to explore novel tools to do so.

## 1.4 Nuclear stellar discs

The need for a reliable method that can help us track the evolution of galaxies, their merging histories and how they influence the properties of the final outcome, even if they all fall under the morphological classification of “elliptical galaxy” is what made us take a closer look at Nuclear Stellar Discs (NSDs).

With the improvement in resolution offered by the Hubble Space Telescope (HST) it was possible to start detecting small features that had before been missed. This was the case of small (few tens to hundreds of parsecs) discs of stars located in the centre of a few galaxies (e.g. van den Bosch *et al.*, 1994). First serendipitously then recognised to possibly being common in ellipticals (e.g. Rest *et al.*, 2001). They were first used as a tool to estimate super massive black hole masses in quiescent galaxies, but we see them as a possible tracer of galaxy assembly. Their creation and destruction is intimately linked to mergers, being formed from the infall of gas that comes with wet mergers and destroyed in subsequent mergers, due to their fragile nature. They are also present in the foundation of the dichotomy we see in ellipticals and, therefore, should be key to understanding these differences.

## 1.5 Thesis aims and outlook

With this work we are trying to answer the questions, is it possible to trace the merging history of galaxies and can we accurately retrieve the look-back time to their last major merger by using nuclear stellar discs? Chapter 2 is based on published work by H. R. Ledo, M. Sarzi, M. Dotti, S. Khochfar and L. Morelli (2010) *A census of nuclear stellar discs in early-type galaxies*. In it we conduct a census of NSDs, which not only provides us with their demographics, but also serves as a sample for further studies. Also in Chapter 2 we investigate the properties of some of these discs. The initial simulations used as an argument for the fragility of the discs

were performed by M. Dotti<sup>1</sup>. In Chapter 3 we develop a method that allows us to narrow the age measurements of the discs' stellar populations by making use of the properties derived as shown in Chapter 2 and using results from Integral Field Spectroscopy. This has been done in collaboration with M. Sarzi, L. Coccato<sup>2</sup> and C. Maraston<sup>3</sup>, who were responsible for the observing proposal, where Figure 3.1 was first used. The observations were done in service mode and the data were processed in a standard manner by L. Coccato using the ESO pipeline. All subsequent data handling and analysis was done by the author of this thesis, with the exception of Figure 3.9, produced by M. Sarzi. In Chapter 4 we explore disc fragility against mergers, for a variety of inclinations and mass ratios, and set limits to their detection after such an event. The simulations were run by M. Dotti and the output was fully analysed by me. General conclusions and future outlook are given in Chapter 5.

---

<sup>1</sup>Dipartimento di Fisica G. Occhialini, Università degli Studi di Milano, Bicocca, Piazza della Scienza 3, 20126 Milano, Italy; INFN, Sezione di Milano-Bicocca, Piazza della Scienza 3, 20126 Milano, Italy

<sup>2</sup>European Southern Observatory, Karl-Schwarzschild-Strasse 2, 85748, Garching bei Muenchen, Germany

<sup>3</sup>Institute of Cosmology and Gravitation, University of Portsmouth, Dennis Sciama Building, Burnaby Road, Portsmouth PO1 3FX, United Kingdom

# References

- Behroozi, P. S., Conroy, C., and Wechsler, R. H. (2010). A Comprehensive Analysis of Uncertainties Affecting the Stellar Mass-Halo Mass Relation for  $0 < z < 4$ . *ApJ*, **717**, 379–403.
- Bertola, F. and Capaccioli, M. (1975). Dynamics of early type galaxies. I - The rotation curve of the elliptical galaxy NGC 4697. *ApJ*, **200**, 439–445.
- Brooks, A. M., Governato, F., Quinn, T., Brook, C. B., and Wadsley, J. (2009). The Role of Cold Flows in the Assembly of Galaxy Disks. *ApJ*, **694**, 396–410.
- Bundy, K., Fukugita, M., Ellis, R. S., Targett, T. A., Belli, S., and Kodama, T. (2009). The Greater Impact of Mergers on the Growth of Massive Galaxies: Implications for Mass Assembly and Evolution since  $z \sim 1$ . *ApJ*, **697**, 1369–1383.
- Buta, R. J. (2013). *Galaxy Morphology*, page 1.
- Caon, N., Capaccioli, M., and D’Onofrio, M. (1993). On the Shape of the Light Profiles of Early Type Galaxies. *MNRAS*, **265**, 1013.
- Cappellari, M., Emsellem, E., Krajnović, D., McDermid, R. M., Serra, P., Alatalo, K., Blitz, L., Bois, M., Bournaud, F., Bureau, M., Davies, R. L., Davis, T. A., de Zeeuw, P. T., Khochfar, S., Kuntschner, H., Lablanche, P.-Y., Morganti, R., Naab, T., Oosterloo, T., Sarzi, M., Scott, N., Weijmans, A.-M., and Young, L. M. (2011). The ATLAS<sup>3D</sup> project - VII. A new look at the morphology of nearby galaxies: the kinematic morphology-density relation. *MNRAS*, **416**, 1680–1696.
- de La Rosa, I. G., La Barbera, F., Ferreras, I., and de Carvalho, R. R. (2011). The link between the star formation history and  $[\alpha/\text{Fe}]$ . *MNRAS*, **418**, L74–L78.
- De Lucia, G., Springel, V., White, S. D. M., Croton, D., and Kauffmann, G. (2006). The formation history of elliptical galaxies. *MNRAS*, **366**, 499–509.
- de Vaucouleurs, G. (1948). Recherches sur les Nebuleuses Extragalactiques. *Annales d’Astrophysique*, **11**, 247.
- de Vaucouleurs, G. (1959). Classification and Morphology of External Galaxies. *Handbuch der Physik*, **53**, 275.
- Djorgovski, S. and Davis, M. (1987). Fundamental properties of elliptical galaxies. *ApJ*, **313**, 59–68.
- Eggen, O. J., Lynden-Bell, D., and Sandage, A. R. (1962). Evidence from the motions of old stars that the Galaxy collapsed. *ApJ*, **136**, 748.

- ESA (2013). Planck CMB. [www.esa.int/spaceinimages/Images/2013/03](http://www.esa.int/spaceinimages/Images/2013/03) Last accessed 1 March 2015
- Faber, S. M. and Jackson, R. E. (1976). Velocity dispersions and mass-to-light ratios for elliptical galaxies. *ApJ*, **204**, 668–683.
- Farouki, R. T. and Shapiro, S. L. (1982). Simulations of merging disk galaxies. *ApJ*, **259**, 103–115.
- Hubble, E. P. (1936). *Realm of the Nebulae*.
- Illingworth, G. D., Magee, D., Oesch, P. A., Bouwens, R. J., Labbé, I., Stiavelli, M., van Dokkum, P. G., Franx, M., Trenti, M., Carollo, C. M., and Gonzalez, V. (2013). The HST eXtreme Deep Field (XDF): Combining All ACS and WFC3/IR Data on the HUDF Region into the Deepest Field Ever. *ApJS*, **209**, 6.
- Kaviraj, S., Kirkby, L. A., Silk, J., and Sarzi, M. (2007). The UV properties of E+A galaxies: constraints on feedback-driven quenching of star formation. *MNRAS*, **382**, 960–970.
- Kaviraj, S., Cohen, S., Windhorst, R. A., Silk, J., O’Connell, R. W., Dopita, M. A., Dekel, A., Hathi, N. P., Straughn, A., and Rutkowski, M. (2013). The insignificance of major mergers in driving star formation at  $z \simeq 2$ . *MNRAS*, **429**, L40–L44.
- Kereš, D., Katz, N., Weinberg, D. H., and Davé, R. (2005). How do galaxies get their gas? *MNRAS*, **363**, 2–28.
- Kitzbichler, M. G. and White, S. D. M. (2008). A calibration of the relation between the abundance of close galaxy pairs and the rate of galaxy mergers. *MNRAS*, **391**, 1489–1498.
- Kormendy, J. (2009). The Elliptical-Spheroidal and Elliptical-Elliptical Galaxy Dichotomies. In S. Jogee, I. Marinova, L. Hao, and G. A. Blanc, editors, *Galaxy Evolution: Emerging Insights and Future Challenges*, volume 419 of *Astronomical Society of the Pacific Conference Series*, page 87.
- Kormendy, J. and Bender, R. (1996). A Proposed Revision of the Hubble Sequence for Elliptical Galaxies. *ApJ*, **464**, L119.
- Kormendy, J., Fisher, D. B., Cornell, M. E., and Bender, R. (2009). Structure and Formation of Elliptical and Spheroidal Galaxies. *ApJS*, **182**, 216–309.
- Kravtsov, A. V., Berlind, A. A., Wechsler, R. H., Klypin, A. A., Gottlöber, S., Allgood, B., and Primack, J. R. (2004). The Dark Side of the Halo Occupation Distribution. *ApJ*, **609**, 35–49.
- Larson, R. B. (1974). Dynamical models for the formation and evolution of spherical galaxies. *MNRAS*, **166**, 585–616.

- López-Sanjuan, C., Le Fèvre, O., Ilbert, O., Tasca, L. A. M., Bridge, C., Cucciati, O., Kampanczyk, P., Pozzetti, L., Xu, C. K., Carollo, C. M., Contini, T., Kneib, J.-P., Lilly, S. J., Mainieri, V., Renzini, A., Sanders, D., Scodreggio, M., Scoville, N. Z., Taniguchi, Y., Zamorani, G., Aussel, H., Bardelli, S., Bolzonella, M., Bongiorno, A., Capak, P., Caputi, K., de la Torre, S., de Ravel, L., Franzetti, P., Garilli, B., Iovino, A., Knobel, C., Kovač, K., Lamareille, F., Le Borgne, J.-F., Le Brun, V., Le Floch, E., Maier, C., McCracken, H. J., Mignoli, M., Pelló, R., Peng, Y., Pérez-Montero, E., Presotto, V., Ricciardelli, E., Salvato, M., Silverman, J. D., Tanaka, M., Tresse, L., Vergani, D., Zucca, E., Barnes, L., Bordoloi, R., Cappi, A., Cimatti, A., Coppa, G., Koekemoer, A., Liu, C. T., Moresco, M., Nair, P., Oesch, P., Schawinski, K., and Welikala, N. (2012). The dominant role of mergers in the size evolution of massive early-type galaxies since  $z \sim 1$ . *A&A*, **548**, A7.
- Maller, A. H., Katz, N., Kereš, D., Davé, R., and Weinberg, D. H. (2006). Galaxy Merger Statistics and Inferred Bulge-to-Disk Ratios in Cosmological SPH Simulations. *ApJ*, **647**, 763–772.
- Oogi, T. and Habe, A. (2013). Dry minor mergers and size evolution of high- $z$  compact massive early-type galaxies. *MNRAS*, **428**, 641–657.
- Rest, A., van den Bosch, F. C., Jaffe, W., Tran, H., Tsvetanov, Z., Ford, H. C., Davies, J., and Schafer, J. (2001). WFPC2 Images of the Central Regions of Early-Type Galaxies. I. The Data. *AJ*, **121**, 2431–2482.
- Sandage, A. (1961). *The Hubble atlas of galaxies*.
- SDSS (2014). Orange Pie. [www.sdss.org/science](http://www.sdss.org/science) Last accessed 1 March 2015
- Searle, L. and Zinn, R. (1978). Compositions of halo clusters and the formation of the galactic halo. *ApJ*, **225**, 357–379.
- Sersic, J. L. (1968). *Atlas de galaxies australes*.
- Shapley, H. and Curtis, H. (1921). *The scale of the universe*. National research council of the National academy of sciences.
- Springel, V., White, S. D. M., Jenkins, A., Frenk, C. S., Yoshida, N., Gao, L., Navarro, J., Thacker, R., Croton, D., Helly, J., Peacock, J. A., Cole, S., Thomas, P., Couchman, H., Evrard, A., Colberg, J., and Pearce, F. (2005). Simulations of the formation, evolution and clustering of galaxies and quasars. *Nature*, **435**, 629–636.
- Thomas, D., Maraston, C., Bender, R., and Mendes de Oliveira, C. (2005). The Epochs of Early-Type Galaxy Formation as a Function of Environment. *ApJ*, **621**, 673–694.
- Toomre, A. (1977). Mergers and Some Consequences. In B. M. Tinsley and R. B. G. Larson, D. Campbell, editors, *Evolution of Galaxies and Stellar Populations*, page 401.

- Trujillo, I. (2013). The size and mass evolution of the massive galaxies over cosmic time. In D. Thomas, A. Pasquali, and I. Ferreras, editors, *IAU Symposium*, volume 295 of *IAU Symposium*, pages 27–36.
- Trujillo-Gomez, S., Klypin, A., Primack, J., and Romanowsky, A. J. (2011). Galaxies in  $\Lambda$ CDM with Halo Abundance Matching: Luminosity-Velocity Relation, Baryonic Mass-Velocity Relation, Velocity Function, and Clustering. *ApJ*, **742**, 16.
- van den Bergh, S. (1976). A new classification system for galaxies. *ApJ*, **206**, 883–887.
- van den Bosch, F. C., Ferrarese, L., Jaffe, W., Ford, H. C., and O’Connell, R. W. (1994). Hubble Space Telescope photometry of the central regions of Virgo cluster elliptical galaxies. II: Isophote shapes. *AJ*, **108**, 1579–1597.
- York, D. G., Adelman, J., Anderson, Jr., J. E., Anderson, S. F., Annis, J., Bahcall, N. A., Bakken, J. A., Barkhouser, R., Bastian, S., Berman, E., Boroski, W. N., Bracker, S., Briegel, C., Briggs, J. W., Brinkmann, J., Brunner, R., Burles, S., Carey, L., Carr, M. A., Castander, F. J., Chen, B., Colestock, P. L., Connolly, A. J., Crocker, J. H., Csabai, I., Czarapata, P. C., Davis, J. E., Doi, M., Dombeck, T., Eisenstein, D., Ellman, N., Elms, B. R., Evans, M. L., Fan, X., Federwitz, G. R., Fiscelli, L., Friedman, S., Frieman, J. A., Fukugita, M., Gillespie, B., Gunn, J. E., Gurbani, V. K., de Haas, E., Haldeman, M., Harris, F. H., Hayes, J., Heckman, T. M., Hennessy, G. S., Hindsley, R. B., Holm, S., Holmgren, D. J., Huang, C.-h., Hull, C., Husby, D., Ichikawa, S.-I., Ichikawa, T., Ivezić, Ž., Kent, S., Kim, R. S. J., Kinney, E., Klaene, M., Kleinman, A. N., Kleinman, S., Knapp, G. R., Korienek, J., Kron, R. G., Kunszt, P. Z., Lamb, D. Q., Lee, B., Leger, R. F., Limmongkol, S., Lindenmeyer, C., Long, D. C., Loomis, C., Loveday, J., Lucinio, R., Lupton, R. H., MacKinnon, B., Mannery, E. J., Mantsch, P. M., Margon, B., McGehee, P., McKay, T. A., Meiksin, A., Merelli, A., Monet, D. G., Munn, J. A., Narayanan, V. K., Nash, T., Neilsen, E., Neswold, R., Newberg, H. J., Nichol, R. C., Nicinski, T., Nonino, M., Okada, N., Okamura, S., Ostriker, J. P., Owen, R., Pauls, A. G., Peoples, J., Peterson, R. L., Petravick, D., Pier, J. R., Pope, A., Pordes, R., Prosapio, A., Rechenmacher, R., Quinn, T. R., Richards, G. T., Richmond, M. W., Rivetta, C. H., Rockosi, C. M., Ruthmansdorfer, K., Sandford, D., Schlegel, D. J., Schneider, D. P., Sekiguchi, M., Sergey, G., Shimasaku, K., Siegmund, W. A., Smee, S., Smith, J. A., Snedden, S., Stone, R., Stoughton, C., Strauss, M. A., Stubbs, C., SubbaRao, M., Szalay, A. S., Szapudi, I., Szokoly, G. P., Thakar, A. R., Tremonti, C., Tucker, D. L., Uomoto, A., Vanden Berk, D., Vogeley, M. S., Waddell, P., Wang, S.-i., Watanabe, M., Weinberg, D. H., Yanny, B., Yasuda, N., and SDSS Collaboration (2000). The Sloan Digital Sky Survey: Technical Summary. *AJ*, **120**, 1579–1587.
- Zheng, W., Postman, M., Zitrin, A., Moustakas, J., Shu, X., Jouvel, S., Høst, O., Molino, A., Bradley, L., Coe, D., Moustakas, L. A., Carrasco, M., Ford, H., Benítez, N., Lauer, T. R., Seitz, S., Bouwens, R., Koekemoer, A., Medezinski, E., Bartelmann, M., Broadhurst, T., Donahue, M., Grillo, C., Infante, L., Jha, S. W.,

---

Kelson, D. D., Lahav, O., Lemze, D., Melchior, P., Meneghetti, M., Merten, J., Nonino, M., Ogaz, S., Rosati, P., Umetsu, K., and van der Wel, A. (2012). A magnified young galaxy from about 500 million years after the Big Bang. *Nature*, **489**, 406–408.

---

# CHAPTER 2: A CENSUS OF NUCLEAR STELLAR DISCS IN EARLY-TYPE GALAXIES

---

Based on Ledo, H. R.; Sarzi, M.; Dotti, M.; Khochfar, S.; Morelli, L. (2010). A census of nuclear stellar discs in early-type galaxies. *MNRAS*, Volume 407, Issue 2, pp. 969-985

## 2.1 Introduction

More than a decade ago, Hubble Space Telescope (HST) observations revealed the presence of Nuclear Stellar Discs (NSD) in several galaxies (van den Bosch *et al.*, 1994a). These discs are distinct nuclear components with a few tens to hundreds of parsecs in diameter and have since then been recognised as a relatively common feature in early-type galaxies (e.g. Rest *et al.*, 2001) while being notably rare in spirals (Pizzella *et al.*, 2002). Despite the relatively high frequency of NSDs only a few studies were aimed at deriving their fundamental properties (Scorza and van den Bosch, 1998a; Pizzella *et al.*, 2002; Morelli *et al.*, 2004; Balcells *et al.*, 2007), whereas the interest in NSD revolved mainly around their dynamically cold character, which facilitates the mass measurement of central supermassive black holes (SMBHs) (e.g. van den Bosch and de Zeeuw, 1996).

Yet, NSDs may constitute a unique tool to constrain the assembling history of galaxies. NSDs are indeed fragile structures that should not survive a major merger event involving their host galaxy, which makes them useful clocks to trace the epoch since such an event occurred. Simple N-body simulations serve to illustrate the delicate nature of NSDs (Fig. 2.1). Following Dotti *et al.* (2007) we set up a stable stellar disc that is 200 pc across,  $10^8 M_{\odot}$  in mass and which is orbiting around a central SMBH of the same mass in the total gravitational potential dictated also by the stellar bulge and dark-matter halo. We have then let loose a second  $10^8 M_{\odot}$  SMBH 80 pc above the galactic plane in a nearly circular polar orbit and follow the evolution of the disc. Given that early-type galaxies share the same black-hole mass content (Ferrarese and Merritt, 2000; Gebhardt *et al.*, 2000), the interaction with a second SMBH of the same mass serves to explore in conservative way (without even considering the interaction with the stars around the second SMBH) the impact on

the disc of a merging event with second galaxy of similar mass. Figure 2.1 shows how after just 2.5 Myr the interaction with the alien SMBH has considerably disrupted the structure of the disc, which by becoming more vertically extended and radially concentrated would be very hard to detect.

A systematic study of the incidence of NSD in early-type galaxies could therefore help constraining their assembling history, which, contrary to their star-formation history (e.g. Thomas *et al.*, 2005), is poorly understood. According to the standard hierarchical paradigm for galaxy formation, the most massive galaxies should have been the last to reach their final configuration as they follow the merging paths of their host dark-matter haloes. The galactic environment should also play a role since once galaxies enter very crowded environments such as galaxy clusters it is more difficult for them to merge due to the high relative velocities with which they cross each other. These dependencies are illustrated in Fig. 2.2, which shows the predictions of the semi-analytical models of Khochfar and Silk (2006a,b) for the epoch of the last major merger experienced by galaxies of different masses and living in cluster or field environments. Semi-analytical models can also track whether the last merging events involved considerable amount of gas as well as the probability that a small gas-rich companion was subsequently acquired, which will then determine whether a NSD is found today. Numerical simulations (e.g. Barnes and Hernquist, 1996; Mayer *et al.*, 2007; Hopkins and Quataert, 2010) have indeed shown that when gas is involved in a merger event, it is always driven towards the centre of the remnant where it could then form a disc, depending on its angular momentum. Such scenario has been invoked to explain the dichotomy seen in elliptical galaxies (e.g. Khochfar and Burkert, 2005; Kormendy *et al.*, 2009a). NSDs could also provide constraints on the assembling history of their host galaxies in a more direct way, by dating the disc stellar population. In general, we expect the age of the stellar disc to represent a lower limit to the look-back time since the epoch of the last major merger event experienced by their host galaxy, since the NSD could have formed also after such an event, unless the last major merger was a gas rich event that led also to the formation of nuclear disc itself.

As a first step to use NSDs as tools to constrain the assembling history of early-type galaxies, in this chapter we will provide for the first time a complete census of the nearby NSD population, providing also estimates for basic physical properties such as their mass and extent. This work will provide the basis for further investigations, which will assess the fragility of the NSD identified here using a more comprehensive set of numerical simulations. Such set of fragile discs will constitute a sample for spectroscopic follow-up aimed at deriving their stellar ages, while the in-

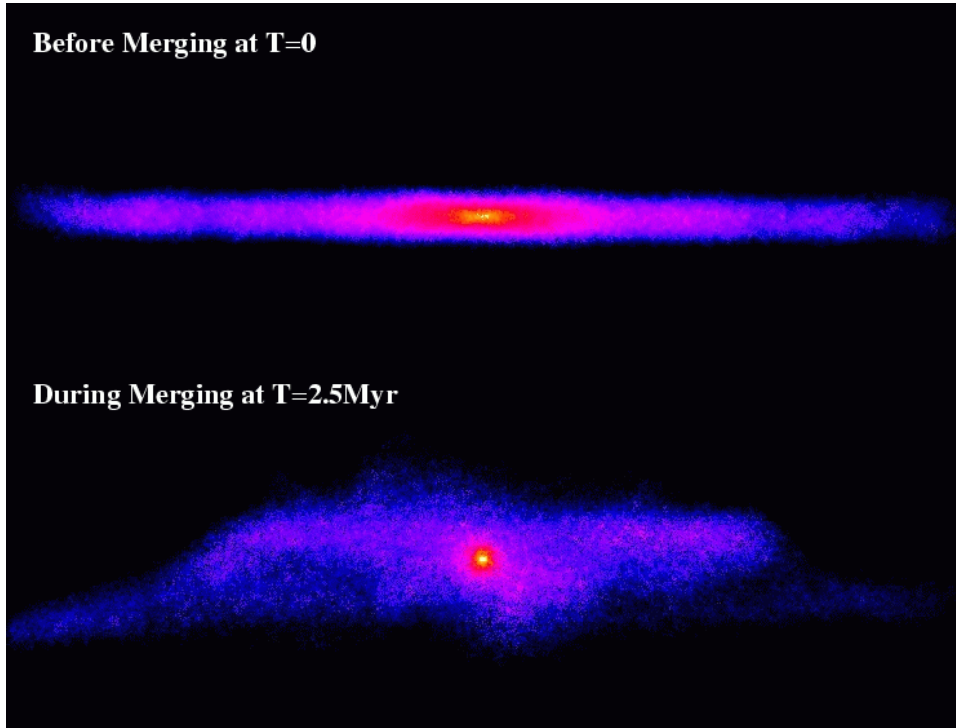


Fig. 2.1: N-body simulation illustrating the fragility of nuclear stellar discs during major merger events. The top panel shows a stable nuclear disc 200 pc in diameter and  $10^8 M_{\odot}$  in mass that is orbiting a SMBH of the same mass in the total gravitational potential dictated also by the bulge and the dark matter particles, which are not shown for the sake of clarity. A second  $10^8 M_{\odot}$  SMBH is let loose in a nearly circular polar orbit 80 pc above the galactic plane, to simulate the impact with a second galaxy of similar mass. The lower panel illustrates the disruption suffered by the disc after just 2.5 Myr, which would be even greater if the bulge and dark matter particle from the incoming galaxy would have been included in the simulation.

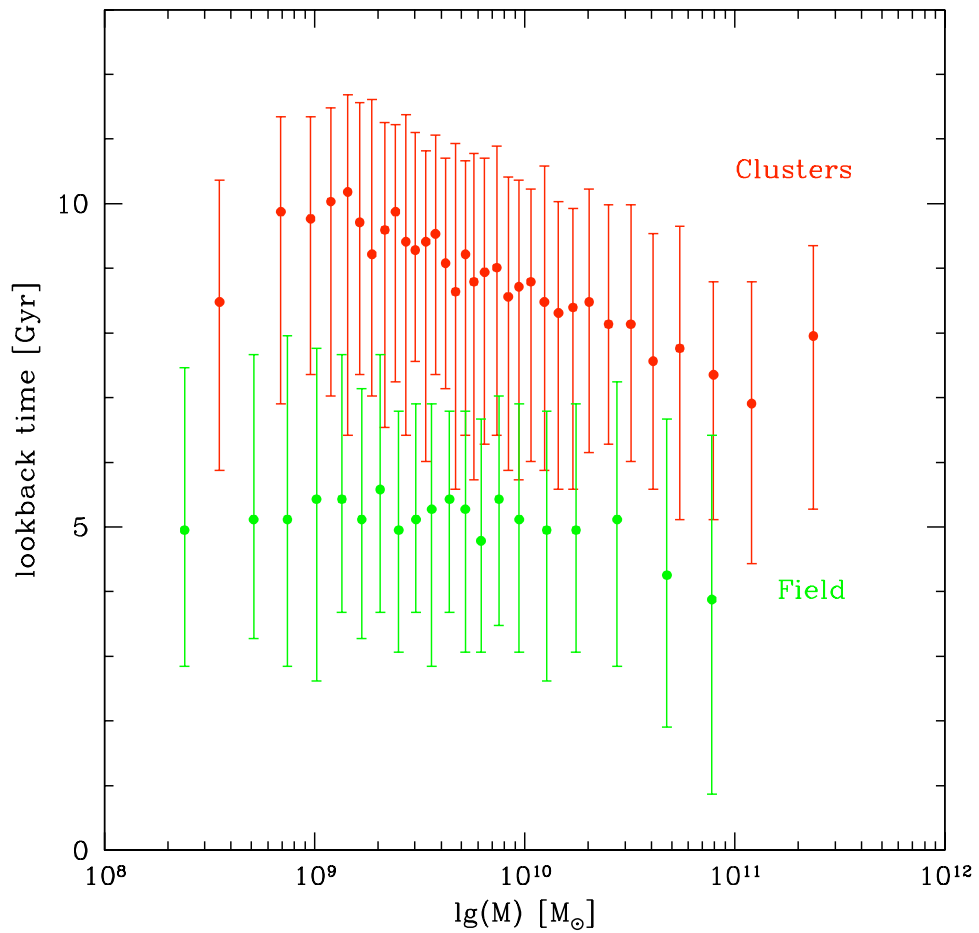


Fig. 2.2: Prediction of semi-analytical models from Khochfar and Silk (2006a,b) for the age of the last major merger event experienced by galaxies of different masses and in different environments. Field early-type galaxies appear to have assembled later than those in clusters. In clusters, the models also predict a clear dependence on mass, with larger galaxies assembling later.

vidence of such fragile discs could be compared with the prediction of semi-analytical models.

This chapter is organised as follows. To compile such a census we had to define a sample and retrieve the images (§2.3), to look for discs in these galaxies and to separate the discs from the bulges in order to find their properties (§2.4). The results will be presented in §2.5 and the conclusions in §2.6.

## 2.2 Sample selection and data mining

### 2.2.1 Selection and acquisition

For this study we have selected, using the LEDA database (Paturel *et al.*, 2003), all early-type galaxies (E, E-S0, S0 and S0-a) within 100 Mpc so as to produce a volume-limited sample. This list was then cross-correlated with the HST archive and all the galaxies with images from the WFPC2 and ACS cameras were requested, preferably the filters F555W and F606W. In some cases these filters were not available and others had to be chosen. The use of different passbands should not bias our estimates of the disc inclination and extent, however, as shown by Morelli *et al.* (2010) nuclear discs do not present strong radial colour gradients.

After downloading the available images they were checked for their quality and those saturated, too dusty or in which the galaxy was lying at the edge of the detector were discarded since in these cases it would have been impossible to find NSDs even if they were present. In the end we collected a sample of 466 early-type galaxies with HST images, out of a parent LEDA sample of 6801 galaxies.

### 2.2.2 Sample properties

Having a sample, we retrieved the global parameters of our galaxies. Of particular interest are  $M_B$  and an estimate of the galactic environment, because they directly relate to the general questions we are trying to answer, and the galaxy inclination because it influences our ability to find the discs. The magnitude of our galaxies and an estimate for their inclination values are available from the LEDA database whereas to obtain a value for the galactic density we used the Nearby Galaxies Catalogue of Tully (1988).

Although the distribution of  $M_B$  and environment values for our HST sample and its parent LEDA sample are somewhat different this does not pose as a problem when we are dealing with the incidence of NSD. Indeed in this case it only matters that in each magnitude bin we have enough objects to obtain secure estimates for

the NSD fraction. Also inclination differences do not matter for constraining the incidence of NSDs, as long as the distribution of inclination in each HST subsample allows a reliable correction of the fraction of NSD (that is if there are enough galaxies where the disc could have been detected, see §2.4.1). On the other hand we need to keep in mind that any conclusion on the structural properties of the NSDs, such as their typical size or mass, will be specific to our HST sample.

### 2.2.3 Inclination

The more face-on a disc is, the harder it is to identify it. Rix and White (1990) have studied this problem and concluded that for inclinations with  $\cos(i) > 0.6$  it is impossible to detect disk signatures in the galaxy isophotes. The inclination,  $i$ , is defined as being  $0^\circ$  for face-on discs and  $90^\circ$  if they are edge-on.

Although we do not know for sure the inclination of the nuclear discs, we will assume that the vast majority of them will have the same inclinations of their host galaxies, which is justified if we consider our sample galaxies as oblate axisymmetric spheroids. The LEDA database provides inclination estimates for the host galaxies based on the method applied by Heidmann *et al.* (1972) and Bottinelli *et al.* (1983). The inclination was calculated assuming all galaxies of a given Hubble type had an axis ratio equal to that observed in the flattest galaxy of that type. By construction, this method provides a conservative lower estimate for our galaxies' inclination, since intrinsically rounder galaxies in a given Hubble type would in reality have a higher inclination. Using such lower estimates to correct the fraction of NSD will lead to an upper limit on their incidence, whereas the uncorrected fraction provides a lower limit as if we were assuming that all galaxies were edge-on.

## 2.3 Analysis

### 2.3.1 Disc identification process

Having collected the HST images of 466 early-type galaxies, we systematically searched for the signature of the presence of a NSD, both in maps for the fine structure of the galaxy and in the shape of the galaxy isophotes.

We have used the code of Pogge and Martini (2002) to generate structure maps for each of our sample galaxies, taking care to use in each case the appropriate WFPC2 or ACS point-spread function from the Tiny Tim code (Krist and Hook, 2004), as

shown in equation 2.1.

$$\text{Structure Map} = \frac{\text{Original Image}}{\text{Original Image} \otimes \text{PSF}} \otimes \text{PSF}^t \quad (2.1)$$

where  $\otimes$  is the convolution operator and  $\text{PSF}^t$  is the transpose of the PSF ( $\text{PSF}^t(x, y) = \text{PSF}(-x, -y)$ ). Within Tiny Tim, the desired parameters such as camera, chip, position, filter, spectrum and PSF size can be defined (routine *tiny1*) in order to generate the model PSF (*tiny2*). At this stage we have the PSF for WFPC and WFPC2, but not for the ACS as this camera is situated away from the telescope’s optical axis, which causes a significant geometric distortion. A further step (*tiny3*) corrects this distortion. Being a model PSF, there are some limitations resulting from the impossibility of knowing exactly the state of the optical system being modelled. Changes in focus, aberrations, degradation (change in detector response, dust, damage) all influence the observed image and are not present in the model.

This procedure removes most of the large scale smooth light distribution and enhances surface-brightness fluctuations and non-circular structures, such as a nuclear disc. When convolving the original image by the PSF, the light from the nuclear disc is spread, leading to a slight light excess outside the disc region and lack of it in the central disc area. When the division is performed, the outcome, if a disc (or any other flattened structure) is present, is a bright elongated structure between dark areas. This means that foreground stars will also be enhanced, although they do not influence our visual disc detection, as they do not affect the overall result caused by central flattened isophotes. In Figure 2.3, several examples of non-detections are shown, where either sharp brightness fluctuations are absent or they do not present themselves as flattened disc-like structures. While the presence of a disc may be revealed by this process, to separate them from otherwise simply highly flattened central regions (e.g. a flattened bulge or a larger galactic-scale disc) we then fitted ellipses to the galaxy isophotes using the IRAF task *ellipse* and, in particular, extracted profiles for the galaxy ellipticity,  $\epsilon$ , and the  $a_4$  parameter, which is the 4<sup>th</sup> coefficient of the cosine term of the Fourier expansion of the considered isophotes (Carter, 1977; Jedrzejewski, 1987). In practice, the  $a_4$  parameter measures the deviation of the isophote’s shape from a perfect ellipse, and is positive in the case of disk-like deviations. *Ellipse* also allows to automatically flag outliers (such as stars or residual artefacts / cosmic-rays).

Figure 2.4 illustrates our disc-identification procedure for two sample galaxies whose structure maps were consistent with the possible existence of a disc. Upon ellipse fitting we search for a distinct peak in both the  $\epsilon$  and  $a_4$  profiles, which was

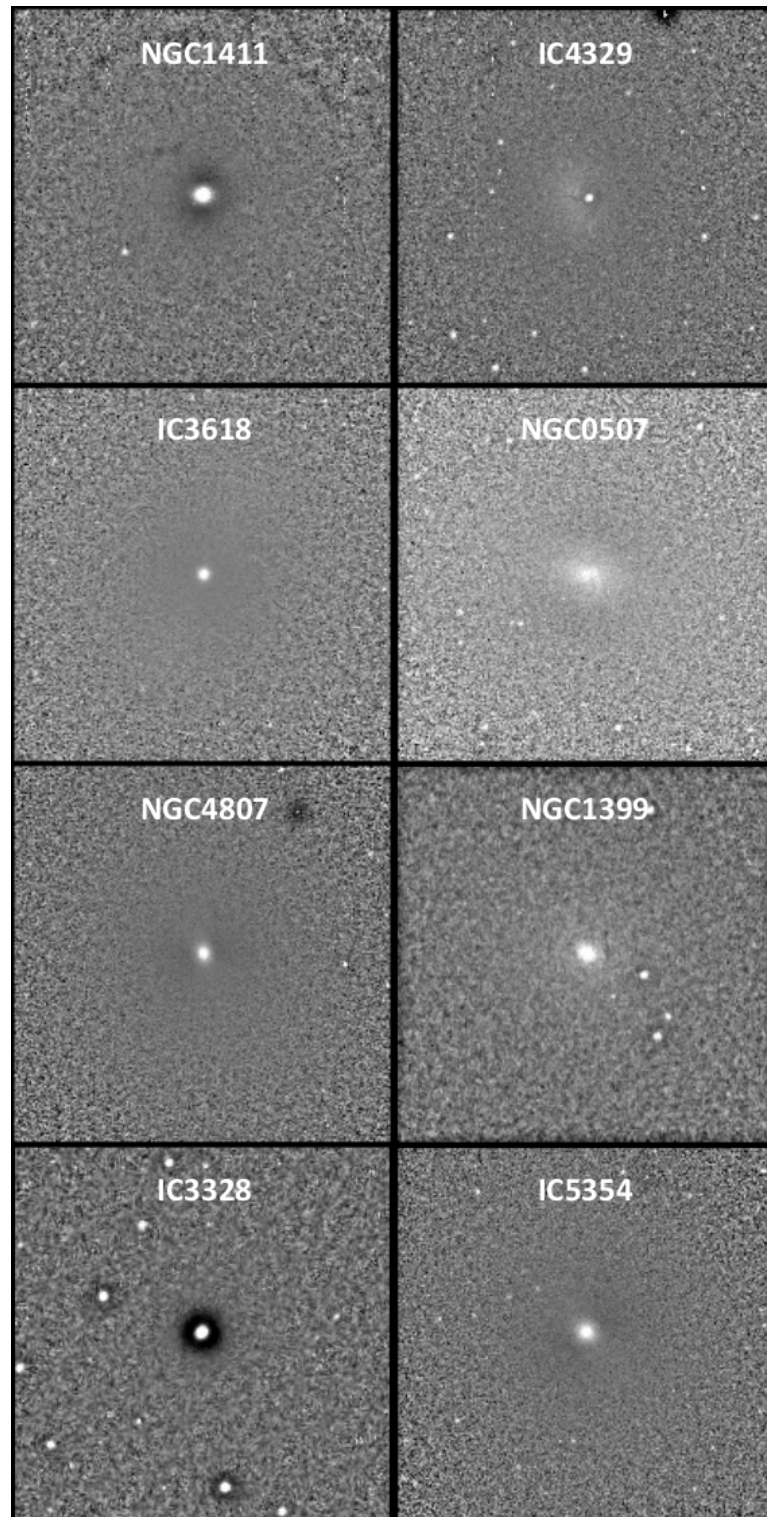


Fig. 2.3: This Figure shows a collection of structure maps that do not indicate the presence of a nuclear disc. Some maps do not show bright regions with the corresponding dark areas (IC 4329, IC 3618, NGC 1399), others may show faintly contrasting areas, which are indicative of a somewhat flattened central region, but not of a disc (NGC 0507, NGC 4807, IC 5354) and others do show sharp brightness fluctuations, but without flattening (NGC 1411, IC 3328).

not observed on NGC 2592 (top panel), but was on ESO 507-027 (bottom panel). Similar figures for all the galaxies where we identified the presence of a nuclear disc are presented in Appendix A.

Some of the galaxies in our sample have been previously studied. In Table 2.1 we present the values for the peak ellipticity and  $a_4$  (in the disc region), when available, and compare them with our own results. Our peak values for  $\epsilon$  and  $a_4$  are consistent with those from other studies, as one would expect given that all these measurements also relied on HST images and the use of the well-documented IRAF task *ellipse*.

### 2.3.2 Disc-bulge decomposition

Having identified which galaxies in our sample host a NSD, we now wish to investigate the basic properties of such discs by disentangling their contribution to the observed surface brightness distribution of the host galaxy. For early-type galaxies where the main bulge component displays simple elliptical isophotes we can adopt the algorithm devised by Scorza and Bender (1995a), whereby the best disc parameters (central brightness, scale-length and inclination) are sought by iteratively subtracting from the galaxy image an exponential disc model until the original signature of the disc is completely erased in the  $\epsilon$  and  $a_4$  profiles that are measured in the residual image. To perform the the Scorza & Bender decomposition on our sample nuclear discs we use the IDL implementation of this method of Morelli *et al.* (2004), where more details about the algorithm can be found.

Figure 2.5 illustrates for the ESO 507-027 how the disky deviations in the  $a_4$  profile are minimised after the subtraction of the best exponential disc model. Appendix B shows similar figures for all NSD that were found embedded in an elliptical bulge, whereas Table 2.9 lists their basic parameters.

### 2.3.3 Disc size estimates

For a large fraction of the NSD that we identified, we could not apply the previously described technique efficiently, mostly owing to the presence of an intrinsically boxy bulge, in particular if the boxiness changes with radius, or the presence of dust, which made it impossible to confidently minimise the  $\chi^2$  for some of the disc parameters. For other discs there was no definite minimum  $\chi^2$  when searching for the best-fitting parameters. The projections as seen in Fig. 2.5 were so broad that we could not confidently determine where the minima were. Under these circumstances we can at least estimate the extent of the NSD by exploiting the fact that the position of the peak of the  $a_4$  deviation introduced by the disc correlates loosely with the actual

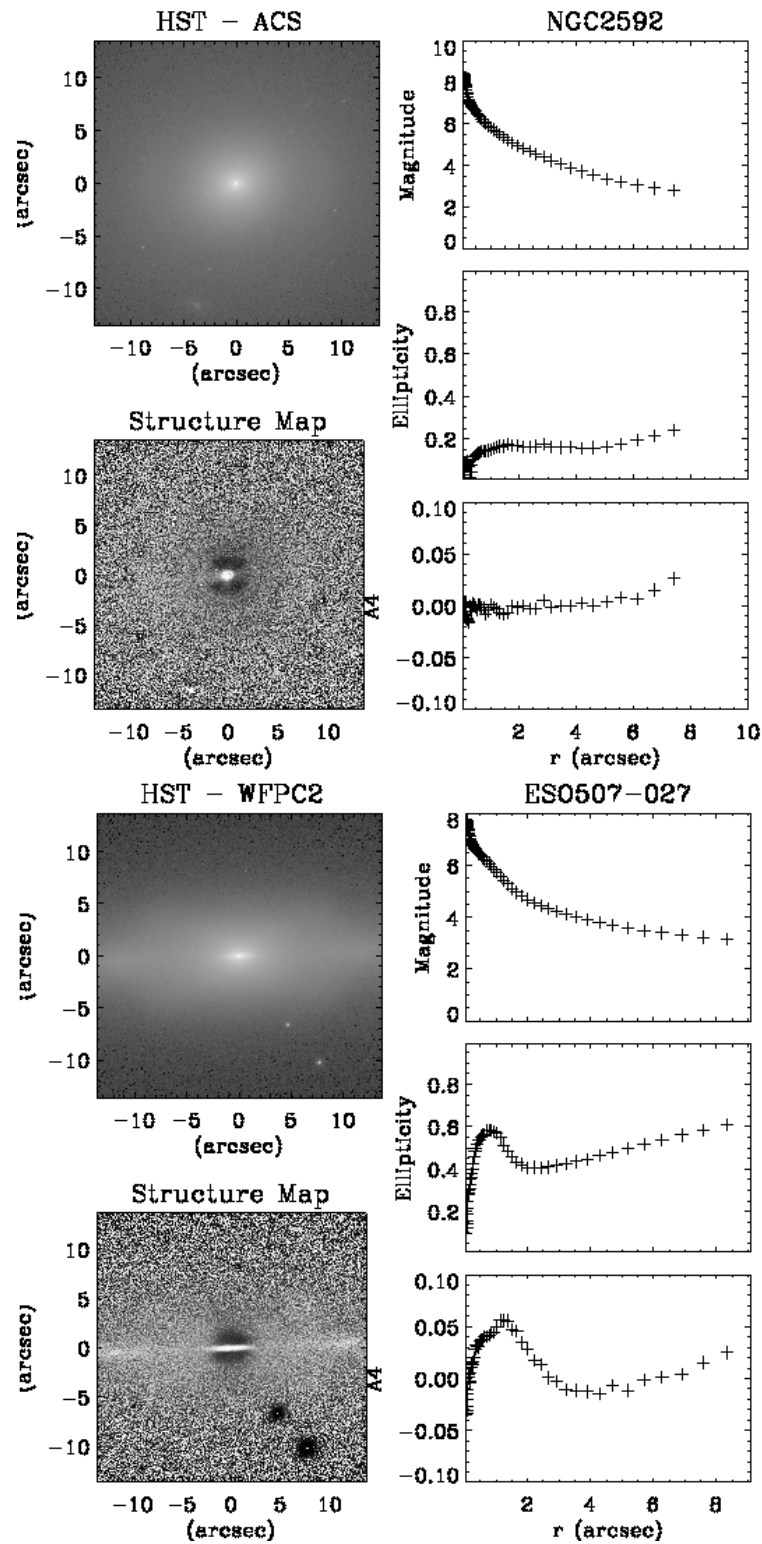


Fig. 2.4: On the top panel we have the original image of NGC 2592, its structure map and magnitude, ellipticity and  $a_4$  profiles where no Nuclear Stellar Disc is visible and, on the bottom we have the same information for ESO 507-027 where its presence is detected first visually on the structure maps and confirmed by the peaks in the ellipticity and  $a_4$ .

Galaxy	Parameter	Source				
		This work	M+04 <sup>a</sup>	K&J04 <sup>b</sup>	K+09 <sup>c</sup>	K&B12 <sup>d</sup>
NGC 4128	ellipticity	0.4	-	0.35	-	0.4
	a <sub>4</sub>	0.13	-	0.03	-	-
NGC 4318	ellipticity	0.3	-	-	0.35	-
	a <sub>4</sub>	0.02	-	-	0.015	-
NGC 4352	ellipticity	0.4	-	-	-	0.4
	a <sub>4</sub>	0.03	-	-	-	-
NGC 4458	ellipticity	0.4	0.5	-	0.6	-
	a <sub>4</sub>	0.04	0.04	-	0.02	-
NGC 4473	ellipticity	0.5	-	-	0.5	-
	a <sub>4</sub>	0.03	-	-	0.015	-
NGC 4478	ellipticity	0.45	0.45	-	0.45	-
	a <sub>4</sub>	0.02	0.02	-	0.02	-
NGC 4483	ellipticity	0.27	-	-	0.27	-
	a <sub>4</sub>	0.03	-	-	-	-
NGC 4515	ellipticity	0.55	-	-	0.55	-
	a <sub>4</sub>	0.04	-	-	0.015	-
NGC 4528	ellipticity	0.25	-	-	-	0.25
	a <sub>4</sub>	0.02	-	-	-	-
NGC 4570	ellipticity	0.3	-	-	0.4	-
	a <sub>4</sub>	0.05	-	-	0.05	-
NGC 4621	ellipticity	0.3	-	0.36	0.38	-
	a <sub>4</sub>	0.04	-	-	0.04	0.035
NGC 4623	ellipticity	0.4	-	-	-	0.45
	a <sub>4</sub>	0.04	-	-	-	-
NGC 4660	ellipticity	0.45	-	-	0.45	-
	a <sub>4</sub>	0.015	-	-	0.011	-
NGC 4762	ellipticity	0.3	-	-	-	0.85
	a <sub>4</sub>	0.04	-	-	-	-
NGC 5308	ellipticity	0.5	-	0.48	-	-
	a <sub>4</sub>	0.08	-	0.075	-	-

Table 2.1: In this table we can see a comparison between the ellipticity and a<sub>4</sub> parameters of some galaxies analysed in this work, for which data from other sources exist.

<sup>a</sup>Morelli *et al.* (2004)

<sup>b</sup>Krajinović and Jaffe (2004)

<sup>c</sup>Kormendy *et al.* (2009a)

<sup>d</sup>Kormendy and Bender (2012)

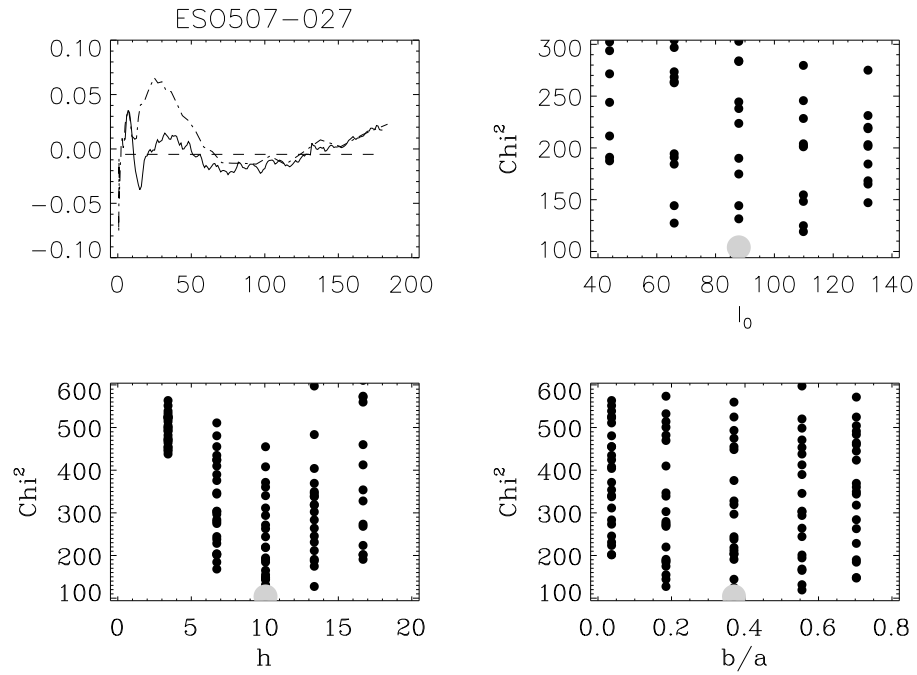


Fig. 2.5: On the top left panel we can see  $a_4$  profiles (radii are in units the HST-WFPC2 pixels) before (dot-dashed line) and after (solid line) the subtraction of the best exponential disc model as derived by the Scorza and Bender decomposition for ESO 507-027 (Section 2.3.2). The other three panels show the disc parameters, apparent central surface brightness (in counts  $s^{-1}$ ), scale length (in pixels) and axis ratio  $b/a$ , with their corresponding  $\chi^2$  values, computed from the residual  $a_4$  profiles after the subtraction of the model disc. The best parameters are represented by the larger grey circles.

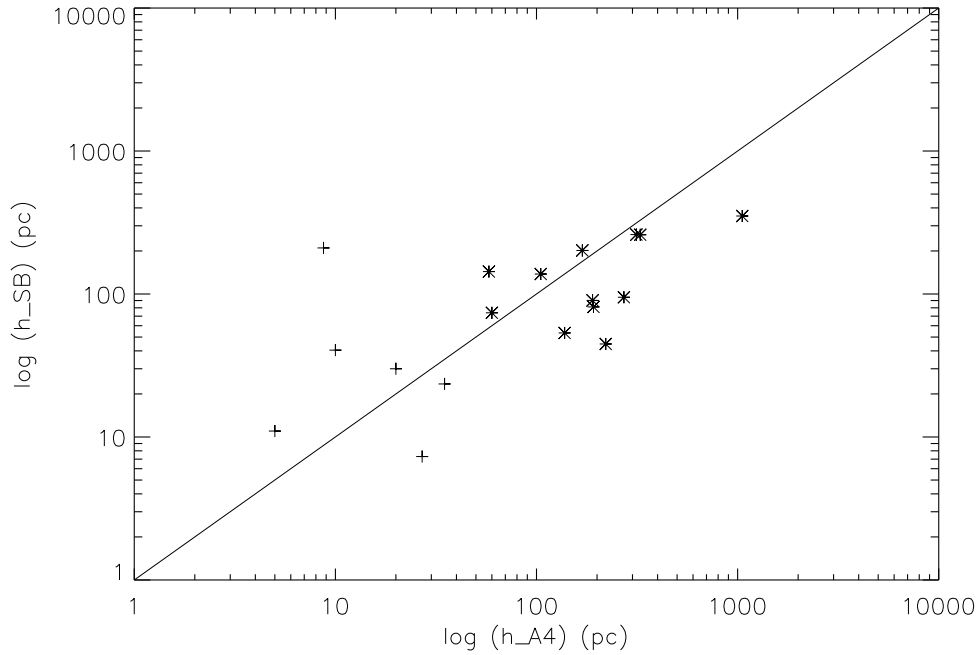


Fig. 2.6: Relation between the sizes derived from the peak in the  $a_4$  profile and those obtained from the Scorza and Bender decomposition. Asterisks represent the discs decomposed in this work and crosses show discs decomposed in previous works (van den Bosch *et al.*, 1994b; Scorza and Bender, 1995b; Scorza and van den Bosch, 1998a; Morelli *et al.*, 2004).

extent of the disc, as found in the objects for which a disc-bulge decomposition has been performed (Fig. 2.6). This allowed us to estimate the sizes of the discs which could not be decomposed with the Scorza and Bender method. They are listed in Tables 2.5 - 2.8.

## 2.4 Results

### 2.4.1 The census

By inspecting the structure maps and the isophotal shape of the central regions of 466 early-type galaxies we have found evidence for a distinct disc component in 63 objects, corresponding to 13.52% of our sample. Table 2.2 breaks down the observed fraction of NSDs as a function of galaxy type, whereas Tab. 2.3 and Tab. 2.4 show the incidence of NSDs as function of the B-band absolute magnitude and galactic environment, when such quantities could be measured.

### Inclination correction and final values

As mentioned in Sec 2.4, the inclination of the nuclear discs greatly affects our ability to detect them. It is indeed very likely that a considerable number of NSDs have escaped our detection because they lie in the equatorial plane of galaxies that are only slightly inclined from the plane of the sky, so that the NSDs appear close to face-on to us. The fraction of NSDs deduced directly from number of observed NSDs therefore represents only a lower limit for the true incidence of NSDs. We can estimate such true fraction considering that the number of NSDs that we have found should reflect the true fraction of NSD when considering only the systems where a NSDs could have in fact been detected, so that

$$f_{NSD} = \frac{f_{NSD,observed}}{f_{detectable,NSD}} \quad (2.2)$$

where  $f_{NSD,observed}$  is the observed fraction of NSDs in the entire sample and  $f_{detectable,NSD}$  is the fraction of galaxies where NSDs can be found. Using the estimates for the inclination of our sample galaxies that we retrieved in Sec 2.4, we can compute  $f_{detectable,NSD}$  considering that according to Rix and White (1990) the ability to detect an embedded disc drops very quickly for  $\cos(i) > 0.6$ , independent of the relative disc contribution to the total light distribution. Using the previous equation, the fraction of galaxies with  $\cos(i) < 0.6$  and considering that our inclination values are only lower estimates we can correct our face values for the incidence of NSDs and obtain upper limits for such fractions. These are also listed in Tabs. 2.2, 2.3 and 2.4.

Table 2.2 indicates that approximately between 13 and 23% of nearby early-type galaxies host nuclear stellar discs, without significant differences depending on their Hubble type. As regards the fraction of nuclear stellar disc as a function of their host absolute magnitude (Tab. 2.3), it would appear that the incidence of the discs peaks in the magnitude range between  $M_B = -20$  and  $-18$ , decreasing sharply in particular towards higher stellar luminosity where no NSD is found. In fact even accounting for the smaller number of surveyed systems in the  $-24$  to  $-22$  magnitude bin we should have found between 1 and 4 objects to be consistent with the fraction estimated in the  $-22$  to  $-20$  bin. Finally, there appears to be no significant trend with environment (Tab 2.4), at least as defined in Tully (1988), although we need to keep in mind that unfortunately only less than half of our sample was found in this particular catalogue.

Type	HST	NSDs	$f_{\text{NSDs,obs}}$	$f_{\text{HST,detect}}$	$f_{\text{NSDs}}$
(1)	(2)	(3)	(4)	(5)	(6)
E	219	22	$10.04 \pm 2.03$	52.97	$18.95 \pm 4$
E-S0	68	9	$13.24 \pm 4.11$	63.24	$20.9 \pm 6.2$
S0	109	21	$19.27 \pm 3.78$	66.97	$28.8 \pm 5.3$
S0-a	70	11	$15.71 \pm 4.35$	64.29	$24.44 \pm 6.8$
Total	466	63	$13.52 \pm 1.58$	59.44	$22.75 \pm 2.52$

Table 2.2: As a function of galaxy Hubble type (1) the number of objects with HST images and of the NSDs found in them (2)-(3) yield a lower limit on the incidence of NSDs in early-type galaxies (4). Using the fraction of objects where disc detection is possible (5) we can correct for inclination biases and obtain an upper limit on the fraction of NSDs (6)

$M_B$	HST	NSDs	$f_{\text{NSDs,obs}}$	$f_{\text{HST,detect}}$	$f_{\text{NSDs}}$
(1)	(2)	(3)	(4)	(5)	(6)
-24 to -22	16	0	0	81.3	0
-22 to -20	175	23	$13.1 \pm 2.6$	59.4	$22.1 \pm 4.1$
-20 to -18	174	34	$19.5 \pm 3.0$	62.6	$31.2 \pm 4.4$
-18 to -16	70	6	$8.6 \pm 3.4$	51.4	$16.7 \pm 6.2$
-16 to -15	17	0	0	53.0	0

Table 2.3: Same as Tab.2.2 but as a function of the galaxy absolute B-band magnitude (1), which was not available for 14 objects.

Density	HST	NSDs	$f_{\text{NSDs,obs}}$	$f_{\text{HST,detect}}$	$f_{\text{NSDs}}$
(1)	(2)	(3)	(4)	(5)	(6)
0-1	128	25	$19.5 \pm 3.5$	19.5	$33.3 \pm 5.4$
1-2	23	6	$26.1 \pm 9.2$	26.1	$35.3 \pm 11.6$
2-3	18	6	$33.3 \pm 11.1$	33.3	$42.9 \pm 13.2$
3-4	22	5	$22.7 \pm 8.9$	22.7	$41.7 \pm 14.2$

Table 2.4: Same as Tab. 2.2 but as a function of galactic environment (1), from Tully (1988). Only 191 objects were listed in this catalogue.

### 2.4.2 Properties of the decomposed discs

We have applied the Scorza & Bender disc-bulge decomposition to 12 discs, which doubles the number of NSD that were previously analysed in this way. Although a few more NSDs appeared embedded in well defined elliptical bulges, it was not possible to disentangle their light contribution. This is mainly because the observed  $a_4$  profile does not appear to be well described by the simple model we used for the discs. Scorza and van den Bosch (1998b) compiled all previous measurements for the structural properties of NSDs and plotted them together with other kinds of galactic discs in a  $\mu_c^0 - h$  plot, which has later been updated by Morelli *et al.* (2004) and that we present in Figure 2.7, to which we now add our own 12 objects. Although our values fall within the range found in previous results, confirming that NSDs follow a similar  $\mu_c^0 - h$  trend as embedded discs or main galactic discs, many of our decomposed NSDs appear to have a lower central surface brightness or smaller scale radius. In fact, the position of all NSDs in Fig 2.7 suggests that these may follow a somewhat steeper and offset relation compared to bigger discs.

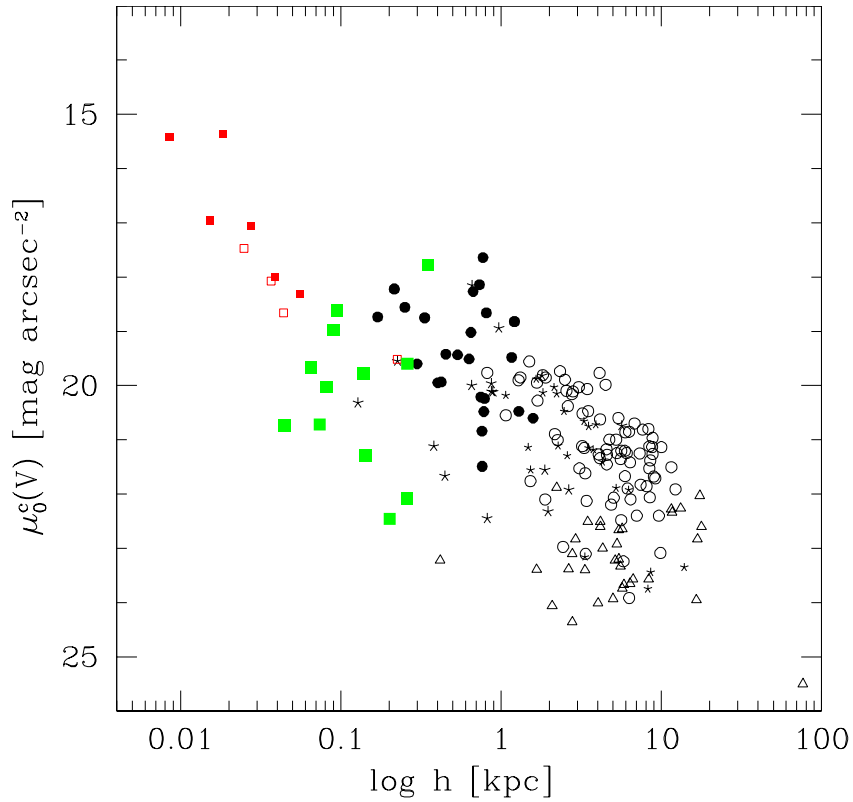


Fig. 2.7: Discs  $\mu_0^c - h$  diagram from Morelli *et al.* (2004). The open circles correspond to high surface-brightness spiral galaxies whereas low surface-brightness spirals are represented by triangles. Stars denote S0s and filled circles diskly ellipticals. NSDs in elliptical and lenticular galaxies are indicated by filled squares and in spirals by open squares. The larger green squares are those added in this work and the smaller red ones are the pre-existing ones.

## 2.5 Conclusions

Nuclear stellar discs have long been regarded as common features in early-type galaxies, but a quantitative assessment of such statements was still lacking prior to this work. By performing the most extensive volume-limited census of NSDs to date we have now shown that between 13 to 23% of nearby early-type galaxies host such systems. The incidence of nuclear stellar discs appears to decline in the most massive systems, consistent with the expectations that dry mergers dominated the most recent history of such objects (Khochfar and Burkert, 2003; Khochfar and Silk, 2009) and also with the finding that NSDs are exceedingly rare in brightest cluster galaxies (2%, Laine *et al.*, 2003). On the other hand, it is less clear what may cause the decrease in the fraction of NSDs that is found also at the faint end of our sample. Similarly, the lack of a dependence on galactic environment seems to contrast the first-order predictions of semi-analytical models (Fig. 2.2). In fact, according to these galaxies in clusters should have assembled much earlier and thus there should have been more time to regrow a nuclear disc. On the other hand, galaxies in cluster may not have ample reservoirs of cold gas at their disposal, in particular if orbiting within the hot-gas halo of the cluster, so that the early assembly of clusters does not make the presence of nuclear discs in cluster galaxies much more likely than in their field counterparts.

Using the well established technique of Scorza and Bender (1995a) to disentangle the light contribution of embedded discs from that of their surrounding bulges, we have extracted the structural parameters of 12 out of the 63 NSDs that we have identified. By doubling the number of NSDs we have shown even more convincingly that NSDs, like other kinds of large galactic discs, follow a correlation between the central surface brightness  $\mu_c^0$  and scale length  $h$ , although it would appear that NSDs obey a somewhat different relation with smaller scale lengths or fainter central surface brightness values. Considering that disc galaxies obey a very precise relation between their total luminosity and their maximum rotation velocity (the Tully-Fisher relation, Tully and Fisher, 1977) that may ultimately derive from the fact that they form in the dark matter halos that surround and dominate the mass budget of galaxies (Steinmetz and Navarro, 1999), it may not be completely unexpected that NSDs, by forming in the central and bulge-dominated regions of galaxies, may have different structural and dynamical properties than that of their larger relatives. In fact, it is also possible that the structural properties of NSDs vary when dealing with different kinds of early-type galaxies such as disky and boxy systems (Kormendy and Bender, 1996). Although the main reason for failing to isolate the disc component

in the presence of a bulge of varying boxiness with radius (Sec 3.3) has mostly to do with an unclear a priori for the intrinsic  $a_4$  profile that the bulge should have in the absence of a disc, we cannot exclude that in boxy ellipticals NSDs may have a different profile than exponential. Along the lines first suggested by Bender and Saglia (1999), NSDs in boxy ellipticals could be akin to the rapidly rotating components that in these objects are generally identified as kinematically decoupled cores, although in general such structures tend to extend over much larger scales than NSDs (McDermid *et al.*, 2006), in particular for massive ellipticals with the oldest stellar populations.

Finally, although for the majority of the NSDs we could not clearly separate the disc and bulge contributions to the central light of their host galaxies, we have nonetheless estimated their sizes using as a reference radius the distance from the centre where the diskiness of the central isophotes appears to peak. Such scale length estimate, coupled with the  $\mu_c^0 - h$  relation that NSDs appear also to obey and the N-body simulations, will be used in future investigations to assess which of our sample NSDs are indeed fragile against major merging events, thus providing good targets for a spectroscopic follow up aimed at constraining their stellar ages and thus, the time of their last major merger.

# References

- Balcells, M., Graham, A. W., and Peletier, R. F. (2007). Galactic Bulges from Hubble Space Telescope NICMOS Observations: Central Galaxian Objects, and Nuclear Profile Slopes. *ApJ*, **665**, 1084–1103.
- Barnes, J. E. and Hernquist, L. (1996). Transformations of Galaxies. II. Gasdynamics in Merging Disk Galaxies. *ApJ*, **471**, 115–+.
- Bender, R. and Saglia, R. P. (1999). Elliptical Galaxies: Detailed Structure, Scaling Relations and Formation. In D. R. Merritt, M. Valluri, & J. A. Sellwood, editor, *Galaxy Dynamics - A Rutgers Symposium*, volume 182 of *Astronomical Society of the Pacific Conference Series*, pages 113–+.
- Bottinelli, L., Gouguenheim, L., Paturel, G., and de Vaucouleurs, G. (1983). H I line studies of galaxies. II - The 21-cm-width as an extragalactic distance indicator. *A&A*, **118**, 4–20.
- Carter, D. (1977). Ph.D. thesis, , University of Cambridge, (1977).
- Dotti, M., Colpi, M., Haardt, F., and Mayer, L. (2007). Supermassive black hole binaries in gaseous and stellar circumnuclear discs: orbital dynamics and gas accretion. *MNRAS*, **379**, 956–962.
- Ferrarese, L. and Merritt, D. (2000). A Fundamental Relation between Supermassive Black Holes and Their Host Galaxies. *ApJ*, **539**, L9–L12.
- Fouqué, P., Solanes, J. M., Sanchis, T., and Balkowski, C. (2001). Structure, mass and distance of the Virgo cluster from a Tolman-Bondi model. *A&A*, **375**, 770–780.
- Gebhardt, K., Bender, R., Bower, G., Dressler, A., Faber, S. M., Filippenko, A. V., Green, R., Grillmair, C., Ho, L. C., Kormendy, J., Lauer, T. R., Magorrian, J., Pinkney, J., Richstone, D., and Tremaine, S. (2000). A Relationship between Nuclear Black Hole Mass and Galaxy Velocity Dispersion. *ApJ*, **539**, L13–L16.
- Heidmann, J., Heidmann, N., and de Vaucouleurs, G. (1972). Inclination and absorption effects on the apparent diameters, optical luminosities and neutral hydrogen radiation of galaxies-I, Optical and 21-cm line data. *MmRAS*, **75**, 85–+.
- Hopkins, P. F. and Quataert, E. (2010). The nuclear stellar disc in Andromeda: a fossil from the era of black hole growth. *MNRAS*, pages L62+.
- Jedrzejewski, R. I. (1987). CCD surface photometry of elliptical galaxies. I - Observations, reduction and results. *MNRAS*, **226**, 747–768.

- Khochfar, S. and Burkert, A. (2003). The Importance of Spheroidal and Mixed Mergers for Early-Type Galaxy Formation. *ApJ*, **597**, L117–L120.
- Khochfar, S. and Burkert, A. (2005). On the origin of isophotal shapes in elliptical galaxies. *MNRAS*, **359**, 1379–1385.
- Khochfar, S. and Silk, J. (2006a). A Simple Model for the Size Evolution of Elliptical Galaxies. *ApJ*, **648**, L21–L24.
- Khochfar, S. and Silk, J. (2006b). On the origin of stars in bulges and elliptical galaxies. *MNRAS*, **370**, 902–910.
- Khochfar, S. and Silk, J. (2009). Dry mergers: a crucial test for galaxy formation. *MNRAS*, **397**, 506–510.
- Kormendy, J. and Bender, R. (1996). A Proposed Revision of the Hubble Sequence for Elliptical Galaxies. *ApJ*, **464**, L119+.
- Kormendy, J. and Bender, R. (2012). A Revised Parallel-sequence Morphological Classification of Galaxies: Structure and Formation of S0 and Spheroidal Galaxies. *ApJS*, **198**, 2.
- Kormendy, J., Fisher, D. B., Cornell, M. E., and Bender, R. (2009a). Structure and Formation of Elliptical and Spheroidal Galaxies. *ApJS*, **182**, 216–309.
- Kormendy, J., Fisher, D. B., Cornell, M. E., and Bender, R. (2009b). Structure and Formation of Elliptical and Spheroidal Galaxies. *ApJS*, **182**, 216–309.
- Krajnović, D. and Jaffe, W. (2004). HST observations of nuclear stellar disks. *A&A*, **428**, 877–890.
- Krist, C. and Hook, R. (2004). *Tiny Tim User's Guide*.
- Laine, S., van der Marel, R. P., Lauer, T. R., Postman, M., O'Dea, C. P., and Owen, F. N. (2003). Hubble Space Telescope Imaging of Brightest Cluster Galaxies. *AJ*, **125**, 478–505.
- Mayer, L., Kazantzidis, S., Madau, P., Colpi, M., Quinn, T., and Wadsley, J. (2007). Rapid Formation of Supermassive Black Hole Binaries in Galaxy Mergers with Gas. *Science*, **316**, 1874–.
- McDermid, R. M., Emsellem, E., Shapiro, K. L., Bacon, R., Bureau, M., Cappellari, M., Davies, R. L., de Zeeuw, T., Falcón-Barroso, J., Krajnović, D., Kuntschner, H., Peletier, R. F., and Sarzi, M. (2006). The SAURON project - VIII. OASIS/CFHT integral-field spectroscopy of elliptical and lenticular galaxy centres. *MNRAS*, **373**, 906–958.
- Morelli, L., Halliday, C., Corsini, E. M., Pizzella, A., Thomas, D., Saglia, R. P., Davies, R. L., Bender, R., Birkinshaw, M., and Bertola, F. (2004). Nuclear stellar discs in low-luminosity elliptical galaxies: NGC 4458 and 4478. *MNRAS*, **354**, 753–762.

- Morelli, L., Cesetti, M., Corsini, E. M., Pizzella, A., Dalla Bontà, E., Sarzi, M., and Bertola, F. (2010). Multiband photometric decomposition of nuclear stellar disks. *A&A*, **518**, A32.
- Paturel, G., Petit, C., Prugniel, P., Theureau, G., Rousseau, J., Brouty, M., Dubois, P., and Cambrésy, L. (2003). HYPERLEDA. I. Identification and designation of galaxies. *A&A*, **412**, 45–55.
- Pizzella, A., Corsini, E. M., Morelli, L., Sarzi, M., Scarlata, C., Stiavelli, M., and Bertola, F. (2002). Nuclear Stellar Disks in Spiral Galaxies. *ApJ*, **573**, 131–137.
- Pogge, R. W. and Martini, P. (2002). Hubble Space Telescope Imaging of the Circumnuclear Environments of the CfA Seyfert Galaxies: Nuclear Spirals and Fueling. *ApJ*, **569**, 624–640.
- Rest, A., van den Bosch, F. C., Jaffe, W., Tran, H., Tsvetanov, Z., Ford, H. C., Davies, J., and Schafer, J. (2001). WFPC2 Images of the Central Regions of Early-Type Galaxies. I. The Data. *AJ*, **121**, 2431–2482.
- Rix, H.-W. and White, S. D. M. (1990). Disks in elliptical galaxies. *ApJ*, **362**, 52–58.
- Scorza, C. and Bender, R. (1995a). The internal structure of disk elliptical galaxies. *A&A*, **293**, 20–43.
- Scorza, C. and Bender, R. (1995b). The internal structure of disk elliptical galaxies. *A&A*, **293**, 20–43.
- Scorza, C. and van den Bosch, F. C. (1998a). Nuclear stellar discs in early-type galaxies - II. Photometric properties. *MNRAS*, **300**, 469–478.
- Scorza, C. and van den Bosch, F. C. (1998b). Nuclear stellar discs in early-type galaxies - II. Photometric properties. *MNRAS*, **300**, 469–478.
- Steinmetz, M. and Navarro, J. F. (1999). The Cosmological Origin of the Tully-Fisher Relation. *ApJ*, **513**, 555–560.
- Thomas, D., Maraston, C., Bender, R., and Mendes de Oliveira, C. (2005). The Epochs of Early-Type Galaxy Formation as a Function of Environment. *ApJ*, **621**, 673–694.
- Tully, R. B. (1988). *Nearby galaxies catalog*.
- Tully, R. B. and Fisher, J. R. (1977). A new method of determining distances to galaxies. *A&A*, **54**, 661–673.
- van den Bosch, F. C. and de Zeeuw, P. T. (1996). Self-Consistent, Axisymmetric Two-Integral Models of Elliptical Galaxies with Embedded Nuclear Discs. *MNRAS*, **283**, 381–399.

van den Bosch, F. C., Ferrarese, L., Jaffe, W., Ford, H. C., and O'Connell, R. W. (1994a). Hubble Space Telescope photometry of the central regions of Virgo cluster elliptical galaxies. II: Isophote shapes. *AJ*, **108**, 1579–1597.

van den Bosch, F. C., Ferrarese, L., Jaffe, W., Ford, H. C., and O'Connell, R. W. (1994b). Hubble Space Telescope photometry of the central regions of Virgo cluster elliptical galaxies. II: Isophote shapes. *AJ*, **108**, 1579–1597.

## 2.6 Appendix A: Nuclear stellar discs

### 2.6.1 Properties of the galaxies with discs

Table 2.5: Galaxies where discs were found and some of their properties. (1) Galaxy's name; (2) Hubble type; (3)  $\log_{10}$  of the axis ratio; (4)  $\log_{10}$  of the apparent major axis diameter  $d_{25}$  at 25 mag;  $\text{arcsec}^{-2}$ ; (5) disc inclination; (6) absolute B-magnitude; (7) radial velocity corrected for Local Group infall towards Virgo ( $208 \text{ km s}^{-1}$ ); (8) Distance derived from (7) and assuming  $H_0=72 \text{ km s}^{-1} \text{ Mpc}^{-1}$ , except for Virgo cluster members for which we adopted a common distance of  $18 \text{ Mpc}$  (Fouqué *et al.*, 2001); (9) Density from Tully (1988); (10) Disc size with the indication in (11) of the source of the values, where  $M$  are those measured with the decomposition procedure,  $E$  have been estimated using the peak of the  $a_4$  and  $L$  come from the literature.

Name	Type	$\log r_{25}$	$\log d_{25}$	inclination ( $^\circ$ )	mabs	$V_{\text{vir}}$ ( $\text{km s}^{-1}$ )	distance (Mpc)	Density ( $\text{Mpc}^{-3}$ )	Disc size (pc)	Source
(1)	(2)	(3)	(4)	(5)	(6)	(7)	(8)	(9)	(10)	(11)
ESO 352-057	S0	0.327	1.014	82.98	-19.842	5736.2	76.11	-	44.74	M
ESO 378-020	S0	0.243	1.186	68.17	-19.899	5479.7	39.87	-	53.39	M
ESO 507-027	S0	0.682	1.251	90.0	-20.079	2870.7	43.27	-	94.87	M
IC 0875	S0	0.234	1.16	67.23	-19.442	3115.4	42.32	-	259.67	M
NGC 0584	E	0.179	1.578	79.78	-20.891	3047.0	24.49	0.42	90.18	M
NGC 1023	E-S0	0.377	1.868	76.7	-20.914	769.9	10.69	0.57	57	E
NGC 1129	E	0.42	1.444	90.0	-21.604	5404.8	75.07	-	146	E
NGC 1351	E-S0	0.189	1.532	65.35	-19.004	1301.0	18.07	1.57	131	E
NGC 1381	S0	0.421	1.405	90.0	-19.338	1520.6	21.12	1.54	131	E
NGC 1426	E	0.175	1.457	78.27	-19.092	1263.2	17.54	0.66	43	E
NGC 1427	E	0.179	1.636	71.35	-19.399	1159.2	16.10	1.59	16	E
NGC 1439	E	0.02	1.473	23.03	-19.507	1486.8	20.65	0.45	130	E
NGC 2549	S0	0.594	1.563	90.0	-19.445	1248.6	17.34	0.13	42	E
NGC 2685	S0-a	0.272	1.636	68.79	-19.092	1094.2	15.2	0.13	66	E
NGC 2787	S0-a	0.249	1.510	65.86	-19.645	949.0	13.18	0.06	115	E
NGC 2865	E	0.082	1.382	45.2	-20.792	2578.8	35.82	0.11	191	E

Table 2.6: Continuation of properties table.

Name	Type	$\log r_{25}$	$\log d_{25}$	inclination	mabs	$V_{\text{vir}}$	distance	Density	Disc size	Source
(1)	(2)	(3)	(4)	(5)	(6)	(7)	(8)	(9)	(10)	(11)
NGC 3115	E-S0	0.383	1.916	81.6	-20.042	642.6	8.93	0.08	30.0	L <sup>1</sup>
NGC 3156	S0	0.28	1.282	79.15	-18.512	1340.3	18.62	0.2	63	E
NGC 3377	E	0.327	1.588	90.0	-19.163	744.5	10.34	0.49	35	E
NGC 3384	E-S0	0.349	1.717	90.0	-19.826	917.1	12.74	0.54	49	E
NGC 3385	S0	0.267	1.182	72.56	-21.927	7824.4	108.67	-	351.19	M
NGC 3610	E	0.027	1.375	25.95	-20.664	1943.4	26.99	0.3	260.38	M
NGC 3613	E	0.315	1.544	90.0	-20.864	2232.9	31.01	-	15	E
NGC 3706	E-S0	0.167	1.477	61.64	-21.117	2817.9	39.14	0.27	114	E
NGC 3818	E	0.199	1.387	90.0	-19.389	1678.7	23.32	0.2	23	E
NGC 3900	S0-a	0.311	1.413	70.82	-20.168	1942.8	26.98	0.13	-	E
NGC 3945	S0-a	0.227	1.744	63.17	-20.085	1496.5	20.78	0.5	50	E
NGC 4026	S0	0.702	1.644	90.0	-19.592	1206.5	16.76	1.71	41	E
NGC 4128	S0	0.519	1.344	90.0	-20.041	2591.1	36.0	0.27	138.01	M
NGC 4270	S0	0.392	1.269	72.8	-19.702	2414.3	18.0	0.83	43.63	E
NGC 4318	E	0.167	0.869	79.12	-17.285	1297.6	18.02	1.47	70	E
NGC 4342	E-S0	0.297	1.101	90.0	-16.954	810.7	11.26	2.64	7.3	L <sup>2</sup>

<sup>a</sup> Scorza and Bender (1995b)<sup>b</sup> Scorza and van den Bosch (1998a)

Table 2.7: Continuation of properties table.

Name	Type	$\log r_{25}$	$\log d_{25}$	inclination ( $^{\circ}$ )	mabs	$V_{\text{vir}}$ ( $\text{kms}^{-1}$ )	distance (Mpc)	Density ( $\text{Mpc}^{-3}$ )	Disc size (pc)	Source
(1)	(2)	(3)	(4)	(5)	(6)	(7)	(8)	(9)	(10)	(11)
NGC 4352	S0	0.331	1.231	90.0	-19.056	2164.4	18.0	-	17.45	E
NGC 4458	E	0.03	1.204	28.77	-17.437	770.0	10.69	3.21	11.0	L <sup>3</sup>
NGC 4473	E	0.235	1.630	90.0	-21.707	2338.1	18.0	2.17	183.26	E
NGC 4474	S0	0.174	1.368	57.3	-19.652	1707.6	18.0	3.8	143.5	M
NGC 4478	E	0.089	1.243	50.85	-19.602	1479.7	20.55	3.92	40.5	L <sup>3</sup>
NGC 4483	S0-a	0.282	1.265	71.34	-17.632	958.3	13.31	3.83	13	E
NGC 4515	E-S0	0.099	1.123	45.77	-17.775	1059.8	14.72	-	36	E
NGC 4528	S0	0.271	1.208	73.43	-18.874	1453.4	20.19	-	10	E
NGC 4546	E-S0	0.254	1.510	75.96	-19.726	1064.1	14.78	0.27	43	E
NGC 4570	S0	0.618	1.597	90.0	-20.444	1813.0	18.0	2.66	23.5	L <sup>2</sup>
NGC 4621	E	0.152	1.658	71.93	-20.789	527.1	18.0	2.6	73.87	M
NGC 4623	S0-a	0.477	1.352	90.0	-19.005	1863.7	18.0	2.36	210	L <sup>4</sup>
NGC 4660	E	0.124	1.323	61.24	-19.241	1185.1	18.0	3.37	81.19	M
NGC 4742	E	0.191	1.358	90.0	-19.376	1257.0	17.46	0.73	51	E
NGC 4762	S0	0.37	1.917	90.0	-19.921	1065.4	18.0	2.65	226.89	E
NGC 4866	S0-a	0.768	1.761	90.0	-20.727	2095.8	18.0	1.08	26.18	E
NGC 5076	S0-a	0.138	1.126	48.83	-19.491	2975.3	41.32	-	621	E

<sup>b</sup> Scorza and van den Bosch (1998a)

<sup>c</sup> Morelli *et al.* (2004)

<sup>d</sup> van den Bosch *et al.* (1994b)

Table 2.8: Continuation of properties table.

Name	Type	$\log r_{25}$	$\log d_{25}$	inclination ( $^{\circ}$ )	mabs	$V_{\text{vir}}$ ( $\text{kms}^{-1}$ )	distance (Mpc)	Density ( $\text{Mpc}^{-3}$ )	Disc size (pc)	Source
(1)	(2)	(3)	(4)	(5)	(6)	(7)	(8)	(9)	(10)	(11)
NGC 5252	S0	0.233	1.111	67.18	-21.039	6967.0	96.76	-	-	E
NGC 5308	S0	0.877	1.642	90.0	-20.439	2279.5	31.66	0.45	201.59	M
NGC 5389	S0-a	0.67	1.51	90.0	-19.65	2109	29.29	-	1377.4	L <sup>5</sup>
NGC 5838	E-S0	0.47	1.59	90.0	-20.05	1451	20.15	-	1684.2	L <sup>5</sup>
NGC 5854	S0-a	0.58	1.483	90.0	-19.698	1833.0	25.46	0.74	1147.9	L <sup>5</sup>
NGC 7173	E	0.088	1.275	47.16	-19.897	2368.8	32.90	0.35	48	E
NGC 7176	E	0.024	1.569	25.29	-20.423	2387.5	33.16	0.39	64	E
NGC 7562	E	0.137	1.338	67.29	-21.427	3571.8	49.61	-	-	E
NGC 7585	S0-a	0.123	1.406	46.52	-21.291	3432.0	47.67	-	69	E
NGC 7619	E	0.106	1.407	56.04	-21.987	3798.5	52.76	-	256	E
NGC 7785	E	0.283	1.447	90.0	-21.411	3875.7	53.83	-	497	E
PGC 013343	E-S0	0.039	1.030	28.55	-16.909	1486.7	20.65	-	100	E
PGC 036465	S0-a	0.307	0.825	67.59	-19.656	5736.2	79.67	-	232	E
PGC 044815	S0	0.35	0.7	90.0	-18.58	6784	94.22	-	1005	E
UGC 01003	S0	0.346	0.922	90.0	-19.488	5192.1	72.11	-	105	E
UGC 03426	S0	0.096	1.224	42.78	-20.869	4292.5	59.62	-	58	E

<sup>e</sup> Balcells *et al.* (2007)

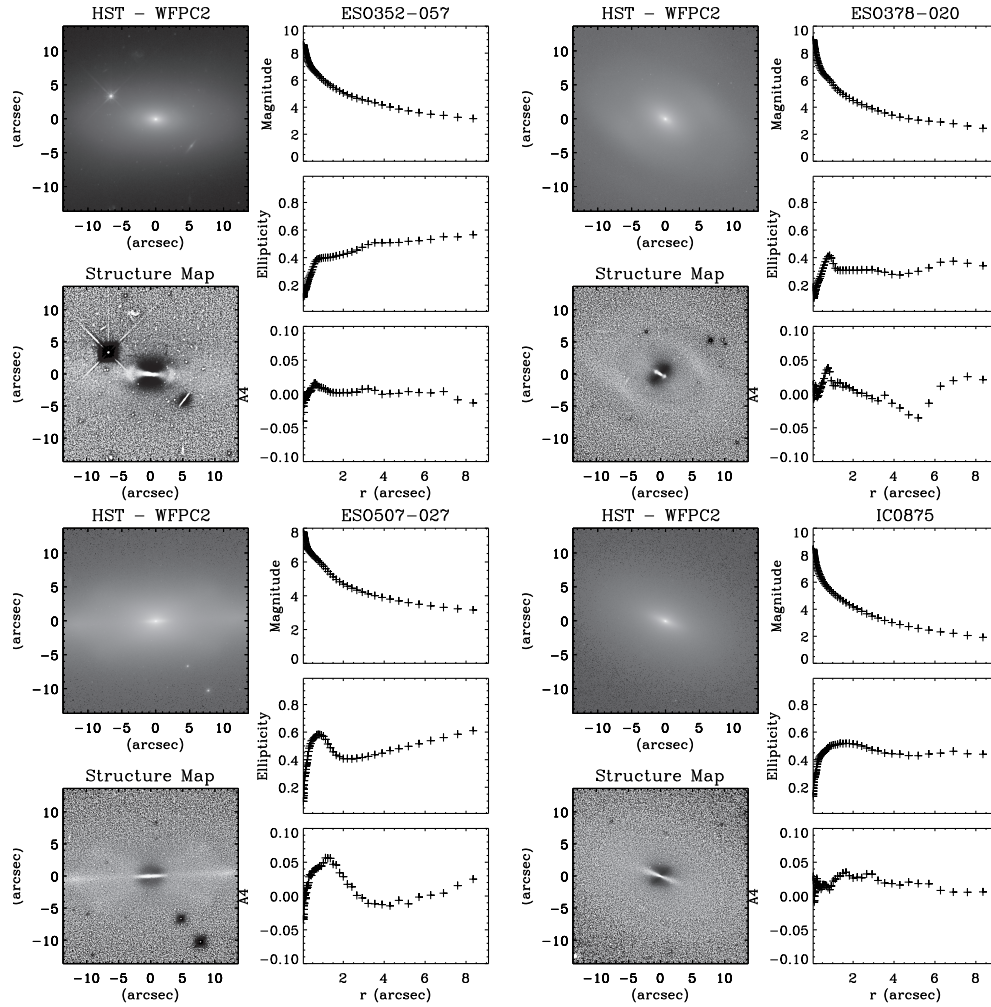
2.6.2 NSD structure maps, ellipticity and  $a_4$  profiles

Fig. 2.8: ESO 352-057 on the top left, ESO 378-020 on the top right, ESO 507-027 on the bottom left and IC 0875 on the bottom right. The original images and the structure maps are shown on the left of each panel and on the right we can see the surface brightness, ellipticity and  $a_4$  profiles.

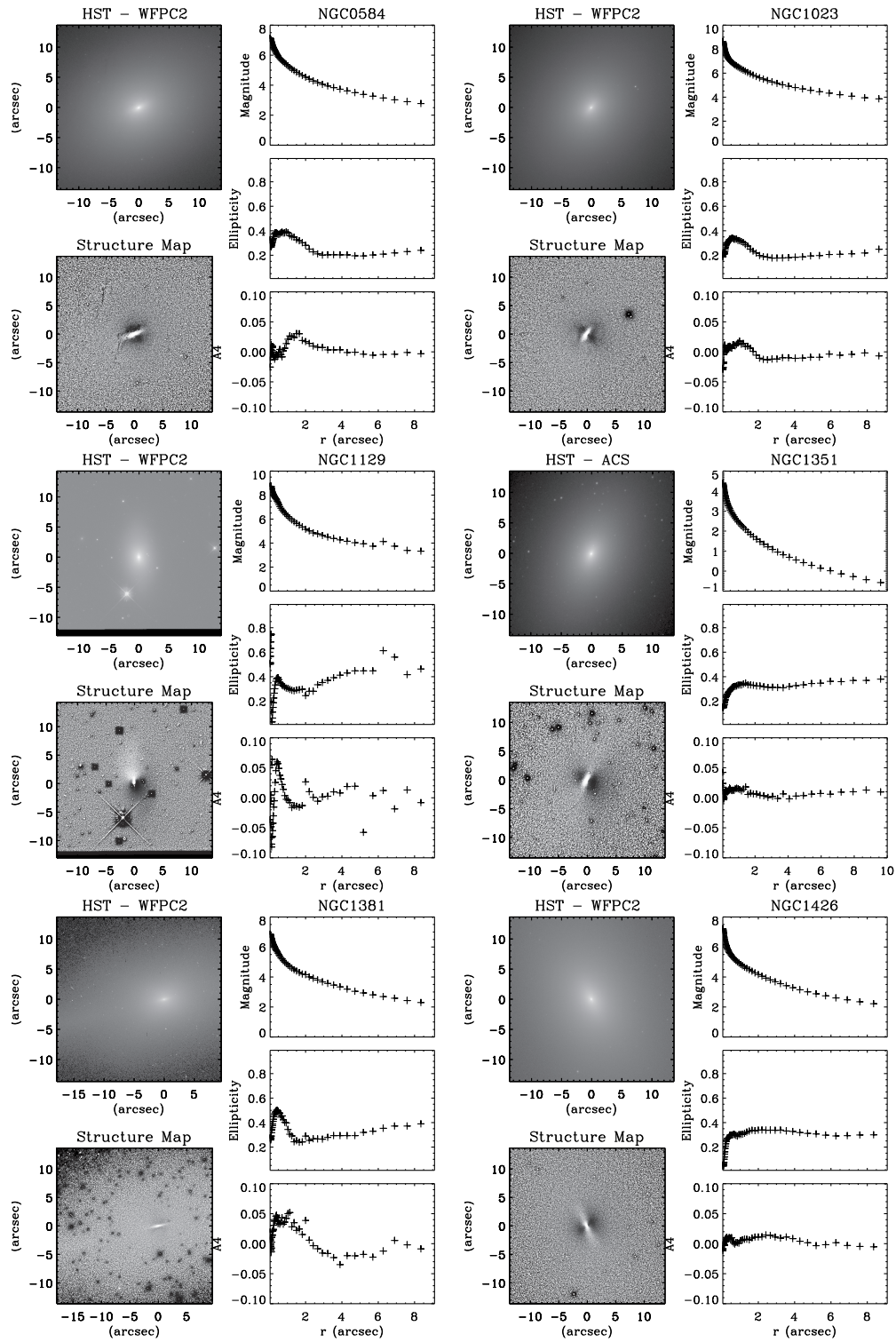


Fig. 2.9: NGC 0584 on the top left, NGC 1023 on the top right, NGC 1129 on the middle left, NGC 1351 on the middle right, NGC 1381 on the bottom left and NGC 1426 on the bottom right.

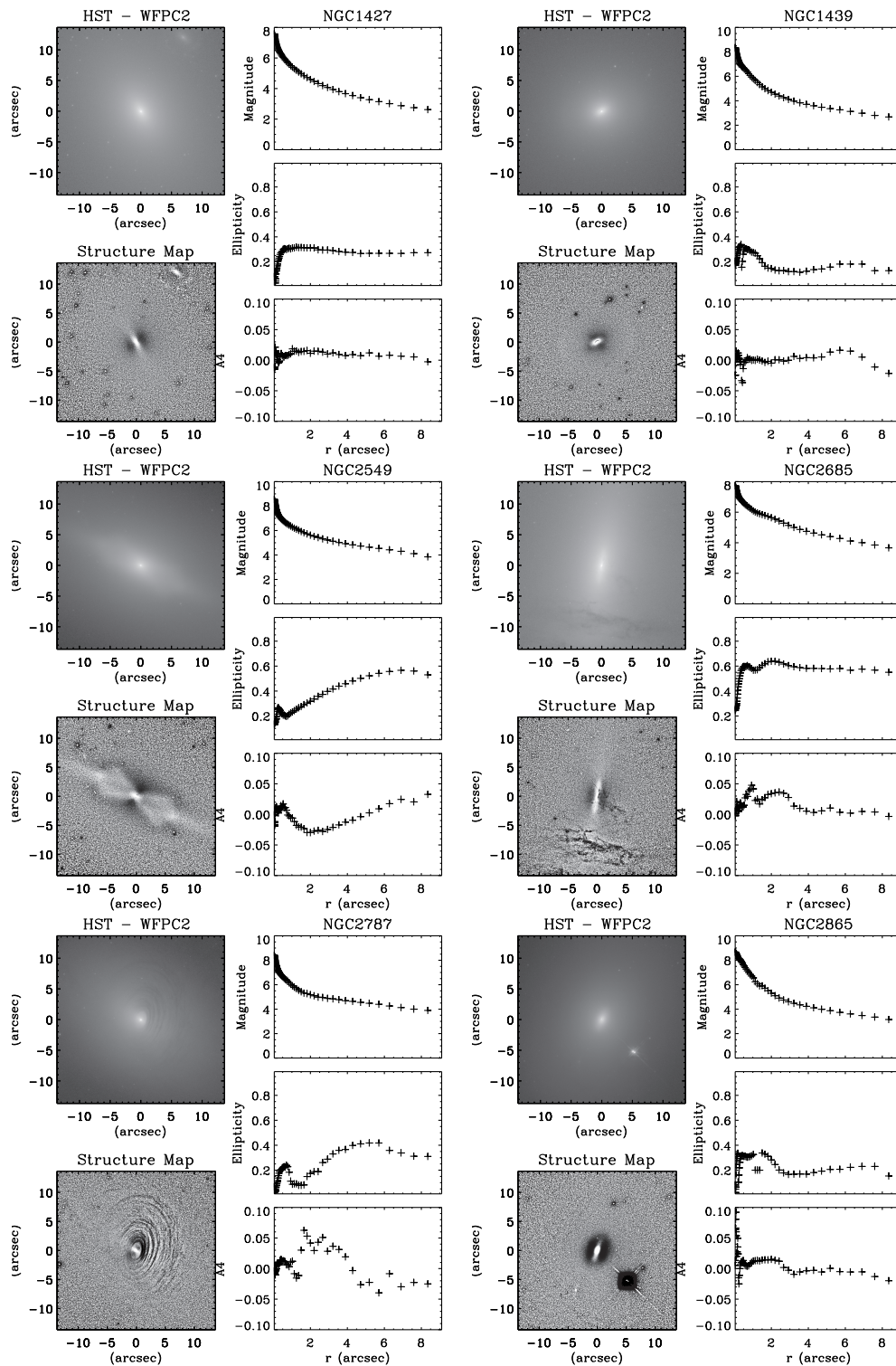


Fig. 2.10: NGC 1427 on the top left, NGC 1439 on the top right, NGC 2549 on the middle left, NGC 2685 on the middle right, NGC 2787 on the bottom left and NGC 2865 on the bottom right.

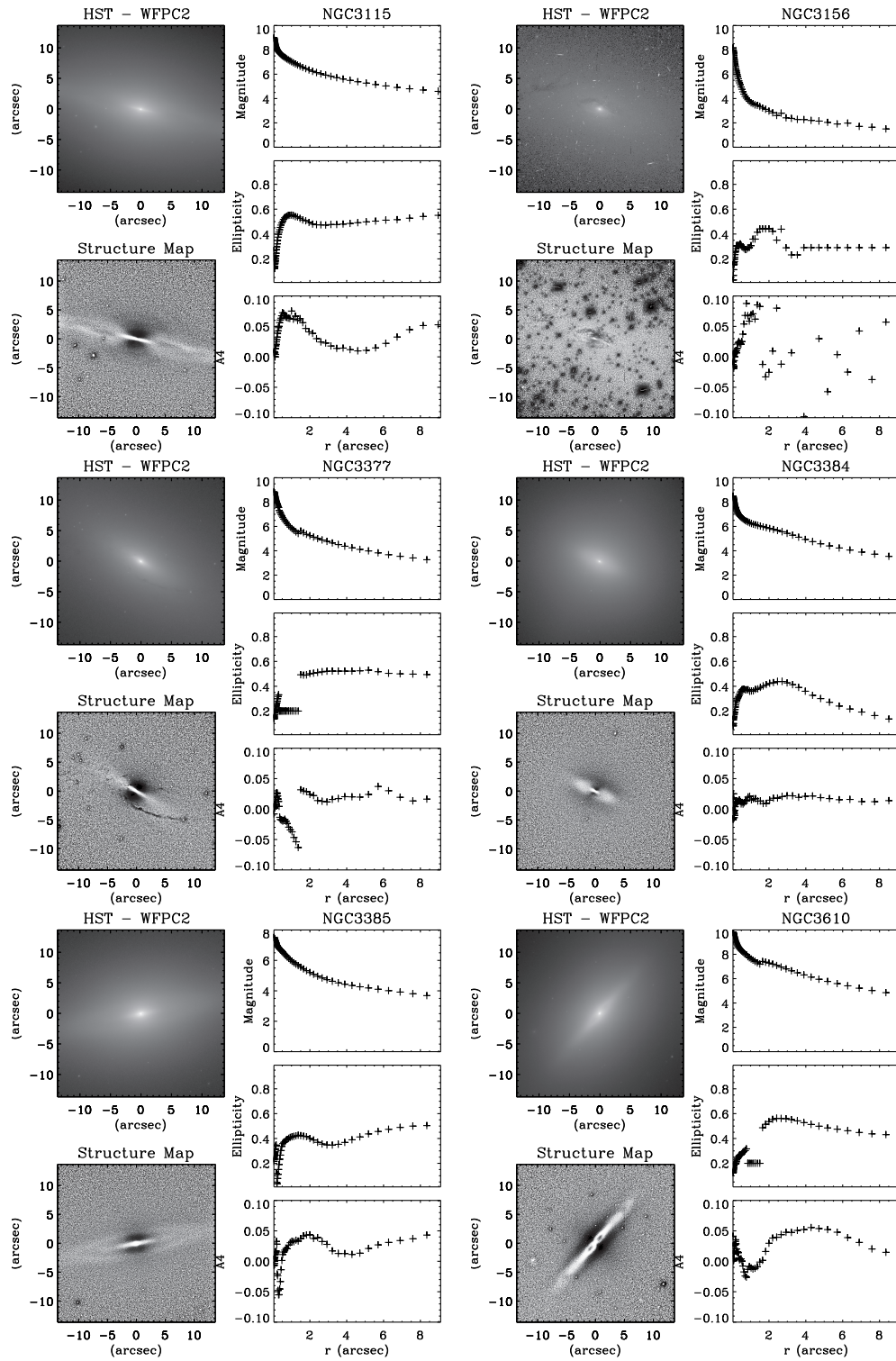


Fig. 2.11: NGC 3115 on the top left, NGC 3156 on the top right, NGC 3377 on the middle left, NGC 3384 on the middle right, NGC 3385 on the bottom left and NGC 3610 on the bottom right.

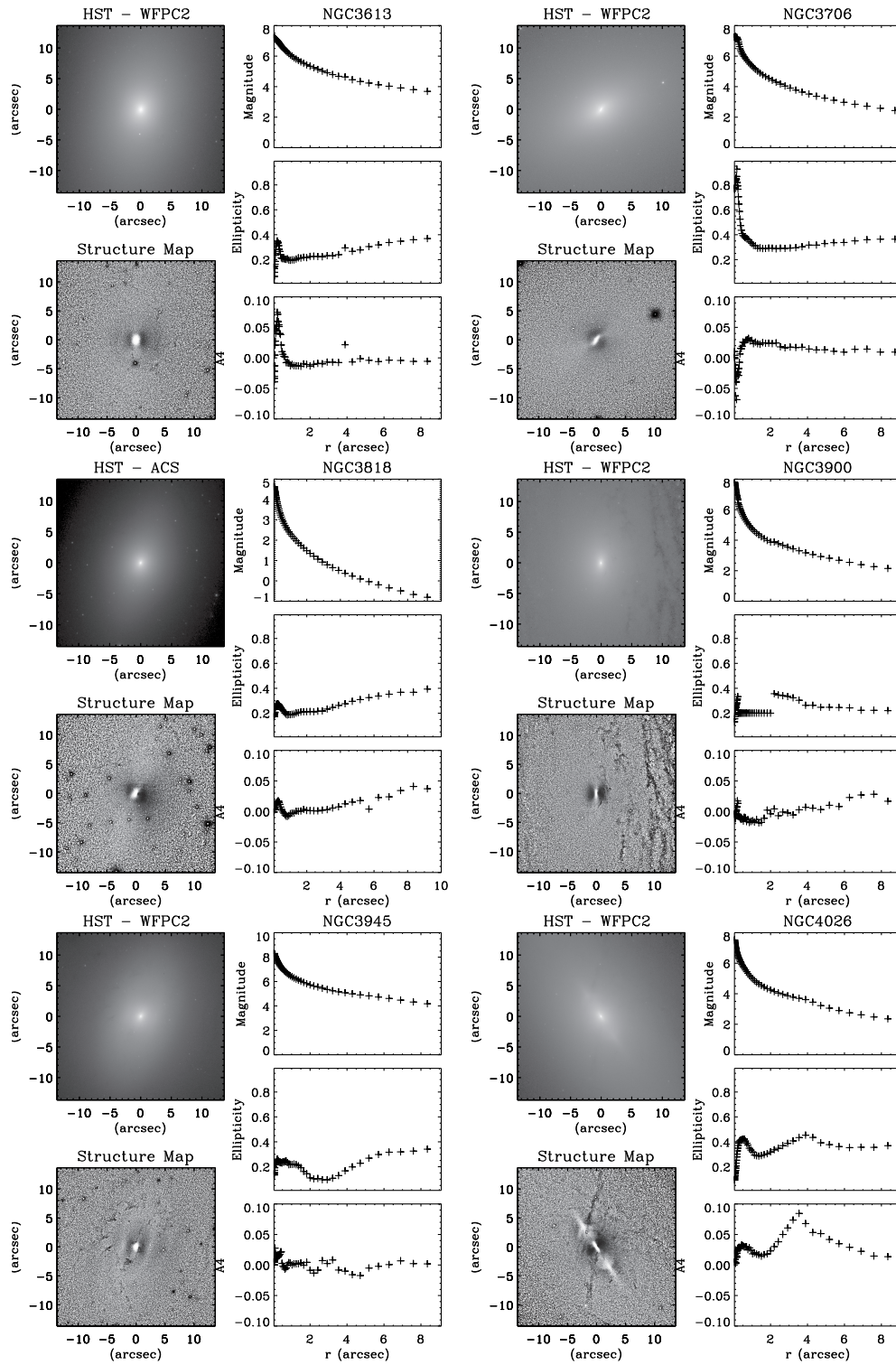


Fig. 2.12: NGC 3613 on the top left, NGC 3706 on the top right, NGC 3818 on the middle left, NGC 3900 on the middle right, NGC 3945 on the bottom left and NGC 4026 on the bottom right.

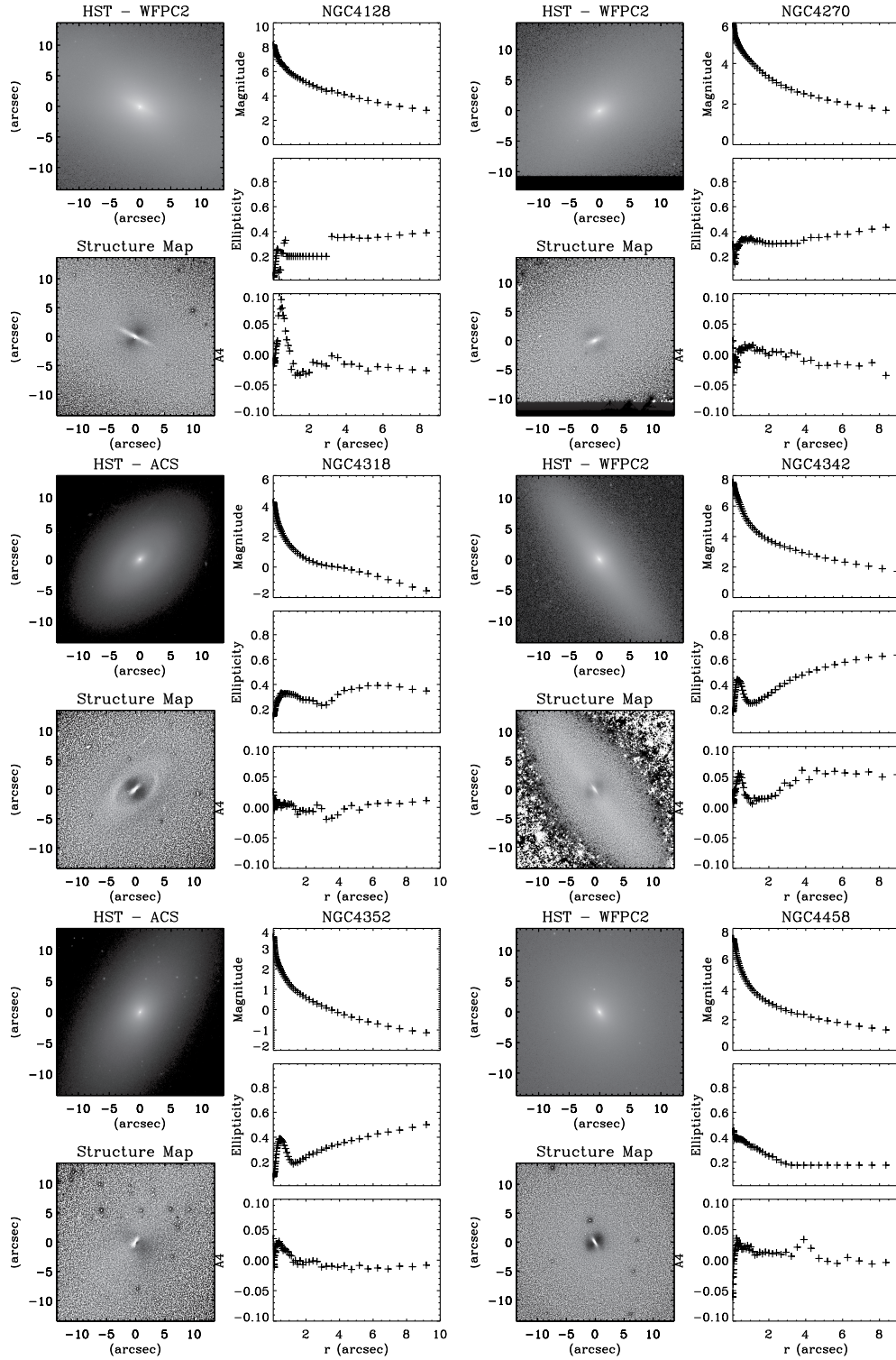


Fig. 2.13: NGC 4128 on the top left, NGC 4270 on the top right, NGC 4318 on the middle left, NGC 4342 on the middle right, NGC 4352 on the bottom left and NGC 4458 on the bottom right.

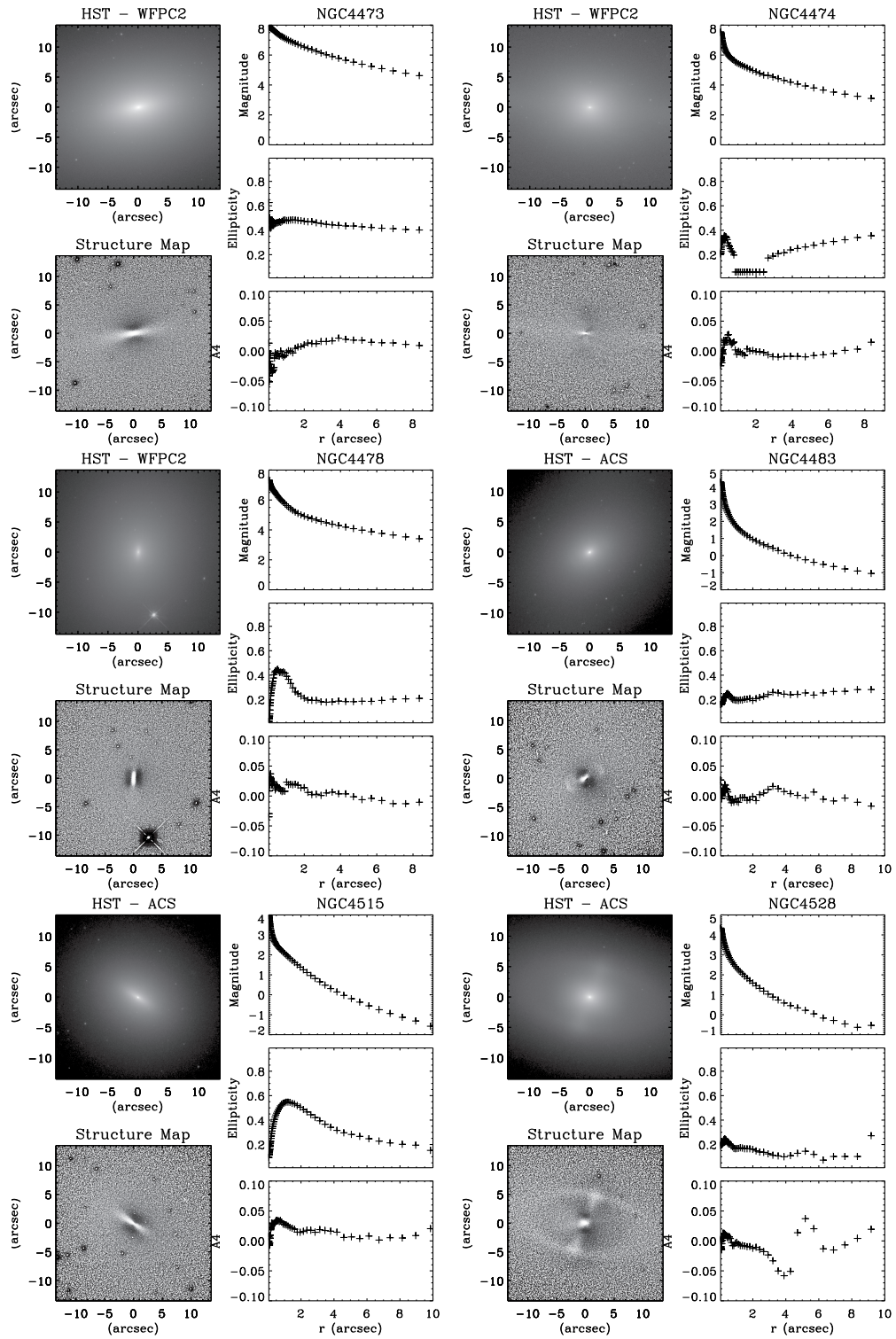


Fig. 2.14: NGC 4473 on the top left, NGC 4474 on the top right, NGC 4478 on the middle left, NGC 4483 on the middle right, NGC 4515 on the bottom left and NGC 4528 on the bottom right.

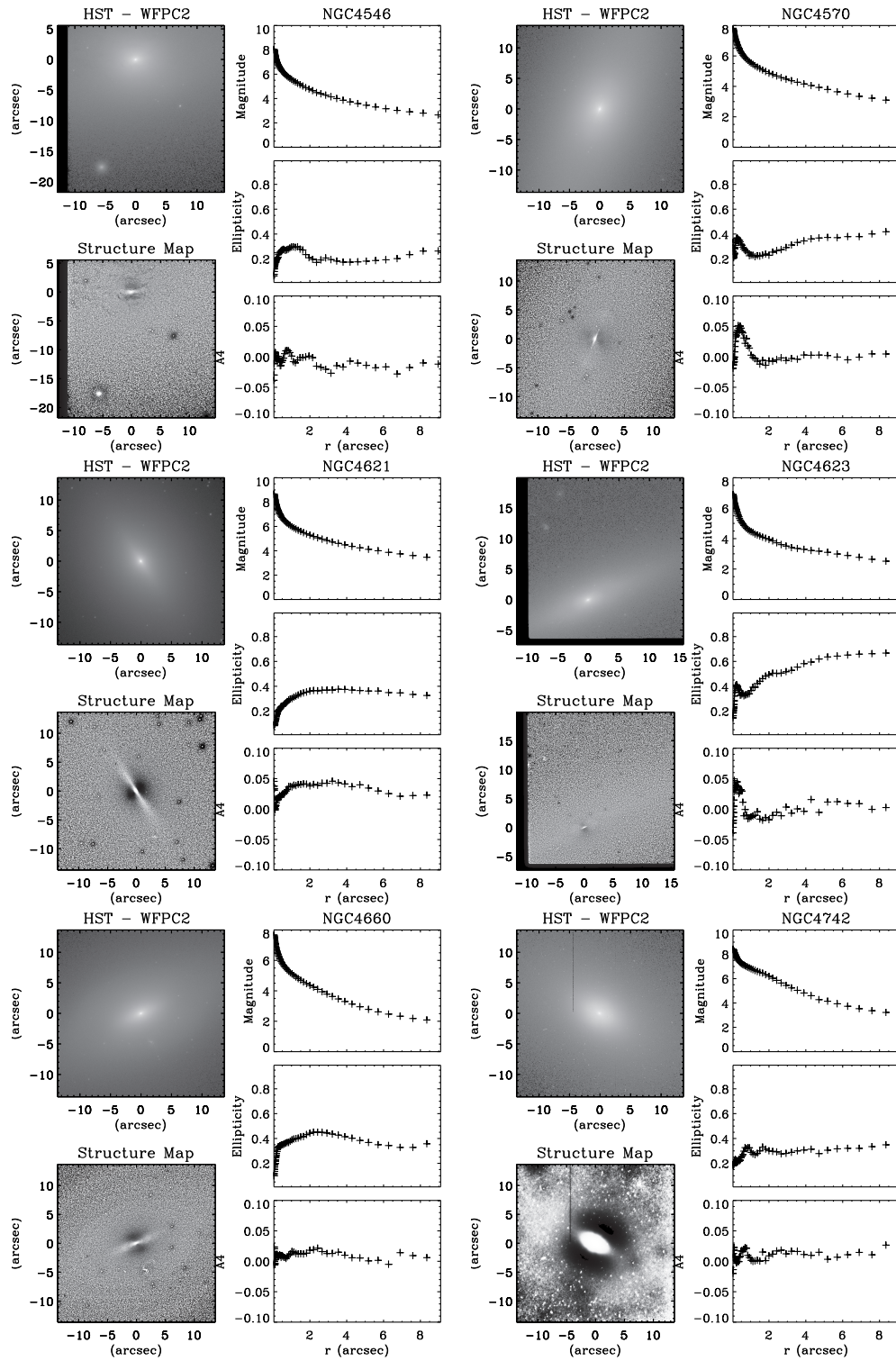


Fig. 2.15: NGC 4546 on the top left, NGC 4570 on the top right, NGC 4621 on the middle left, NGC 4623 on the middle right, NGC 4660 on the bottom left and NGC 4742 on the bottom right.

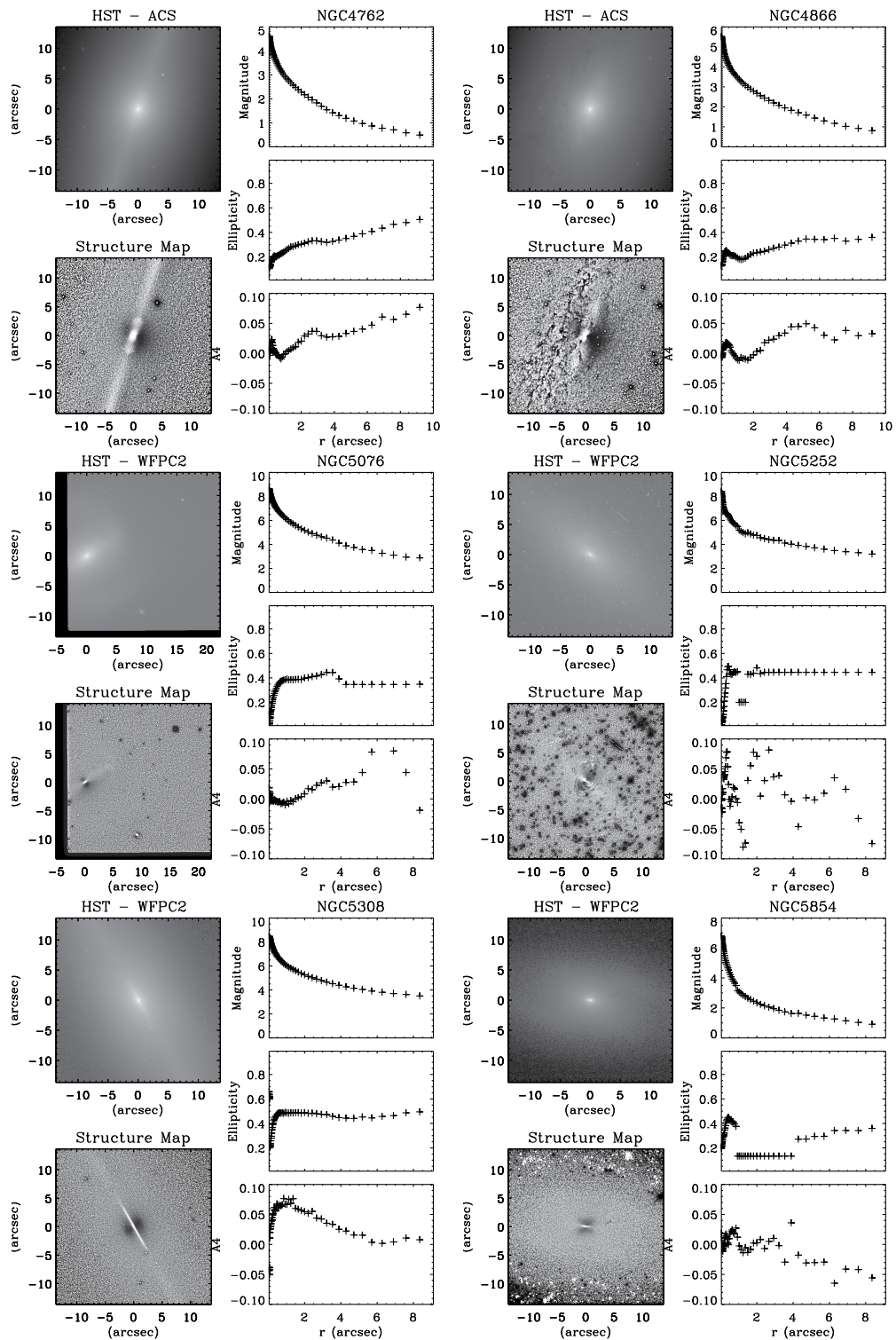


Fig. 2.16: NGC 4762 on the top left, NGC 4866 on the top right, NGC 5076 on the middle left, NGC 5252 on the middle right, NGC 5308 on the bottom left and NGC 5854 on the bottom right.

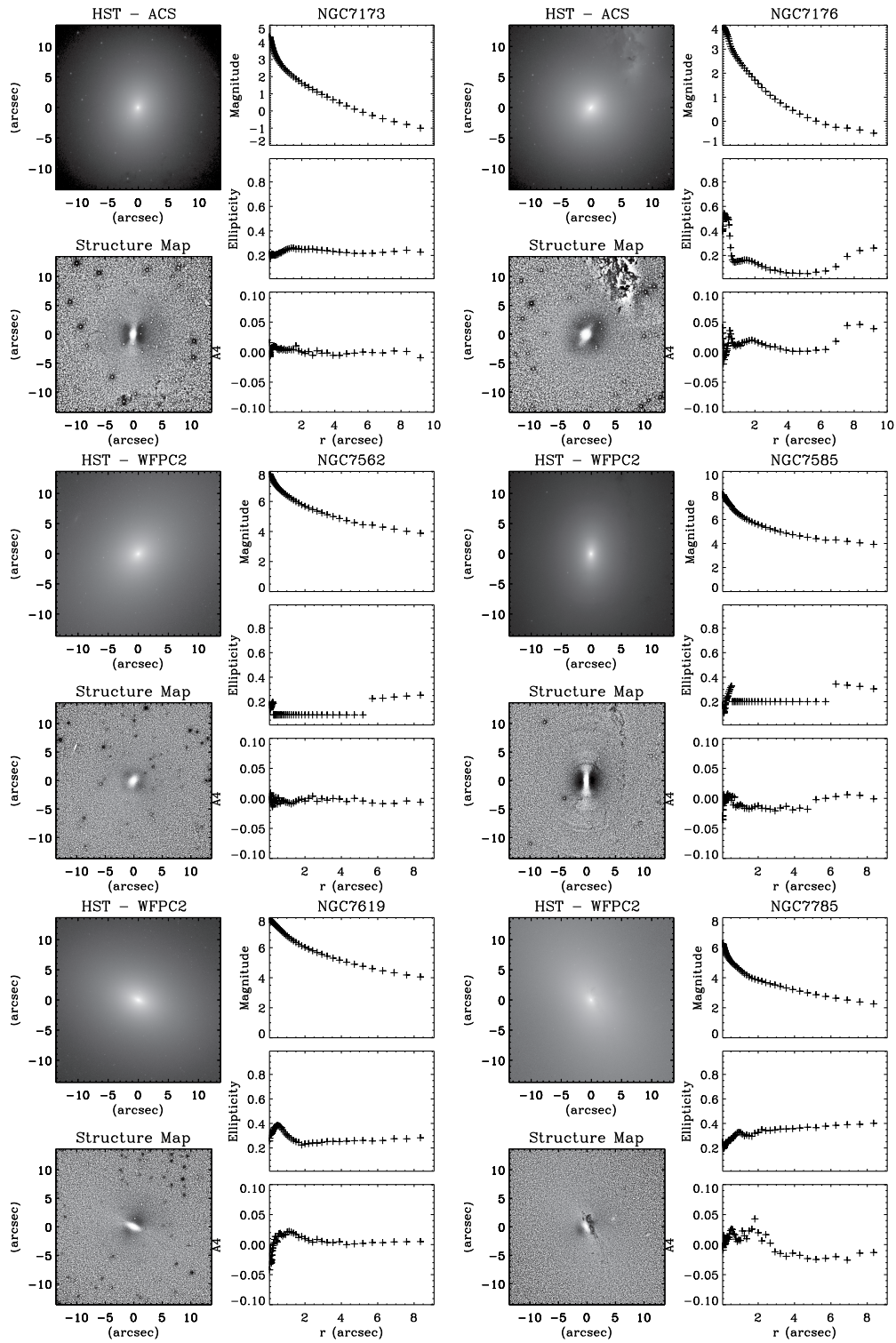


Fig. 2.17: NGC 7173 on the top left, NGC 7176 on the top right, NGC 7562 on the middle left, NGC 7585 on the middle right, NGC 7619 on the bottom left and NGC 7785 on the bottom right.

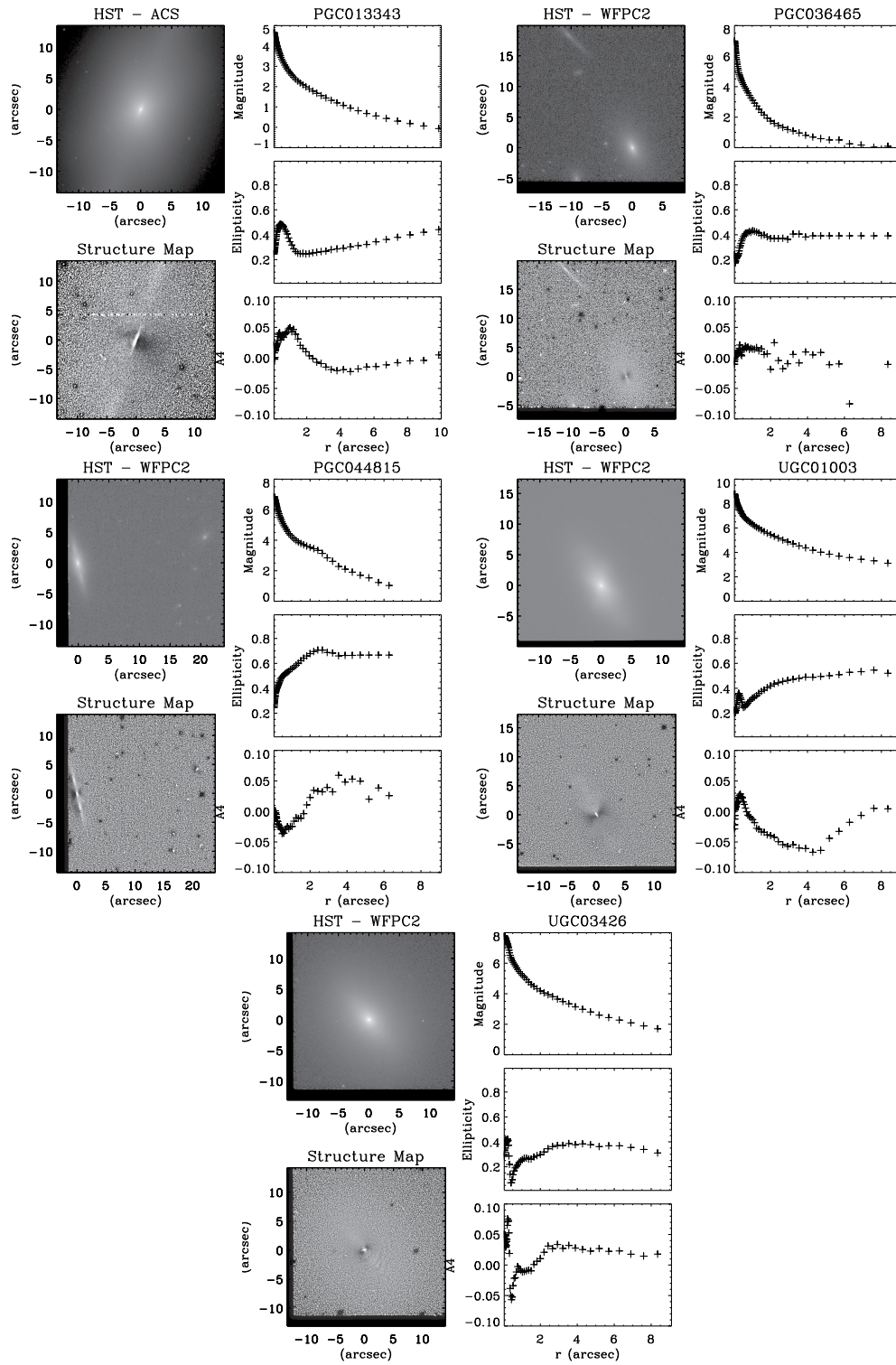


Fig. 2.18: PGC 013343 on the top left, PGC 036465 on the top right, PGC 044815 on the middle left, UGC 01003 on the middle right and UGC 03426 on the bottom.

## 2.7 Appendix B: Disc decomposition

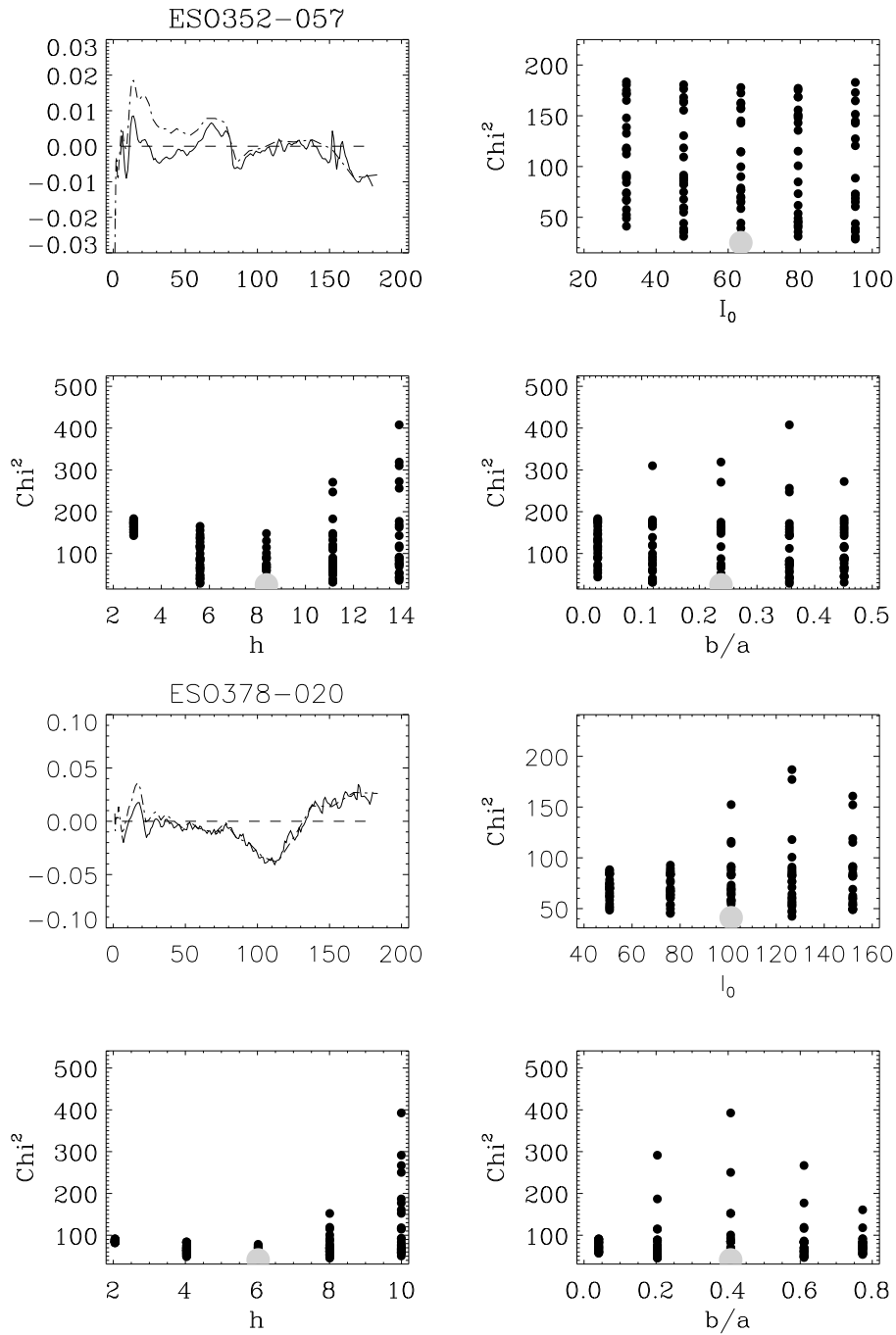


Fig. 2.19: Scorza and Bender decomposition of ESO 352-057 on the top and ESO 378-020 on the bottom.

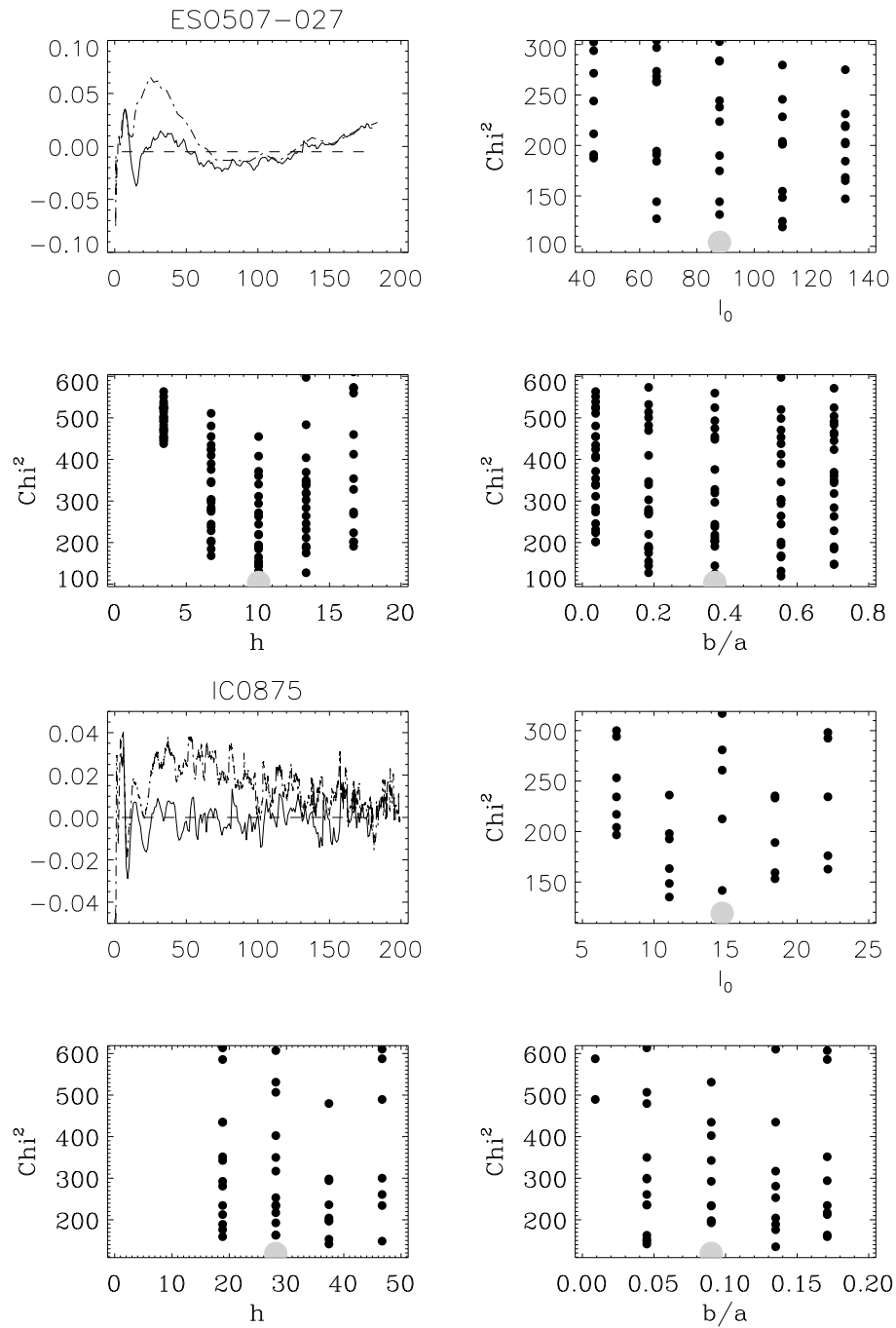


Fig. 2.20: Scorza and Bender decomposition of ESO 507-027 on the top and IC 0875 on the bottom.

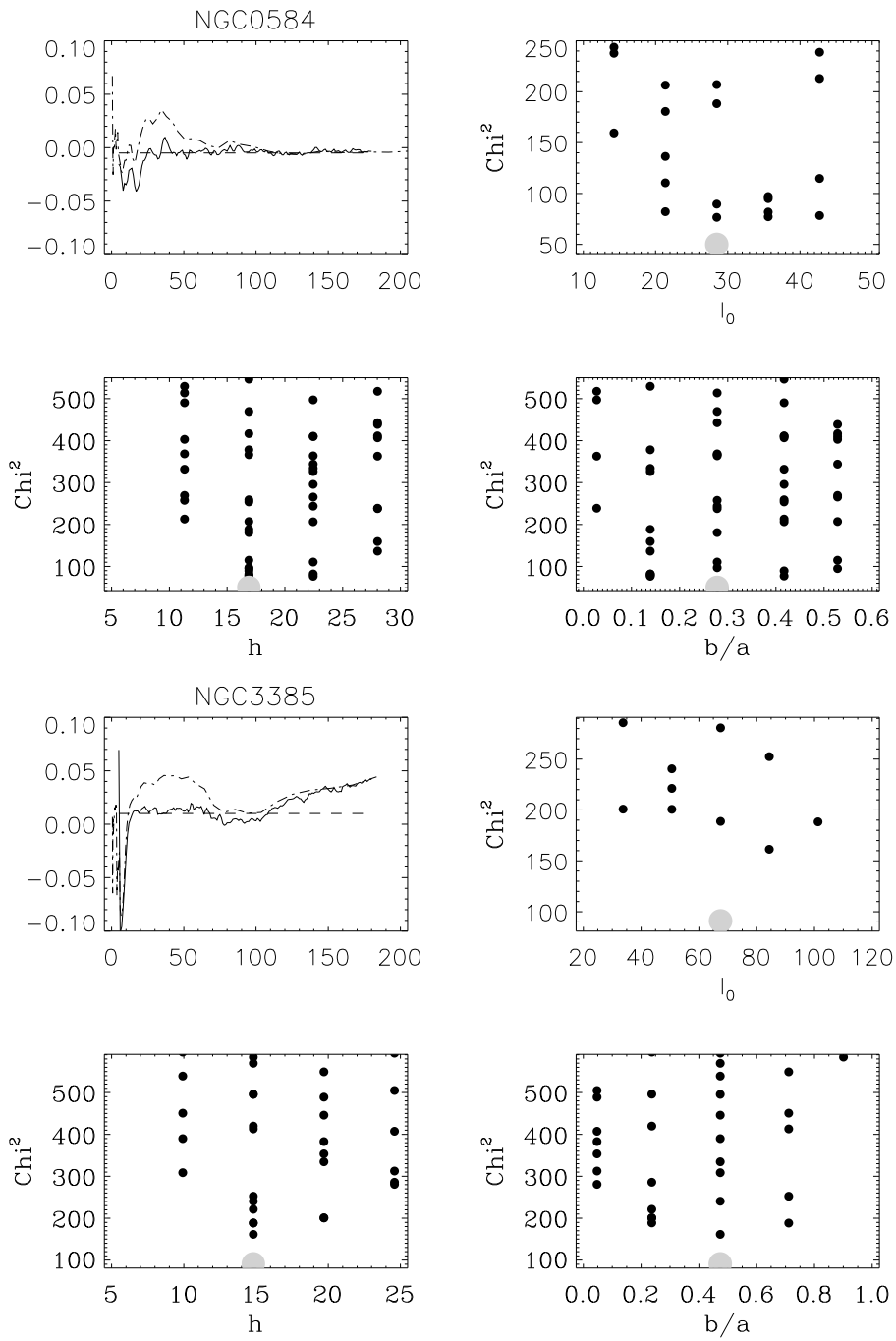


Fig. 2.21: Scorza and Bender decomposition of NGC 0584 on the top and NGC 3385 on the bottom.

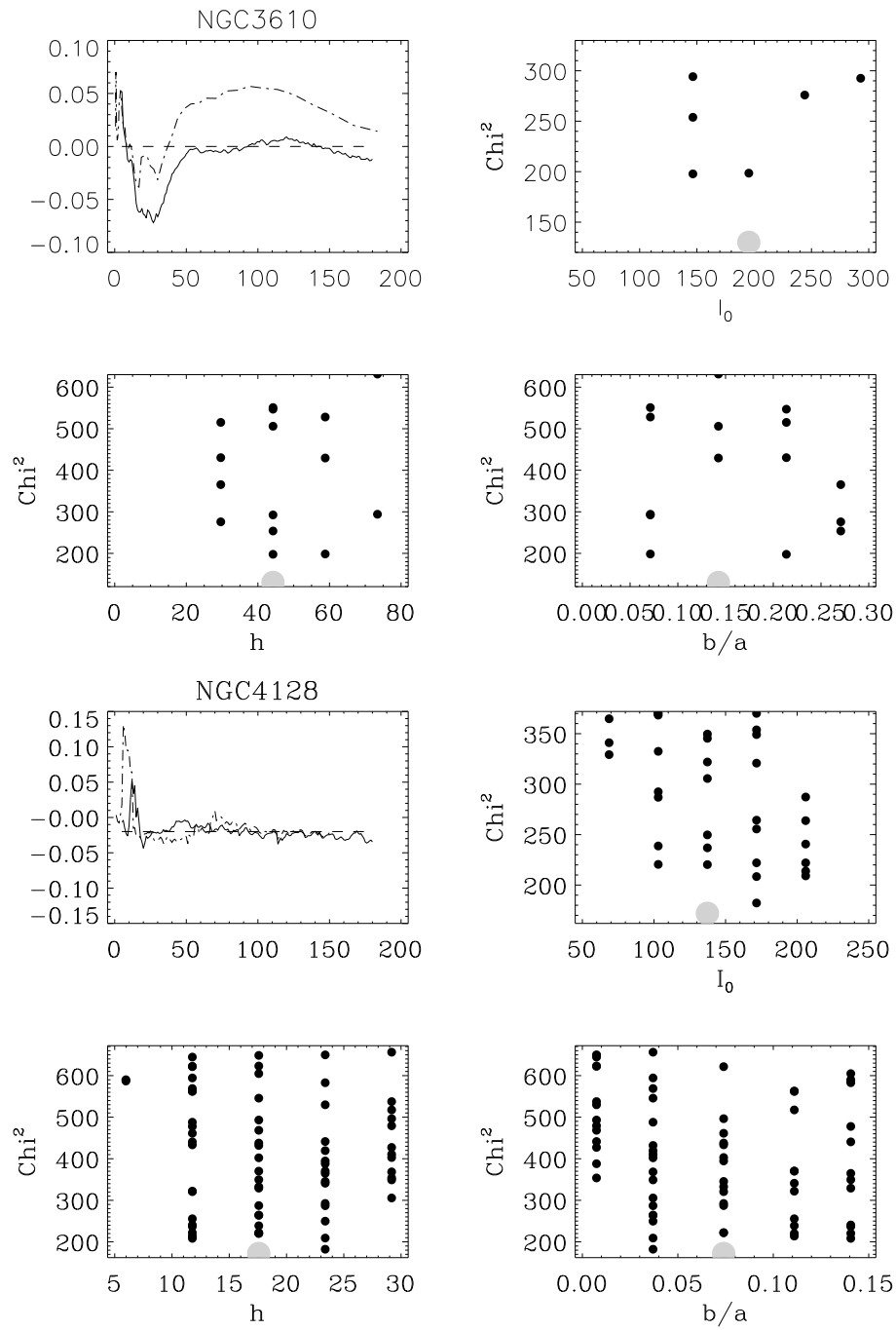


Fig. 2.22: Scorza and Bender decomposition of NGC 3610 on the top and NGC 4128 on the bottom.

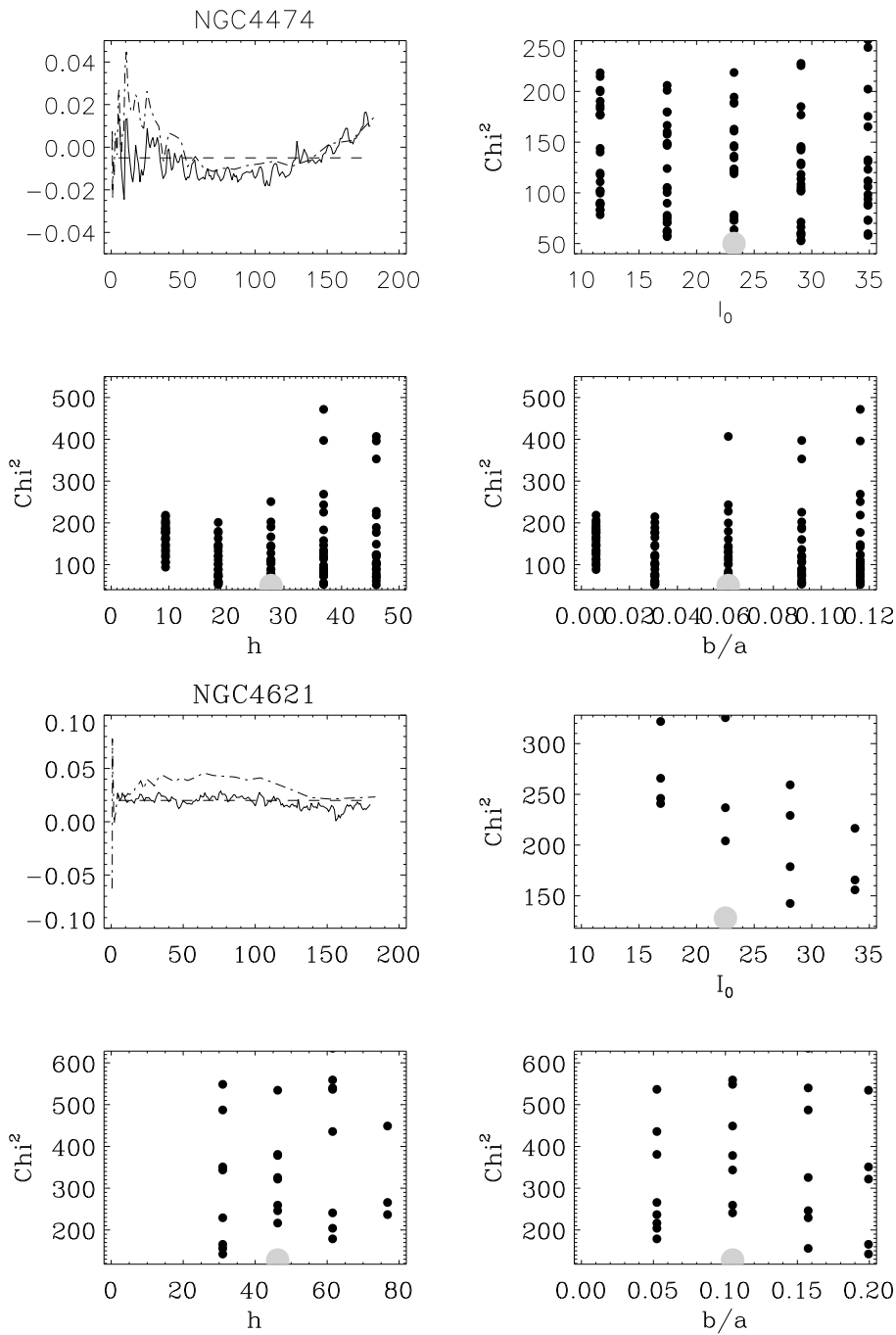


Fig. 2.23: Scorza and Bender decomposition of NGC 4474 on the top and NGC 4621 on the bottom.

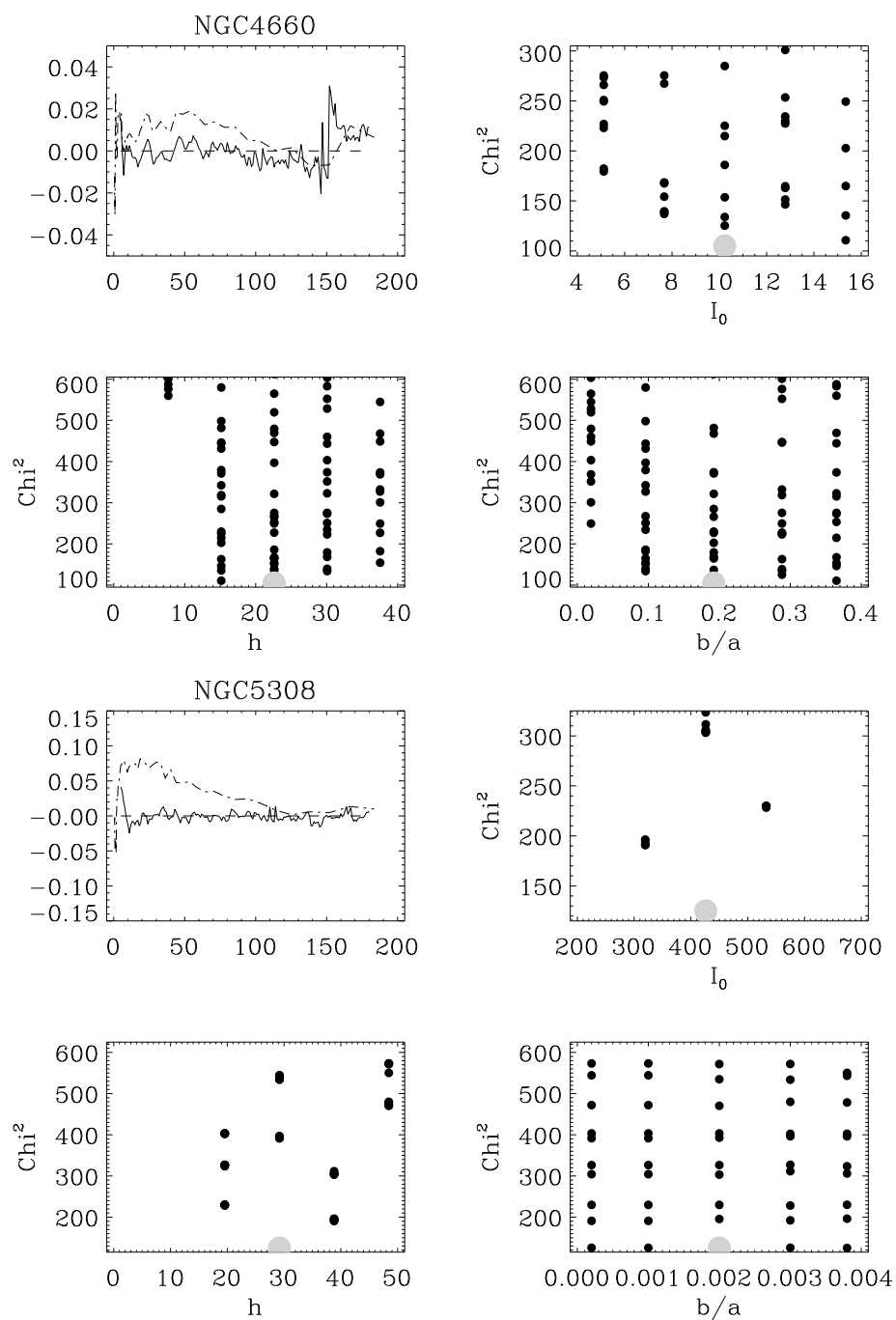


Fig. 2.24: Scorza and Bender decomposition of NGC 4660 on the top and NGC 5308 on the bottom.

Table 2.9: Properties of the decomposed discs where  $h$  is the scale-length, the inclination is as defined in §2.3 and  $\mu_{0,V}^c$  is the central surface brightness.

Galaxy name	$h$ (pc)	inclination ( $^\circ$ )	$\mu_{0,V}^c$ (mag arcsec $^{-2}$ )
ESO 352-057	$44.74 \pm_{16.05}^{23.16}$	$76.26 \pm_{22.42}^{8.58}$	$20.74 \pm_{1.04}^{1.05}$
ESO 378-020	$53.39 \pm_{18.54}^{33.51}$	$65.98 \pm_{19.69}^{16.78}$	$19.1 \pm_{0.58}^{1.27}$
ESO 507-027	$94.87 \pm_{16.8}^{23.22}$	$68.28 \pm_{9.61}^{7.83}$	$18.61 \pm_{0.37}^{0.47}$
IC 0875	$259.67 \pm_{77.71}^{59.41}$	$84.84 \pm_{2.31}^{2.29}$	$22.08 \pm_{0.4}^{0.63}$
NGC 0584	$90.18 \pm_{18.37}^{24.82}$	$73.86 \pm_{4.96}^{6.93}$	$18.97 \pm_{0.28}^{0.6}$
NGC 3385	$351.19 \pm_{55.07}^{52.33}$	$61.71 \pm_{5.08}^{1.55}$	$17.78 \pm_{0.16}^{0.06}$
NGC 3610	$260.38 \pm_{79.84}^{44.81}$	$81.81 \pm_{1.6}^{4.19}$	$19.60 \pm_{0.2}^{0.77}$
NGC 4128	$138.01 \pm_{38.68}^{43.84}$	$85.76 \pm_{0.92}^{1.95}$	$19.77 \pm_{0.21}^{0.67}$
NGC 4474	$143.5 \pm_{59.21}^{59.28}$	$86.49 \pm_{2.23}^{2.36}$	$21.29 \pm_{0.54}^{1.21}$
NGC 4621	$73.87 \pm_{24.26}^{13.71}$	$83.97 \pm_{2.02}^{2.59}$	$20.72 \pm_{0.32}^{0.6}$
NGC 4660	$81.19 \pm_{27.19}^{12.32}$	$78.92 \pm_{3.99}^{4.19}$	$20.02 \pm_{0.33}^{0.51}$
NGC 5308 <sup>a</sup>	$201.59 \pm_{45.56}^{30.21}$	$89.89 \pm_{-}$	$22.46 \pm_{-}$

<sup>a</sup>We were unable to derive the errors for the inclination.

---

# CHAPTER 3: NUCLEAR DISCS AS CLOCKS FOR THE ASSEMBLY HISTORY OF EARLY-TYPE GALAXIES: THE CASE OF NGC 4458

---

With collaborators M. Sarzi<sup>1</sup>, L. Coccato<sup>2</sup> and C. Maraston<sup>3</sup>.

<sup>1</sup>Centre for Astrophysics Research, University of Hertfordshire, College Lane, Hatfield AL10 9AB, United Kingdom

<sup>2</sup>European Southern Observatory, Karl-Schwarzschild-Strasse 2, 85748, Garching bei Muenchen, Germany

<sup>3</sup>Institute of Cosmology and Gravitation, University of Portsmouth, Dennis Sciama Building, Burnaby Road, Portsmouth PO1 3FX, United Kingdom

## 3.1 Introduction

In the context of a dark-matter dominated, Universe galaxies should have grown through a combination of star formation and merging processes, whereby on the one hand star formation was regulated by the presence of fresh gaseous material and the negative feedback of supernovae and possibly also active nuclei, and on the other hand merging events should have proceeded in a hierarchical fashion. A steady increase in the quality and scope of spectroscopic investigations of nearby galaxies has allowed to constrain directly their star-formation history (e.g. Thomas *et al.*, 2005, 2010, for early-type galaxies), but reconstructing the assembly history of galaxies has proved so far to be more difficult. Attempts to quantify the rate of merging events by searching close galactic pairs and interacting galaxies (e.g. Darg *et al.*, 2010) depend on the depth and the area covered by the images used in these studies, whereas individual investigations of morphological signatures of past mergers, such as galaxy shells (e.g. Ebrova *et al.*, 2010), can hardly pinpoint the epoch of such a galactic encounter (but see Hau *et al.*, 1999). The lack of constraints on the assembly history of nearby galaxies leaves unchecked several predictions of the hierarchical standard paradigm. For instance, the most massive galaxies should have assembled only recently (e.g. De Lucia *et al.*, 2006) whereas, at a given mass, galaxies

in clusters should have experienced less merging events than their counterparts in the field since they entered such crowded galactic environments. Indeed, galaxies in clusters fly too fast by each other for them to merge (Binney and Tremaine, 1987).

Understanding the assembly history of galaxies is particularly important in the case of early-type galaxies, as these systems have long been thought to originate during merging events (Toomre, 1977). In fact, the recent kinematic distinction between fast and slowly-rotating early-type galaxies that emerged thanks to integral-field data (Cappellari *et al.*, 2007; Emsellem *et al.*, 2007) is suggestive also of a separate merging history for these two kinds of objects (Emsellem *et al.*, 2011; Naab, 2013), where slow rotators would owe their low angular momentum to a more systematic bombardment by smaller satellite galaxies.

In this respect, nuclear stellar discs (NSDs) could prove important tools to directly constrain the assembly history of early-type galaxies. Initially discovered in images taken with the Hubble Space Telescope (HST, van den Bosch *et al.*, 1994) and now known to be common in early-type galaxies (in up to 20% of them Ledo *et al.*, 2010, Chapter 2), such small discs (a few  $\sim 100$ pc in radius at most) are indeed fragile structures that should not survive a significant merger event (see, e.g. the simulations shown in Chapter 2). This means that by dating the stellar age of the NSDs it is possible to place a lower limit for the look-back time since their host galaxies experienced a major encounter, as NSDs could form also after such an event. In fact, the stellar age of NSDs can be constrained even more precisely than is generally the case for other kinds of galactic component, thanks to the possibility to derive in advance their relative contribution to the total galaxy light.

The main difficulty in disentangling a superposition of two stellar populations in the spectra of a galaxy, in this case the nuclear disc and the bulge, is the degeneracy between the age and light fractions of each component. Using good-quality and extended spectra allows to better exploit the information encoded in the stellar absorption lines and can help mitigating this problem, but in the presence of relatively old stellar populations further complications arise from the degeneracy between age and metallicity or reddening. On the other hand, in the case of structurally different and, to some extent, well described, galactic components it may be possible to infer from images their individual light fractions in the considered spectra (in the wavelength range covered by the images), and exploit this constrain to break the previous degeneracies. This is precisely the case of a nuclear disc embedded in a stellar bulge, where the surface brightness distribution of the disc can be inferred using the disc-bulge decomposition technique introduced by Scorza and Bender (1995), which relies only on the assumption of an exponential radial profile for the disc and

an elliptical shape for the bulge isophotes.

Simple simulations such as those shown in Fig. 3.1 serve to illustrate the dramatic effect that an *a priori* knowledge of the disc light contribution should have in estimating the age and metallicity of NSD embedded in a bulge. Fig. 3.1 shows the case of a 7-Gyr-old disc population embedded in a 13-Gyr-old bulge, where both components contribute to the input model spectrum with the same broad-band flux in the 4500 Å – 5500 Å range and are represented by single-age stellar population models of solar metallicity (from Bruzual and Charlot, 2003) that cover a wavelength range similar to that of the observations that will be presented later in this chapter. The  $\chi^2$  contours around the input disc stellar age of 7 Gyr increase steeply to high values when trying to match different realisations of the input model with disc model populations of varying age and metallicity when the relative contribution of the bulge and disc component are fixed to their input value (as if they were known from a disc-bulge decomposition). On the other hand, when the relative contribution of the disc and bulge templates are not constrained it is possible to obtain a very good match to the input spectrum also when using disc populations of considerably different age and metallicity than the input that of the input disc template (see the caption of Fig. 3.1 for further details). In other words, this experiment shows that knowing in advance the disc light contribution should allow estimating more robustly the NSD age and metallicity. Both kinds of simulations were run using the correct bulge template, which mimics the situation where the bulge stellar properties have been also previously constrained from off-axis, yet central, observations.

Motivated by the potential use of NSDs as clocks for the assembly history of their host galaxies and encouraged by the previous kind of simulations, this chapter presents a pilot investigation based on VLT VIMOS integral-field spectroscopic observations of the NSD in the Virgo elliptical galaxy NGC 4458, with the goal of assessing the accuracy with which the stellar age of NSD can be estimated. This chapter is organised as follows. In § 3.2 we describe our VLT observations and the reduction of the VIMOS data. The core of our analysis is found in § 3.3, where in the order we proceed to derive with the aid of HST image the relative contribution of the bulge and NSD light in our central VIMOS spectra (§ 3.3.1 and §3.3.2), extract a template for stellar bulge population (§ 3.3.3) and finally constrain the stellar age of the nuclear disc (§ 3.3.4). Finally, in § 3.4 we discuss our results, suggesting also some future avenues for the methodology developed here (§ 3.4.1).

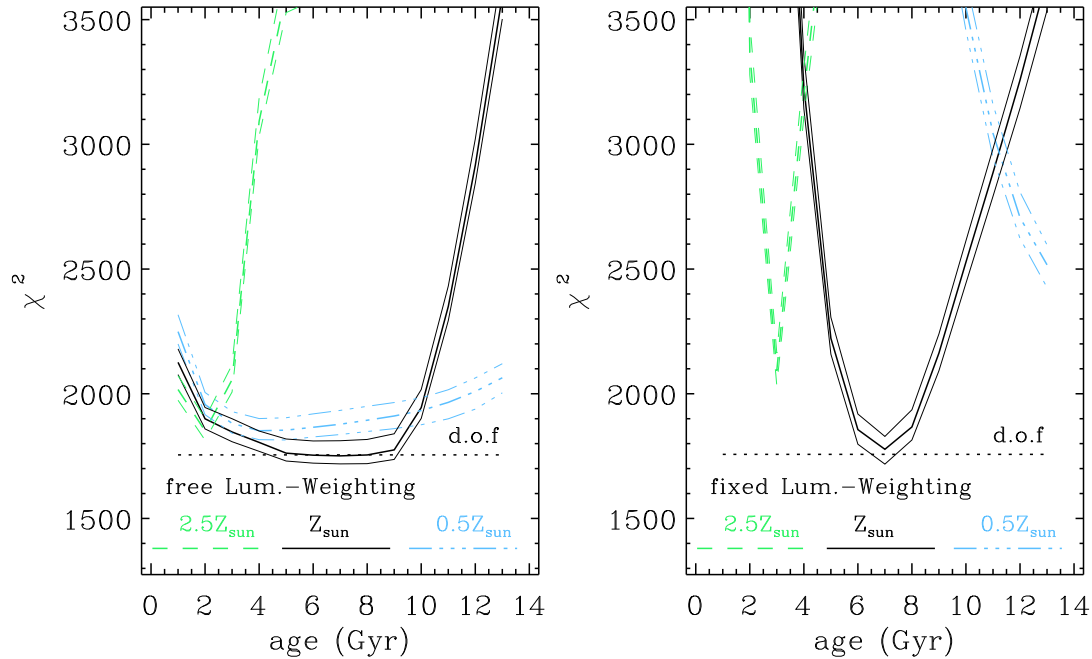


Fig. 3.1: Simulations showing the accuracy in recovering the age of a 7-Gyr-old disc population that is embedded in a 13-Gyr-old bulge population. In both cases, the bulge and disc populations contribute to the input model with the same broad-band flux between  $4500 \text{ \AA}$  and  $5500 \text{ \AA}$ , and are represented by single-age stellar population models of solar metallicity from Bruzual and Charlot (2003), covering the entire wavelength range of our VIMOS observations (§ 3.3). Different amounts of kinematical broadening were also included in the bulge and disc models ( $\sigma = 200$  and  $100 \text{ km s}^{-1}$ ), and statistical fluctuations were added to simulate a  $S/N \sim 100$ . In each panel, the thick solid line shows the average quality of the fit to the input model as disc single-age models of increasing ages are combined with the right, 13-Gyr-old, bulge population model. The thin solid lines indicate the  $1\sigma$  fluctuation that is derived by fitting different realisations of the input model. The dashed and dot-dashed lines show the quality of the fits obtained while considering disc populations of super- and sub-solar metallicities. On the left panel the relative contribution to the fit of the bulge and disc populations is left free to vary, whereas on the right panel each component is constrained to contribute the same broad-band flux in the  $4500 \text{ \AA}$ – $5500 \text{ \AA}$  range as in the input model. In both cases the kinematic broadening of the templates is also freely adjusted during the fit. This simulates the situation where the fraction of bulge and disc starlight along the line of sight is known a priori from the decomposition of broad-band images. The comparison between  $\chi^2$  curves in the left and right illustrates how knowing in advance the disc light contribution allows one to recover the correct disc age and metallicity, whereas without such an initial clue, estimating the disc age and metallicity would be complicated by the well-known degeneracy between these two parameters in stellar populations

## 3.2 VIMOS observations and data reduction

### 3.2.1 Observations

The VIMOS Integral Field Unit (Le Fèvre *et al.*, 2003), installed on the UT3 of the Very Large Telescope (VLT), presented itself as one of the best instruments for this study. With VIMOS it is indeed possible to extract spectra of intermediate spectral resolution over a relatively long wavelength range and at different spatial locations, which allows to study the stellar population of NSDs while constraining also the properties of the surrounding stellar bulge. Yet, it is the large collecting power of VLT and the possibility to obtain observations under the best seeing conditions that make VIMOS ideal to study NSDs, as these contribute significantly to the total stellar light only over very small spatial scales.

Over the course of the ESO observing periods P79 and P81 we collected VIMOS data for NGC 4458 using the HR blue grating with no filter and while opting for highest spatial magnification. Such a configuration lead to datacubes comprising of 1600 spectra extending from 4150 Å to 6200 Å and with spectral resolution of 2 Å (FWHM), each sampling an area  $0''.33 \times 0''.33$  within a total field-of-view of  $13''.0 \times 13''.0$ . To allow for a proper sky subtraction and minimise the impact the dead fibres or pixels, each observing block consisted of two, slightly offset on-source pointing (each 940s long in P79 and 1025s in P81), bracketing a shorter sky exposure (for 480s and 500s in P79 and P81, respectively). Out of a total allocated time of 23h, considering that only one observing block was executed in P79, this strategy yielded a total of 5.7h on target. All these observations were taken under very good seeing conditions, on average around our requested limit of  $0''.8$  for the atmospheric seeing. Tab. 3.1 summarises the details of our observations.

### 3.2.2 Data reduction

We started the reduction of our data by running each of our single sky and on-target exposures through the VIMOS ESO pipeline (version 2.2.1 <http://www.eso.org/>-

Table 3.1: Table with details for the two runs of VIMOS observations of NGC 4458

<b>Epoch</b>	<b>Number of obs.</b>	<b>Total on-target time (s)</b>	<b>Average seeing (arcsec)</b>	<b>Average airmass</b>
P79	1	1880	0.76	1.335
P81	9	18450	0.81	1.332

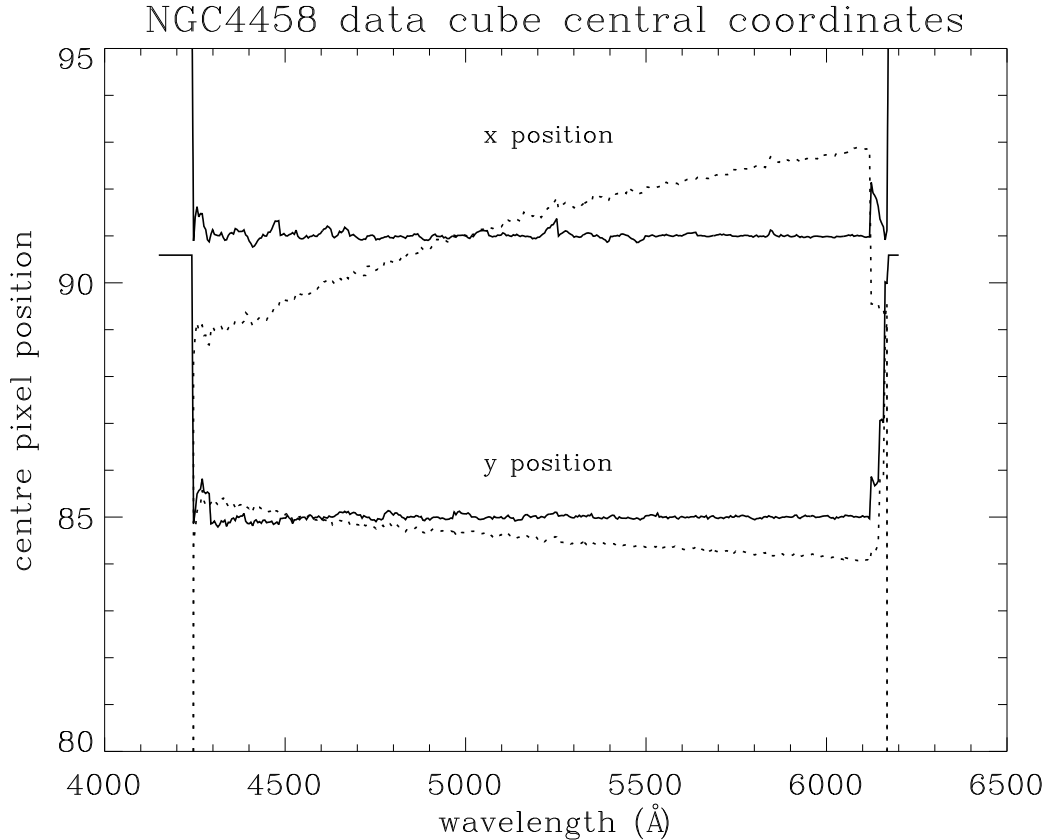


Fig. 3.2: The  $x$  and  $y$  centre coordinates of NGC 4458 as a function of wavelength along the data cube ( $x$  at the top and  $y$  at the bottom) before (dotted lines) and after our extra rectification (solid lines).

sci/software/pipelines/), thus carrying out the bias subtraction, flat fielding, fibre identification and tracing, and wavelength calibration. We then used in-house IDL and IRAF procedures to further correct for the different relative transmission of the VIMOS quadrants, which we adjusted by requiring the same intensity for the night-sky lines across the field-of-view, and in order to subtract the sky spectrum from the galaxy pointings. During this last step, we compensate for time variations in the night sky spectrum between the on-target and sky pointing by adjusting the strength of the strongest night sky lines in the sky exposures to match what found in the galaxy pointings. Finally, each on-target exposure was organised in data cubes using the tabulated position in the field-of-view of each fibre, which were then merged in a final data cube by aligning the bright nuclear regions of NGC 4458 in the total reconstructed images corresponding to each single cube.

Although these steps should have sufficed in providing a fully reduced data cube, we noticed that an extra rectification was needed to account for a residual systematic

shift of the galaxy centre as we move along the wavelength direction in the data cube. Such a shift is likely due to an imperfect correction for atmospheric differential refraction, as the galaxy centre moves mostly along the x axis of our data cube and that this is close to north-south direction. Fortunately, the nuclear regions of NGC 4458 are sufficiently cuspy for us to accurately locate the galaxy centre as a function of wavelength, thus correcting for this systematic shift. Fig. 3.2 shows the galaxy centre x and y pixel coordinates as a function of wavelength, before and after rectifying our final data cube. Even though the centre of NGC 4458 moved only by  $1''.5$  between the blue and red ends of our data cube, correcting for this shift is particularly important in the context of this work, since the NSD of this galaxy contributes significantly to the central light distribution only within a few tens of an arcsecond (see Morelli *et al.*, 2004 and § 3.3.1). In fact, ensuring an accurate rectification meant restricting the final wavelength range of our data cube between  $4220 \text{ \AA}$  and  $6000 \text{ \AA}$ . The final quality of our data can be appreciated in Fig. 3.3, where we show the integrated spectrum of NGC 4458 within the central  $5''$ . Based on the residuals of the best-fitting model for the stellar spectrum, obtained the pixel-fitting code of (Cappellari and Emsellem, 2004, pPXF) and the whole MILES stellar library (Sarzi *et al.*, 2006), we obtain an average value of 175 for the signal over residual-noise ratio. For comparison, within a similar aperture and for 2h of on-source exposure time, the SAURON integral-field data for NGC 4458, first presented by (Emsellem *et al.*, 2004), come with a signal over residual-noise ratio  $\sim 250$  in the  $4850 - 5300 \text{ \AA}$  wavelength region.

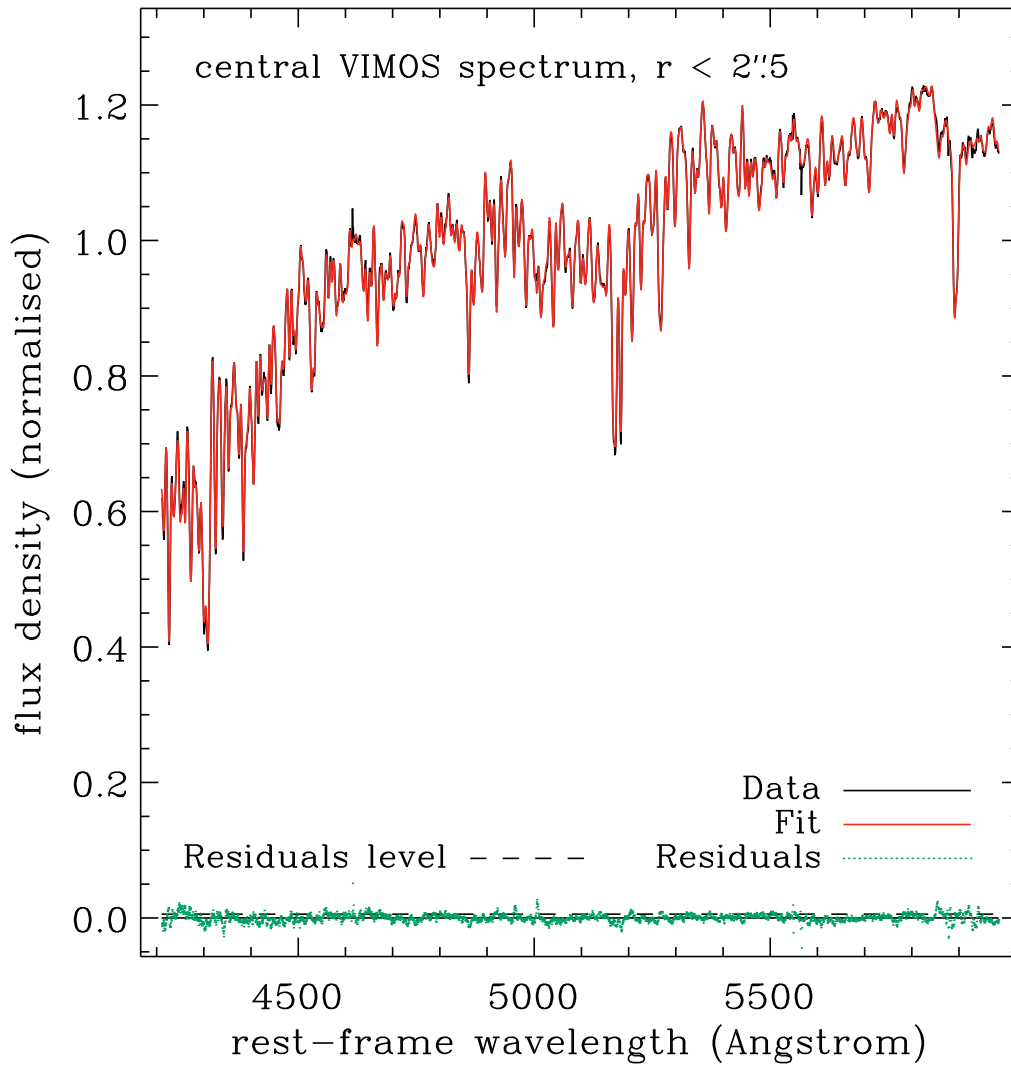


Fig. 3.3: Central  $5''$  VIMOS spectrum of NGC 4458 and our corresponding best pPXF fit using the entire MILES spectral library.

### 3.3 Analysis

In order to best estimate the stellar age of the nuclear disc in NGC 4458, we ought to know the relative contribution of the disc and its surrounding bulge to the central stellar surface brightness distribution, preferably within a wavelength range that is covered by our spectra. For this we will perform a disc-bulge decomposition using HST images in the visible domain (§ 3.3.1) and, by then accounting for the difference in spatial resolution and spatial sampling between HST and VIMOS, finally estimate the disc contribution to each of our central VIMOS spectra (§ 3.3.2). Thanks to the integral-field nature of our data, we will then be able to extract a central aperture spectrum while striking a good compromise between signal-to-noise ratio and disc light contribution, as well as extracting an off-centred aperture dominated by the bulge light that could be used as a template for such a component (§3.3.3) in our final stellar-population analysis of the nuclear regions (§3.3.4).

#### 3.3.1 Nuclear disc and bulge decomposition

In order to derive the properties of the nuclear disc of NGC 4458 and its contribution to the central surface brightness we used the disc-bulge decomposition procedure devised by Scorza and Bender (1995), as we did in Chapter 2. NGC 4458 was not previously decomposed because that work had already been done by Morelli *et al.* (2004) and this specific galaxy was not central to our work. However, knowledge of its disc-light contribution is crucial for the present analysis, which led us to perform a disc-bulge decomposition. The Scorza & Bender algorithm assumes that the bulge surface brightness is characterised by elliptical isophotes, and that the additional presence of a disc induces both a global flattening in the isophotes and a characteristic “lemon-shape” deviation from a purely elliptical form. This latter feature can be quantified by measuring positive values for the  $a_4$  coefficients in the Fourier series for the deviations of an isophote from an elliptical contour, and the Scorza & Bender method works by looking for the best disc model to subtract from the galaxy image in order to minimise the  $a_4$  coefficients and thus restore the elliptical shape of the bulge isophotes. More specifically, the model adopts an exponential profile for the disc surface profile and that the disc in itself is infinitesimally thin, so that only three parameters enter such minimisation: the central value for the disc surface brightness  $I_0$ , its scale length  $h$  and its apparent minor-to-major axis ratio  $b/a$ .

We perform such a disc-bulge decomposition using 335s-long Wide-Field Planetary Camera 2 (WFPC2) HST images for NGC 4458 in the F555W filter, which

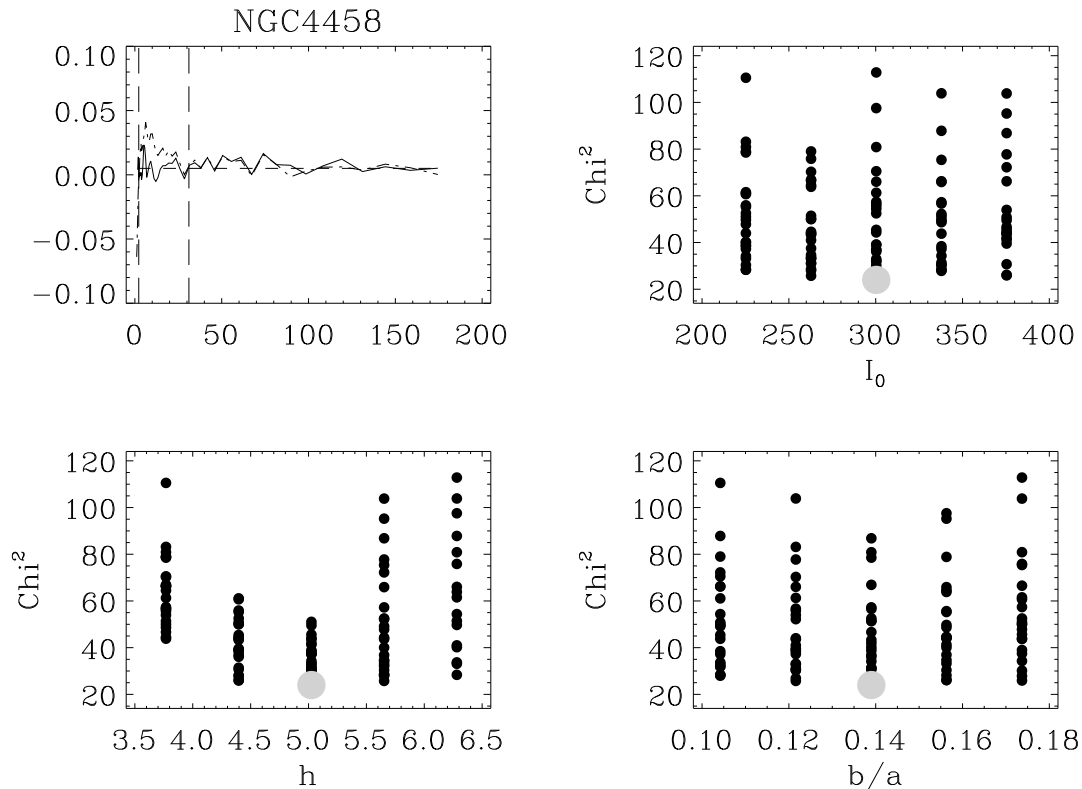


Fig. 3.4: Scorza & Bender disc-bulge decomposition of the nuclear regions of NGC 4458. Top left:  $a_4$  profile (radii are in units the HST-WFPC2 pixels) before (dot-dashed line) and after (solid line) the subtraction of our best exponential disc model. The considered values for the disc apparent central surface brightness (in counts  $s^{-1}$ ), scale length (in pixels) and axis ratio  $b/a$  are plotted against the corresponding  $\chi^2$  of each disc model, in the top right, lower left and lower right panels, respectively. These  $\chi^2$  values, corresponding to each set of nuclear disc parameters, are computed from the  $a_4$  profile measured in the central regions after the subtraction of the model disc (within  $2''$  and  $31''$ , dashed vertical lines in the top left panel) and considering that those coefficients should intrinsically be equal to zero for a perfect disc subtraction and an elliptical bulge. The parameters of the disc that best flattens the  $a_4$  profile, are shown by the large grey circles.

were available in the HST archive (from programme GO-5512). Fig. 3.4 shows the best values for the  $I_0$ ,  $h$  and  $b/a$  parameters, as well as an illustration of how the  $a_4$  profile changes when subtracting the best exponential disc. Tab. 3.2 also lists the corresponding best-fitting values for the disc central face-on surface brightness ( $\mu_{0,V}^c$  in mag arcsec $^2$ ), inclination  $i$  and scale length (in pc). These numbers agree well with the values found by Morelli *et al.* (2004), when noticing also that they reported the observed disc central surface brightness rather than a value corrected for inclination.

Table 3.2: Properties of the nuclear disc following our disc-bulge decomposition.  $h$  is the disc scale-length,  $i$  is the inclination defined as the arccosine of the disc axis ratio  $b/a$  and  $\mu_{0,V}^c$  is the central, face-on value of the disc surface brightness in V-band.

Galaxy	$h$ (pc)	$i$ ( $^\circ$ )	$\mu_{0,V}^c$ (mag arcsec $^{-2}$ )
NGC 4458	$11.72 \pm_{2.18}^{4.58}$	$82.01 \pm_{17.48}^{3.40}$	$17.27 \pm_{1.81}^{0.91}$

### 3.3.2 HST to VIMOS matching

Given the previous disc-bulge decomposition obtained at the exquisite spatial resolution of HST we can now account for the lower spatial (seeing-limited) resolution and the coarser spatial sampling of the VIMOS observations to compute the fraction of disc light that would have been observed within each VIMOS resolution element, if using the same filter of the HST images. Since the F555W filter response overlaps fairly well with the wavelength range of VIMOS this fraction provides already a good estimate of the disc contribution to the total stellar light collected within each of the VIMOS spectra. On the other hand, this match is not perfect either (e.g. the F555W filter response tails off to longer wavelength), and one would need to know *a priori* the age of the nuclear disc and bulge populations in order to refine such an estimate. This is still unknown to us, however, and in the spectral analysis that will follow we will instead use the fraction of light that each considered stellar population model for the bulge and disc contributes within the F555W filter, given that this is what we can precisely compute here.

We started our matching procedure by rotating the HST image of NGC 4458 to match the alignment of the VIMOS reconstructed image. Then, after extracting only its central regions, we proceeded to convolve the HST image by a double-Gaussian meant to represent the atmospheric point-spread function (PSF) of VIMOS and finally resampled the resulting degraded image within the  $0''.33 \times 0''.33$  VIMOS spaxels. To match the VIMOS reconstructed image this procedure required a rather vertically elongated PSF, which effectively greatly reduces our spatial resolution in that direction. This problem is only briefly mentioned in the VIMOS documentation and would appear to be due to the placing of the IFU at the edge of the VIMOS field of view (Anguita *et al.*, 2008). On the other hand, the extent of the PSF along the horizontal direction would appear to remain at the nominal level we requested (of  $0''.8$ , § 3.2).

Fig. 3.5 helps assessing the accuracy of our HST to VIMOS matching, and further shows the final map for the values of the disc to total ratio in the VIMOS resolution elements. The latter was obtained by simply applying the same rotation, convolution

and resampling steps (using the previously derived best double-Gaussian PSF) to the best-fitting disc model image that was derived during our previous Scorza & Bender disc-bulge decomposition (§ 3.3.1), and by then dividing the result by the degraded HST image of NGC 4458. Such a disc-to-total ratio map shows that in the central VIMOS spectra we can expect a disc contribution nearly up to  $\sim 5\%$ .

### 3.3.3 Bulge spectrum analysis

To better constrain the age of the nuclear stellar disc in the central region where its light contribution is the greatest, we ought to also have the best possible model for the bulge stellar spectrum, which will nonetheless dominate the central spectrum we are about to analyse. For this we combined two symmetric bulge spectra extracted within two  $3 \times 3$  pixels apertures  $2''.5$  away from the centre along the major axis of NGC 4458. Since we aim to reduce the impact of stellar population gradients in the bulge, these are indeed the closest regions to the centre where the contribution of the nuclear disc is negligible, well below 1%, the level at  $2''$ , as can be seen on the lower right panel of Fig. 3.5. Were it not for the peculiar vertically-elongated character of the VIMOS point-spread function, we would have extracted our bulge aperture spectrum along the minor axis.

Following the extraction of the such a representative bulge spectrum, we proceeded to match it in the best possible way using the pixel-fitting pPXF program (Cappellari and Emsellem, 2004) and the entire stellar spectral library of (Sánchez-Blázquez *et al.*, 2006, also known as the MILES library). Using all the 985 stellar spectra in the MILES library allowed us to match also those spectral features that are notably hard to reproduce when using stellar population synthesis models owing to abundance patterns that can only be partially accounted for in these templates (e.g. the Mgb region; see also Sarzi *et al.*, 2010). In this fit we allowed for interstellar extinction (adopting a Calzetti *et al.*, 2000 reddening law) and for an additional fourth-order additive polynomial correction of the stellar continuum. The weights assigned to each MILES template during the pPXF fit were then used to construct an optimal template for the bulge stellar population.

### 3.3.4 Nuclear stellar population analysis

To estimate the age of the nuclear disc in NGC 4458, we extracted a  $3 \times 1$  pixels central aperture along the minor axis where the disc-light contribution (in the F555W filter wavelength region) amounts to  $\sim 5\%$  and the S/N per pixel reaches values of 120. We then used pPXF to fit such a nuclear spectrum with the previously-derived

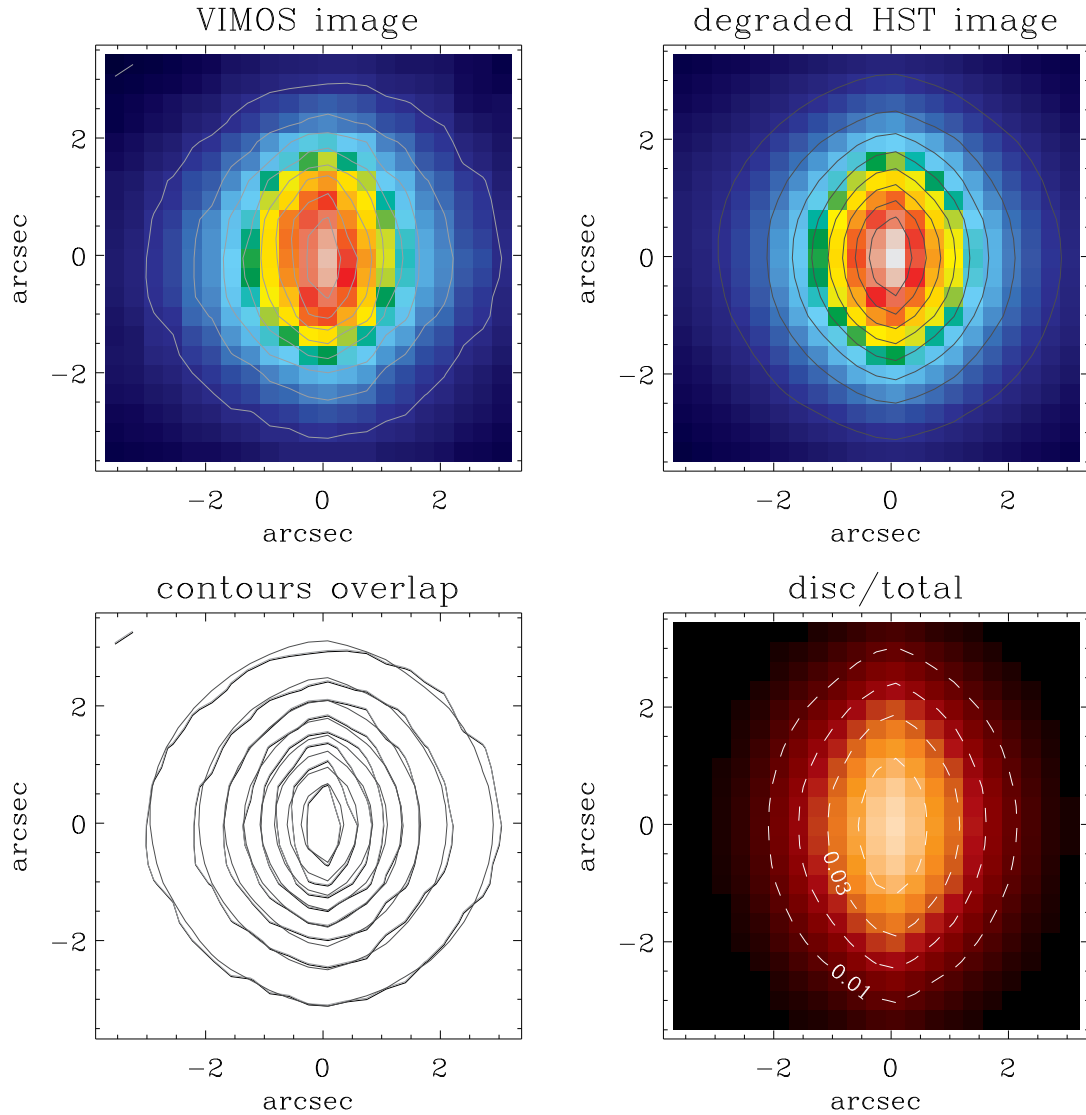


Fig. 3.5: Upper panels: Central parts of the VIMOS reconstructed image of NGC 4458 (left) and the same for the F555W WFPC2 image, once degraded to match the spatial resolution of VIMOS and resampled within the  $0''.33 \times 0''.33$  resolution elements of the high-resolution configuration of VIMOS (right). Lower left: overlap of the surface brightness contours for the VIMOS and degraded HST image (in light and dark grey lines, respectively), which are also shown in the corresponding upper panels. Lower right: map for the disc-to-total light ratio computed from the HST degraded image shown in the upper right panel and a similarly convolved and resampled version for the image of the best-fitting disc model that we obtained during the Scorza & Bender disc-bulge decomposition (§ 3.3.1). The dashed contours on this last image show the level of disc-light contribution in the VIMOS spaxels (but see text). Note that the major axis of NGC 4458 and its nuclear disc runs nearly parallel to the x-axis our VIMOS cube, and the vertical elongation shown here is the results of the rather elongated point-spread function of VIMOS and the steep profile of the intrinsic surface brightness of this galaxy.

bulge template and one of the single-age stellar population models of the Vazdekis *et al.* (2010, based on the MILES spectral atlas) library in order to represent the disc, which we indeed assume to have formed very quickly. We constrained the age of the nuclear disc by considering, at a given stellar metallicity, each one of the stellar population models for the disc at a time, combining them with our empirical bulge template in two different ways. In the first approach (the free fit), we allow pPXF to choose freely the relative weight of these two templates, whereas in the second (the constrained fit) we accounted for the relative light contribution that bulge and disc templates should contribute to the nuclear spectrum, that is 95% and 5% for the bulge and disc, respectively. More specifically, since the disc-light contribution within our central to VIMOS aperture derived in § 3.3.2 refers to the light fraction in the same band-pass of the HST images for NGC 4458, prior to our pPXF fit we integrated the flux of our templates within the F555W passband, and then used such integrated fluxes when weighting them during the constrained fit. During this preliminary step, we also reddened each of the model templates and the bulge template by our best measurement of the interstellar extinction toward the nucleus. This was obtained by performing a pPXF fit to the nuclear spectrum using the entire MILES stellar library, as done previously for the bulge aperture.

Fig. 3.6 shows the first results of this exercise, where the quality of the pPXF fit in the free and constrained cases are compared as a function of stellar-population age for the disc template, in this case, of Solar metallicity. In both instances, the formal uncertainties in the flux density values of the nuclear spectra were rescaled in order for our best possible fit, the one obtained using the entire MILES library, to have  $\chi^2$  value equal to the number of degree of freedom of our fit (NDOF). Both free and constrained approaches indicate that the nuclear disc must indeed be very old, possibly as old as the bulge. The bulge spectrum is indeed best fitted by the oldest and slightly metal-poor (half Solar) single-age templates in the Vazdekis *et al.* library (consistent with the results of both Morelli *et al.*, 2004 and Kuntschner *et al.*, 2010). The free pPXF fit generally prefers to use only our bulge optimal template, and starts including a small fraction (up to 10%) of the single-age disc template only when this corresponds to very old populations. This is a more dramatic behaviour than our initial simulations, which stems from the presence of an overabundance pattern in alpha elements in our nuclear data, in particular in the spectral region corresponding to the Mgb Lick index (González, 1993). This abundance pattern is partially accounted for by our empirical bulge template, and whereas the fit to the Mgb region improved by further including old and Solar or super-Solar single-age population models, the inclusion of younger templates considerably worsens it.

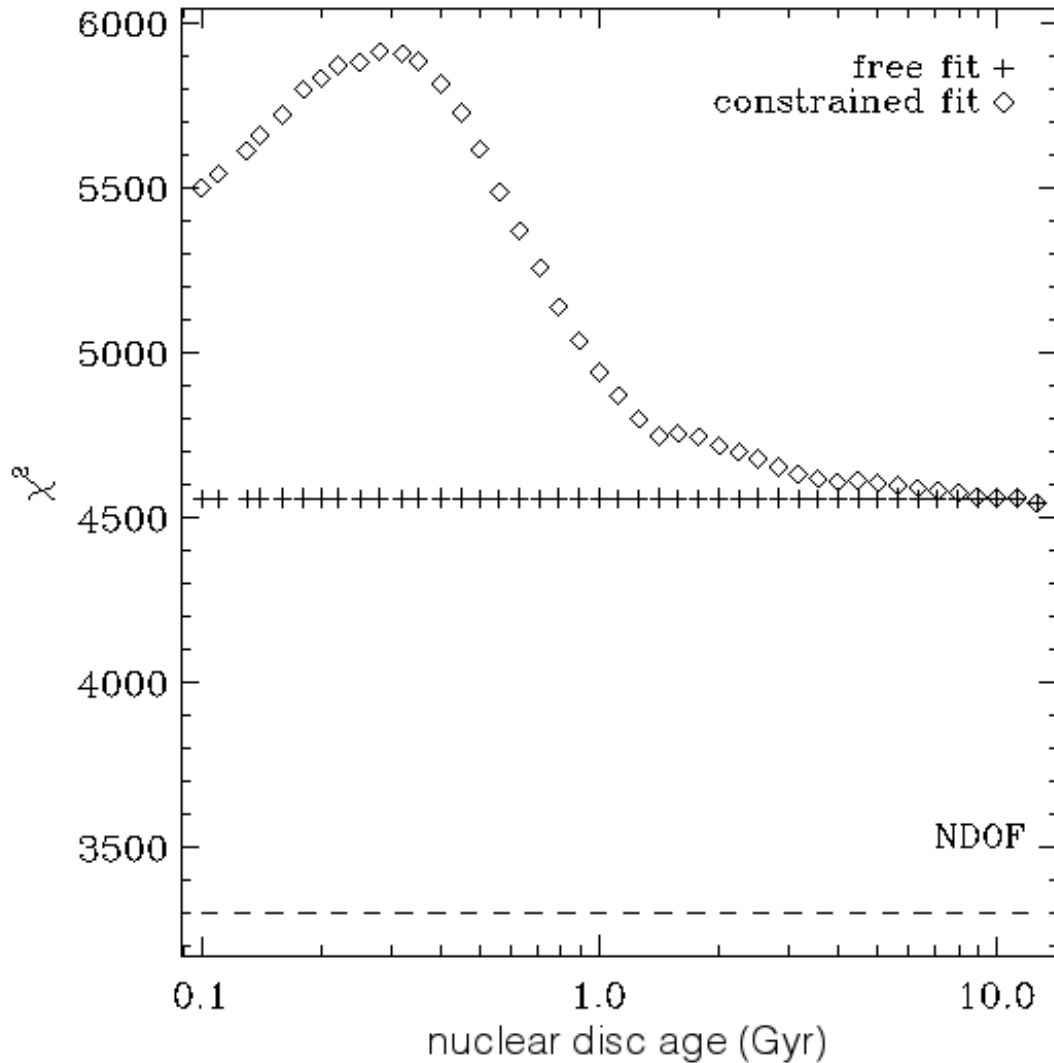


Fig. 3.6: Quality of our constrained (diamonds) and free (plus signs) fits as a function of the stellar age of the nuclear stellar disc, or more specifically, of the single-age stellar population model for disc that is combined with our empirical bulge template. Even though the quality of these fits is relatively poor compared to the quality of the fit that can be achieved through a free combination of all the stellar templates in the MILES library (shown by the horizontal dashed line), the observed trends for both our constrained and free approaches indicate a very old stellar age for the nuclear disc. All  $\chi^2$  values were computed after rescaling the formal uncertainties on the flux densities of our nuclear spectrum so that the best fit based on the entire MILES stellar library sets our standard for a good fit, thus making the corresponding  $\chi^2 = \text{NDOF}$ .

Indeed, this mismatch is considerably exacerbated during the constrained fit, where the quality of the fit quickly deteriorates as we force the use of a progressively younger disc template that contributes to nuclear spectra as expected from our disc-bulge decomposition (i.e.  $\sim 5\%$ ).

In Fig. 3.6 our rescaling of the formal uncertainties on the values of the flux density in our spectra is useful to show that our models for estimating the age of the disc cannot quite match the quality of a fit that does not constrain the possible mix of stellar spectra entering our nuclear spectrum of NGC 4458. Indeed, even while adopting a similarly empirical description for the bulge, the use of single-age stellar population models for the disc lead to fits that are  $\gtrsim 40\%$  worse than our best fit. This may highlight the limitations of such spectral synthesis models or that the disc formation was instead rather prolonged. Given that our tools of trade are not optimal, in order to be as conservative as possible in placing a lower limit on the age of the disc based on  $\Delta\chi^2$  statistics, we ought to further artificially broaden our flux-density errors until our best constrained pPXF fit becomes formally a good fit (i.e. until the corresponding  $\chi^2$  reaches down to NDOF). In fact, for our final estimate of the disc age, we decided to further restrict our analysis to the spectral regions around the age-sensitive  $H\delta$  and  $H\beta$  stellar absorption features. This does not bring much loss of information, since most of the difference between our models occur in these spectral regions (from 90% to 40% of the quadratic difference when comparing models including young and old disc models or for old disc ages only, respectively; see also Fig. 3.7), and has the advantage of making our age estimates less sensitive to the way the polynomials adjust the continuum shape of our models, on which we have little control during the pPXF fit. Finally, we considered single-age stellar population models for the nuclear disc of half and twice Solar metallicity, in addition to the Solar metallicity models used in our first attempt of Fig. 3.6.

Fig. 3.8 shows the run of the quality of our constrained fit in the  $H\delta$  and  $H\beta$  spectral windows as a function of the age of the disc population model that is combined with our empirical bulge template, with different lines indicating the use of single-age models of different stellar metallicity. As anticipated above, all formal uncertainties on the flux density values of our nuclear spectra have been rescaled until our best constrained pPXF fit - in this case including a stellar disc of super-Solar metallicity - lead to a  $\chi^2$  value equal to NDOF across the entire wavelength range. The  $\chi^2$  values plotted in Fig. 3.8 correspond then only to the portion of our spectra within  $30 \text{ \AA}$  of the  $H\delta$  and  $H\beta$  absorption lines at  $4340 \text{ \AA}$  and  $4861 \text{ \AA}$ , respectively. Setting a 1-parameter  $\Delta\chi^2 = 9$  bar above the  $\chi^2$  value of our best-fitting constrained model allows to finally place a  $3\sigma$  lower limit of  $\sim 5\text{--}6$  Gyr on the

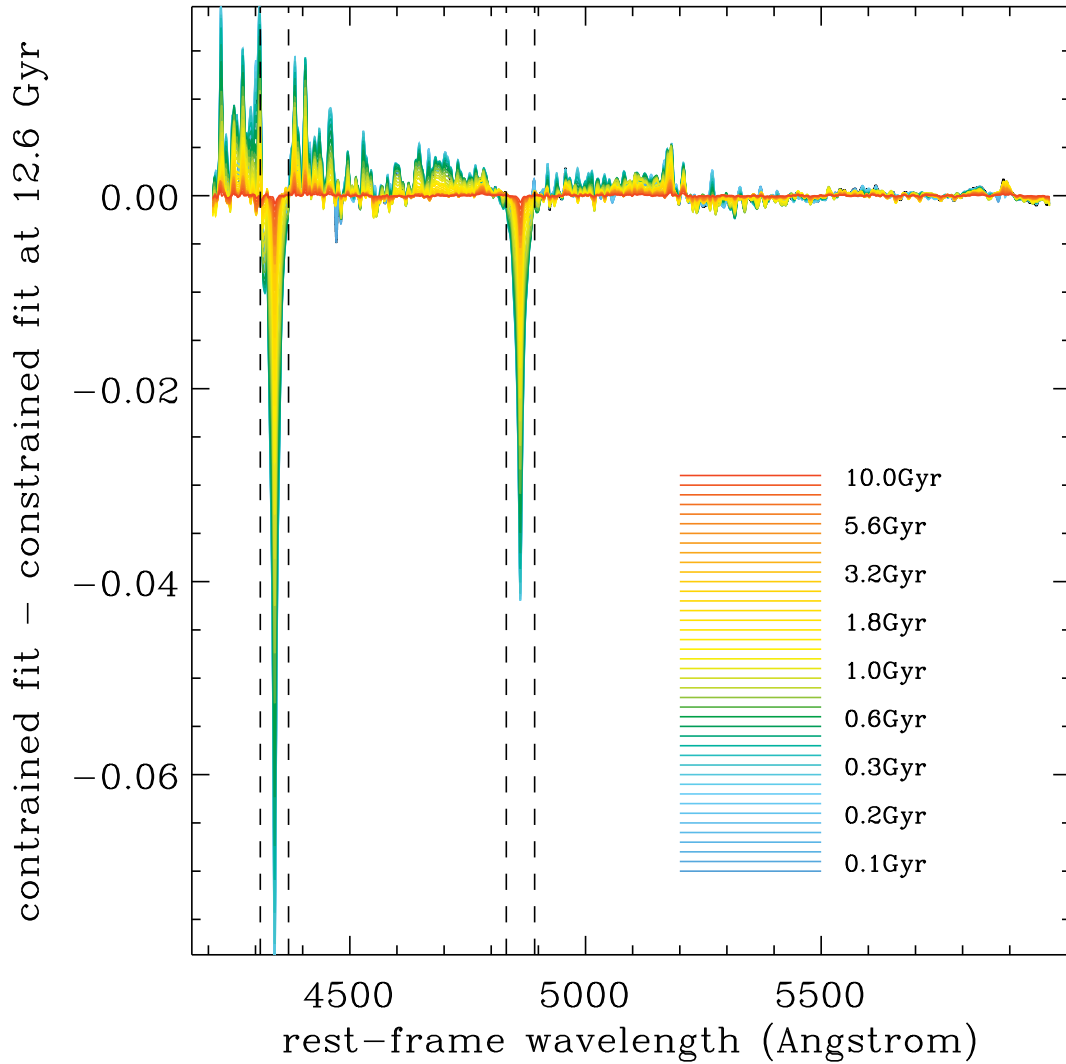


Fig. 3.7: Difference between the best-fitting constrained fit model, which features a 12.6-Gyr-old disc, and all other constrained fits including different single-age disc templates. The largest deviations are observed within the spectral regions identified by the vertical dashed lines, which correspond to the age-sensitive  $H\delta$  and  $H\beta$  stellar absorption features (at 4340 Å and 4861 Å, respectively). Nearly  $\sim 90\%$  of the quadratic difference (relevant for comparing model  $\chi^2$  values) with the youngest disc model is contained across these 30 Å-wide spectral windows, with this fraction lowering to  $\sim 40\%$  when comparing our best model with other models featuring old discs.

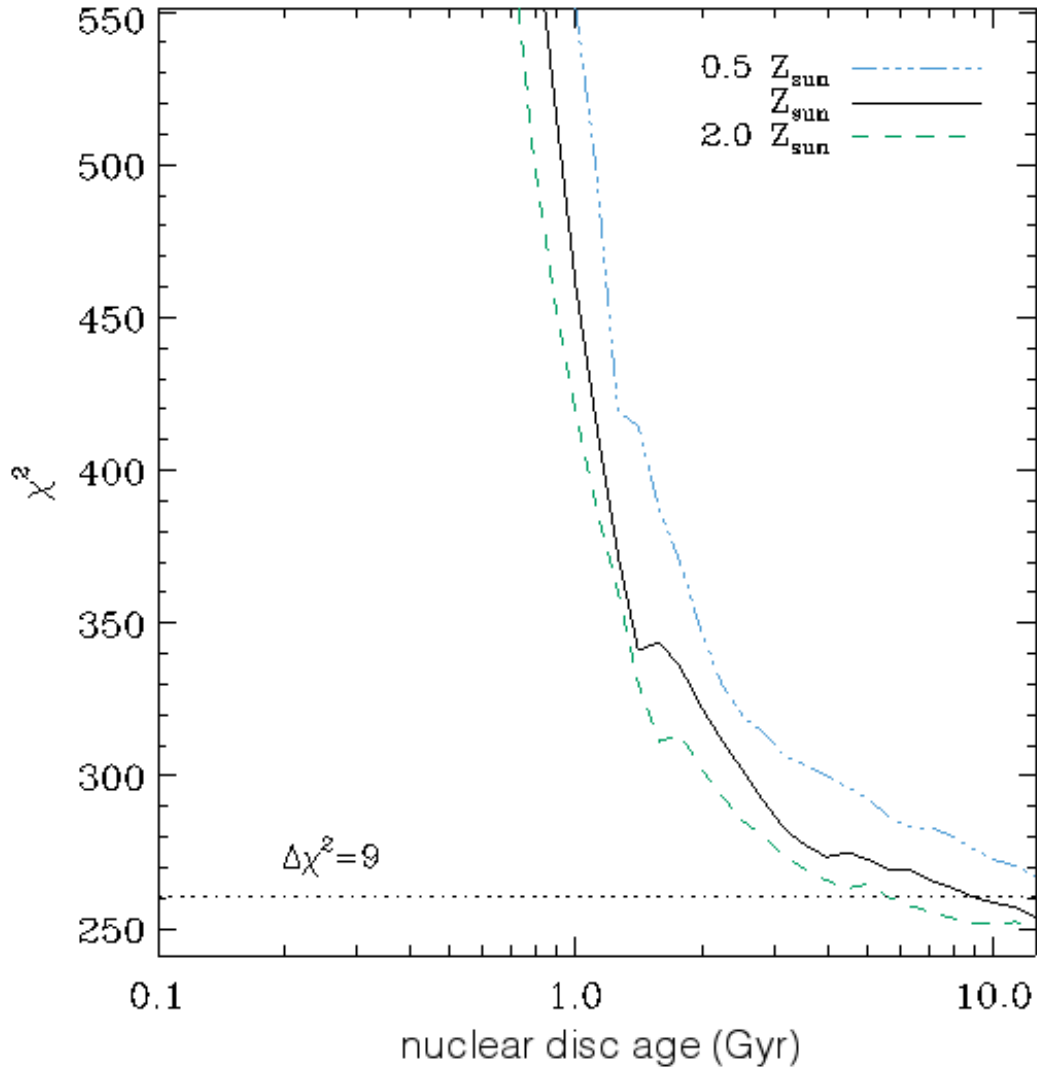


Fig. 3.8: Final stellar age estimate for the nuclear disc of NGC 4458. Similar to Fig. 3.6, but now based only on constrained fit model featuring single-age disc templates of different metallicities (solid lines for Solar values, dot-dashed and dashed for half and twice Solar values, respectively) and while assessing the quality of the fits within the  $H\delta$  and  $H\beta$  spectral windows shown in Fig. 3.7. All plotted  $\chi^2$  values within this spectral region have been computed after rescaling all flux density errors assuming that the best constrained fit model would yield a  $\chi^2 = \text{NDOF}$  across the *entire* spectrum. A  $\Delta\chi^2 = 9$  threshold set from the best  $\chi^2$  value obtained within the  $H\delta$  and  $H\beta$  windows indicate that at best, when considering populations of super-Solar metallicity, the nuclear disc could have formed as recently as  $\sim 5\text{--}6$  Gyr ago.

stellar age of the nuclear disc of NGC 4458. Using the whole spectral range would have yielded a tighter lower limit of  $\sim 7\text{--}8$  Gyr. We also note that possible nebular in-fill contamination in the  $H\delta$  and  $H\beta$  spectral regions is excluded as there is little evidence for  $[\text{O III}]\lambda\lambda 4859, 5007$  emission in the central regions of NGC 4458, either from our data (see Fig. 3.3) or in the SAURON integral-field data shown by Sarzi *et al.* (2006). In fact, considering alternatively only the wavelength regions *outside* the  $H\delta$  and  $H\beta$  windows lead to the same lower limit on the age of the disc as when using the whole spectral range of our VIMOS data.

### 3.4 Discussion

By combining high-quality VIMOS integral-field spectroscopic observations with constraints from HST images on the relative contribution of the nuclear disc of NGC 4458 to the central surface brightness of this galaxy we have been able to set a tight limit on the stellar age of such nuclear disc. Our analysis indicates that its formation must have occurred at least  $\sim 5\text{--}6$  Gyr ago, which in turn suggests that NGC 4458 did not experience any major merger event since that time.

Besides serving as a proof of concept for further measurements in larger samples of NSD-hosting galaxies that could lead to a better understanding of their assembly history, the finding of such an old NSD in NGC 4458 already provides food for thoughts on the formation of the specific class of early-type galaxies that display very little or no bulk rotation. Over the course of the SAURON survey (de Zeeuw *et al.*, 2002) NGC 4458 was in fact classified as one of those so-called slow-rotators (Emsellem *et al.*, 2007), which the ATLAS<sup>3D</sup> survey (Cappellari *et al.*, 2011) firmly recognised as forming only a minority,  $\sim 14\%$ , of the entire early-type galaxy population (Emsellem *et al.*, 2011). More specifically, NGC 4458 falls in the kind of slow-rotators that exhibit a central slowly-rotating core within a non-rotating main stellar body. As in the case of other galaxies in this class, the kinematic transition to the rotating core (which in the case of NGC 4458 occurs  $\sim 5''$  from the centre) does not appear related to any noticeable photometric or stellar-population feature, except that in the case of NGC 4458 a nuclear stellar disc is further found well within it (at  $1''$  scales).

The formation of slow-rotators is still an open issue for theoretical models. Indeed, whereas from a simple semi-analytical approach the present-day relative fraction of fast and slowly-rotating early-type galaxies is well reproduced by considering as fast rotators all objects that in these models have at least 10% of their total stellar mass in a disc component (thanks to a more prolonged gas accretion history,

(Khochfar *et al.*, 2011), numerical simulations for galaxy interactions still have a hard time reproducing both the kinematic and photometric properties of slow rotators. Under certain conditions binary mergers between discs can lead to remnants resembling slow-rotators with a kinematically decoupled core (Jesseit *et al.*, 2009), but generally such simulated objects are much flatter than real slow-rotators. Additional major merger encounters do not address such a discrepancy, but instead destroy the central core and lead to an overall larger angular momentum (Bois *et al.*, 2011). In fact, it is generally difficult to decrease the stellar angular momentum through major mergers since these encounters bring a great deal of orbital angular momentum that must be conserved. For this reason, frequent minor mergers have been advocated as a more efficient means for both removing the angular momentum of galaxies and making them rounder (Khochfar *et al.*, 2011). Yet, even though the negative impact of minor mergers on the angular momentum and flattening has been observed in several numerical simulations carried out in a cosmological context (Naab *et al.* in preparation), there is still limited agreement as regards the intrinsic flattening of simulated and real early-type galaxies (for the latter, see Weijmans *et al.* (2014), based on the ATLAS<sup>3D</sup> sample).

In this respect we note that NGC 4458, with its perfectly edge-on nuclear disc that presumably sits in the equatorial plane, must intrinsically be a nearly spherical galaxy given its apparent axis ratio  $b/a = 1 - \epsilon = 0.88$  (where the flattening  $\epsilon$  is from Emsellem *et al.*, 2011). Furthermore, NGC 4458 is special among slow-rotators, in that it is the least massive object in this class. Its dynamical mass is estimated at  $10^{10}M_{\odot}$  (Cappellari *et al.*, 2013), whereas most non-rotators and slow-rotators with a kinematically decoupled core have mass values of  $10^{11.25}M_{\odot}$  (Emsellem *et al.*, 2011). Both these characteristics make NGC 4458 particularly puzzling. Indeed if the roundness of NGC 4458 could suggest that minor mergers were particularly important in shaping it, its small mass would argue against it since presumably only the most massive systems would have seen many smaller galaxies coming their way during their history. The presence of a nuclear disc could represent an additional argument against a late satellite bombardment, or alternatively suggest that such minor mergers rarely end up affecting the central parts of a galaxy (as already pointed out by Callegari *et al.*, 2009, 2011).

Finally, NGC 4458 also hosts a KDC that, as suggested already by many authors for this kind of structures (e.g. Balcells and Quinn, 1990; Hernquist and Barnes, 1991; Di Matteo *et al.*, 2008; Bois *et al.*, 2011), could have formed during a gas-poor merger event, not necessarily far back in time. Yet, if that were the case, the presence of an embedded NSD indicates that such an event must have preceded the

formation of the disc, or perhaps lead also its formation if some gas material was present. In fact, a closer look to the central stellar kinematics of NGC 4458 may further suggest a link between these two structures. After extracting with pPXF not only the mean stellar velocity  $V$  and velocity dispersion  $\sigma$  but also the first two high-order Gauss-Hermite moments  $h_3$  and  $h_4$  of the line-of-sight velocity distribution (LOSVD, where  $h_3$  and  $h_4$  relate to its skewness and kurtosis deviations from a Gaussian form, respectively), we indeed notice that the KDC of NGC 4458 appears to be more rotationally-supported than all other KDCs found during the ATLAS<sup>3D</sup> survey. This is shown in Fig. 3.9, which compares the KDC of NGC 4458 with all other KDCs identified by Krajnović *et al.* (2011) in the resolved  $h_3$  vs.  $V/\sigma$  diagnostic that serves to highlight both the trailing low-velocity tail in the LOSVD of stellar discs, by means of a strong anti-correlation between  $h_3$  and  $V$ , and the degree of rotational support through the  $V/\sigma$  ratio. Fast rotating early-type galaxies show strongly anti-correlated  $V/\sigma$  and  $h_3$  that can reach absolute values up to  $\sim 2$  and 0.2 respectively. Slow-rotators on the other hand generally show much smaller values for both quantities, with only a hint of an anti-correlation for slow-rotators with such structures (i.e. class “c” of Krajnović *et al.*). However, when only the KDC-dominated regions of such objects (see Fig. C4 of Krajnović *et al.*) are plotted in this diagram, a weak but significant  $h_3$ – $V/\sigma$  anti-correlation emerges. It is within this context, that our VIMOS data show that our  $h_3$  and  $V/\sigma$  measurements in the central  $6''$  of NGC 4458 extend to significantly larger values than observed in the ATLAS<sup>3D</sup> KDCs,<sup>1</sup> although these are still far from what is found in fast-rotators (in particular for  $V/\sigma$ ). We speculate that this peculiarity of the KDC in NGC 4458 could indicate that at least a fraction of this structure was initially part of a larger central disc, the outer reaches of which would have then been disrupted by successive minor mergers (as would seem required to make the whole galaxy round and slowly-rotating), provided that those interactions also failed to affect the very central regions (Callegari *et al.*, 2009, 2011).

---

<sup>1</sup>SAURON data exist also for NGC 4458 but do not show strong  $h_3$  values, most likely due to the poor seeing conditions ( $1''.6$  FWHM) under which this object was observed (Emsellem *et al.*, 2004). This may suggest that the results shown in Fig. 3.9 are sensitive to spatial resolution and the apparent size of KDCs, but in fact a very similar picture emerges when only the most extended and fast-rotating of the KDCs shown in Fig. C4 of Krajnović *et al.* are used for comparison with our VIMOS data for NGC 4458. For a comparison between the VIMOS and SAURON central kinematics of NGC 4458, please refer to Appendix C.

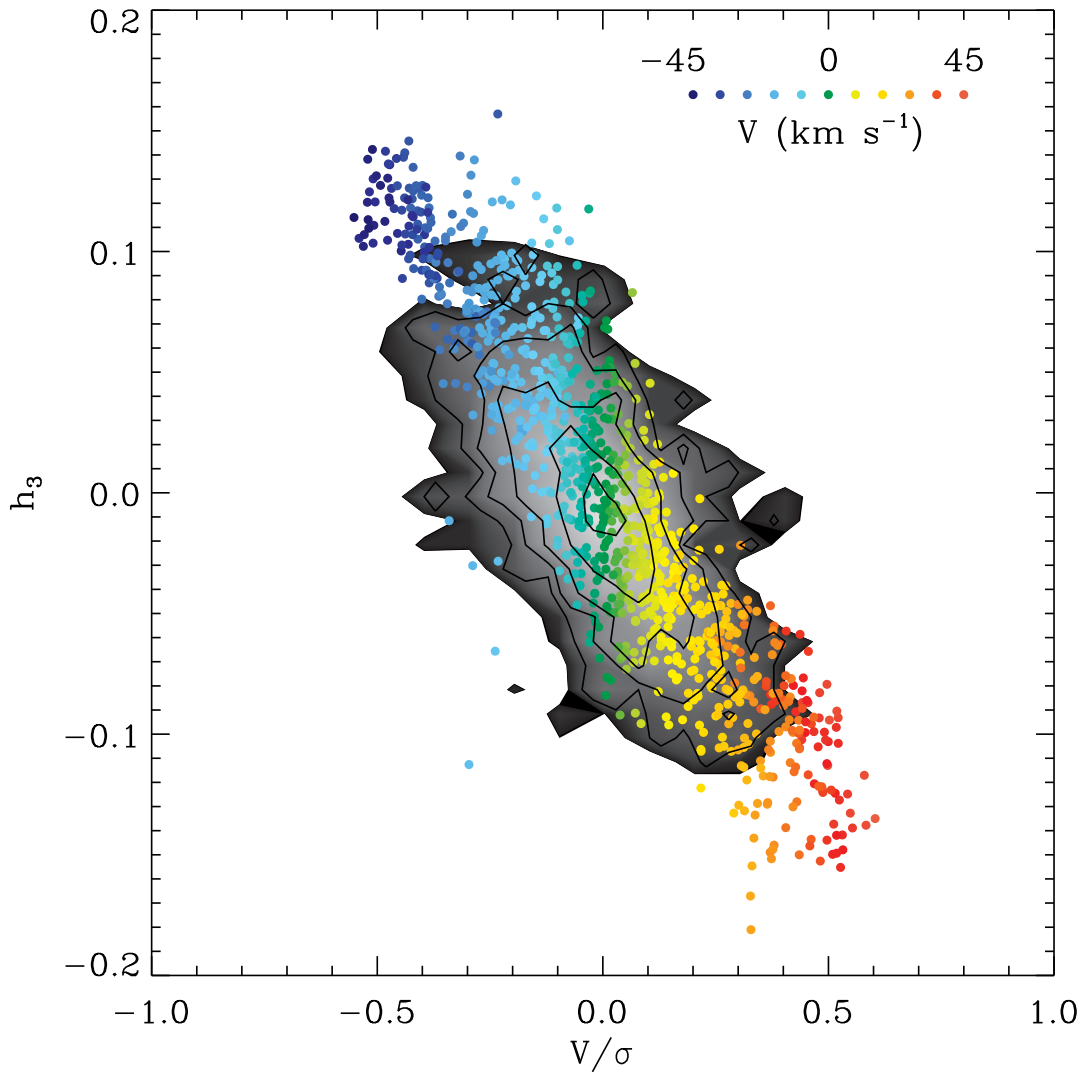


Fig. 3.9: Local  $h_3$ - $V/\sigma$  relation for the kinematically decoupled core of NGC 4458 (coloured points) compared to that observed for all such structures found in the ATLAS<sup>3D</sup> survey (grey contours). The data points correspond to measurements performed with pPXF in all VIMOS spectra within the central 6'' of NGC 4458, and are colour-coded according to the value of the stellar velocity  $V$ . The grey contours show the relative density in the  $h_3$ - $V/\sigma$  plane of similar measurements from all the individual SAURON spectra of galaxies with KDC in the ATLAS<sup>3D</sup> survey similarly to Fig. 9 of Krajnović et al. (2011, for class “c” objects), except that here we show only the central KDC-dominated regions of such objects. The contour lines show densities of 5, 10, 20, 40 and 80 SAURON data points. Our data extend to larger  $V/\sigma$  and  $h_3$  values than these contours, suggesting that the KDC of NGC 4458 is more rotationally-supported than the typical KDC in nearby early-type galaxies.

### 3.4.1 Future outlook

The results of our stellar-population analysis for the central regions of NGC 4458 demonstrate the accuracy with which it is possible to constrain the age of NSDs with integral-field data. Considering that such structures are present in up to 20% of early-type galaxies (Chapter 2), a similar but systematic investigation of NSDs in galaxies of different mass and across different galactic environments would constitute a promising avenue for constraining the assembly history of early-type galaxies. In fact, Chapter 2 already provides the most extensive sample of nearby NSDs on which such a follow-up survey could be based.

In this respect, the next generation integral-field spectrograph MUSE (Bacon *et al.*, 2010), soon to be mounted at the UT4 of VLT, will be particularly suited for such an NSD census, for several reasons. MUSE is indeed expected to be much more efficient than VIMOS (with an overall throughput reaching up to  $\sim 40\%$ ), it will extend to a longer wavelength range (from 4650 Å to 9300 Å) allowing a neater separation of the nebular emission from the stellar continuum, while retaining a spectral resolution of  $R \sim 3000$  sufficient for a detailed estimate of the stellar LOSVD. Finally, and most importantly for the study of NSDs, MUSE will eventually also work with adaptive optics and reach a spatial resolving power comparable to that of HST, which will dramatically boost the disc contribution to the nuclear spectra. This will lead to even tighter constraints of the NSD age, in particular if the stellar kinematics observed in the nuclear regions are also brought in as an additional constraint.

A better NSD-to-bulge contrast and the ability to constrain the stellar LOSVD (in turn thanks to an excellent data quality and of a respectable spectral resolution) should allow to fold into our analysis a self-consistent dynamical model for the central kinematics (e.g. based on Jeans equations, Cappellari, 2008), which will be also very sensitive to the age of the disc. For instance, at a given disc-light contribution, choosing an older stellar population for the disc will mean considering a more massive nuclear disc that will imprint a larger rotation velocity to the disc stars in the models, whereas picking a very young age will translate into a disc dynamics almost entirely determined by the gravitational potential of the bulge.

If our ability to constrain the stellar age of nearby NSDs seems set to improve in the near future, steps will also have to be made on a more theoretical side in order to better understand the implications of such age estimates. In particular it will be paramount to assess the extent to which NSDs are fragile to merger episodes, so that the presence of these discs can be firmly translated into a maximum mass ratio for any accretion event that could have followed the formation of the disc. At the

same time, it will also be interesting to follow the disruption of NSDs during more dramatic encounters, looking for instance for the possible kinematic signature of the past presence of such structures. Progress in this direction has already been made, as it will be discussed in Chapter 4, using a relatively large set of numerical simulations, which show not only how NDSs emerge relatively unscathed from minor mergers (e.g. for a 1 to 10 mass ratio or less) but also that a central rotating structure could still be present at the end of more important interactions that leave no photometric trace of the NSD. Although encouraging, these results are still based on simple initial conditions mimicking the final phases of a merger event and which always lead the central black hole of the satellite galaxy to sink towards the centre, whereas this may not always be the case as we already noted. More comprehensive simulations are therefore needed to fully understand the fragility of NSDs against minor mergers, possibly shedding also more light on the origin of kinematically decoupled central structures and the possible link to past central discs.

Finally, we note that the advantage of knowing *a priori* the stellar light contribution of a given stellar subpopulation to the optical spectra of a galaxy may be used to constrain also the stellar age of other kinds of galactic components beside NSDs, such as more extended discs, nuclear rings or other photometrically distinguishable structures.

# References

- Anguita, T., Faure, C., Yonehara, A., Wambsganss, J., Kneib, J.-P., Covone, G., and Alloin, D. (2008). Integral field spectroscopy of four lensed quasars: analysis of their neighborhood and evidence for microlensing. *A&A*, **481**, 615–627.
- Bacon, R., Accardo, M., Adjali, L., Anwand, H., Bauer, S., Biswas, I., Blaizot, J., Boudon, D., Brau-Nogue, S., Brinchmann, J., Caillier, P., Capoani, L., Carollo, C. M., Contini, T., Couderc, P., Daguisé, E., Deiries, S., Delabre, B., Dreizler, S., Dubois, J., Dupieux, M., Dupuy, C., Emsellem, E., Fechner, T., Fleischmann, A., François, M., Gallou, G., Gharsa, T., Glindemann, A., Gojak, D., Guiderdoni, B., Hansali, G., Hahn, T., Jarno, A., Kelz, A., Koehler, C., Kosmalski, J., Laurent, F., Le Floch, M., Lilly, S. J., Lizon, J.-L., Loupiau, M., Manescau, A., Monstein, C., Nicklas, H., Olaya, J.-C., Pares, L., Pasquini, L., Pécontal-Rousset, A., Pelló, R., Petit, C., Popow, E., Reiss, R., Remillieux, A., Renault, E., Roth, M., Rupprecht, G., Serre, D., Schaye, J., Soucail, G., Steinmetz, M., Streicher, O., Stuik, R., Valentin, H., Vernet, J., Weilbacher, P., Wisotzki, L., and Yerle, N. (2010). The MUSE second-generation VLT instrument. In *Society of Photo-Optical Instrumentation Engineers (SPIE) Conference Series*, volume 7735 of *Society of Photo-Optical Instrumentation Engineers (SPIE) Conference Series*.
- Balcells, M. and Quinn, P. J. (1990). The formation of counterrotating cores in elliptical galaxies. *ApJ*, **361**, 381–393.
- Binney, J. and Tremaine, S. (1987). *Galactic dynamics*.
- Bois, M., Emsellem, E., Bournaud, F., Alatalo, K., Blitz, L., Bureau, M., Cappellari, M., Davies, R. L., Davis, T. A., de Zeeuw, P. T., Duc, P.-A., Khochfar, S., Krajnović, D., Kuntschner, H., Lablanche, P.-Y., McDermid, R. M., Morganti, R., Naab, T., Oosterloo, T., Sarzi, M., Scott, N., Serra, P., Weijmans, A.-M., and Young, L. M. (2011). The ATLAS<sup>3D</sup> project - VI. Simulations of binary galaxy mergers and the link with fast rotators, slow rotators and kinematically distinct cores. *MNRAS*, **416**, 1654–1679.
- Bruzual, G. and Charlot, S. (2003). Stellar population synthesis at the resolution of 2003. *MNRAS*, **344**, 1000–1028.
- Callegari, S., Mayer, L., Kazantzidis, S., Colpi, M., Governato, F., Quinn, T., and Wadsley, J. (2009). Pairing of Supermassive Black Holes in Unequal-Mass Galaxy Mergers. *ApJ*, **696**, L89–L92.
- Callegari, S., Kazantzidis, S., Mayer, L., Colpi, M., Bellovary, J. M., Quinn, T., and Wadsley, J. (2011). Growing Massive Black Hole Pairs in Minor Mergers of Disk Galaxies. *ApJ*, **729**, 85.

- Calzetti, D., Armus, L., Bohlin, R. C., Kinney, A. L., Koornneef, J., and Storchi-Bergmann, T. (2000). The Dust Content and Opacity of Actively Star-forming Galaxies. *ApJ*, **533**, 682–695.
- Cappellari, M. (2008). Measuring the inclination and mass-to-light ratio of axisymmetric galaxies via anisotropic Jeans models of stellar kinematics. *MNRAS*, **390**, 71–86.
- Cappellari, M. and Emsellem, E. (2004). Parametric Recovery of Line-of-Sight Velocity Distributions from Absorption-Line Spectra of Galaxies via Penalized Likelihood. *PASP*, **116**, 138–147.
- Cappellari, M., Emsellem, E., Bacon, R., Bureau, M., Davies, R. L., de Zeeuw, P. T., Falcón-Barroso, J., Krajnović, D., Kuntschner, H., McDermid, R. M., Peletier, R. F., Sarzi, M., van den Bosch, R. C. E., and van de Ven, G. (2007). The SAURON project - X. The orbital anisotropy of elliptical and lenticular galaxies: revisiting the  $(V/\sigma, \epsilon)$  diagram with integral-field stellar kinematics. *MNRAS*, **379**, 418–444.
- Cappellari, M., Emsellem, E., Krajnović, D., McDermid, R. M., Scott, N., Verdoes Kleijn, G. A., Young, L. M., Alatalo, K., Bacon, R., Blitz, L., Bois, M., Bournaud, F., Bureau, M., Davies, R. L., Davis, T. A., de Zeeuw, P. T., Duc, P.-A., Khochfar, S., Kuntschner, H., Lablanche, P.-Y., Morganti, R., Naab, T., Oosterloo, T., Sarzi, M., Serra, P., and Weijmans, A.-M. (2011). The ATLAS<sup>3D</sup> project - I. A volume-limited sample of 260 nearby early-type galaxies: science goals and selection criteria. *MNRAS*, **413**, 813–836.
- Cappellari, M., Scott, N., Alatalo, K., Blitz, L., Bois, M., Bournaud, F., Bureau, M., Crocker, A. F., Davies, R. L., Davis, T. A., de Zeeuw, P. T., Duc, P.-A., Emsellem, E., Khochfar, S., Krajnović, D., Kuntschner, H., McDermid, R. M., Morganti, R., Naab, T., Oosterloo, T., Sarzi, M., Serra, P., Weijmans, A.-M., and Young, L. M. (2013). The ATLAS<sup>3D</sup> project - XV. Benchmark for early-type galaxies scaling relations from 260 dynamical models: mass-to-light ratio, dark matter, Fundamental Plane and Mass Plane. *MNRAS*, **432**, 1709–1741.
- Darg, D. W., Kaviraj, S., Lintott, C. J., Schawinski, K., Sarzi, M., Bamford, S., Silk, J., Proctor, R., Andreescu, D., Murray, P., Nichol, R. C., Raddick, M. J., Slosar, A., Szalay, A. S., Thomas, D., and Vandenberg, J. (2010). Galaxy Zoo: the fraction of merging galaxies in the SDSS and their morphologies. *MNRAS*, **401**, 1043–1056.
- De Lucia, G., Springel, V., White, S. D. M., Croton, D., and Kauffmann, G. (2006). The formation history of elliptical galaxies. *MNRAS*, **366**, 499–509.
- de Zeeuw, P. T., Bureau, M., Emsellem, E., Bacon, R., Carollo, C. M., Copin, Y., Davies, R. L., Kuntschner, H., Miller, B. W., Monnet, G., Peletier, R. F., and Verolme, E. K. (2002). The SAURON project - II. Sample and early results. *MNRAS*, **329**, 513–530.

- Di Matteo, P., Combes, F., Melchior, A.-L., and Semelin, B. (2008). Old stellar counter-rotating components in early-type galaxies from elliptical-spiral mergers. *A&A*, **477**, 437–442.
- Ebrova, I., Jungwiert, B., Canalizo, G., Bennert, N., and Jilkova, L. (2010). Shell Galaxies: Dynamical Friction, Gradual Satellite Decay and Merger Dating. In B. Smith, J. Higdon, S. Higdon, and N. Bastian, editors, *Galaxy Wars: Stellar Populations and Star Formation in Interacting Galaxies*, volume 423 of *Astronomical Society of the Pacific Conference Series*, page 236.
- Emsellem, E., Cappellari, M., Peletier, R. F., McDermid, R. M., Bacon, R., Bureau, M., Copin, Y., Davies, R. L., Krajnovic, D., Kuntschner, H., Miller, B. W., and de Zeeuw, P. T. (2004). The SAURON project - III. Integral-field absorption-line kinematics of 48 elliptical and lenticular galaxies. *MNRAS*, **352**, 721–743.
- Emsellem, E., Cappellari, M., Krajnovic, D., van de Ven, G., Bacon, R., Bureau, M., Davies, R. L., de Zeeuw, P. T., Falcon-Barroso, J., Kuntschner, H., McDermid, R., Peletier, R. F., and Sarzi, M. (2007). The SAURON project - IX. A kinematic classification for early-type galaxies. *MNRAS*, **379**, 401–417.
- Emsellem, E., Cappellari, M., Krajnovic, D., Alatalo, K., Blitz, L., Bois, M., Bournaud, F., Bureau, M., Davies, R. L., Davis, T. A., de Zeeuw, P. T., Khochfar, S., Kuntschner, H., Lablanche, P.-Y., McDermid, R. M., Morganti, R., Naab, T., Oosterloo, T., Sarzi, M., Scott, N., Serra, P., van de Ven, G., Weijmans, A.-M., and Young, L. M. (2011). The ATLAS<sup>3D</sup> project - III. A census of the stellar angular momentum within the effective radius of early-type galaxies: unveiling the distribution of fast and slow rotators. *MNRAS*, **414**, 888–912.
- Gonzalez, J. J. (1993). *Line strength gradients and kinematic profiles in elliptical galaxies*. Ph.D. thesis, Thesis (PH.D.)–UNIVERSITY OF CALIFORNIA, SANTA CRUZ, 1993.Source: Dissertation Abstracts International, Volume: 54-05, Section: B, page: 2551.
- Hau, G. K. T., Carter, D., and Balcells, M. (1999). The shell elliptical galaxy NGC 2865: evolutionary population synthesis of a kinematically distinct core. *MNRAS*, **306**, 437–460.
- Hernquist, L. and Barnes, J. E. (1991). Origin of kinematic subsystems in elliptical galaxies. *Nature*, **354**, 210–212.
- Jesseit, R., Cappellari, M., Naab, T., Emsellem, E., and Burkert, A. (2009). Specific angular momentum of disc merger remnants and the  $\lambda_R$ -parameter. *MNRAS*, **397**, 1202–1214.
- Khochfar, S., Emsellem, E., Serra, P., Bois, M., Alatalo, K., Bacon, R., Blitz, L., Bournaud, F., Bureau, M., Cappellari, M., Davies, R. L., Davis, T. A., de Zeeuw, P. T., Duc, P.-A., Krajnovic, D., Kuntschner, H., Lablanche, P.-Y., McDermid, R. M., Morganti, R., Naab, T., Oosterloo, T., Sarzi, M., Scott, N., Weijmans, A.-M., and Young, L. M. (2011). The ATLAS<sup>3D</sup> project - VIII. Modelling the

- formation and evolution of fast and slow rotator early-type galaxies within  $\Lambda$ CDM. *MNRAS*, **417**, 845–862.
- Krajnović, D., Emsellem, E., Cappellari, M., Alatalo, K., Blitz, L., Bois, M., Bournaud, F., Bureau, M., Davies, R. L., Davis, T. A., de Zeeuw, P. T., Khochfar, S., Kuntschner, H., Lablanche, P.-Y., McDermid, R. M., Morganti, R., Naab, T., Oosterloo, T., Sarzi, M., Scott, N., Serra, P., Weijmans, A.-M., and Young, L. M. (2011). The ATLAS<sup>3D</sup> project - II. Morphologies, kinematic features and alignment between photometric and kinematic axes of early-type galaxies. *MNRAS*, **414**, 2923–2949.
- Kuntschner, H., Emsellem, E., Bacon, R., Cappellari, M., Davies, R. L., de Zeeuw, P. T., Falcón-Barroso, J., Krajnović, D., McDermid, R. M., Peletier, R. F., Sarzi, M., Shapiro, K. L., van den Bosch, R. C. E., and van de Ven, G. (2010). The SAURON project - XVII. Stellar population analysis of the absorption line strength maps of 48 early-type galaxies. *MNRAS*, **408**, 97–132.
- Le Fèvre, O., Saisse, M., Mancini, D., Brau-Nogue, S., Caputi, O., Castinel, L., D’Odorico, S., Garilli, B., Kissler-Patig, M., Lucuix, C., Mancini, G., Pauget, A., Sciarretta, G., Scodreggio, M., Tresse, L., and Vettolani, G. (2003). Commissioning and performances of the VLT-VIMOS instrument. In M. Iye and A. F. M. Moorwood, editors, *Society of Photo-Optical Instrumentation Engineers (SPIE) Conference Series*, volume 4841 of *Society of Photo-Optical Instrumentation Engineers (SPIE) Conference Series*, pages 1670–1681.
- Ledo, H. R., Sarzi, M., Dotti, M., Khochfar, S., and Morelli, L. (2010). A census of nuclear stellar discs in early-type galaxies. *MNRAS*, **407**, 969–985.
- Morelli, L., Halliday, C., Corsini, E. M., Pizzella, A., Thomas, D., Saglia, R. P., Davies, R. L., Bender, R., Birkinshaw, M., and Bertola, F. (2004). Nuclear stellar discs in low-luminosity elliptical galaxies: NGC 4458 and 4478. *MNRAS*, **354**, 753–762.
- Naab, T. (2013). Modelling the formation of today’s massive ellipticals. In D. Thomas, A. Pasquali, and I. Ferreras, editors, *IAU Symposium*, volume 295 of *IAU Symposium*, pages 340–349.
- Sánchez-Blázquez, P., Peletier, R. F., Jiménez-Vicente, J., Cardiel, N., Cenarro, A. J., Falcón-Barroso, J., Gorgas, J., Selam, S., and Vazdekis, A. (2006). Medium-resolution Isaac Newton Telescope library of empirical spectra. *MNRAS*, **371**, 703–718.
- Sarzi, M., Falcón-Barroso, J., Davies, R. L., Bacon, R., Bureau, M., Cappellari, M., de Zeeuw, P. T., Emsellem, E., Fathi, K., Krajnović, D., Kuntschner, H., McDermid, R. M., and Peletier, R. F. (2006). The SAURON project - V. Integral-field emission-line kinematics of 48 elliptical and lenticular galaxies. *MNRAS*, **366**, 1151–1200.

- Sarzi, M., Shields, J. C., Schawinski, K., Jeong, H., Shapiro, K., Bacon, R., Bureau, M., Cappellari, M., Davies, R. L., de Zeeuw, P. T., Emsellem, E., Falcón-Barroso, J., Krajnović, D., Kuntschner, H., McDermid, R. M., Peletier, R. F., van den Bosch, R. C. E., van de Ven, G., and Yi, S. K. (2010). The SAURON project - XVI. On the sources of ionization for the gas in elliptical and lenticular galaxies. *MNRAS*, **402**, 2187–2210.
- Scorza, C. and Bender, R. (1995). The internal structure of disk elliptical galaxies. *A&A*, **293**, 20–43.
- Thomas, D., Maraston, C., Bender, R., and Mendes de Oliveira, C. (2005). The Epochs of Early-Type Galaxy Formation as a Function of Environment. *ApJ*, **621**, 673–694.
- Thomas, D., Maraston, C., Schawinski, K., Sarzi, M., and Silk, J. (2010). Environment and self-regulation in galaxy formation. *MNRAS*, **404**, 1775–1789.
- Toomre, A. (1977). Mergers and Some Consequences. In B. M. Tinsley and R. B. G. Larson, D. Campbell, editors, *Evolution of Galaxies and Stellar Populations*, page 401.
- van den Bosch, F. C., Ferrarese, L., Jaffe, W., Ford, H. C., and O’Connell, R. W. (1994). Hubble Space Telescope photometry of the central regions of Virgo cluster elliptical galaxies. II: Isophote shapes. *AJ*, **108**, 1579–1597.
- Vazdekis, A., Sánchez-Blázquez, P., Falcón-Barroso, J., Cenarro, A. J., Beasley, M. A., Cardiel, N., Gorgas, J., and Peletier, R. F. (2010). Evolutionary stellar population synthesis with MILES - I. The base models and a new line index system. *MNRAS*, **404**, 1639–1671.
- Weijmans, A.-M., de Zeeuw, P. T., Emsellem, E., Krajnović, D., Lablanche, P.-Y., Alatalo, K., Blitz, L., Bois, M., Bournaud, F., Bureau, M., Cappellari, M., Crocker, A. F., Davies, R. L., Davis, T. A., Duc, P.-A., Khochfar, S., Kuntschner, H., McDermid, R. M., Morganti, R., Naab, T., Oosterloo, T., Sarzi, M., Scott, N., Serra, P., Verdoes Kleijn, G., and Young, L. M. (2014). The ATLAS <sup>3D</sup> project - XXIV. The intrinsic shape distribution of early-type galaxies. *MNRAS*, **444**, 3340–3356.

### 3.5 Appendix C: Comparison between VIMOS and SAURON

In this Appendix we compare our VIMOS stellar kinematic measurements for the central regions of NGC 4458 (extracted using the pPXF code of Cappellari and Emsellem (2004)) with the ones based on SAURON data and published by Emsellem *et al.* (2004). This comparison is shown by Fig. 3.10.

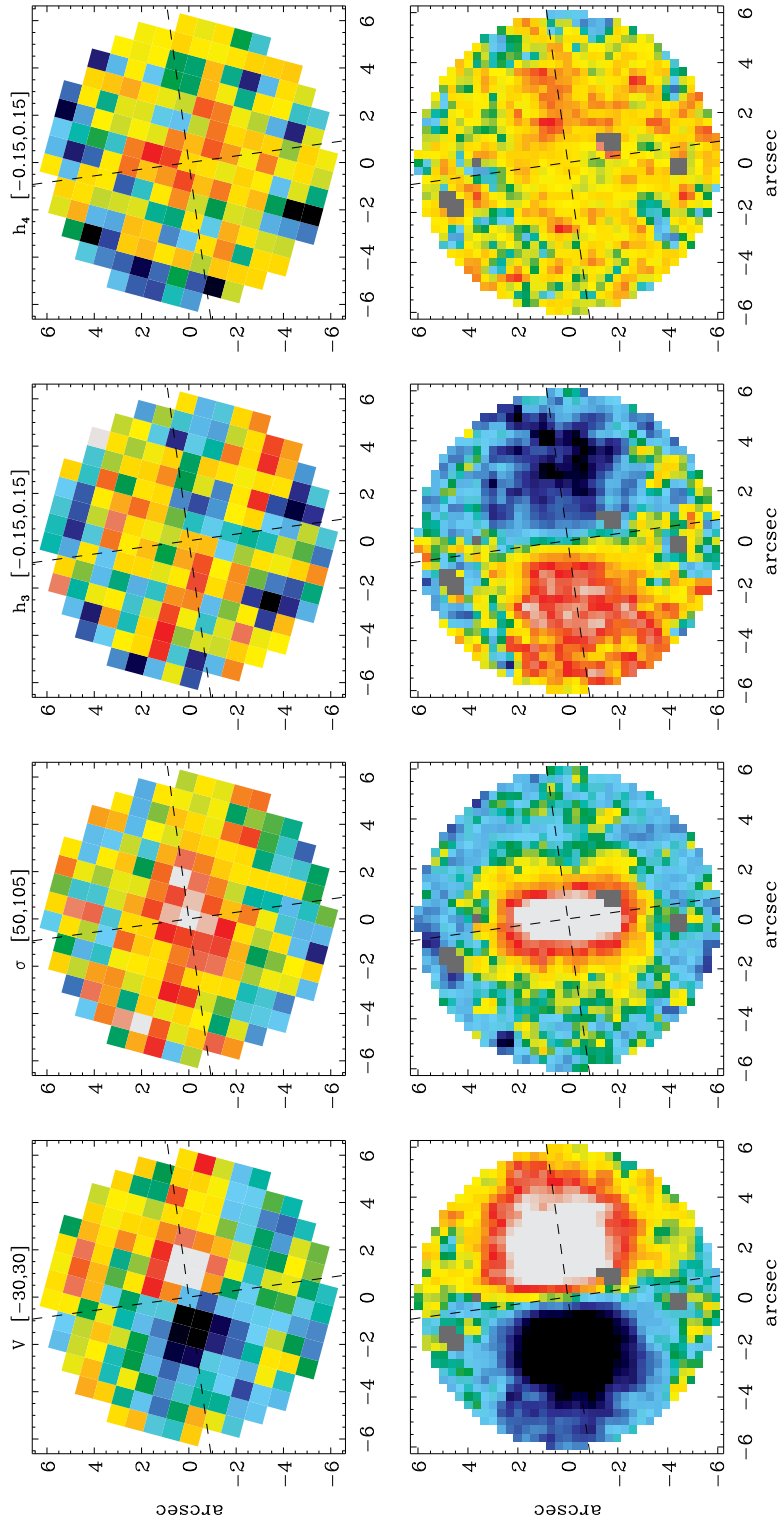


Fig. 3.10: A comparison between the SAURON (top row) and VIMOS (lower row) stellar kinematic measurements for the central regions of NGC 4458. From left to right, the panels show the stellar velocity, velocity dispersion  $\sigma$  and the  $h_3$  and  $h_4$  Gauss-Hermite moments of the line-of-sight velocity distribution. In the velocity field black/blue and red/white colours indicate approaching and receding stars, where in the other panel the same colour scale indicates low or high values. The limits for  $V$ ,  $\sigma$ ,  $h_3$  and  $h_4$  are shown at the top of each column.

Our VIMOS kinematic measurements are somewhat different when compared to the SAURON ones, in particular as we detect a much cleaner  $h_3$  field and a more extended velocity field. We ascribe these differences mostly to the superior spectral resolutions and sampling of VIMOS (FWHM=2.0 Å sampled at 30 km/s velocity steps when the spectra are log-rebinned, compared to 4.2 Å and 60 km/s in the case of the SAURON spectra), which allows to better constrain the line-of-sight velocity distribution in the central regions of NGC 4458, in particular given the small velocity dispersion observed in this galaxy. Furthermore, the longer wavelength range of the VIMOS spectra (ranging from 4300 Å till 6000 Å compared to 4800 Å till 5300 Å for SAURON) also contributes to a more robust kinematic extraction.

Our vertically extended PSF leads only to an overall vertical stretch of our  $V$ ,  $\sigma$ , and  $h_3$  field, but fortunately this does not affect the overall appearance of our data in the  $V/\sigma$  vs.  $h_3$  diagram of Fig. 3.9. Our elongated PSF is indeed aligned with the zero-velocity line of the central KDC, so that even if the central  $\sigma$  values are more extended in this direction, the  $V/\sigma$  ratio remains close to zero.

The SAURON data were also taken under worse seeing conditions, with a FWHM of 1".6 compared to 0".8 for the VIMOS observations, which still applies in the horizontal direction of our datacubes. This would contribute to explain both the wider extent of the KDC in the VIMOS data and larger central values for the velocity dispersion. A poorer spatial resolution would indeed dilute a central peak of velocity dispersion and reduce the extent of detectable rotation as the KDC region is more contaminated by light from the non-rotating outer parts of this galaxy.

---

# CHAPTER 4: ON THE FRAGILITY OF NUCLEAR STELLAR DISCS AGAINST GALAXY MERGERS

---

With collaborators M. Dotti<sup>1,2</sup> and M. Sarzi<sup>3</sup>.

<sup>1</sup>Dipartimento di Fisica G. Occhialini, Università degli Studi di Milano, Bicocca, Piazza della Scienza 3, 20126 Milano, Italy

<sup>2</sup>INFN, Sezione di Milano-Bicocca, Piazza della Scienza 3, 20126 Milano, Italy

<sup>3</sup>Centre for Astrophysics Research, University of Hertfordshire, College Lane, Hatfield AL10 9AB, United Kingdom

## 4.1 Introduction

Nuclear stellar discs (NSDs) were first discovered in images taken with the Hubble Space Telescope (HST, e.g. Jaffe *et al.*, 1994; van den Bosch *et al.*, 1994), which allows for the detection of such structures that are often of only tens to hundreds of parsecs across and which reside mainly in the centre of early-type galaxies (Pizzella *et al.*, 2002). Previous studies have focused on the properties of few of such discs (e.g. Morelli *et al.*, 2004, Pizzella *et al.*, 2002, Scorza and van den Bosch, 1998) but now thanks to the census in Chapter 2 (Ledo *et al.*, 2010) we have a sufficiently large sample to study these features more systematically.

NSDs are not only interesting tools for determining the masses of supermassive black holes (SMBH, van den Bosch and de Zeeuw, 1996), but can also be a powerful tool to trace galaxy merging history. In Chapter 2 we have shown evidence pointing to the destruction of these discs during a merger event, even though if there is gas involved during such an event, part of this gas can fall to the centre and form a new stellar disc. Therefore, when present, NSDs provide us with a look-back time to the last merger experienced by their host galaxies, a precise one if they were born at that moment, or at least a lower limit if they formed afterward. This look-back time can be used to test and improve galaxy formation scenarios and the predictions of semi-analytical models (e.g. Khochfar and Silk, 2006a; De Lucia *et al.*, 2006). In fact, NSDs are particularly apt for this role since their stellar age can be determined very precisely. Typical degeneracies between the stellar age and metallicity that

affect population studies can indeed be reduced using integral-field spectroscopic data and by knowing in advance (thanks to a photometric disc-bulge decomposition Scorza and Bender, 1995) the disc-light contribution (Sarzi et al., in preparation). What is still unknown to us is understanding more precisely to which extent these discs are fragile and what kind of merging events they actually trace. Do they trace only major mergers (as shown in the preliminary simulations published in Chapter 2), or do smaller satellite galaxies also have the ability to destroy them? If so, how small and in which circumstances?

The impact of mergers has previously been explored in the case of kinematically decoupled cores (KDC, see Bois *et al.*, 2011) or metallicity gradients (Kobayashi, 2004), but so far little is known about the survival of NSDs. In fact, in this study we are not only interested in whether a NSD survives a given merger event, for instance by following in simulations only those particles that originally formed the NSD, but instead, we would like to establish if the presence of an NSD would still be detectable in the merger remnant, by measuring the typical photometric and kinematic signatures of such structures.

In this work, we present a new approach to the study of the effects of mergers in the characteristics and structures present in the original galaxy. To do so, we will, in this publication, discuss the merging process and describe the set of simulations used to address this problem (Section 2), describe the analysis strategy (Section 3), present the obtained results (Section 4) and analyse them in the context of galaxy evolution and our aims of tracing galaxy mergers (Section 5).

## 4.2 Simulation thought and design

We are interested in understanding how a merger affects the innermost parts of a galaxy and, in particular, of a small embedded disc. This is likely to depend on the nature of the encounter, for instance on it being either a major or minor merger, on the geometry of the collision, such as prograde as opposed to retrograde, and finally on the mass of the central disc, given that more massive discs should be more stable. In this chapter we deal only with the magnitude and geometry of the perturbing event, and focus on nuclear stellar discs, which typically extend over a few 100 pc and have stellar masses comparable to that of their host galaxy supermassive black hole (Scorza and van den Bosch, 1998).

To study the fragility of NSDs we thus conducted a series of simulations meant to mimic the final stages of a merging event, when the central supermassive black hole of the perturbing galaxy and its surrounding stellar cusp reach the central

regions of the galaxy hosting the nuclear disc and a primary supermassive black hole. Dynamical friction will indeed cause such a secondary black hole to sink towards the central regions of the primary galaxy or what would eventually become the merger remnant. Most of the stellar cusp around the secondary is likely to be stripped during the early stages of the galaxy pairing, even though the total stellar mass that would remain bound to the secondary could depend on a plethora of factors, such as the initial mass concentration of the secondary galaxy or the mass ratio between the merging galaxies, the orbital parameters of the mergers, and so on (Callegari *et al.*, 2009; Van Wassenhove *et al.*, 2014).

### 4.2.1 Simulation set-up

Initial conditions were set for a nuclear disc embedded in a bulge with its own central supermassive black hole. In order to ensure that the results of our simulations are not affected by out-of-equilibrium initial conditions, we ran our initial conditions “in isolation”, i.e. without including any perturber (no secondary BH). This test run was let to evolve for up to 40 Myr, and we compared the stellar distributions (surface density maps and profiles, and vertical profile at different radii) at different times. The profiles clearly show that the system remains in equilibrium, but for a small readjustment in the central profile on scales of the order of our spatial resolution (few parsec).

Regarding the disc, any self-gravitating flat stellar distribution supported by its rotation could, in principle, evolve into a different equilibrium configuration. The analysis of the profiles at different times for the test performed in isolation demonstrated that the disc is stable against global axisymmetric perturbations (it is initially in dynamical equilibrium).

Nevertheless, the system could undergo non-axisymmetric local and global instabilities, such as: 1) local fragmentation, 2) global spiral instabilities, and 3) global bar instability. We checked that such instabilities do not occur in our initial conditions, by comparing the surface density maps of the isolated system at different times.

We stress that the system stability against non-axisymmetric perturbations was expected, as the stabilising effect of the spherical stellar bulge (that in our simulations is significantly more massive than the disc, increasing the rotational velocity and, as a consequence, the Toomre parameter) increase the “dynamical temperature” of the system, providing a velocity support against the gravitational growth of substructures.

### 4.2.2 Colliding bulge

An additional massive particle is introduced in the simulations at an initial distance of 80 pc from the centre, on a circular orbit. This particle mimics the presence of a perturbing SMBH (the secondary, hereafter), either naked or embedded in its central stellar cusp (see the discussion below), reaching the centre of the primary galaxy during the last stages of a galaxy merger. The secondary interacts with the star particles of the primary nucleus, inevitably sinking toward the centre while perturbing the local and global distribution of the stars. After the secondary had reached the centre, the simulations were let to evolve for several dynamical times as to allow the system to relax to a point where we would not expect further perturbations to the dynamics of the stars. We designed and ran a set of simulations wide enough to probe a variety of merging scenarios with different mass ratios and orbital inclinations (see Table 1). The spatial resolution of our simulations is determined by the gravitational softening of the particles, that is equal to 0.5 pc for all the particles except for the secondary in a few runs, where we assume that the secondary does not enter the remnant nucleus completely naked, so that the particle mimics the SMBH embedded in its central cusp.

In the runs where the secondary is considered naked, we vary the mass ratio between the primary and secondary SMBH from 1:1 to 1:10 to explore the cosmologically relevant parameter space. This argument assumes a constant mass ratio between the SMBHs and the host galaxies (Håring and Rix, 2004), so that a 1:1 ratio in SMBH masses simulates a 1:1 galaxy merger. Even if this is the case at the beginning of a merger, the SMBHs can accrete a significant amount of gas, changing their initial mass ratio. Since the smaller secondary galaxy is more perturbed by the merger and suffers a higher gas inflow toward its centre, the secondary can accrete more (relatively to its initial mass, Callegari *et al.*, 2011; Van Wassenhove *et al.*, 2012). This results in the formation of more equal mass SMBH pairs when they reach the nucleus of the merger remnant. For these reasons we consider our 1:10 lower limit to the SMBH mass ratio a conservative choice. There is no consensus on what constitutes a major merger, which we have represented by a 1:1 mass ratio. Different authors set limits as high as 1:2 (e.g. Brook *et al.*, 2012) or as low as 1:4 (e.g. López-Sanjuan *et al.*, 2012; Bundy *et al.*, 2009; Maller *et al.*, 2006). Therefore we chose to simulate a large minor merger, just below this limit, with a mass ratio of 1:5 and a smaller case of 1:10. For even more unequal mergers, works from Callegari *et al.* (2011, 2009) suggest that such encounters do not lead to the formation of a close pair of SMBHs, since the tidal field of the primary quickly strips the secondary of most of its mass, thus decreasing the efficiency of the dynamical friction at the

<b>BH Mass ratio</b>	<b>Collision angle (<math>^{\circ}</math>)</b>	<b>BH softening (pc)</b>
1:1	0	0.5
1:1	30	0.5
1:1	60	0.5
1:1	90	0.5
1:1	120	0.5
1:1	150	0.5
1:1	180	0.5
1:5	0	0.5
1:5	30	0.5
1:5	60	0.5
1:5	90	0.5
1:5	120	0.5
1:5	150	0.5
1:5	180	0.5
1:10	0	0.5
1:10	30	0.5
1:10	60	0.5
1:10	90	0.5
1:10	120	0.5
1:10	150	0.5
1:10	180	0.5

Table 4.1: Set of simulations with mass ratios, collision angles and the gravitational softening of the secondary SMBH. Collision angles  $i_{\text{BH}}$  from 0 to  $60^{\circ}$  are prograde encounters whereas  $i_{\text{BH}}$  values larger than  $90^{\circ}$  denote retrograde ones.

<b>BH mass ratio</b>	<b>Central mass ratio</b>	<b>Collision angle (<math>^{\circ}</math>)</b>	<b>BH softening (pc)</b>
1:5	2:5	0	2
1:5	3:5	0	3.5
1:5	1:1	0	6.25
1:5	2:5	90	2
1:5	3:5	90	3.5
1:5	1:1	90	6.25

Table 4.2: Set of simulations based on the 1:5 mass ratio, but with increased softening mimicking an attached cusp of stars. In practice, that changes the mass ratios of the central components, i.e. primary black hole versus composite secondary and stellar core structure. Also shown are the collision angles  $i_{\text{BH}}$  and the gravitational softenings of the secondary SMBH.

early stages of the merger and leaving the secondary wandering at Kpc separations.

To model the case in which the secondary is still embedded in a significant stellar core we re-an a sub-set of encounters for the 1:5 merger case (see Table 2) changing the mass of the perturbing particle and its gravitational softening. In practice we adopted the mass for the bound stellar core to be 1, 2 and 4 times that of the secondary black hole, so that the mass of the particle mimicking the perturbing SMBH-core structure is 2, 3 and 5 times that of the secondary black hole at the standard softening of 0.5 pc. Furthermore, we adopted as softening for such composite SMBH-core perturbers the radius that would enclose the stellar mass attached to the secondary black hole while assuming the same radial scaling as set up for the stellar mass around the primary black hole. We notice that our simple implementation fails in reproducing the possible stripping of stars from the secondary core during its interaction with the primary system, keeping the perturbing mass artificially high. As a consequence, we regard these runs as upper limits to the perturbation of the nuclear disc.

### 4.2.3 Technical aspects

The simulations were conducted using GADGET-2 (Springel, 2005), a parallel code designed for cosmological N-body/smoothed particle hydrodynamics simulations. Each simulation involved 600K stellar particles and two additional collisionless particles to model two SMBHs. 300K particles have been used to model the nuclear stellar disc of total mass  $M_{\text{disc}} = 10^8 M_{\odot}$  and an initial outer radius of 100 pc. The disc surface density,  $\Sigma$ , follows a Mestel (Mestel, 1963) profile

$$\Sigma \propto 1/R, \quad (4.1)$$

and has an aspect ratio  $H/R \approx 0.05$ , similarly to previously used nuclear discs (e.g. Dotti *et al.*, 2007, 2006; Escala *et al.*, 2005) and to the nuclear discs outcome of cosmological simulations (e.g. Levine, 2008). The latter were produced using a different type of code, adaptive mesh refinement, that allows for a local increase in resolution in regions where specific criteria are fulfilled. These simulations included prescriptions for radiative cooling and star formation, and started within a large scale cosmological box of  $6h^{-1}$  Mpc at redshift 50. A fraction of this box was resampled and re-ran at a higher resolution, achieving as high as  $\approx 0.1$  pc, with 20 levels of refinement and a dynamical range of  $1.10^7$ . The resulting (gas-dominated) disc is locally stable against self-gravity, as is ours, but since it is embedded in a less massive stellar structure, it is unstable to global perturbations and forms weak

spiral features. It also shows a clear cusp in its density distribution, as does ours.

The modelled disc is different from the ones used in Chapter 2 and 3. Nevertheless, in order to assess the stability of a real nuclear disc, the most important parameter to keep under control is the mass fraction. Our initial disc extends to 100 pc, which is the median radius of the nuclear discs that we have measured in Chapter 2 (see green squares in Fig. 2.7) and comes with a  $1/7^{\text{th}}$  of the mass of the bulge. This is certainly larger than the case of very small nuclear discs such as NGC 4458 or those first explored by Scorza and van den Bosch (1998, with D/B 1%), but is more appropriate for larger and more typical nuclear discs (see Fig. 2.7 in Chapter 2), considering also that our simulation does not cover the entire extent of the bulge, as we focus closer to the central regions of galaxies with nuclear discs. As regards the singularity inherent to the Mestel profile, this is avoided since the position of the disc particles is randomly generated when the initial conditions are first set. Furthermore, our initial conditions are taken only after the initial black-hole / disc / bulge system has been left to evolve for a few dynamical timescales, which tends to smooth the most extreme cusps.

In addition to the disc, further 300k particles have been used to model the central regions of the spherical stellar bulge hosting the disc. The bulge follows a Plummer profile

$$\rho = \frac{3}{4\pi} \frac{M_{\text{bulge}}}{b^3} \left(1 + \frac{r^2}{b^2}\right)^{-5/2}, \quad (4.2)$$

where  $b$  (50 pc) is the core radius,  $r$  the radial coordinate and  $M_{\text{bulge}} (= 6.98M_{\text{disc}})$  the total mass of the spheroid. Finally, the bulge and disc stellar structure hosts a  $10^8 M_{\odot}$  SMBH. While the SMBH is initially at rest at the centre of the structure, the velocities of the star particles modelling the disc and the bulge are chosen to set the system in dynamical equilibrium. Since an analytic formulation of the distribution function of the composite structure is not available, we let the system to stabilise into dynamical equilibrium in isolation. We further verified that over the typical timescale of our simulated encounters (a few ten Myr, see Figure 4.1) the stability of such initial condition was maintained.

The number of used particles is high enough to prevent any spurious 2-body relaxation. As discussed above, the simulation in isolation does not show any trace of relaxation (the disc and bulge profiles are constant in time) within few tens of Myr. We cannot exclude that the system would undergo any spurious instability on longer timescales, but this does not affect our results. In reality the stronger constraint comes from the requirement that the dynamical friction onto the secondary is well resolved. This translates into having a small  $m_*/M_{BH}$  ratio, which for these simula-

tions corresponds to  $\approx 10^{-5} - 10^{-6}$  (depending on the secondary mass), enough to ensure that dynamical friction will take place. A larger number of particles would have increased the ability to follow the final stages of the BH pairing (when the effect on stellar distribution is smaller and limited to the very central region), but the computational cost would have prevented us from running such a large suite of simulations.

The initial conditions for these simulations are idealised. They should not be considered as the analysis of the time evolution of a specific galaxy, but as proof of concepts, since they allow us to isolate the effect of a perturber on an otherwise stable system. The use of a significant spherical bulge comes from the requirement of having the system stable against non-axisymmetric perturbations (e.g. bars and spirals), which would exert a torque on the stellar system re-shuffling the stellar distribution even in the absence of an external perturbation. Under this point of view, a large, spherical and dispersion-supported bulge is thought to be the natural outcome of a previous major merger, i.e. our initial conditions are probably not representative of a disc galaxy in a deeply underdense field that evolved for most of its life in isolation. However, running a simulation without a bulge would not result in a clear test case, since, as already commented, the stellar distribution would not remain stable in time, allowing for an analysis of the effect of the secondary SMBH only.

Individual simulations run time will vary slightly, depending on how fast the secondary BH sinks toward the centre and forms a binary with the primary (see Figure 4.1). After this happens we let the simulations continue for a few ( $\approx 5$ ) dynamical times to let the system relax. Only then we analyse the results as follows.

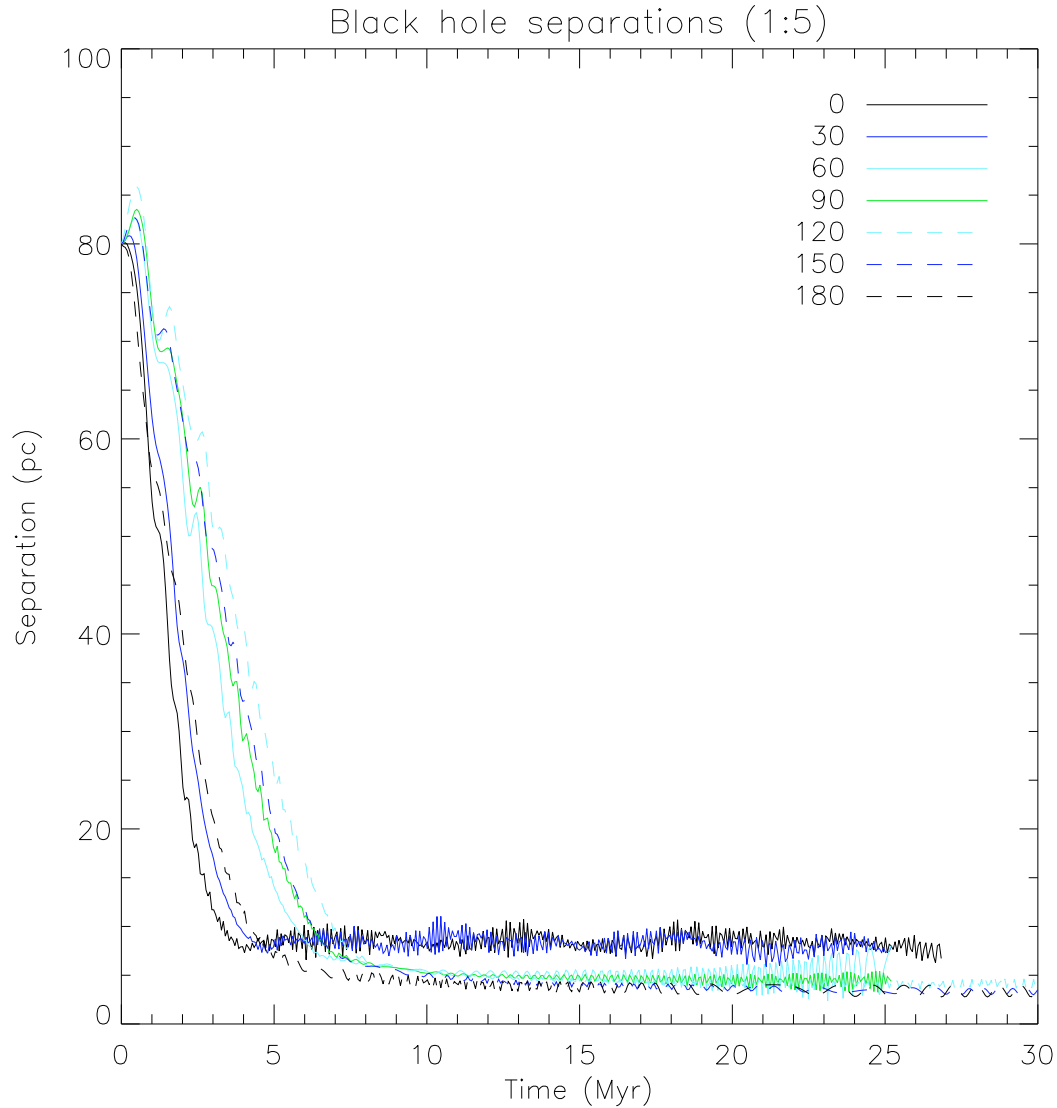


Fig. 4.1: Time evolution for the separation between the primary and secondary black holes for the 1:5 mass ratio encounters. Solid lines denote prograde encounters, whereas dashed lines represent retrograde ones. The case of 1:1 (1:10) mergers would follow similar decays although at shorter (longer) time scales. The asymptotic behaviour present in the plots is due to dynamical friction not being efficient at radii at which the mass enclosed within the binary is less than the secondary mass, which roughly corresponds to the so called hardening radius (e.g Begelman *et al.*, 1980).

## 4.3 Simulation analysis

The simulations follow in time steps the positions and velocities of the black holes and disc and bulge stars. To understand what happens to the discs and to our ability to detect them, in particular when embedded in a bulge, we will need a way to quantify the disc disruption and to evaluate if the results of these encounters still show the signatures of a disc.

### 4.3.1 Stellar surface brightness and velocity maps

The simulation outputs were first binned in regular grids to create the equivalent to a surface brightness and velocity maps. This is a requirement of the code we used to detect the presence of discs, as it is of others such as IRAF task *ellipse* (Jedrzejewski, 1987). Such grids also allow us to visually follow the merging event and have an equivalent to an image as it would be the case in real observations. For simplicity, the grids were made only for the central regions where the disc was initially present, measuring 400 x 400 pc, using a grid spacing of 5 pc. Because, as we will discuss later, the viewing angle ( $i$ ) affects our ability to detect the disc remnants, we generated maps for  $\cos(i) = 0.0, 0.1, 0.2, 0.3, 0.4$  and  $0.5$ , spanning from an edge-on view to  $60^\circ$ . There is little or no point to analyse projections with values of  $\cos(i)$  larger than  $0.6$  since Rix and White (1990) have shown that at this point it becomes very hard to photometrically detect the presence of discs.

Figure 4.2 shows the disc, bulge and total surface density maps with corresponding velocity maps, for their initial conditions.

### 4.3.2 Kinemetry

A visual inspection of the maps for the surface brightness and velocity fields of the merging results allows us to already appreciate the effects of the different merger simulations, but to better analyse and quantify the results and disc disruption we have used KINEMETRY (Krajinović *et al.*, 2006) to analyse the moments of the line-of-sight velocity distribution (LOSVD). The gridding described in the previous section was done not only to aid visualisation and qualitative assessment but also as a necessity for the photometric side of KINEMETRY.

The KINEMETRY algorithm works under the assumption that the even moments of the LOSVD, such as the surface brightness, are described by a constant profile along ellipses, and that the odd moments, such as mean velocity, can be described by a cosine law along such contours. In particular, we will be looking for peaks

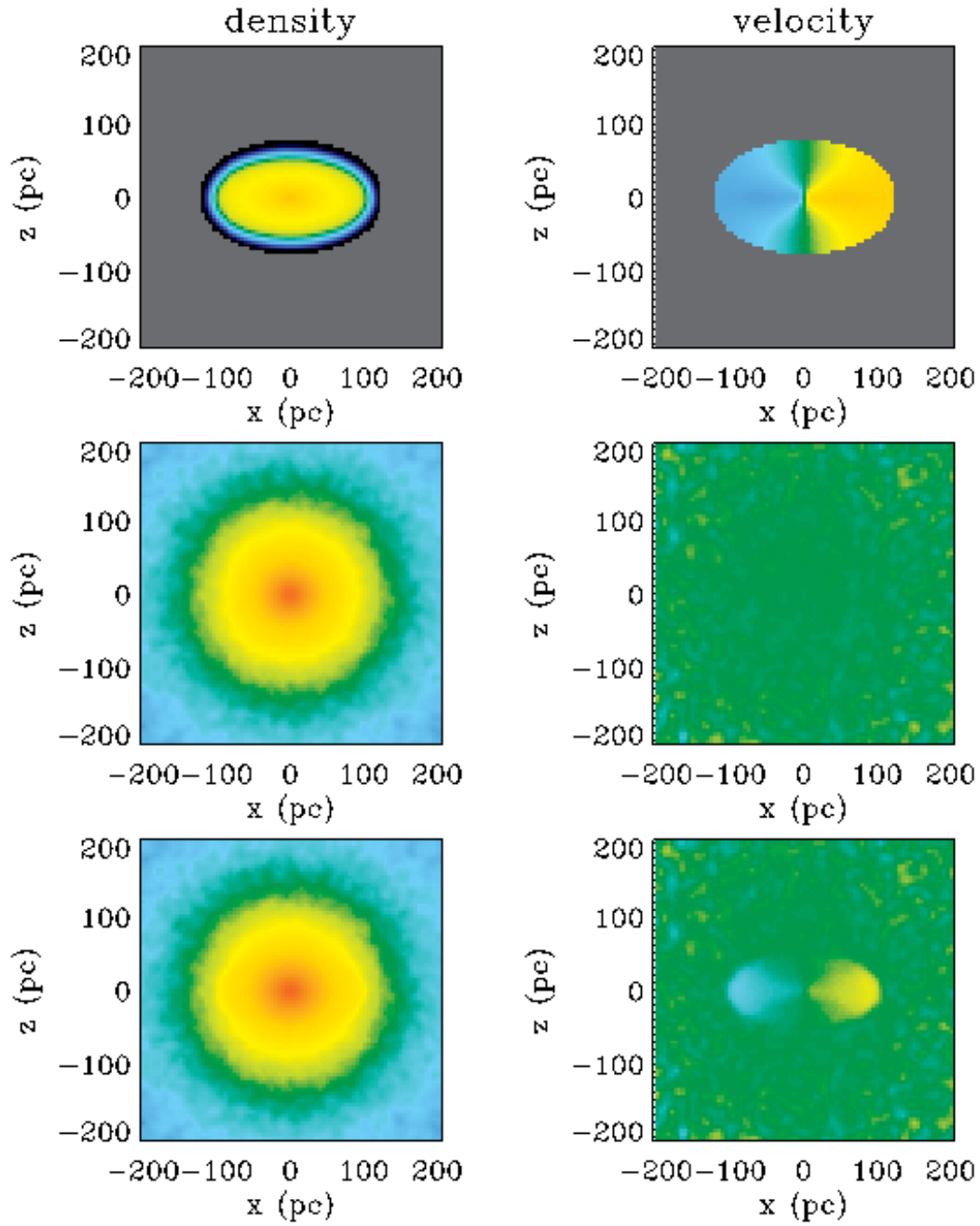


Fig. 4.2: Surface density (left panels) and velocity fields (right panels) for the initial conditions of our simulations, showing, from top to bottom the disc particles, the bulge particles and the entire system. This figure zooms in a 400 x 400 pc region around the centre that encompasses the entire disc, which is being viewed at a  $60^\circ$  inclination. Receding and approaching particles are shown in yellow and blue colours, respectively.

in the coefficient of the fourth cosine term on the Fourier series expansion of the deviations from the elliptical isophotes ( $a_4$ ) in the photometry, and for very small values of the  $k5/k1$  ratio (analogous to the  $a_4$ ) in the velocity fields. Large  $a_4$  values will indicate disk isophotes, whereas small  $k5/k1$  values will ensure the presence of a regular, disk-like rotation. As done in other photometric tools such as the IRAF task ellipse (Jedrzejewski, 1987), KINEMETRY begins by identifying the best-fitting ellipses to the isophotes to retrieve the radial profiles for the average surface brightness, position angle (PA), flattening ( $q$ ) and higher moments such as the  $a_4$ . Similarly, from the odd moments, we obtain a velocity curve, a kinematic PA and flattening, and the  $k5/k1$  values (see Krajnović *et al.*, 2006, for more details).

In Figure 4.3 we show the main outputs from KINEMETRY for the same initial conditions shown in Figure 4.2. As expected, we can see  $a_4$  and velocity peaks in both the disc and total surface brightness (blue and black lines respectively) whereas the bulge (red line) stays flat. On the other hand, the  $k5/k1$  values for the disc and total velocity field present very low values, tracing disk-like rotation, whereas the bulge displays a noisy  $k5/k1$  profile. These are the quantities that will allow us to tell photometrically and spectroscopically, once compared to appropriate detection thresholds (§4.3.3) if a disc is present or not when looking at the final stages of the interaction.

Figures 4.4 to 4.6 show examples of the surface brightness and velocity maps with corresponding KINEMETRY outputs for the final stages of the 1:1, 1:5 and 1:10 mass ratios after a  $i_{\text{BH}} = 30^\circ$  encounter and seen at a  $60^\circ$  inclination, similar to what was shown for the initial conditions. The bulge results have been omitted for simplicity as they are not key to our goals. Similarly, we do not follow the behaviour of the disc alone (blue lines) since, although interesting, what observations trace is the surface brightness and average velocity of all the stars. For the purpose of detecting the signature of a disc, we will therefore look at and analyse the surface density and kinematics of all the particles in our simulations (black lines), in particular, the region where the disc was originally present, which corresponds to the solid line in the plots and is delimited by the vertical dashed line, placed at the 100 pc radius. Similar plots for all the simulations can be found in the Appendix.

### 4.3.3 Disc kinematic signature

In order to assess at the end of which kind of merger events we could still find the photometric or kinematic signatures of a disc, we considered the results of the KINEMETRY analysis inside the central 100 pc region originally occupied by the

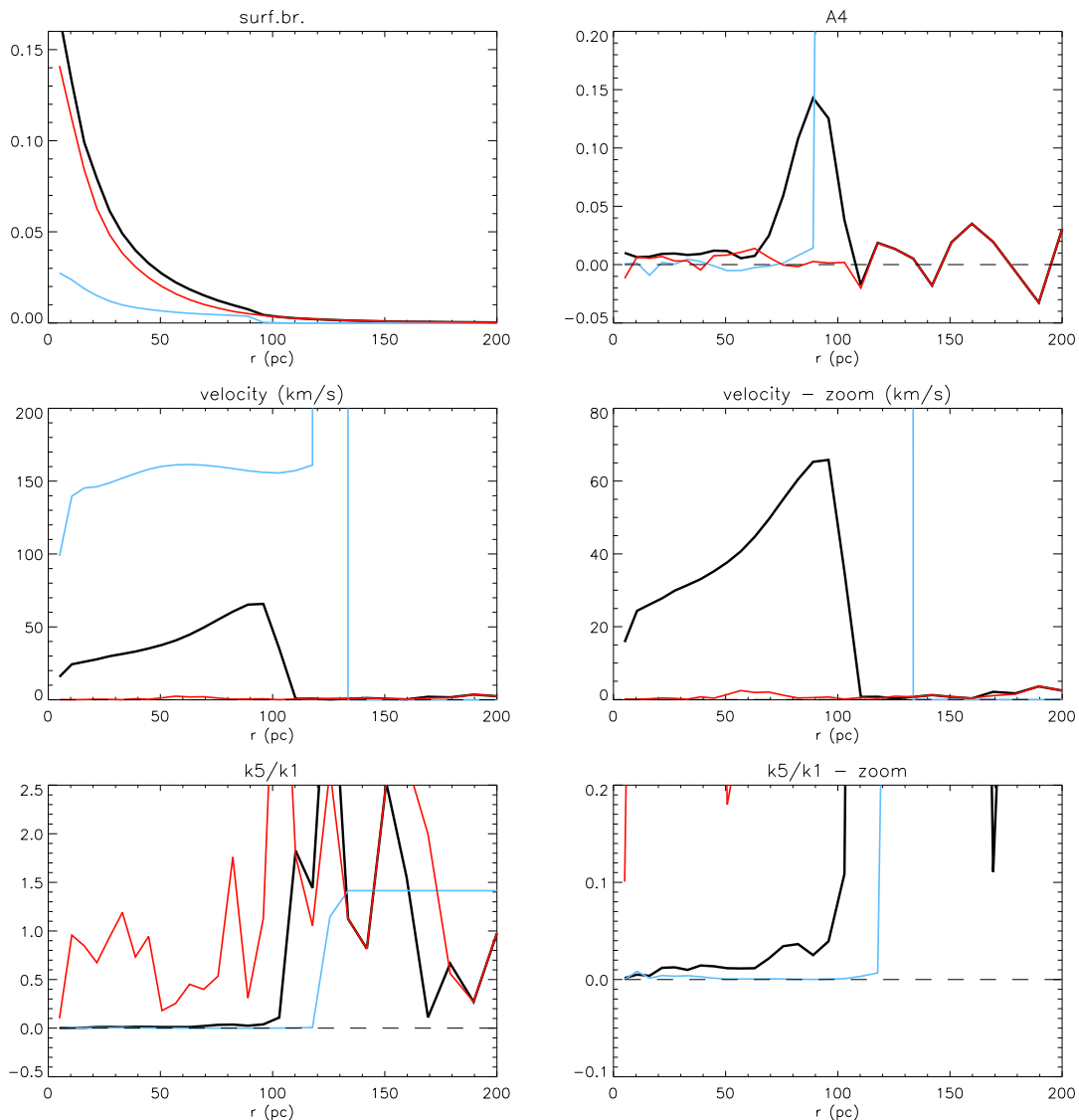


Fig. 4.3: Kinemetry results for the initial conditions shown in the previous figure. The blue, red and black lines show radial trends for the surface brightness,  $a_4$ , velocity and  $k_5/k_1$  of the disc, bulge and all particles, respectively and as indicated at the top of each panel. Looking at the red bulge line across the panels, we can see that it does not present an intrinsic diskiness nor boxiness, as shown by an  $a_4$  close to zero, does not present a bulk rotation, and the high values of  $k_5/k_1$  show that it is not disc-like. The nuclear disc, on the other hand, presents a sharp rise in the  $a_4$  at its edge, as expected, high rotation, and low values of  $k_5/k_1$ , all indicative of a disc. When looking at the total, we observe the typical signature of the presence of an embedded disc, shown both by the peak of the  $a_4$  parameter and the low values of  $k_5/k_1$ .

disc, although for edge-on projections this radius was decreased in order for the KINEMETRY procedure to converge. In Figures 4.4 to 4.6 such a limit is indicated by a vertical dashed line, and the KINEMETRY descriptions inside this radius are plotted as solid lines.

To identify the presence of a disc, we will use the mean values for the KINEMETRY parameters in such central regions, in particular to isolate fluctuations caused only by a fraction of the disc particles which had acquired extreme behaviours, such as those ejected at large radii. More specifically, in the next section we will compare the average values for the  $a_4$  parameter, the rotation velocity  $V$  and for the  $k5/k1$  ratio, with corresponding threshold values that indicate the presence of a disc. For the  $a_4$  parameter we considered a generous minimum average value of 0.02 for detecting disk isophotes in our simulations, which is comparable to what is observed in real NSD-hosting galaxies (see e.g. Morelli *et al.*, 2004; Pizzella *et al.*, 2002) but somehow below what is observed in the most face-on projections for our initial conditions ( $\sim 0.03$ – $0.04$ , for  $\cos(i) = 0.5$ ). As regards kinematics, we require an average velocity above  $10\text{kms}^{-1}$  to detect global rotation, in line with typical errors on this quantity, and average  $k5/k1$  values below 0.04 to recognise the presence of disc-like motions. The latter threshold, which lies just above the typical average value found in our initial conditions, is taken from Krajnović *et al.* (2011) who based their judgement on integral-field data for 260 early-type galaxies.

Figures 4.7 to 4.9 present the central average values for the  $a_4$ ,  $V$  and  $k5/k1$  parameters measured in the surface-density and velocity maps for the final step of each of the simulations involving a naked secondary supermassive black holes, and as observed from different viewing angles from edge-on down to a 60 degree inclination. The different panels in these figures group together simulations with similar impact angle  $i_{\text{BH}}$ , whereas the size of the circles showing the average  $a_4$ ,  $V$  and  $k5/k1$  values correspond to the mass-ratios of the merger events (i.e. 1:1 mergers are shown with the largest symbols). Finally, the asterisks in Figs. 4.7–4.9 also show the average values of these parameters from our initial conditions. These are the figures that will be discussed in the next section.

## 4.4 Assessment of disc survival

Photometrically, the search for the presence of nuclear discs generally starts with the visual inspection of unsharped images or structure maps, which highlight small scale features (e.g. Pizzella *et al.*, 2002, Chapter 2) This is then followed by a more quantitative analysis of the shape of the stellar isophotes, looking in particular for pos-

itive peaks in the  $a_4$  parameter. With integral-field spectroscopic data it will further be possible to look for rotating structures that may not show up photometrically, which are likely to be discs when finding very low values for the  $k5/k1$  kinematic parameter.

Having defined earlier the thresholds for the detection of a disc in our simulations, based on average values for the  $a_4$ ,  $V$  and  $k5/k1$  parameters, and after checking that all our simulations reached a post-interaction relaxed state, we now proceed to assess in which kind of simulation and down to which inclination we can still find clear photometric and/or kinematic signatures of a disc.

#### 4.4.1 Photometric assessment

Starting from the plots for the  $a_4$  parameter (Fig 4.7), we observe the expected trend whereby the photometric signature of a disc gets more easily erased during the interactions involving a more massive secondary black hole. Indeed, 1:1 mergers leave little or no trace of a nuclear disc in 86% of the cases whereas the final steps of the 1:5 and 1:10 mergers display average  $a_4$  values suggestive of a disc structure in 62% and 86% of the cases. Prograde encounters would appear to be generally more destructive, as can be noticed by comparing the trends for the 1:5 and 1:10 remnants for  $i_{\text{BH}} = 30$  and 60 degrees with their counterparts at  $i_{\text{BH}}$  values of 120 and 150 degrees, or by observing that most of the 1:1 merger remnants showing disk-like isophotes are found in the case of a perfectly retrograde encounter ( $i_{\text{BH}} = 180$ ). In fact, the edge-on projection of the 1:1 prograde merger ( $i_{\text{BH}} = 0$ ) owes its large  $a_4$  values only to a distinct ring-like structure in the remnant, which would not be mistaken for a disc upon a simple visual inspection.

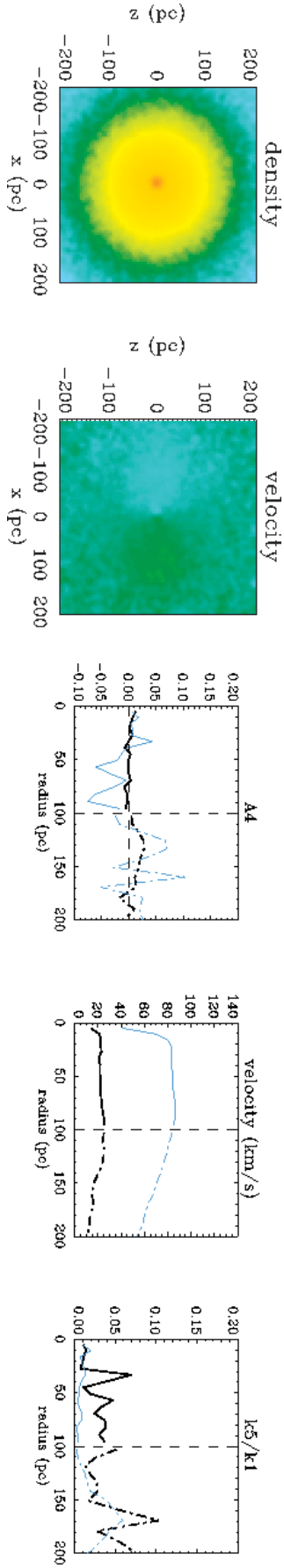


Fig. 4.4: Final outcome of encounter featuring a 1 to 1 mass ratio,  $i_{\text{BH}} = 30^\circ$ ,  $i = 60^\circ$ . The two maps on the left show the final density and velocity field of all particles, whereas the three plots on the right show the radial trends for the  $a_4$ , velocity and  $k_5/k_1$  parameter as measured with kinemetry. In these panels, the black lines show these measurements for the entire system whereas blue lines are for the disc particles only. Vertical dashed lines indicate the original extent of the disc. We compute average values for those kinemetry parameters inside that radius, and ignore the outer values that we indicate with dot-dashed lines.

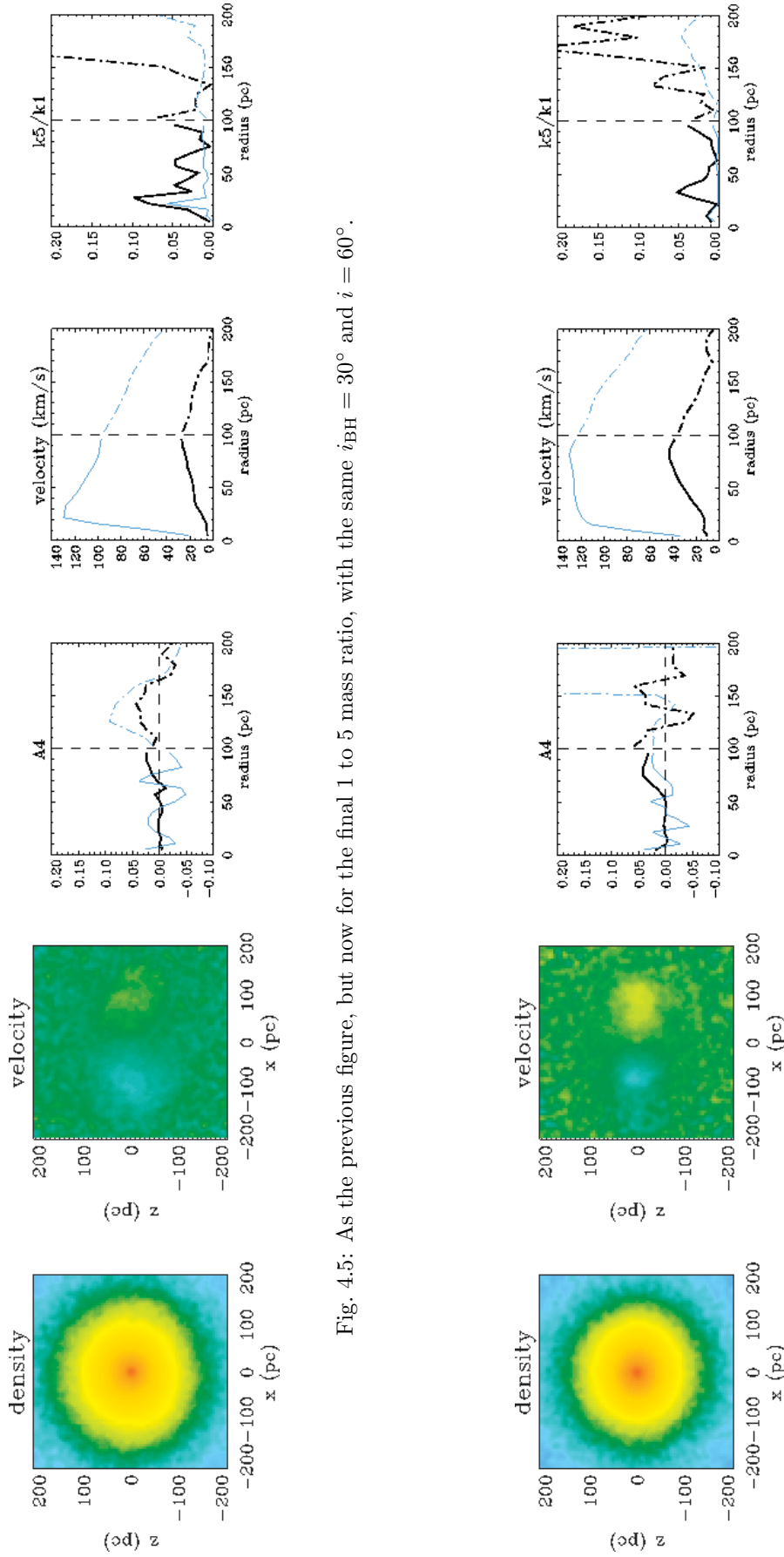


Fig. 4.5: As the previous figure, but now for the final 1 to 5 mass ratio, with the same  $i_{\text{BH}} = 30^\circ$  and  $i = 60^\circ$ .

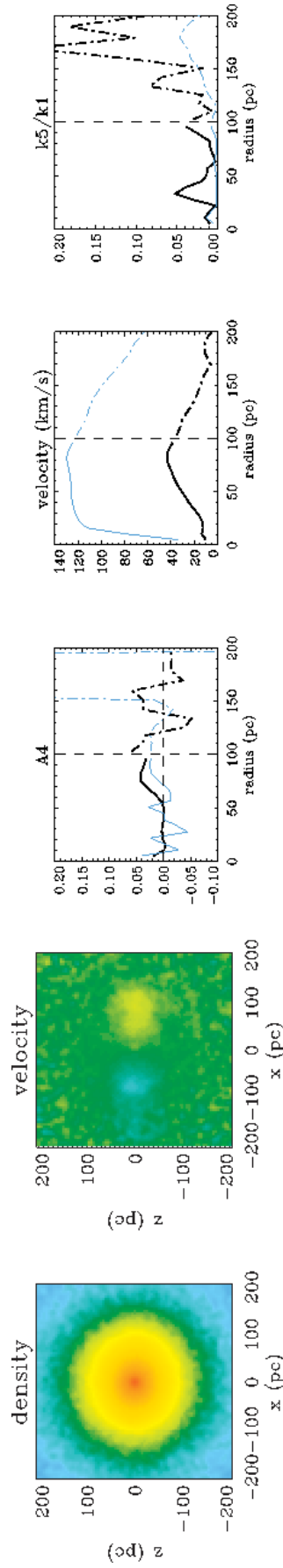


Fig. 4.6: As the previous figures but, now for the final 1 to 10 mass ratio, with  $i_{\text{BH}} = 30^\circ$  and  $i = 60^\circ$

The difference between prograde and retrograde can be understood considering that stars are more easily deflected by the secondary black hole when this travels alongside rather than against them, which is also why dynamical friction on the secondary is more efficient in the prograde cases making it sink faster towards the centre. This can be appreciated in Fig. 4.1 which shows the evolution of the black holes separation as a function of time, where the prograde tracks for  $i_{\text{BH}} = 0, 30$  and  $60$  indicate always a faster sinking than their retrograde counterparts for  $i_{\text{BH}} = 180, 150$  and  $120$ . Meiron and Laor (2013) provide another example of this behaviour in the somehow different context of a binary black-hole interaction within a non-rotating bulge, which ends up showing a central rotating structure as the coalescing black holes evacuated preferentially the stars that co-rotate with them. The larger impact of a prograde encounter on discs was also already shown by Velazquez and White (1999) in the case of Milky Way-like galactic discs and satellites. Although the initial conditions for these simulations were idealised and do not pretend to simulate any particular galaxy, we can, nonetheless, establish a connection to the galaxies studied in Chapter 2. The disruption of the NSDs, caused mainly in 1:1 mergers leaves an  $a_4$  profile similar to what can be seen on the top panel of Fig. 2.3, a flat  $a_4$ , not necessarily around zero as in the simulations, since bulges can have an intrinsic boxiness or diskiness. Simulations where the disc survived were mostly in the 1:5 and 1:10 mass ratios. Other differences when comparing to real galaxies are that we do not know if those have suffered further mergers after the creation of their nuclear discs and we do not know how long ago it was created, with the exception of NGC 4458, as discussed in Chapter 3. Simulations can show higher peak values for  $a_4$ , as high as 0.15 in several situations (e.g. Fig. 4.15, 4.22, 4.23 and 4.29), whereas the strongest signature of a real disc is a single case at  $\sim 0.13$  (Fig. 2.21). Apart from these extremes, the remaining signatures are comparable, with most peak values below 0.10 and as low as 0.03 (Fig. 4.21), in agreement with the observations in Chapter 2.

#### 4.4.2 Spectroscopic assessment

Moving on to the trends for the peak velocity  $V$  traced by our kinematic fit (Fig. 4.8), we observe that - except for the planar and polar 1:1 encounter and the planar prograde 1:5 merger - some level of bulk stellar rotation would always remain detectable in the remnant, even in cases where no photometric signature of disc was identified in the  $a_4$  profiles. This suggests, as one would expect, that while perturbing the radial and vertical structure of a thin disc is relatively easy, entirely

Mass ratio	$f_{phot}$		$f_{kin}$	
	raw	$\sin(i_{BH})$	raw	$\sin(i_{BH})$
1:1	14.3	10.0	35.7	43.3
1:5	61.9	72.8	81.0	92.3
1:10	85.7	85.0	100.0	100.0

Table 4.3: Fractions of merger remnants where the disc can still be detected, for the three mass ratios and according to whether the disc is detected photometrically or kinematically. The “raw” columns list uncorrected fractions, whereas the “ $\sin(i_{BH})$ ” columns list fraction that are corrected by this factor to take into account that co-planar encounters are much less likely to happen than those with higher  $i_{BH}$  inclinations.

erasing the signature of the rotation of its stars is much more difficult, and requires a rather dramatic scattering of the disc stars at larger radii. This is for instance the case of the aforementioned ring-like structure in the 1:1 planar prograde merger, which is all that is left of the disc and does not contain a sufficient number of particles to imprint a signature of bulk rotation in the merger remnant, even when seen edge-on.

Not all rotating remnants show regular disc-like kinematics, however. Looking finally at the average values for the  $k5/k1$  parameters (Fig. 4.9) shows in particular that nearly half of the 1:1 remnants do not rotate regularly when they do show bulk rotation. On the other hand, except for a few projections of the prograde encounter, the remnants of 1:5 interactions generally display regular kinematics, with this being always the case of the 1:10 remnants.

Overall, a sufficiently ample and regular rotation is found in 36%, 81% and all of the remnants of the 1:1, 1:15 and 1:10 mergers, respectively.

Based on this limited number of simulations we can attempt to draw a general picture for the chance of nuclear stellar discs surviving a galaxy merger and of being detected, considering in particular that co-planar encounters are, for a purely probabilistic perspective, much less likely to happen than merger events where the secondary black hole initially moved in an highly inclined orbit. We can account for this effect by correcting for a  $\sin(i_{BH})$  factor our raw fractions of remnants with kinematic and photometric disc signatures, which effectively removes the perfectly co-planar cases and accentuates the impact of polar or nearly polar impacts. Since the former simulations tend to be the more disruptive for the disc, this correction tends to produce larger detection rates for disky or regularly rotating structures. These fractions do not vary dramatically, however, in particular since the perfectly polar impact can also be quite damaging for the disc.

The values for both our raw and  $\sin(i_{BH})$ -corrected fractions of merger remnants with photometric disk features or regular velocity fields are reported in Tab. 3.

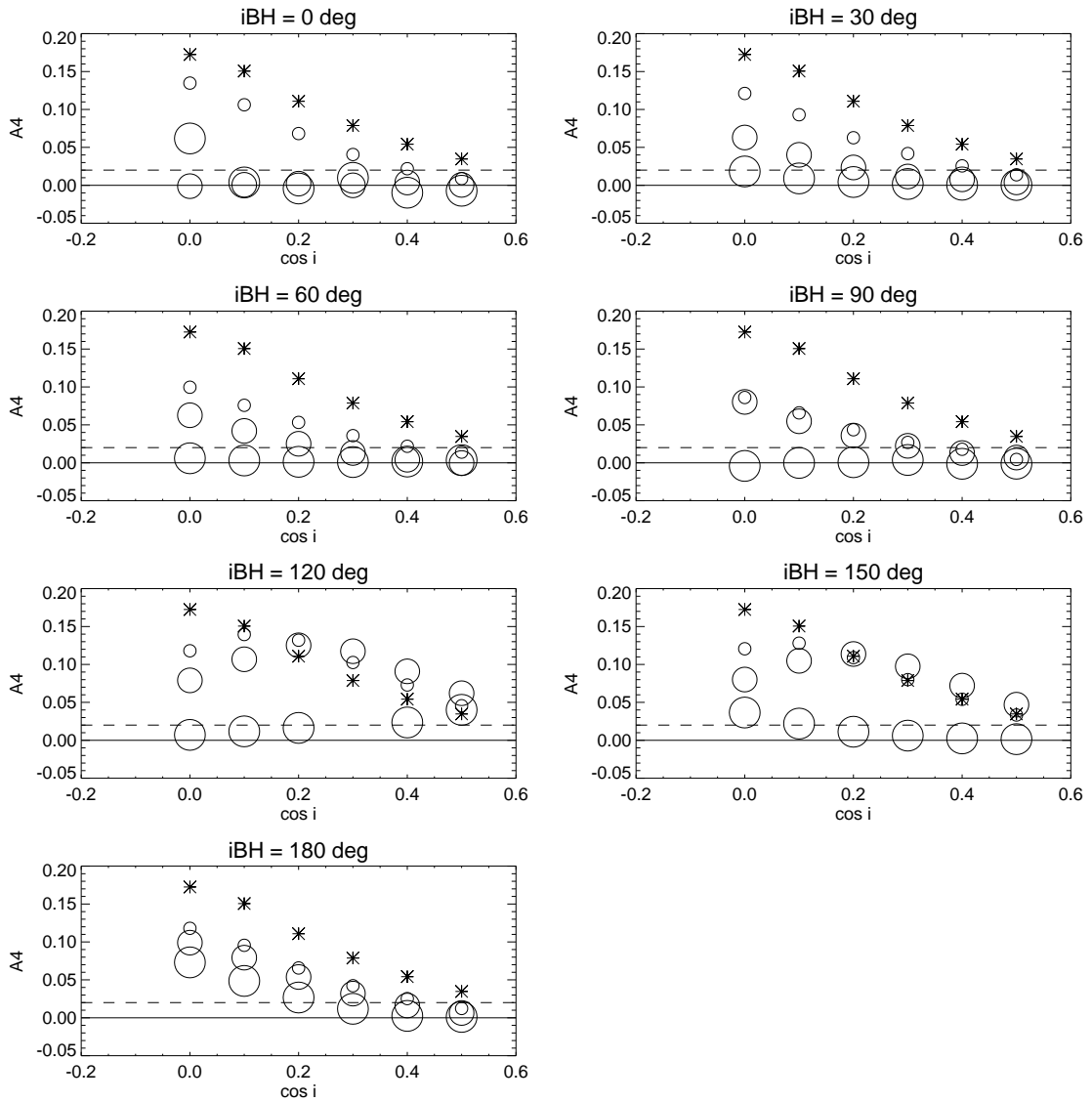


Fig. 4.7: Average values for the  $a_4$  parameter (inside 100 pc) as measured at the final step of each of our simulations and as a function of our viewing angle ( $\cos i$ ). The different panels show the results from simulations of similar values for collision angles  $i_{\text{BH}}$ , with the size of the circles tracing the average  $a_4$  value of simulations with increasing merger mass ratio of our simulations (i.e. from 1:10, 1:5 to 1:1). In each panel the asterisks indicate the average  $a_4$  values measured at the beginning of each simulation, and the dashed horizontal line indicates our threshold for detecting the photometric signature of a disc in the merger remnants.

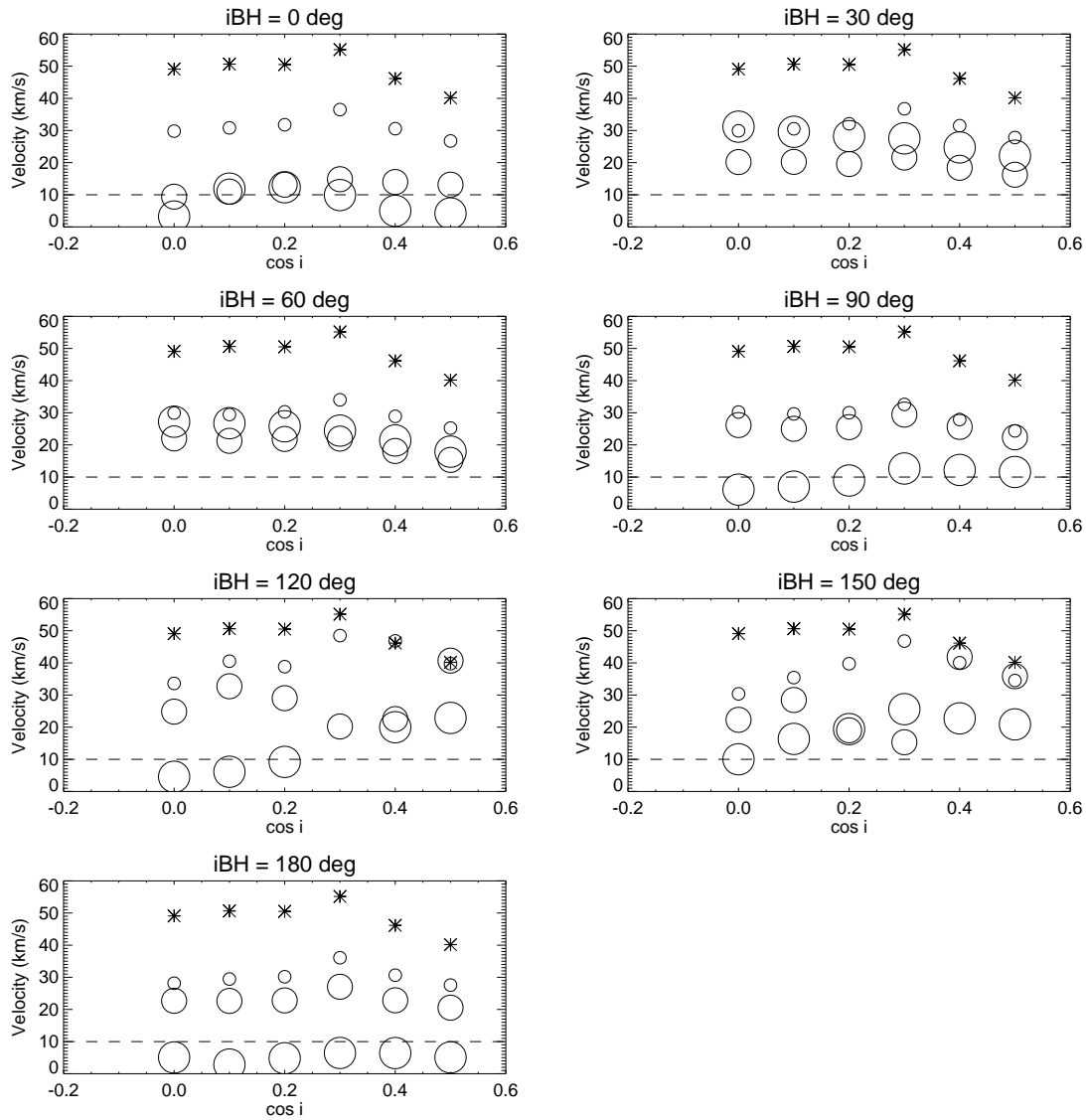


Fig. 4.8: Similar to Fig. 4.7 but now showing the average stellar velocity of our merger remnants and initial conditions, inside a 100 pc radius. The dashed horizontal line in each panel indicates here our threshold for detecting coherent rotation, which is a prerequisite to the kinematic detection of a disc in the merger remnants.

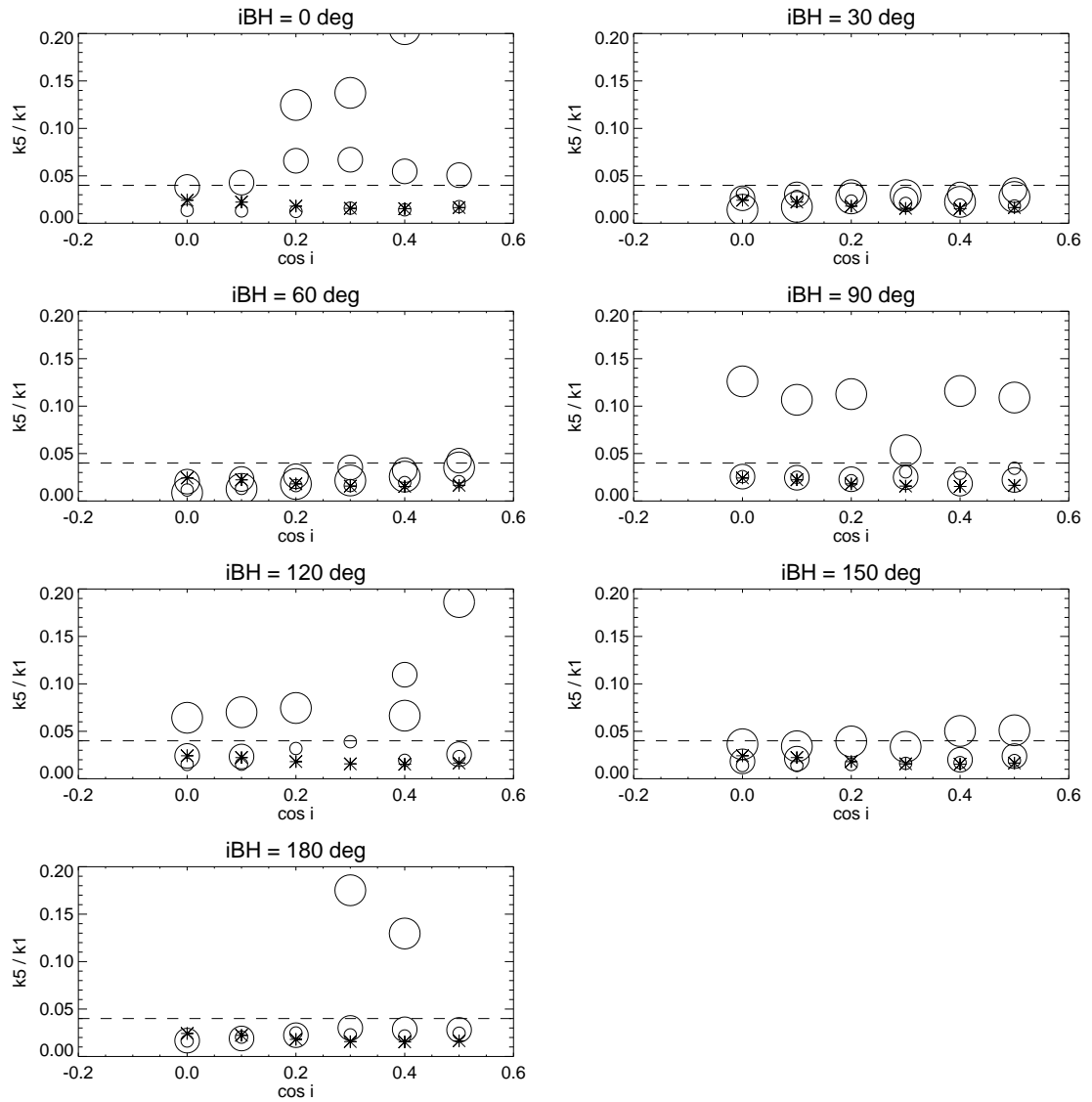


Fig. 4.9: Similar to Figs. 4.7 and 4.8, but now showing the average value for the  $k_5/k_1$  ratio inside the 100 pc radius. The dashed horizontal line in each panel indicates here our threshold for detecting regular, disc like rotation, which represent the kinematic signature of a disc in the merger remnants.

### 4.4.3 Impact of softening

The previous conclusions are still based on the idealised situation whereby during mergers the secondary black hole approaches the nuclear regions hosting the nuclear disc while already stripped of all the stars that were once orbiting it. We designed these simple simulations under the assumption that if we were to attach even more stellar mass to the secondary black hole, its impact on the nuclear stellar disc would be even more dramatic, so that such first experiment could provide a conservative estimate of the impact of mergers on the survival of nuclear discs. To verify this hypothesis we present in Fig. 4.10 the results of the simulations that we ran while softening the massive particle representing the secondary black hole, for a 1:5 mass ratio and for polar and co-planar prograde encounters. To do so, we assumed that a stellar cusp of 1, 2, and 4 times the mass the secondary remained bound to the BH, hence increasing the mass of the perturbing particle, that now represents the composite BH - cluster system (see Table 2). We further assumed the same profile for the primary and secondary stellar profile, so that the softenings of the new perturber particles have increased to 2, 3.5 and 6.25 pc respectively.

Comparing the  $a_4$ ,  $V$  and  $k5/k1$  values of these simulations with the corresponding numbers for the 1:5 simulations without softening, we see that whereas in the polar case a more extended and massive secondary source (mimicking a secondary black hole and its stellar nucleus) would indeed reduce the signature of a disc in the remnant (in particular in the images), the disc would appear to survive a co-planar prograde encounter with such an extended secondary. The stark contrast with the outcome of the prograde co-planar encounter with a naked secondary is largely due to a much reduced vertical scattering of the disc stars as a more extended secondary, with size comparable to the 5 pc vertical extent of the disc, travels within it. On the other hand, the larger impact on the disc structure observed in the “softened” version of our polar 1:5 encounter relates to the fact that in this case what matters most is the raw amount of black hole and core mass that plunges in and out of the disc, driving disc particles off the equatorial plane.

If we consider that co-planar encounters are likely to be relatively rare, and that the mass of the secondary will likely matter also for the outcome of the more inclined merger events, we may conclude that, indeed, in a more realistic situation of a secondary black hole still surrounded by its stellar nucleus, the impact on the nuclear disc would be even more disruptive than what previously inferred.

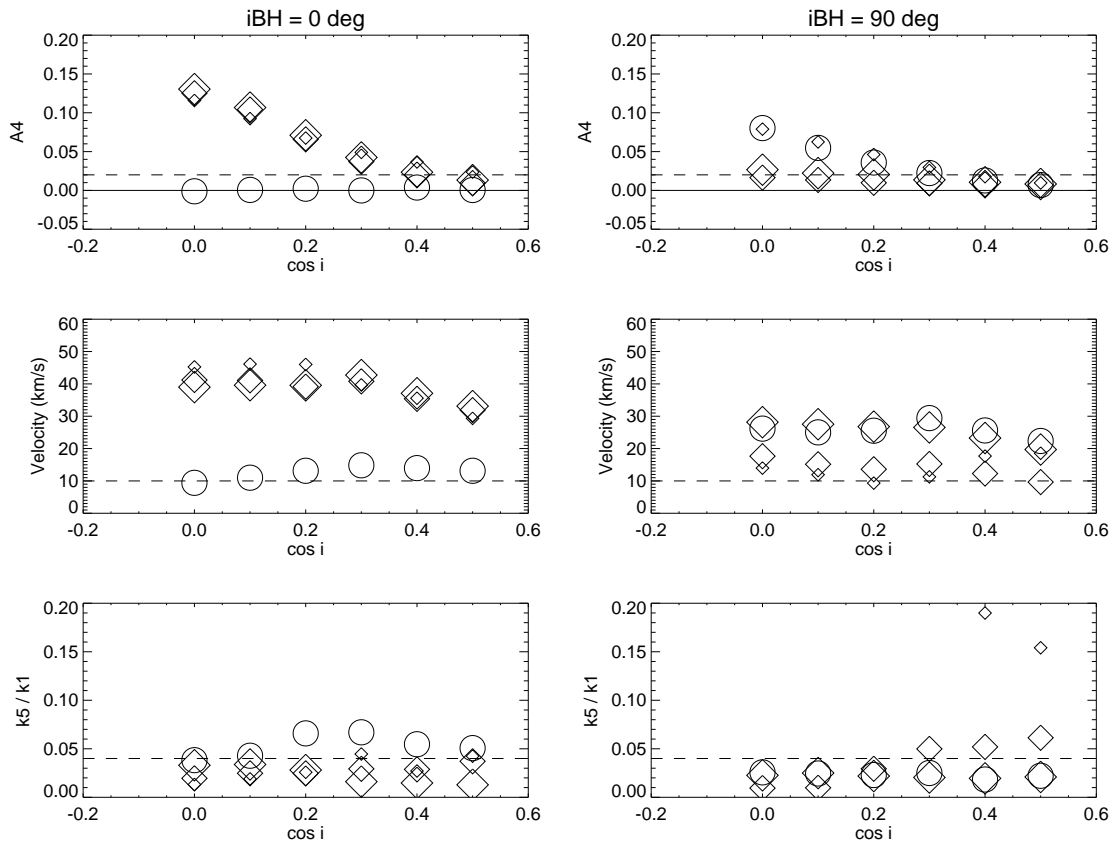


Fig. 4.10: Similar to Figs. 4.7, 4.8 and 4.9 but now illustrating the effect of increasing the softening parameter and the mass of the secondary perturbing particle, as to mimic the presence of a stellar core around the secondary black hole (see text). The impact on the average  $a_4$ ,  $V$  and  $k_5/k_1$  values is explored here only for 1 to 5 mass-ratio mergers and for two limiting situations, a prograde encounter on the plane of the disc ( $i_{\text{BH}} = 0$ ) and a polar impact ( $i_{\text{BH}} = 90$ ). Diamonds show the results of simulations with softening (and of increasing size for increasing softening, see Tab. 2), whereas the circles show for comparison the results for our standard softening value.

## 4.5 Discussion

Using a suite of numerical simulations we have explored the fragility of nuclear stellar discs in order to establish their usefulness as tools to constrain merging histories of early-type galaxies. Our results show that NSDs are destroyed in major merger situations whereas photometric and, even more generally, kinematic signatures of a disc would be detectable in the remnants of minor mergers (see Table 3). Future integral-field studies should prove particularly useful to compile a more complete census of NSDs than already done based on HST images in Chapter 2. New instruments such as MUSE (Bacon *et al.*, 2010), with its superior sensitivity and the ability to work in conjunction with adaptive optics, should prove particularly useful for detecting NSDs. MUSE should also prove an excellent tool for dating the age of these structure, improving on the first experiment of Sarzi *et al.* (in preparation) based on VIMOS data.

A large sample of nuclear stellar discs with well constrained values for their stellar age, combined with the knowledge gained here on the fragility of such structures, should allow to paint a more detailed picture for the assembly history of galaxies.

Galaxy evolution models predict merging trees of a combination of mergers (e.g. Khochfar and Silk, 2006b,a; González *et al.*, 2011) and there is great debate on the influence of major and minor mergers in the size and mass growth of galaxies, with current theory favouring 1:5 - 1:10 mergers (e.g. Oser *et al.*, 2012; Bédorf and Portegies Zwart, 2013). Interestingly, this corresponds to the minor merger range of mass ratios studied in this work. Yet major mergers cannot be discarded, as other studies (e.g. Lidman *et al.*, 2013) have suggested that in recent epochs they may have caused large mass increases. Therefore, the ability of these NSDs to discriminate between merger scenarios is central to today's questions.

We are aware that the set up of the simulations presented here is simplified. For instance considering a Mestel profile for the nuclear disc and a purely spherical Plummer distribution for the bulge does not convey the complexity of real nuclei where e.g. the disc is better described by an exponential law and bulges can be flattened and present both core and cuspy profiles. Yet, with a bulge mass approximately 5 times that of the disc within 100 pc, the corresponding disc to total surface brightness ratio of our initial model does span the observed values between 20 and 40% (e.g. Morelli *et al.*, 2004), depending on the inclination. We therefore regard this work a first exploratory study, which could be improved on the one hand by exploring a larger parameter space, for instance by varying the mass of the nuclear disc compared to its host bulge and central supermassive black hole, and on the

other hand by considering a more realistic model for the stellar cusp around the secondary black hole. The actual amount of stellar mass bounded to the sinking nucleus of a satellite galaxies may well remain a free parameter in a future analysis, unless new insights will emerge from larger sets of simulations such as those of Callegari *et al.* (2009), but we plan to improve our current framework by including an actual evolving set of collisionless particles around the secondary. This will better show the effect of tidal stripping of such a stellar core, and provide a more realistic picture of the disc disruption. In fact, our preliminary exploration in this direction (Section 4.1) already indicates as expected that the presence of a stellar cusp around the secondary will further contribute to the disc disruption.

To conclude, we note that better simulations may as well shed more light also on the origin of the kinematically decoupled cores (KDC) that are often found in early-type galaxies (e.g. Bender, 1988; Franx *et al.*, 1989; McDermid *et al.*, 2006). Indeed a significant number of our simulated encounters result in remnants that display regular rotation, characterised even by a low average  $k_5/k_1$  value, despite not showing any photometric  $a_4$  signatures of disky structures. This resembles the situation observed for the KDCs of massive elliptical galaxies (see, for instance, the SAURON data for NGC 4406 of NGC 5813 in Krajnović *et al.*, 2013), and suggest a possible link between KDCs and puffed-up thick discs. A closer look to the higher-order moments of the stellar LOSVD, both in future simulations and in high-quality integral-field data should provide more valuable insights on the nature of these structures.

# References

- Bacon, R., Accardo, M., Adjali, L., Anwand, H., Bauer, S., Biswas, I., Blaizot, J., Boudon, D., Brau-Nogue, S., Brinchmann, J., Caillier, P., Capoani, L., Carollo, C. M., Contini, T., Couderc, P., Daguisé, E., Deiries, S., Delabre, B., Dreizler, S., Dubois, J., Dupieux, M., Dupuy, C., Emsellem, E., Fechner, T., Fleischmann, A., François, M., Gallou, G., Gharsa, T., Glindemann, A., Gojak, D., Guiderdoni, B., Hansali, G., Hahn, T., Jarno, A., Kelz, A., Koehler, C., Kosmalski, J., Laurent, F., Le Floch, M., Lilly, S. J., Lizon, J.-L., Loupiau, M., Manescau, A., Monstein, C., Nicklas, H., Olaya, J.-C., Pares, L., Pasquini, L., Pécontal-Rousset, A., Pelló, R., Petit, C., Popow, E., Reiss, R., Remillieux, A., Renault, E., Roth, M., Rupprecht, G., Serre, D., Schaye, J., Soucail, G., Steinmetz, M., Streicher, O., Stuijk, R., Valentin, H., Vernet, J., Weilbacher, P., Wisotzki, L., and Yerle, N. (2010). The MUSE second-generation VLT instrument. In *Society of Photo-Optical Instrumentation Engineers (SPIE) Conference Series*, volume 7735 of *Society of Photo-Optical Instrumentation Engineers (SPIE) Conference Series*.
- Bédorf, J. and Portegies Zwart, S. (2013). The effect of many minor mergers on the size growth of compact quiescent galaxies. *MNRAS*, **431**, 767–780.
- Begelman, M. C., Blandford, R. D., and Rees, M. J. (1980). Massive black hole binaries in active galactic nuclei. *Nature*, **287**, 307–309.
- Bender, R. (1988). Rotating and counter-rotating cores in elliptical galaxies. *A&A*, **202**, L5–L8.
- Bois, M., Emsellem, E., Bournaud, F., Alatalo, K., Blitz, L., Bureau, M., Cappellari, M., Davies, R. L., Davis, T. A., de Zeeuw, P. T., Duc, P.-A., Khochfar, S., Krajnović, D., Kuntschner, H., Lablanche, P.-Y., McDermid, R. M., Morganti, R., Naab, T., Oosterloo, T., Sarzi, M., Scott, N., Serra, P., Weijmans, A.-M., and Young, L. M. (2011). The ATLAS<sup>3D</sup> project - VI. Simulations of binary galaxy mergers and the link with fast rotators, slow rotators and kinematically distinct cores. *MNRAS*, **416**, 1654–1679.
- Brook, C. B., Stinson, G., Gibson, B. K., Roškar, R., Wadsley, J., and Quinn, T. (2012). Hierarchical formation of bulgeless galaxies - II. Redistribution of angular momentum via galactic fountains. *MNRAS*, **419**, 771–779.
- Bundy, K., Fukugita, M., Ellis, R. S., Targett, T. A., Belli, S., and Kodama, T. (2009). The Greater Impact of Mergers on the Growth of Massive Galaxies: Implications for Mass Assembly and Evolution since  $z \sim 1$ . *ApJ*, **697**, 1369–1383.
- Callegari, S., Mayer, L., Kazantzidis, S., Colpi, M., Governato, F., Quinn, T., and Wadsley, J. (2009). Pairing of Supermassive Black Holes in Unequal-Mass Galaxy Mergers. *ApJ*, **696**, L89–L92.

- Callegari, S., Kazantzidis, S., Mayer, L., Colpi, M., Bellovary, J. M., Quinn, T., and Wadsley, J. (2011). Growing Massive Black Hole Pairs in Minor Mergers of Disk Galaxies. *ApJ*, **729**, 85.
- De Lucia, G., Springel, V., White, S. D. M., Croton, D., and Kauffmann, G. (2006). The formation history of elliptical galaxies. *MNRAS*, **366**, 499–509.
- Dotti, M., Colpi, M., and Haardt, F. (2006). Laser Interferometer Space Antenna double black holes: dynamics in gaseous nuclear discs. *MNRAS*, **367**, 103–112.
- Dotti, M., Colpi, M., Haardt, F., and Mayer, L. (2007). Supermassive black hole binaries in gaseous and stellar circumnuclear discs: orbital dynamics and gas accretion. *MNRAS*, **379**, 956–962.
- Escala, A., Larson, R. B., Coppi, P. S., and Mardones, D. (2005). The Role of Gas in the Merging of Massive Black Holes in Galactic Nuclei. II. Black Hole Merging in a Nuclear Gas Disk. *ApJ*, **630**, 152–166.
- Franx, M., Illingworth, G., and Heckman, T. (1989). Major and minor axis kinematics of 22 ellipticals. *ApJ*, **344**, 613–636.
- González, J. E., Lacey, C. G., Baugh, C. M., and Frenk, C. S. (2011). The role of submillimetre galaxies in hierarchical galaxy formation. *MNRAS*, **413**, 749–762.
- Häring, N. and Rix, H.-W. (2004). On the Black Hole Mass-Bulge Mass Relation. *ApJ*, **604**, L89–L92.
- Jaffe, W., Ford, H. C., O’Connell, R. W., van den Bosch, F. C., and Ferrarese, L. (1994). Hubble Space Telescope photometry of the central regions of Virgo Cluster elliptical galaxies. 1: Observations, discussion, and conclusions. *AJ*, **108**, 1567–1578.
- Jedrzejewski, R. I. (1987). CCD surface photometry of elliptical galaxies. I - Observations, reduction and results. *MNRAS*, **226**, 747–768.
- Khochfar, S. and Silk, J. (2006a). A Simple Model for the Size Evolution of Elliptical Galaxies. *ApJ*, **648**, L21–L24.
- Khochfar, S. and Silk, J. (2006b). On the origin of stars in bulges and elliptical galaxies. *MNRAS*, **370**, 902–910.
- Kobayashi, C. (2004). GRAPE-SPH chemodynamical simulation of elliptical galaxies - I. Evolution of metallicity gradients. *MNRAS*, **347**, 740–758.
- Krajnović, D., Cappellari, M., de Zeeuw, P. T., and Copin, Y. (2006). Kinemetry: a generalization of photometry to the higher moments of the line-of-sight velocity distribution. *MNRAS*, **366**, 787–802.

- Krajnović, D., Emsellem, E., Cappellari, M., Alatalo, K., Blitz, L., Bois, M., Bournaud, F., Bureau, M., Davies, R. L., Davis, T. A., de Zeeuw, P. T., Khochfar, S., Kuntschner, H., Lablanche, P.-Y., McDermid, R. M., Morganti, R., Naab, T., Oosterloo, T., Sarzi, M., Scott, N., Serra, P., Weijmans, A.-M., and Young, L. M. (2011). The ATLAS<sup>3D</sup> project - II. Morphologies, kinematic features and alignment between photometric and kinematic axes of early-type galaxies. *MNRAS*, **414**, 2923–2949.
- Krajnović, D., Karick, A. M., Davies, R. L., Naab, T., Sarzi, M., Emsellem, E., Cappellari, M., Serra, P., de Zeeuw, P. T., Scott, N., McDermid, R. M., Weijmans, A.-M., Davis, T. A., Alatalo, K., Blitz, L., Bois, M., Bureau, M., Bournaud, F., Crocker, A., Duc, P.-A., Khochfar, S., Kuntschner, H., Morganti, R., Oosterloo, T., and Young, L. M. (2013). The ATLAS<sup>3D</sup> Project - XXIII. Angular momentum and nuclear surface brightness profiles. *MNRAS*, **433**, 2812–2839.
- Ledo, H. R., Sarzi, M., Dotti, M., Khochfar, S., and Morelli, L. (2010). A census of nuclear stellar discs in early-type galaxies. *MNRAS*, **407**, 969–985.
- Levine, R. (2008). *Simulating the growth of a disk galaxy and its supermassive black hole in a cosmological context*. Ph.D. thesis, University of Colorado at Boulder.
- Lidman, C., Iacobuta, G., Bauer, A. E., Barrientos, L. F., Cerulo, P., Couch, W. J., Delaye, L., Demarco, R., Ellingson, E., Faloon, A. J., Gilbank, D., Huertas-Company, M., Mei, S., Meyers, J., Muzzin, A., Noble, A., Nantais, J., Rettura, A., Rosati, P., Sánchez-Janssen, R., Strazzullo, V., Webb, T. M. A., Wilson, G., Yan, R., and Yee, H. K. C. (2013). The importance of major mergers in the build up of stellar mass in brightest cluster galaxies at  $z = 1$ . *MNRAS*, **433**, 825–837.
- López-Sanjuan, C., Le Fèvre, O., Ilbert, O., Tasca, L. A. M., Bridge, C., Cucciati, O., Kampczyk, P., Pozzetti, L., Xu, C. K., Carollo, C. M., Contini, T., Kneib, J.-P., Lilly, S. J., Mainieri, V., Renzini, A., Sanders, D., Scodreggio, M., Scoville, N. Z., Taniguchi, Y., Zamorani, G., Aussel, H., Bardelli, S., Bolzonella, M., Bongiorno, A., Capak, P., Caputi, K., de la Torre, S., de Ravel, L., Franzetti, P., Garilli, B., Iovino, A., Knobel, C., Kovač, K., Lamareille, F., Le Borgne, J.-F., Le Brun, V., Le Floc’h, E., Maier, C., McCracken, H. J., Mignoli, M., Pelló, R., Peng, Y., Pérez-Montero, E., Presotto, V., Ricciardelli, E., Salvato, M., Silverman, J. D., Tanaka, M., Tresse, L., Vergani, D., Zucca, E., Barnes, L., Bordoloi, R., Cappi, A., Cimatti, A., Coppa, G., Koekemoer, A., Liu, C. T., Moresco, M., Nair, P., Oesch, P., Schawinski, K., and Welikala, N. (2012). The dominant role of mergers in the size evolution of massive early-type galaxies since  $z \sim 1$ . *A&A*, **548**, A7.
- Maller, A. H., Katz, N., Kereš, D., Davé, R., and Weinberg, D. H. (2006). Galaxy Merger Statistics and Inferred Bulge-to-Disk Ratios in Cosmological SPH Simulations. *ApJ*, **647**, 763–772.
- McDermid, R. M., Emsellem, E., Shapiro, K. L., Bacon, R., Bureau, M., Cappellari, M., Davies, R. L., de Zeeuw, T., Falcón-Barroso, J., Krajnović, D., Kuntschner,

- H., Peletier, R. F., and Sarzi, M. (2006). The SAURON project - VIII. OASIS/CFHT integral-field spectroscopy of elliptical and lenticular galaxy centres. *MNRAS*, **373**, 906–958.
- Meiron, Y. and Laor, A. (2013). The kinematic signature of the inspiral phase of massive binary black holes. *MNRAS*, **433**, 2502–2510.
- Mestel, L. (1963). On the galactic law of rotation. *MNRAS*, **126**, 553.
- Morelli, L., Halliday, C., Corsini, E. M., Pizzella, A., Thomas, D., Saglia, R. P., Davies, R. L., Bender, R., Birkinshaw, M., and Bertola, F. (2004). Nuclear stellar discs in low-luminosity elliptical galaxies: NGC 4458 and 4478. *MNRAS*, **354**, 753–762.
- Oser, L., Naab, T., Ostriker, J. P., and Johansson, P. H. (2012). The Cosmological Size and Velocity Dispersion Evolution of Massive Early-type Galaxies. *ApJ*, **744**, 63.
- Pizzella, A., Corsini, E. M., Morelli, L., Sarzi, M., Scarlata, C., Stiavelli, M., and Bertola, F. (2002). Nuclear Stellar Disks in Spiral Galaxies. *ApJ*, **573**, 131–137.
- Rix, H.-W. and White, S. D. M. (1990). Disks in elliptical galaxies. *ApJ*, **362**, 52–58.
- Scorza, C. and Bender, R. (1995). The internal structure of disky elliptical galaxies. *A&A*, **293**, 20–43.
- Scorza, C. and van den Bosch, F. C. (1998). Nuclear stellar discs in early-type galaxies - II. Photometric properties. *MNRAS*, **300**, 469–478.
- Springel, V. (2005). The cosmological simulation code GADGET-2. *MNRAS*, **364**, 1105–1134.
- van den Bosch, F. C. and de Zeeuw, P. T. (1996). Self-Consistent, Axisymmetric Two-Integral Models of Elliptical Galaxies with Embedded Nuclear Discs. *MNRAS*, **283**, 381–399.
- van den Bosch, F. C., Ferrarese, L., Jaffe, W., Ford, H. C., and O’Connell, R. W. (1994). Hubble Space Telescope photometry of the central regions of Virgo cluster elliptical galaxies. II: Isophote shapes. *AJ*, **108**, 1579–1597.
- Van Wassenhove, S., Volonteri, M., Mayer, L., Dotti, M., Bellovary, J., and Callegari, S. (2012). Observability of Dual Active Galactic Nuclei in Merging Galaxies. *ApJ*, **748**, L7.
- Van Wassenhove, S., Capelo, P. R., Volonteri, M., Dotti, M., Bellovary, J. M., Mayer, L., and Governato, F. (2014). Nuclear coups: dynamics of black holes in galaxy mergers. *MNRAS*, **439**, 474–487.
- Velazquez, H. and White, S. D. M. (1999). Sinking satellites and the heating of galaxy discs. *MNRAS*, **304**, 254–270.

## 4.6 Appendix D: Density and velocity maps with corresponding kinemetry

In this appendix we present the density and velocity maps of the final stages for all the simulations with the softening parameter corresponding to 0.5 pc (naked black holes), with the corresponding kinemetry for the total (bulge and disc), all seen at  $60^\circ$ .

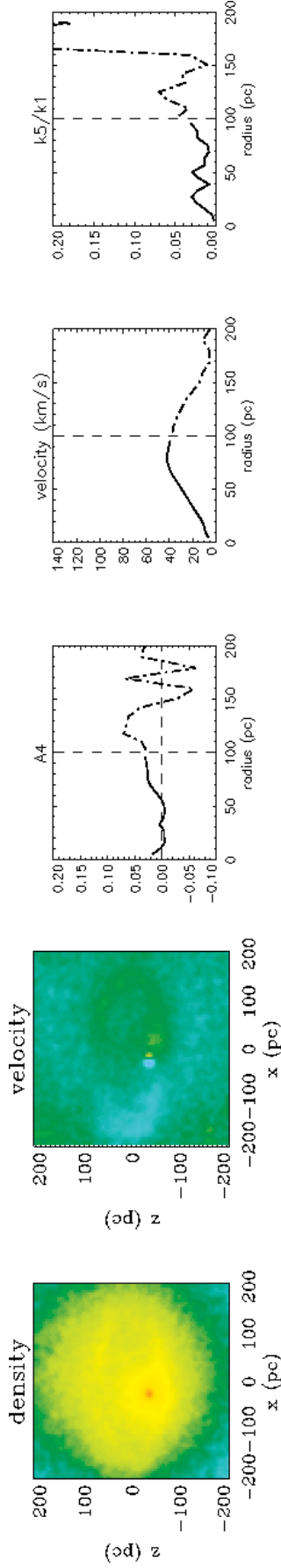


Fig. 4.11: Final outcome of encounter featuring a 1 to 1 mass ratio,  $i_{\text{BH}} = 0^\circ$ ,  $i = 60^\circ$ . The two maps on the left show the final density and velocity field of all particles, whereas the three plots on the right show the radial trends for the  $a_4$ , velocity and  $k5/k1$  parameter as measured with kinemetry. In these panels, the black lines show these measurements for the entire system whereas blue lines are for the disc particles only. Vertical dashed lines indicate the original extent of the disc. Average values for those kinemetry parameters are computed inside that radius, whereas the outer values are ignore and indicated by dot-dashed lines

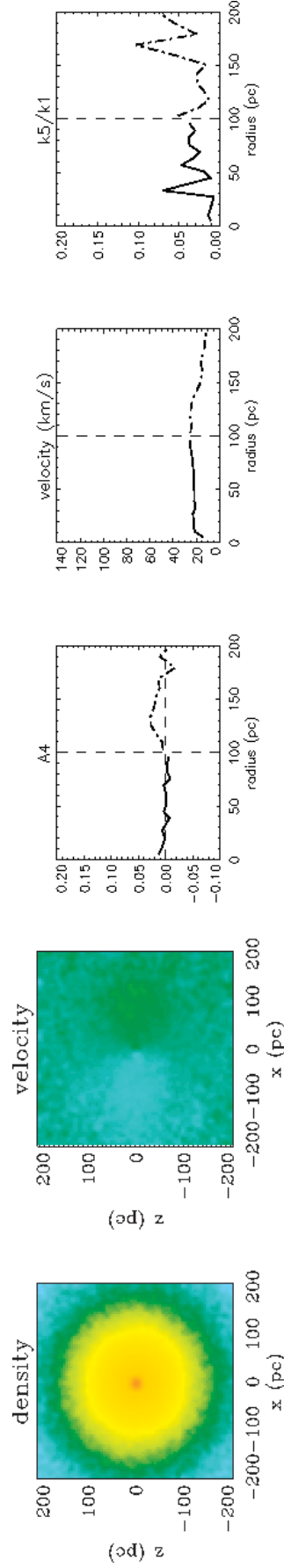


Fig. 4.12: Similar to the first figure in this appendix but now showing the outcome of a 1 to 1 merger with  $i_{\text{BH}} = 30^\circ$  and viewed from an inclination  $i = 60^\circ$

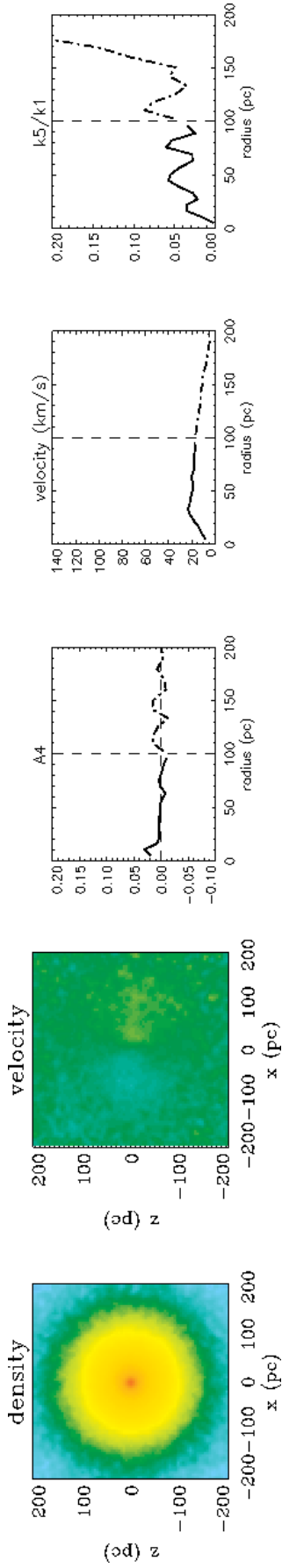


Fig. 4.13: Similar to the first figure in this appendix but now showing the outcome of a 1 to 1 merger with  $i_{\text{BH}} = 60^\circ$  and viewed from a inclination  $i = 60^\circ$

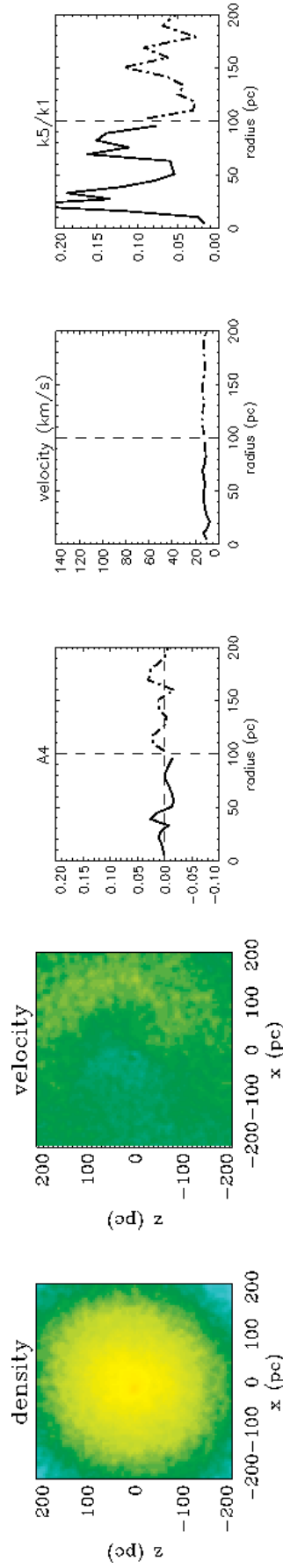


Fig. 4.14: Similar to the first figure in this appendix but now showing the outcome of a 1 to 1 merger with  $i_{\text{BH}} = 90^\circ$  and viewed from a inclination  $i = 60^\circ$

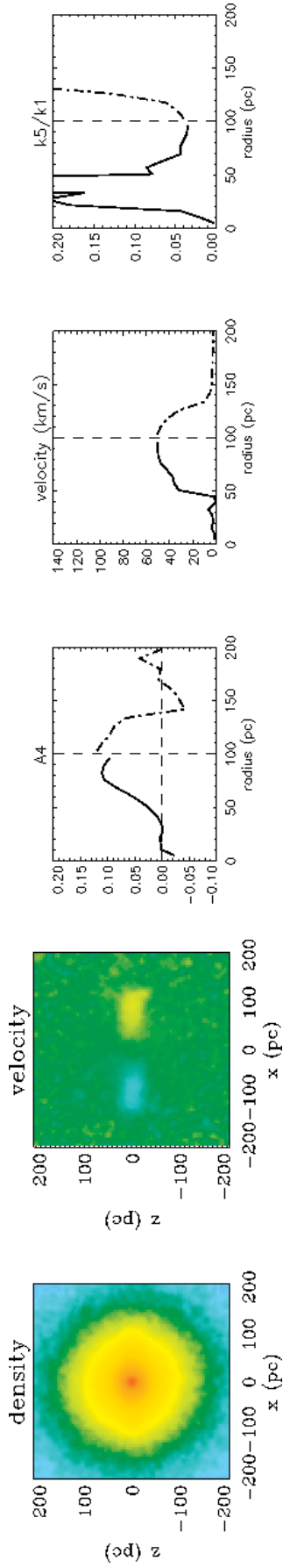


Fig. 4.15: Similar to the first figure in this appendix but now showing the outcome of a 1 to 1 merger with  $i_{\text{BH}} = 120^\circ$  and viewed from an inclination  $i = 60^\circ$

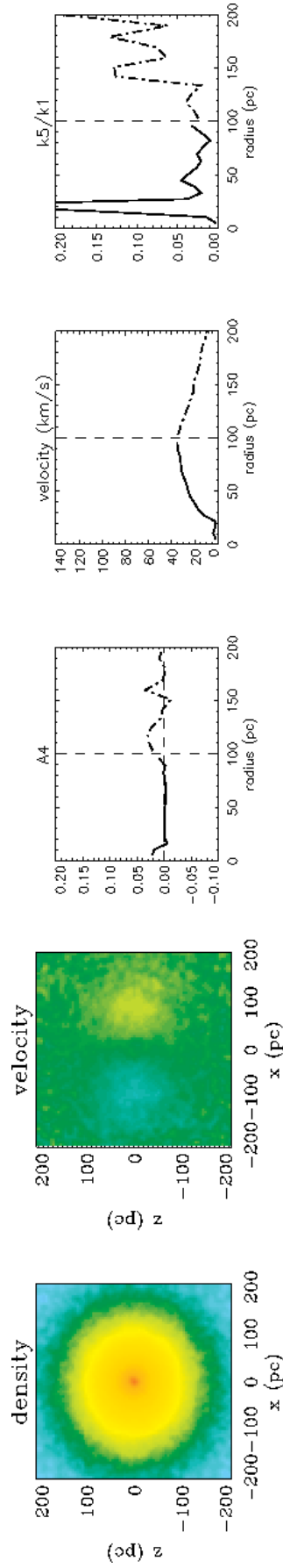


Fig. 4.16: Similar to the first figure in this appendix but now showing the outcome of a 1 to 1 merger with  $i_{\text{BH}} = 150^\circ$  and viewed from an inclination  $i = 60^\circ$

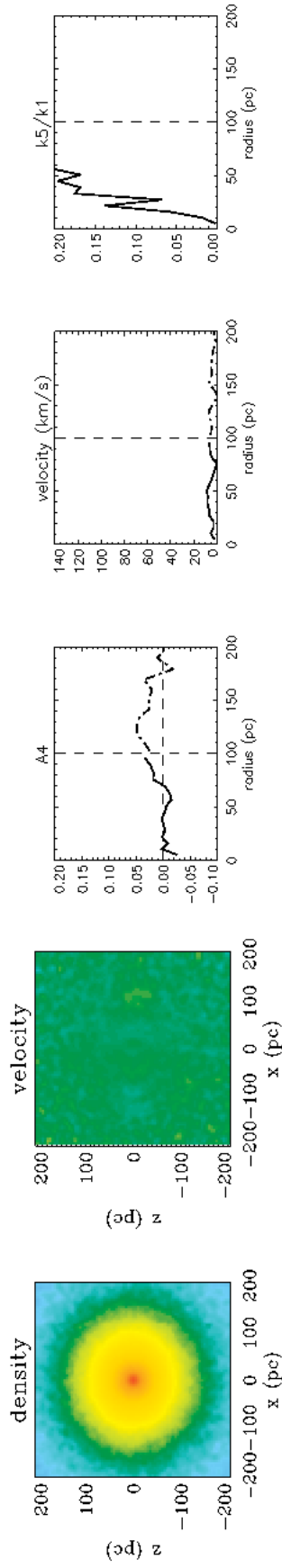


Fig. 4.17: Similar to the first figure in this appendix but now showing the outcome of a 1 to 1 merger with  $i_{\text{BH}} = 180^\circ$  and viewed from an inclination  $i = 60^\circ$

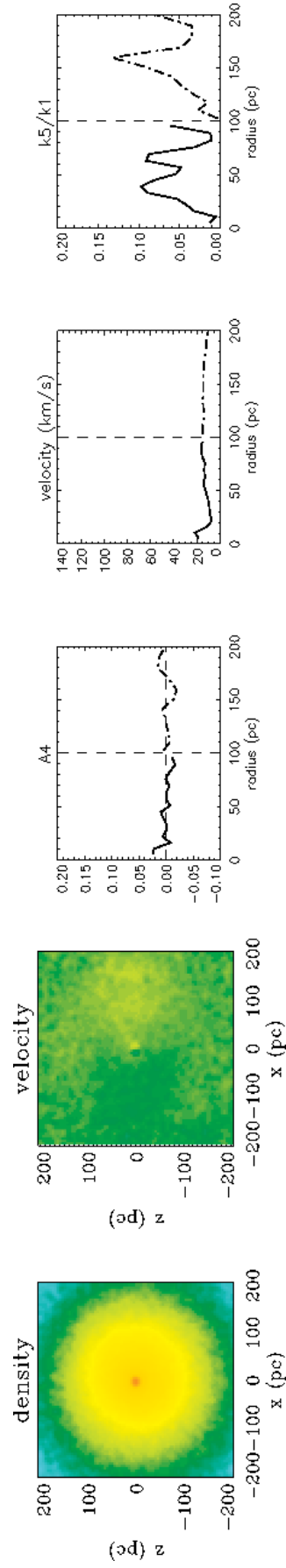


Fig. 4.18: Similar to the first figure in this appendix but now showing the outcome of a 1 to 5 merger with  $i_{\text{BH}} = 0^\circ$  and viewed from an inclination  $i = 60^\circ$

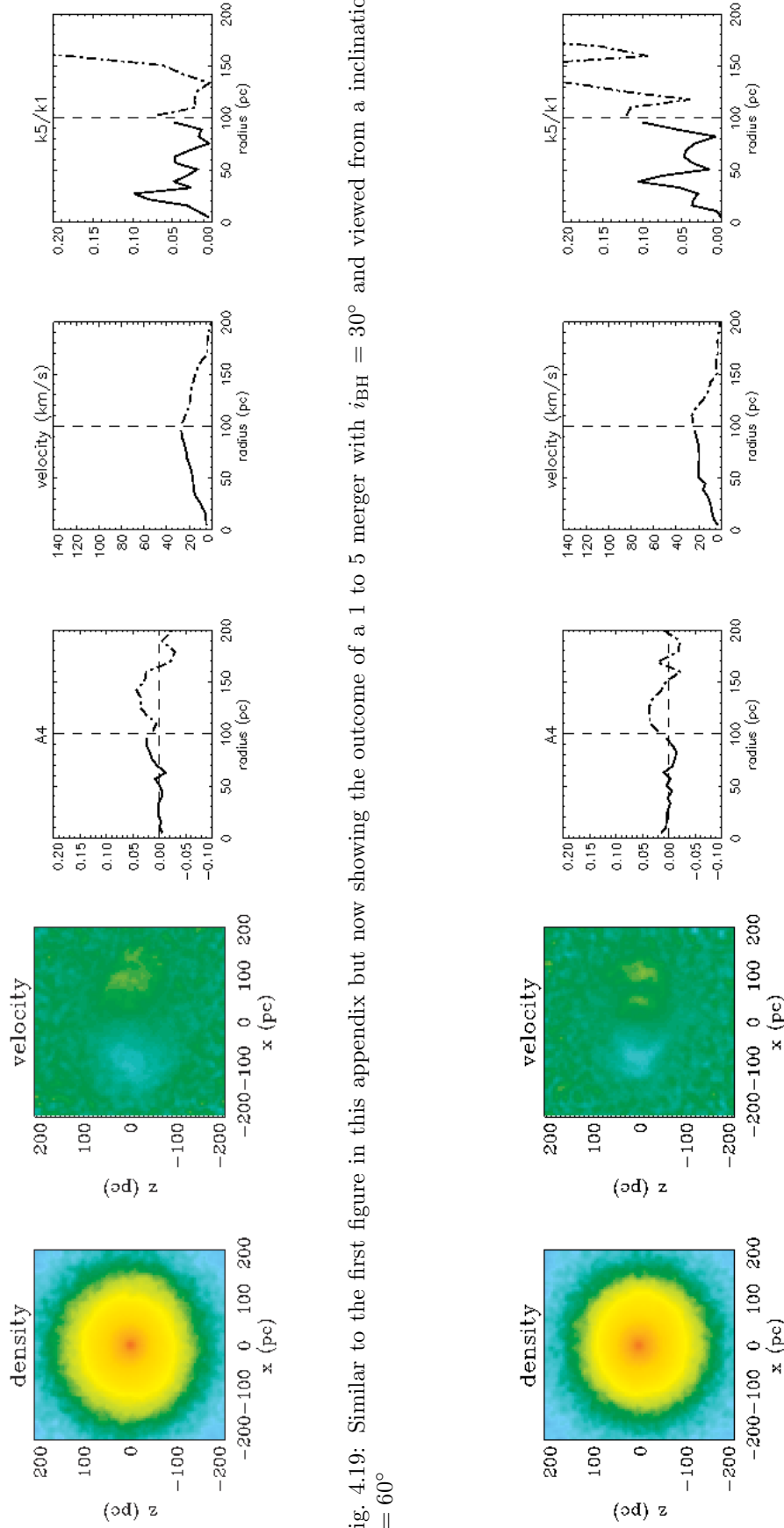


Fig. 4.19: Similar to the first figure in this appendix but now showing the outcome of a 1 to 5 merger with  $i_{\text{BH}} = 30^\circ$  and viewed from an inclination  $i = 60^\circ$

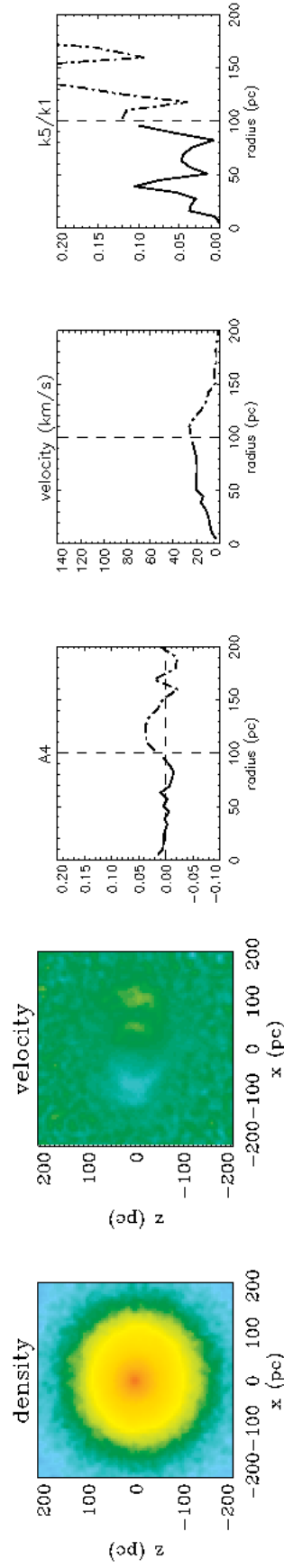


Fig. 4.20: Similar to the first figure in this appendix but now showing the outcome of a 1 to 5 merger with  $i_{\text{BH}} = 60^\circ$  and viewed from an inclination  $i = 60^\circ$

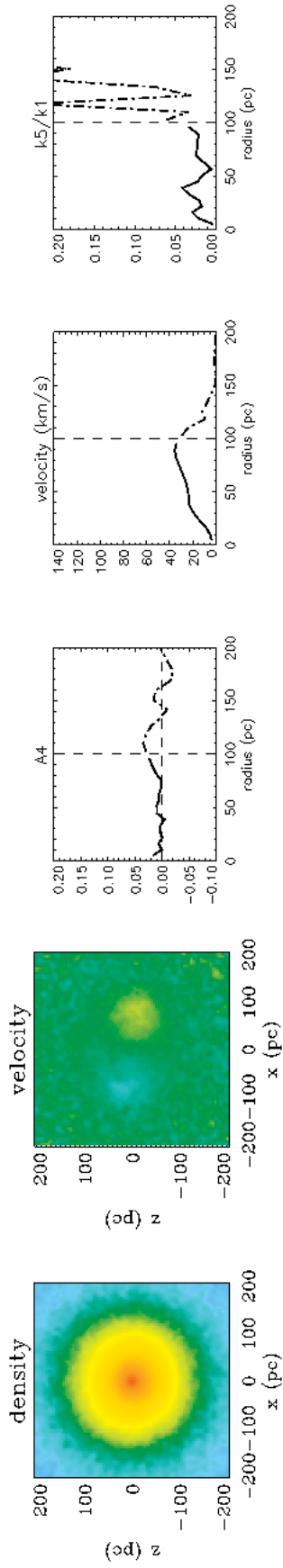


Fig. 4.21: Similar to the first figure in this appendix but now showing the outcome of a 1 to 5 merger with  $i_{\text{BH}} = 90^\circ$  and viewed from a inclination  $i = 60^\circ$

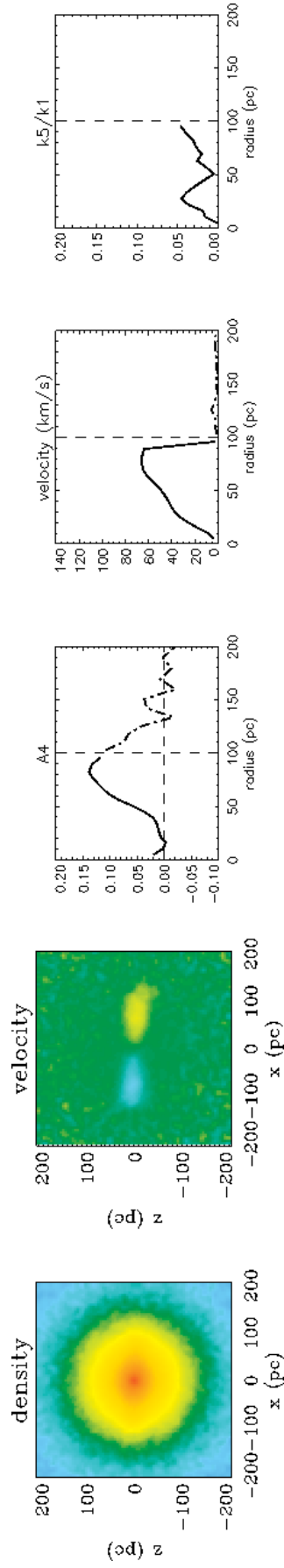


Fig. 4.22: Similar to the first figure in this appendix but now showing the outcome of a 1 to 5 merger with  $i_{\text{BH}} = 120^\circ$  and viewed from a inclination  $i = 60^\circ$

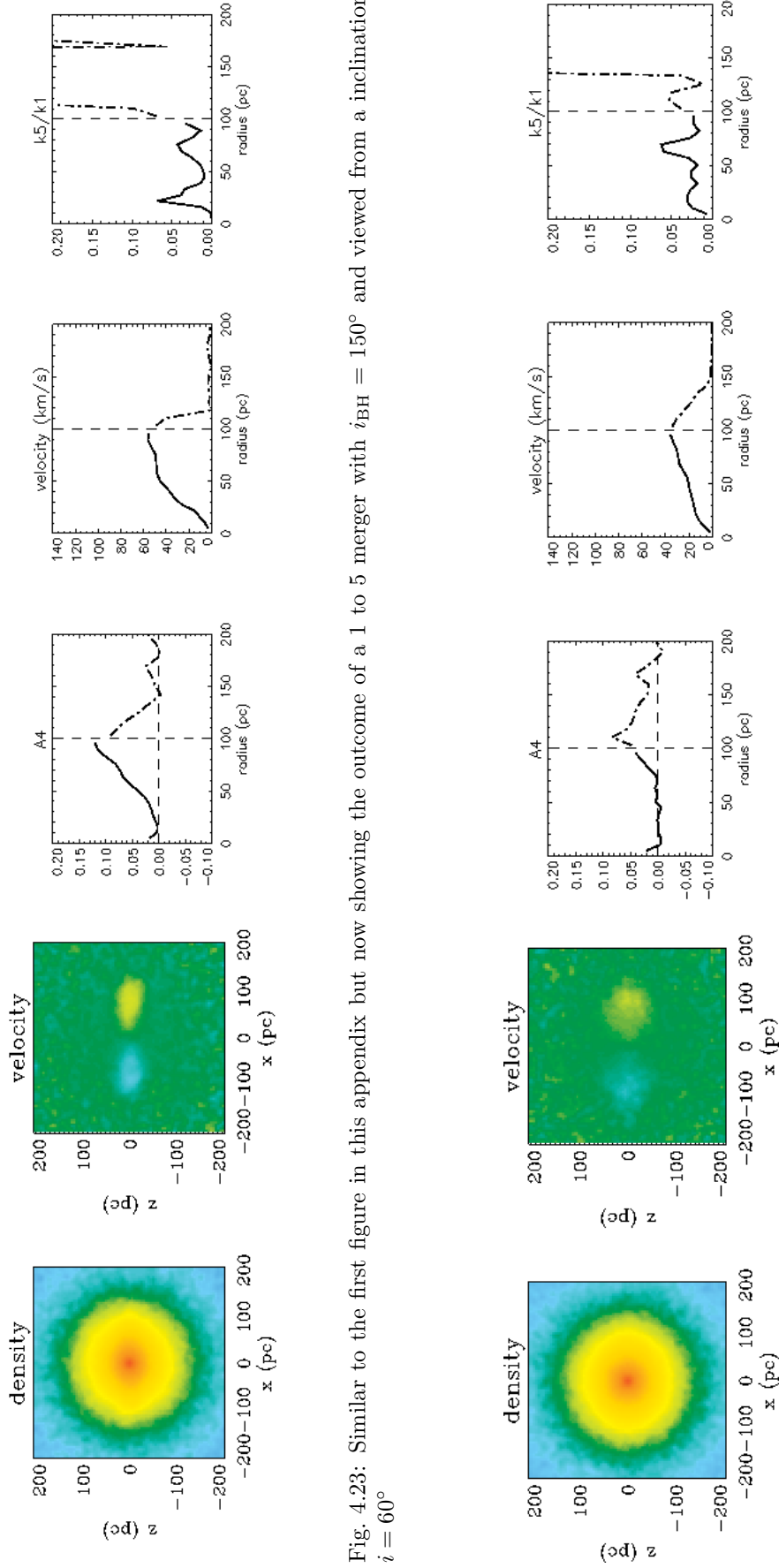


Fig. 4.23: Similar to the first figure in this appendix but now showing the outcome of a 1 to 5 merger with  $i_{\text{BH}} = 150^\circ$  and viewed from an inclination  $i = 60^\circ$

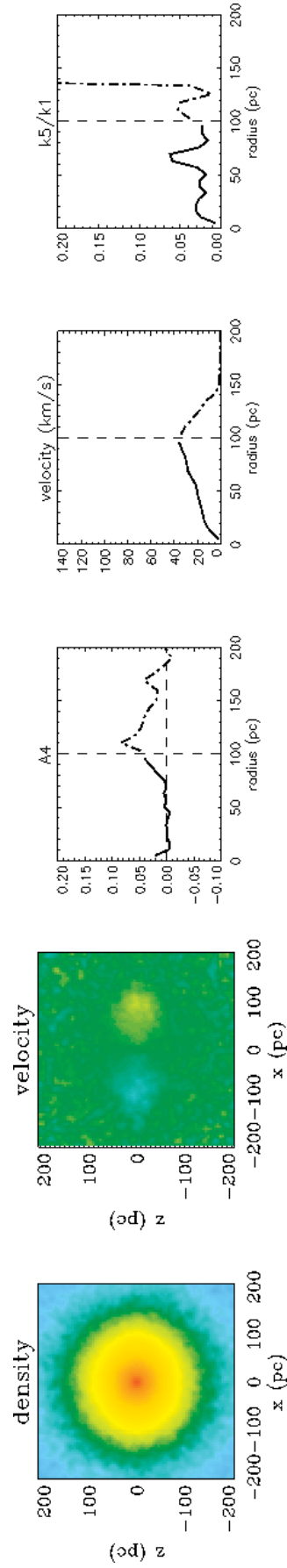


Fig. 4.24: Similar to the first figure in this appendix but now showing the outcome of a 1 to 5 merger with  $i_{\text{BH}} = 180^\circ$  and viewed from an inclination  $i = 60^\circ$

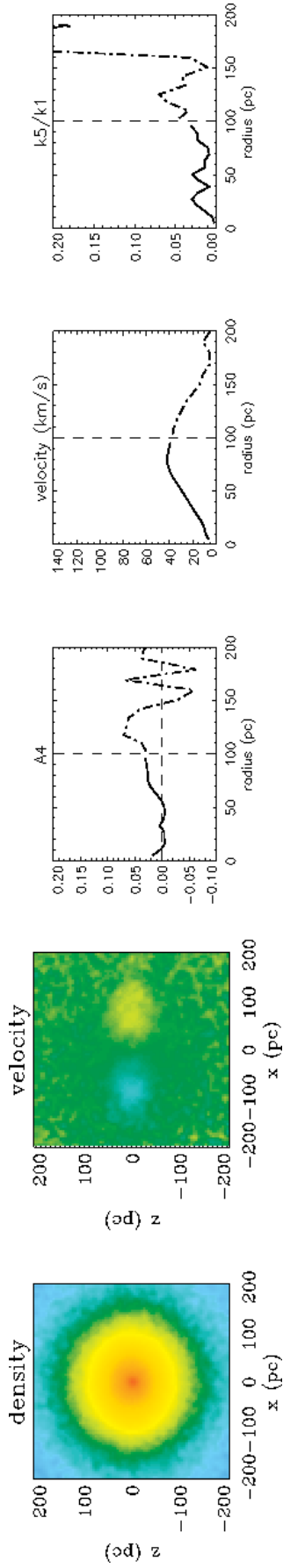


Fig. 4.25: Similar to the first figure in this appendix but now showing the outcome of a 1 to 10 merger with  $i_{\text{BH}} = 0^\circ$  and viewed from a inclination  $i = 60^\circ$

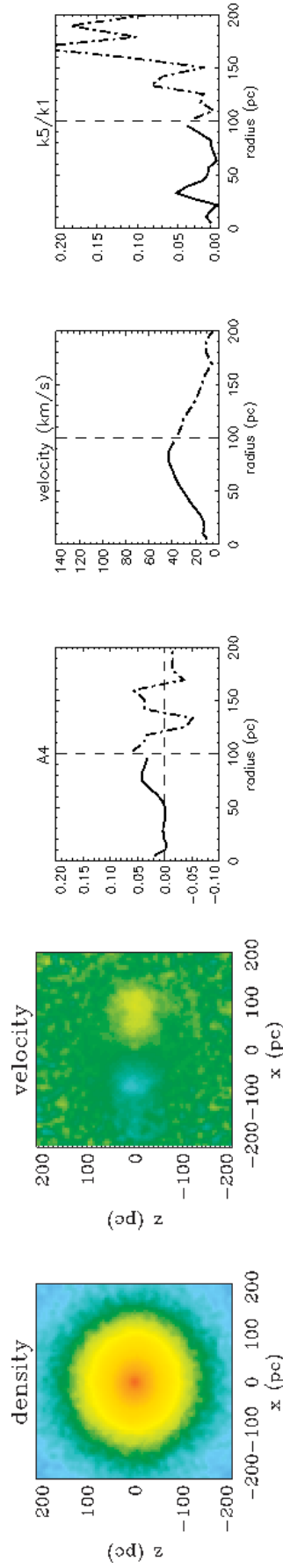


Fig. 4.26: Similar to the first figure in this appendix but now showing the outcome of a 1 to 10 merger with  $i_{\text{BH}} = 30^\circ$  and viewed from a inclination  $i = 60^\circ$

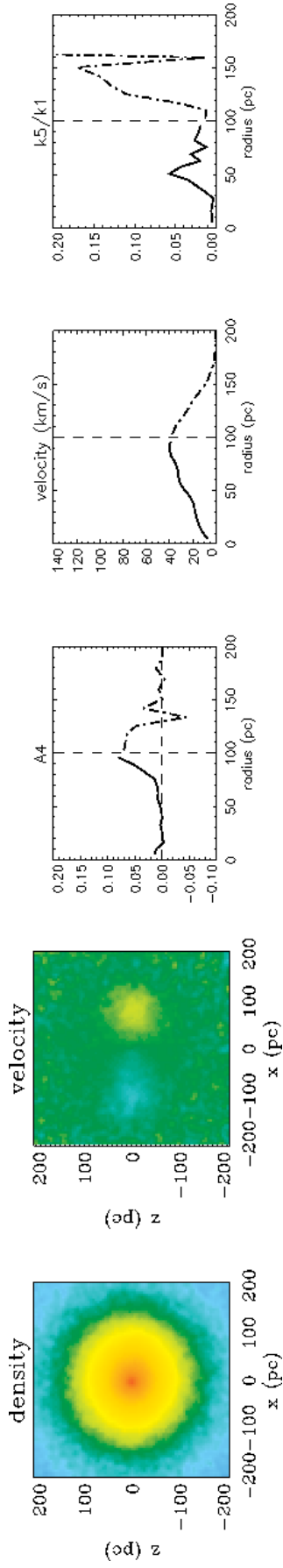


Fig. 4.27: Similar to the first figure in this appendix but now showing the outcome of a 1 to 10 merger with  $i_{\text{BH}} = 60^\circ$  and viewed from an inclination  $i = 60^\circ$

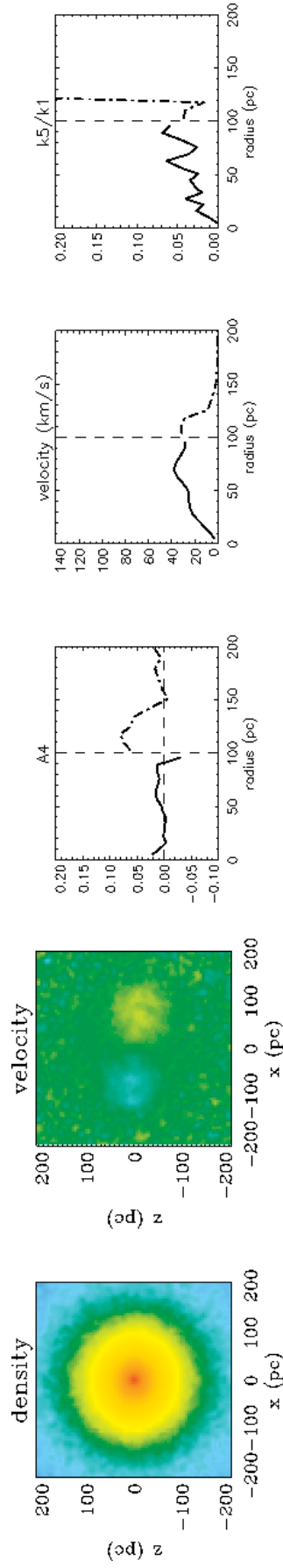


Fig. 4.28: Similar to the first figure in this appendix but now showing the outcome of a 1 to 10 merger with  $i_{\text{BH}} = 90^\circ$  and viewed from an inclination  $i = 60^\circ$

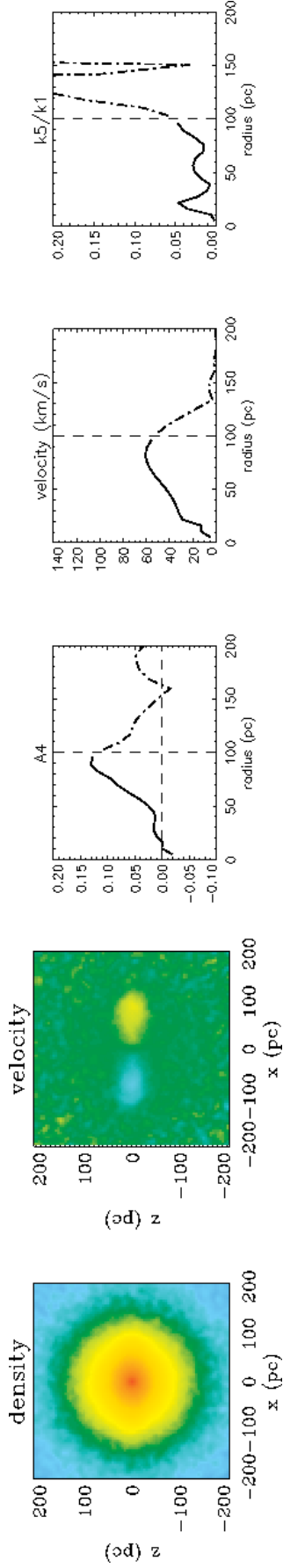


Fig. 4.29: Similar to the first figure in this appendix but now showing the outcome of a 1 to 10 merger with  $i_{\text{BH}} = 120^\circ$  and viewed from a inclination  $i = 60^\circ$

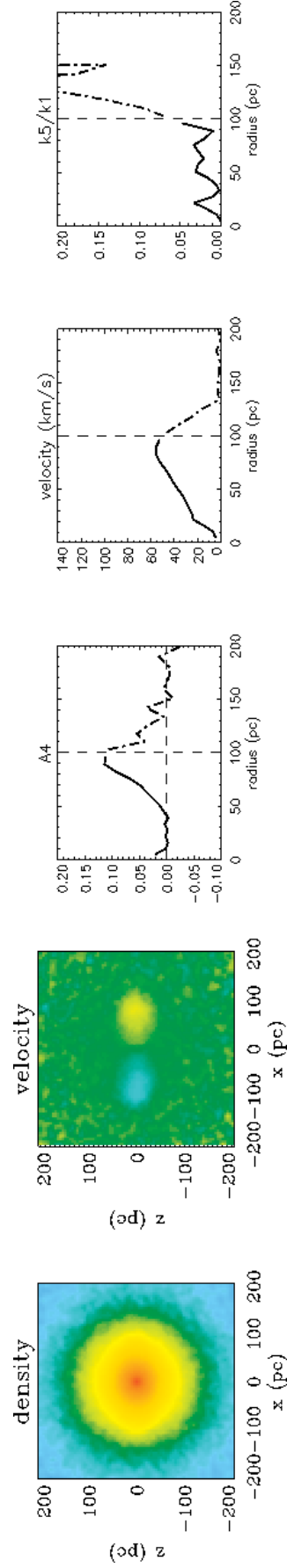


Fig. 4.30: Similar to the first figure in this appendix but now showing the outcome of a 1 to 10 merger with  $i_{\text{BH}} = 150^\circ$  and viewed from a inclination  $i = 60^\circ$

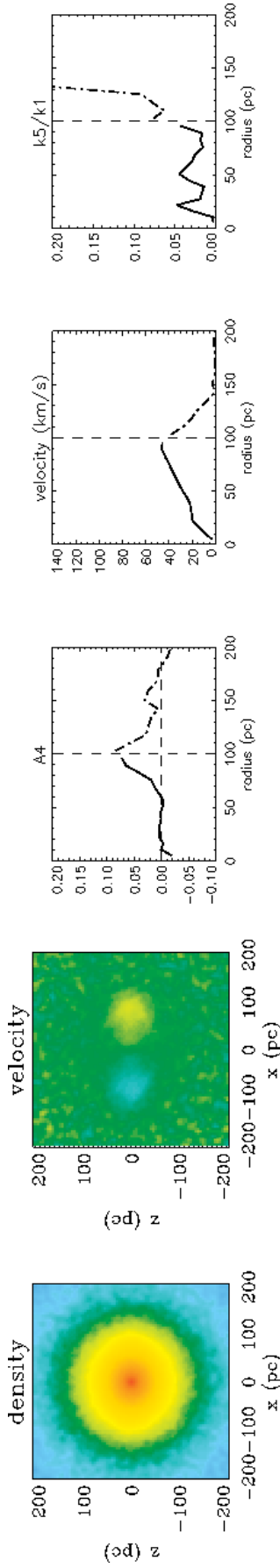


Fig. 4.31: Similar to the first figure in this appendix but now showing the outcome of a 1 to 10 merger with  $i_{\text{BH}} = 180^\circ$  and viewed from an inclination  $i = 60^\circ$

## 4.7 Appendix E: Density and velocity maps with corresponding kinemetry for collisions with softened black holes

In this appendix we show the effects of increasing the softening and mass of the secondary perturbing particle as to mimic the presence of a stellar core around the secondary black hole. This experiment was run in the case of mergers with a 1 to 5 mass ratio with  $i_{\text{BH}} = 0^\circ$  and  $i_{\text{BH}} = 90^\circ$ . We also replot Fig. 4.18 and 4.21 for a more immediate comparison with our standard softening the case representing a naked secondary black hole.

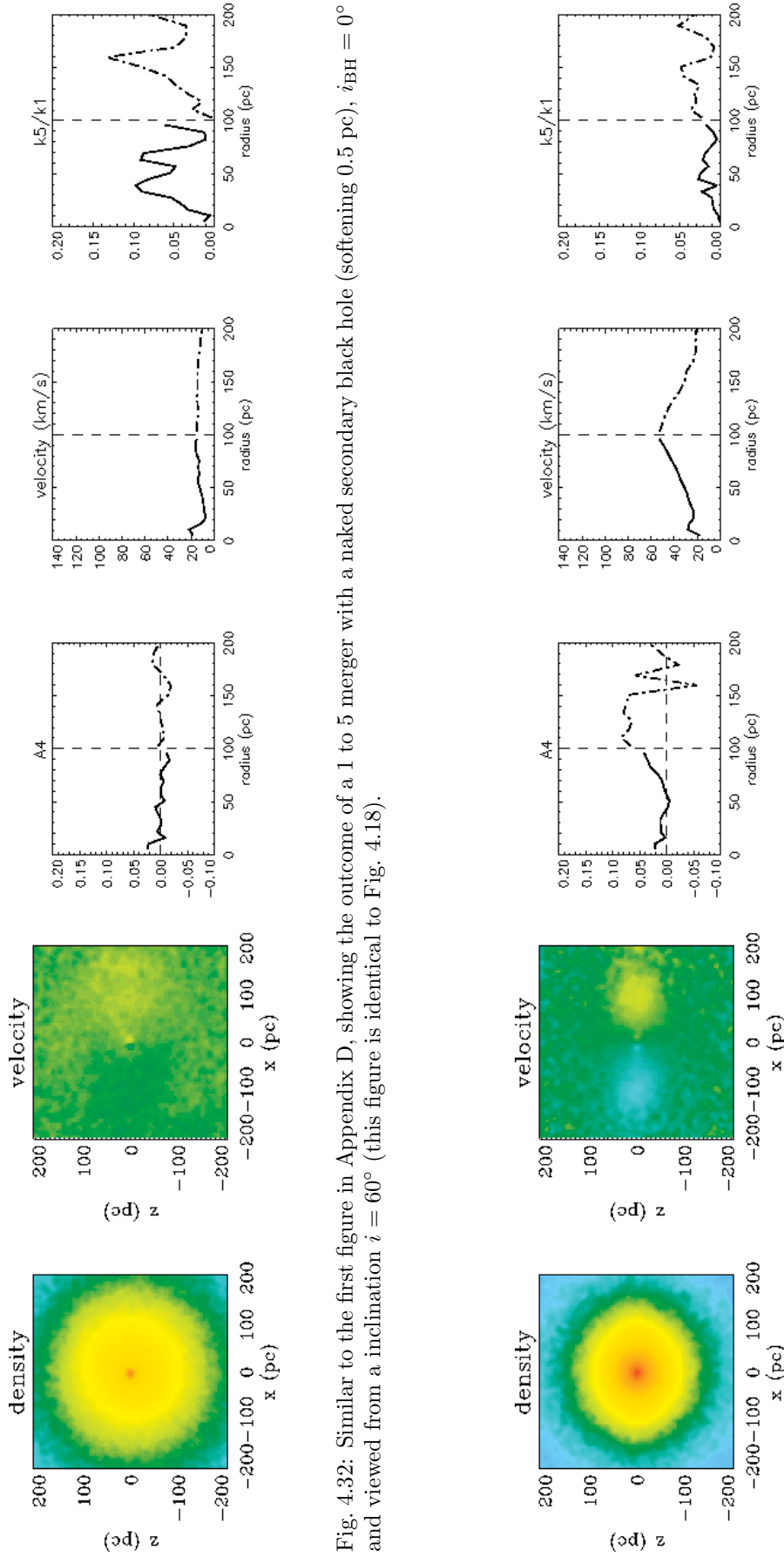


Fig. 4.32: Similar to the first figure in Appendix D, showing the outcome of a 1 to 5 merger with a naked secondary black hole (softening 0.5 pc),  $i_{\text{BH}} = 0^\circ$  and viewed from a inclination  $i = 60^\circ$  (this figure is identical to Fig. 4.18).

Fig. 4.33: Similar to the first figure in Appendix D, showing the outcome of a 1 to 5 merger with  $i_{\text{BH}} = 0^\circ$  and viewed from a inclination  $i = 60^\circ$ , but now with a softening of 2 pc.

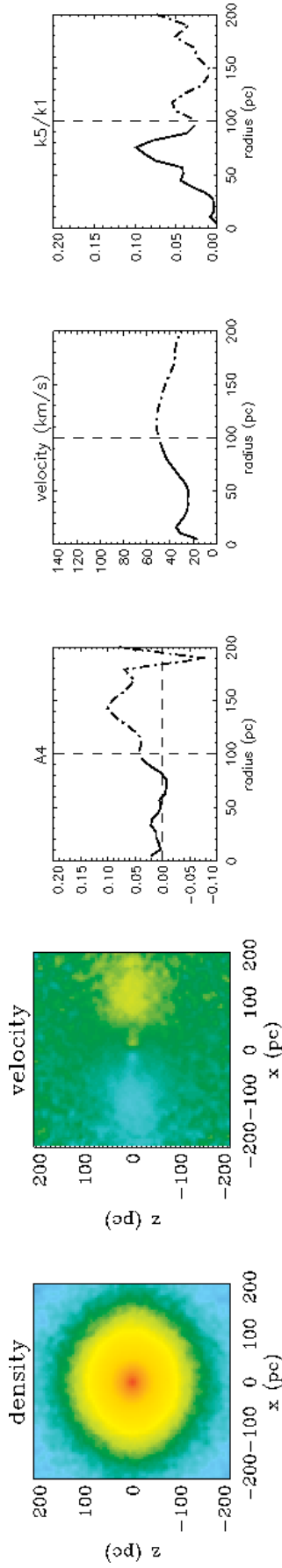


Fig. 4.34: Similar to the first figure in Appendix D, showing the outcome of a 1 to 5 merger with  $i_{\text{BH}} = 0^\circ$  and viewed from an inclination  $i = 60^\circ$ , but now with a softening of 3.5 pc.

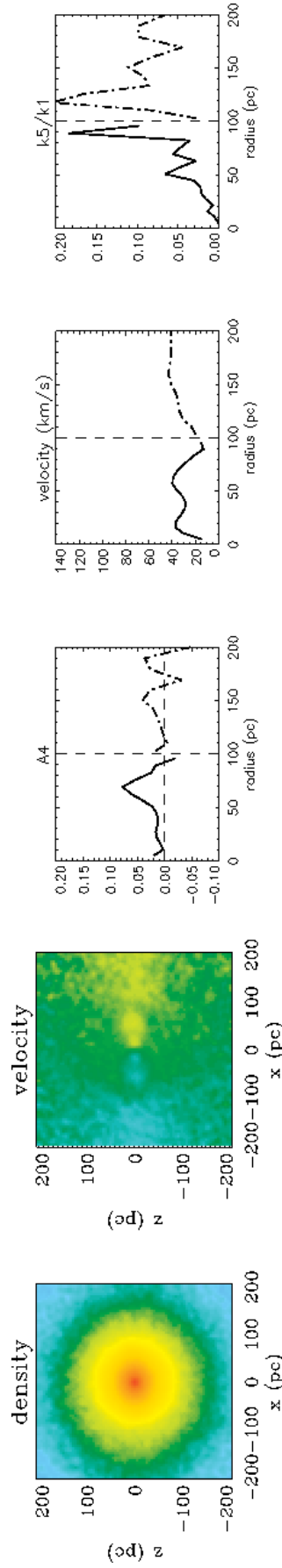


Fig. 4.35: Similar to the first figure in Appendix D, showing the outcome of a 1 to 5 merger with  $i_{\text{BH}} = 0^\circ$  and viewed from an inclination  $i = 60^\circ$ , but now with a softening of 6.25 pc.

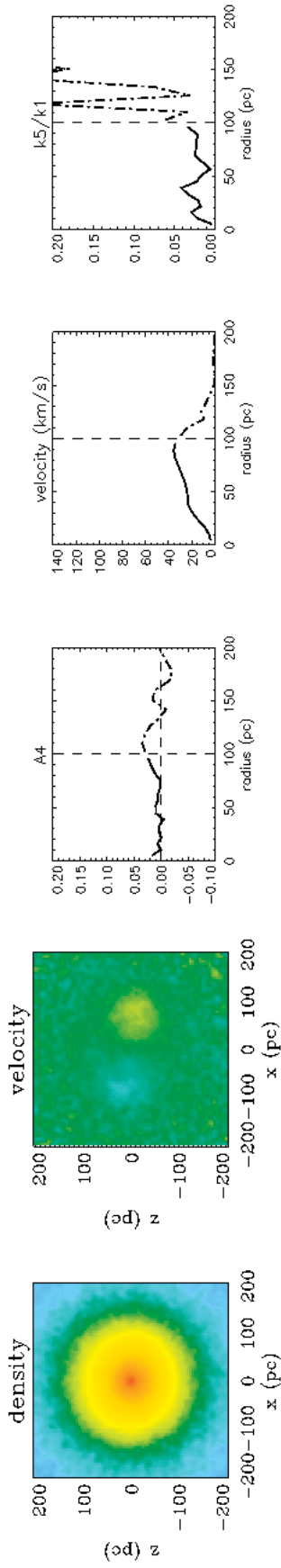


Fig. 4.36: Similar to the first figure in Appendix D, showing the outcome of a 1 to 5 merger with a naked secondary black hole (softening 0.5 pc),  $i_{\text{BH}} = 90^\circ$  and viewed from a inclination  $i = 60^\circ$  (this figure is identical to Fig. 4.21).

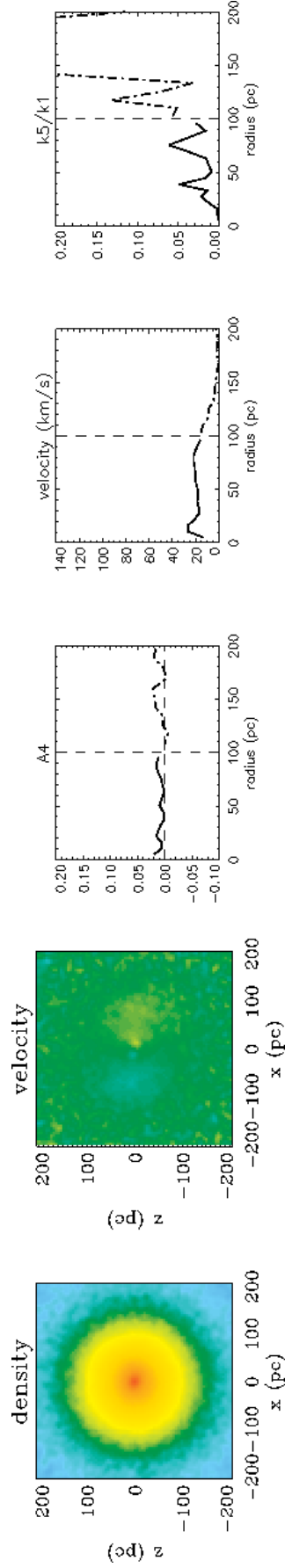


Fig. 4.37: Similar to the first figure in Appendix D, showing the outcome of a 1 to 5 merger with  $i_{\text{BH}} = 90^\circ$  and viewed from a inclination  $i = 60^\circ$ , but now with a softening of 2 pc.

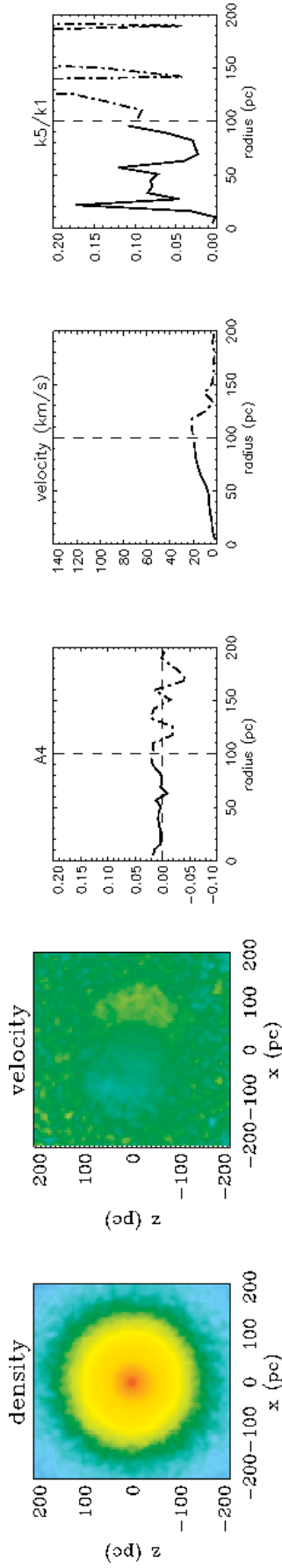


Fig. 4.38: Similar to the first figure in Appendix D, showing the outcome of a 1 to 5 merger with  $i_{\text{BH}} = 90^\circ$  and viewed from an inclination  $i = 60^\circ$ , but now with a softening of 3.5 pc.

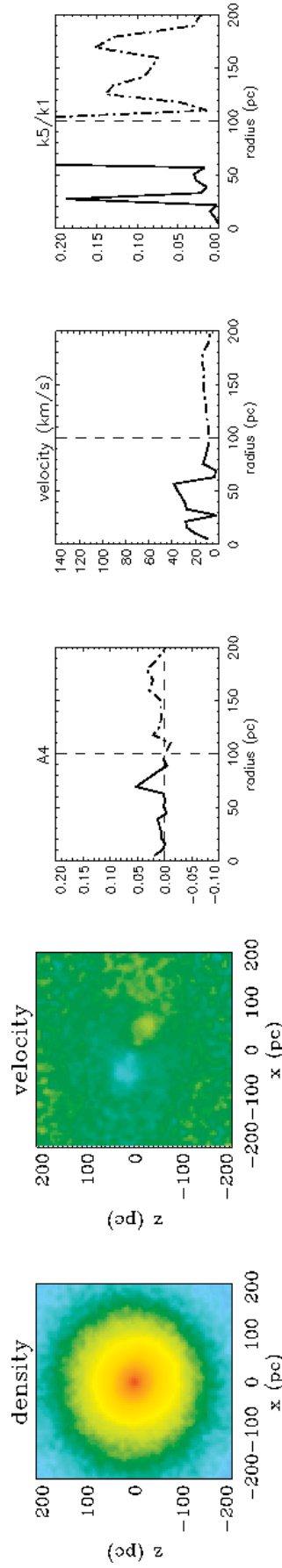


Fig. 4.39: Similar to the first figure in Appendix D, showing the outcome of a 1 to 5 merger with  $i_{\text{BH}} = 90^\circ$  and viewed from an inclination  $i = 60^\circ$ , but now with a softening of 6.25 pc.

---

# CHAPTER 5: CONCLUSIONS AND FUTURE WORK

---

## 5.1 Conclusions

Understanding the evolution of galaxies from the early stages of the universe through to their current appearance is an ambitious task. Its undertaking has started less than 100 years ago and, in our progress, we have captured glimpses of their histories like stills taken from a film. Yet, many gaps remain to be filled. Elliptical galaxies have, for a long time, stood aside as they were thought to be easy to explain and not suffering any further changes. This view has changed though and they now form a focal point of our research. Galaxies can have formed most of their stars *in-situ* or assembled via a series of mergers, taking stars from other galaxies as their own, turning into different galaxies, as different as an elliptical can be from a spiral. Indeed there is compelling evidence that these transformations occur during major mergers and therefore, ellipticals should be marked by such important assembling episodes.

Our objective was to explore the merger history of these galaxies and to do so by using a small feature, nuclear stellar discs (NSDs). These discs, discovered serendipitously in observations with the Hubble Space Telescope, were considered common features in early-type galaxies, although they had not been the subject of a systematic search.

We

- Conducted the most extensive volume-limited census of NSDs in early-type galaxies.
- Found that they are present in  $\approx 20\%$  of them.
- Found that their incidence is not sensitive to galaxy type (from E to S0-a) nor environment and appears to decline at both ends of the mass range in our sample.

For the most massive systems, that is to be expected since their most recent history should have been dominated by dry mergers (Khochfar and Burkert, 2003; Khochfar and Silk, 2009), which would have destroyed possible existing discs without offering the necessary gas to rebuild them. More surprising though, was to find the incidence also dropping at the low-mass end of our sample. Perhaps this reflects

a selection bias, since small early-type galaxies often display signs of recent star-formation and substantial amounts of molecular gas and dust (Young *et al.*, 2011), which would complicate the detection of small discs. Further to the compiling of the sample, we

- obtained the structural characteristics of 12 of such discs,

doubling the number of discs with known parameters. By separating the disc’s light contribution from that of the bulge (using the disc-bulge decomposition technique of Scorza and Bender, 1995) we were able to obtain the scale lengths, central intensities and inclinations, enabling us to compare these discs with larger galactic discs.

- We have shown that, similarly to larger galactic discs, NSDs also follow a correlation between central surface brightness  $\mu_c^0$  and scale length  $h$ , although with smaller scale length or fainter central surface brightness.

It is not surprising that large discs, formed in dark matter halos, acquire different characteristics than NSDs, which are formed in bulge-dominated regions of galaxies.

Having such a sample and the capacity to extract their disc properties spurred to the idea of using such information in conjunction with spectroscopic data to better constrain the age of the disc’s stellar population.

- Using VIMOS integral-field spectroscopic data of NGC 4458 along with disc and bulge light fractions derived from HST observations we were able to constrain the age of the disc to  $\sim 5 - 6$  Gyr, or above. According to the simulations shown in Chapter 4, this suggests that NGC 4458 has not suffered a major merger since then.
- This exercise also serves to validate the method we have introduced.

This method will not only allow us in the future to more precisely constrain the assembly history of galaxies, but the specific results pertaining to NGC 4458 are also important in what concerns the formation history of the particular class of early-type galaxies to which it belongs. NGC 4458 is indeed part of that minority of early-type galaxies that display no global stellar rotation except for a central kinematically decoupled core (KDC; Emsellem *et al.*, 2007; Callegari *et al.*, 2011; Emsellem *et al.*, 2011). In fact, NGC 4458 is also among the less massive objects of this kind. Such slow-rotators must be intrinsically quite round (Weijmans *et al.*, private communication), as is generally the case of the most massive early-type

galaxies at the centre of clusters, which indeed do not rotate at all. The existing theoretical models of galaxy formation still have difficulties creating accurate models for slow-rotators (either with or without a kinematically decoupled core), producing instead objects with higher flattening and angular momentum than observed (Jesseit *et al.*, 2009). A possible means of slowing down the rotation of the models and of making them rounder is to have them going through several minor mergers (Khochfar *et al.*, 2011). In the particular case of NGC 4458, however, there could have been only a limited number of minor mergers, due to the galaxy's low mass, and these must have either left the nuclear disc intact (as Callegari *et al.* (2009, 2011) have shown to be possible) or must have led to its very formation. The simultaneous presence of a disc and a KDC, both intimately connected to merger events, led us also to speculate a possible link between these two structures. Further analysis of the galaxy's central kinematics showed its KDC to be more rotationally supported than any other KDC found during the ATLAS<sup>3D</sup> survey.

- Possibly, NGC 4458 initially hosted an extended disc whose outer stretches were disrupted by successive minor mergers, causing not only the galaxy to be round and slowly-rotating, but also the formation of the KDC.
- NGC 4458 definitely still defies our current thinking of galaxy formation.

At this stage, we felt it necessary to further explore the briefly addressed problem of disc fragility against mergers. This requirement is of extreme importance if we want to use NSDs as look-back time indicators. To do so, we set up a range of simulations in which an elliptical galaxy bearing a nuclear stellar disc orbiting a central supermassive black hole of similar mass to the disc suffers a collision by a secondary SMBH (with or without a stellar cusp around it), in a simplified model for the latest stages of a merging with a secondary galaxy.

- Results from the simulated encounters showed that indeed, nuclear stellar discs are fragile in major merger situations while generally surviving minor mergers.

A note should be made about survival and detection. Working with simulations allows us to have access to information not accessible to an observer. It was with that in mind that the disc survival was assessed using the combined bulge and disc light of the final time-step and taking into account observational limits while measuring any surviving photometric signatures of a disc. We also found that

- The angular momentum of the discs is difficult to erase

- Integral-field data should be useful in detecting the kinematics signature of disc, even when photometrically there would appear to be none.

In fact, since this is generally the situation observed in slow-rotators with kinematically-decoupled cores, we speculate that some of these structure may indeed be related to disc structures, just like our observations suggested in the case of NGC 4458

We have addressed the ongoing problem of galaxy mass assembly and followed a hypothesis of using nuclear stellar discs as tools to constrain the epoch of the last wet major merger experienced by early-type galaxies. During the course of our work we have compiled the first census of these features, while also describing some of their properties. We have shown that it is possible to use these parameters, in conjunction with integral field spectra to obtain a tighter constraint on the age of that merging event and explored a central idea in which our work is based, the fragility of the discs in major merger situations. Here we have presented a consistent piece of work, which delivers a working sample and a method, ready to be used in the future.

## 5.2 Aims for the future and opportunities

Each of the previous chapters has opened a door to further developments and the pursuing of follow-up ideas. With new observations being constantly taken, often from large ground-based telescopes equipped with adaptive-optics facilities working at near-infrared wavelengths, it may be always possible to expand our initial census using archival data, although we do not expect dramatic changes from our results unless to embark on a more focussed survey of low-mass objects where indeed infrared data may circumvent the impact of dust. On the other hand, performing a structural analysis of even an handful more nuclear stellar disks could bring more insights in understanding their position in the  $\mu_c^0 - h$  relation compared to larger discs.

The method we have implemented for the stellar-population analysis of NGC 4458 has shown it is possible to determine with accuracy the age of NSDs. Based on the census results we can select a sample of NSD-hosting galaxies of different masses and situated in different environments in which to perform a similar investigation. This will finally allow us to compare direct observations to models that predict, for example, that field and cluster galaxies should have assembled at different epochs and that this look-back time should have different dependencies on mass (Khochfar and Silk, 2006a,b). Collecting such data with VIMOS, as we have done for NGC 4458,

would be very time-consuming, but the next generation integral-field spectrograph MUSE (Bacon *et al.*, 2010), also being installed at the VLT, will enable such an endeavour. Indeed, MUSE will be more efficient than VIMOS and offer a similar wavelength range, thus allowing for a better separation of the nebular emission from the stellar continuum and for more accurate models of the latter. Of particular interest for our study of nuclear stellar discs is the fact that MUSE will work with adaptive optics, reaching a resolving power comparable to that of HST, which will increase the disc contribution in the central region, leading to tighter age constraints. Additionally, we can also use the stellar kinematics to constrain the disc age. For a given luminosity, a disc with an older stellar population should be more massive than a younger one, leading to a larger rotational velocity. A similar approach has been taken by Coccato *et al.* (2011) and Coccato *et al.* (2013) when disentangling the populations of two counter-rotating discs. In these particular cases, the line of sight velocity distributions (LOSVD) take the extreme shape of a double Gaussian. They have not, however, included photometric constraints such as the ones we have used in our method. In the future we could combine these two techniques to study systems with disc and bulge, for which we will have to reach a good trade off between spectral resolution (which helps studying the LOSVD) and excellent S/N provided by 8m-class or larger telescopes.

The use of this method is not confined to the study of NSDs. Similar studies can be performed on extended discs where we can even sample different regions separately, or on other structures where there is a superposition of stellar populations, such as nuclear rings.

There is also a clear strategy for the development of the merger simulations. The simplified set up we developed was sufficient to confirm the fragility of NSDs in major merger situations, but it can be further improved. We have introduced a simple size estimate for the discs during our census on Chapter 2 and shown that nuclear discs can span a range of sizes, which most presumably translates also in a range of relative mass fractions between the nuclear disc and the central supermassive black hole. We should therefore explore a wider range of disc masses, when compared to the central SMBH and the bulge. This will allow us to identify up to which mass ratio discs can still be fragile and use that information to compile a sample of follow-up targets. Additionally, we can adopt a more realistic description of the stellar cusp around the secondary black hole, representing it by a set of collisionless particles instead of a single softened particle representing the SMBH and stars around it. This will enable us to follow the tidal stripping of the stellar cusp and study not only the effect on the disc, but also what happens to the cusp stars. Finally, better simulations

should also provide us with a clearer picture of the possible connection between disc disruption and the formation of kinematically decoupled cores. The similarity of some results from our simulations with these KDCs (regular rotation with a low average  $k_5/k_1$  although without showing an increased  $a_4$ ), which are also found in early-type galaxies (e.g. Bender, 1988; Franx *et al.*, 1989; McDermid *et al.*, 2006), suggests puffed-up discs may be linked to KDCs. For this investigation, we will need to study the higher moments of the LOSVD not only in better simulations but also in high quality integral-field data.

Important steps have been taken to address the problem of tracing the mass assembly of galaxies. These have not only shed some light on current issues, but, more importantly, have left us with several questions in need of follow-up and with clear ideas for the future.

# References

- Bacon, R., Accardo, M., Adjali, L., Anwand, H., Bauer, S., Biswas, I., Blaizot, J., Boudon, D., Brau-Nogue, S., Brinchmann, J., Caillier, P., Capoani, L., Carollo, C. M., Contini, T., Couderc, P., Daguisé, E., Deiries, S., Delabre, B., Dreizler, S., Dubois, J., Dupieux, M., Dupuy, C., Emsellem, E., Fechner, T., Fleischmann, A., François, M., Gallou, G., Gharsa, T., Glindemann, A., Gojak, D., Guiderdoni, B., Hansali, G., Hahn, T., Jarno, A., Kelz, A., Koehler, C., Kosmalski, J., Laurent, F., Le Floch, M., Lilly, S. J., Lizon, J.-L., Loupiau, M., Manescau, A., Monstein, C., Nicklas, H., Olaya, J.-C., Pares, L., Pasquini, L., Pécontal-Rousset, A., Pelló, R., Petit, C., Popow, E., Reiss, R., Remillieux, A., Renault, E., Roth, M., Rupprecht, G., Serre, D., Schaye, J., Soucail, G., Steinmetz, M., Streicher, O., Stuijk, R., Valentin, H., Vernet, J., Weilbacher, P., Wisotzki, L., and Yerle, N. (2010). The MUSE second-generation VLT instrument. In *Society of Photo-Optical Instrumentation Engineers (SPIE) Conference Series*, volume 7735 of *Society of Photo-Optical Instrumentation Engineers (SPIE) Conference Series*.
- Bender, R. (1988). Rotating and counter-rotating cores in elliptical galaxies. *A&A*, **202**, L5–L8.
- Callegari, S., Mayer, L., Kazantzidis, S., Colpi, M., Governato, F., Quinn, T., and Wadsley, J. (2009). Pairing of Supermassive Black Holes in Unequal-Mass Galaxy Mergers. *ApJ*, **696**, L89–L92.
- Callegari, S., Kazantzidis, S., Mayer, L., Colpi, M., Bellovary, J. M., Quinn, T., and Wadsley, J. (2011). Growing Massive Black Hole Pairs in Minor Mergers of Disk Galaxies. *ApJ*, **729**, 85.
- Cocato, L., Morelli, L., Corsini, E. M., Buson, L., Pizzella, A., Vergani, D., and Bertola, F. (2011). Dating the formation of the counter-rotating stellar disc in the spiral galaxy NGC 5719 by disentangling its stellar populations. *MNRAS*, **412**, L113–L117.
- Cocato, L., Morelli, L., Pizzella, A., Corsini, E. M., Buson, L. M., and Dalla Bontà, E. (2013). Spectroscopic evidence of distinct stellar populations in the counter-rotating stellar disks of NGC 3593 and NGC 4550. *A&A*, **549**, A3.
- Emsellem, E., Cappellari, M., Krajnović, D., van de Ven, G., Bacon, R., Bureau, M., Davies, R. L., de Zeeuw, P. T., Falcón-Barroso, J., Kuntschner, H., McDermid, R., Peletier, R. F., and Sarzi, M. (2007). The SAURON project - IX. A kinematic classification for early-type galaxies. *MNRAS*, **379**, 401–417.
- Emsellem, E., Cappellari, M., Krajnović, D., Alatalo, K., Blitz, L., Bois, M., Bournaud, F., Bureau, M., Davies, R. L., Davis, T. A., de Zeeuw, P. T., Khochfar, S., Kuntschner, H., Lablanche, P.-Y., McDermid, R. M., Morganti, R., Naab, T.,

- Oosterloo, T., Sarzi, M., Scott, N., Serra, P., van de Ven, G., Weijmans, A.-M., and Young, L. M. (2011). The ATLAS<sup>3D</sup> project - III. A census of the stellar angular momentum within the effective radius of early-type galaxies: unveiling the distribution of fast and slow rotators. *MNRAS*, **414**, 888–912.
- Franx, M., Illingworth, G., and Heckman, T. (1989). Major and minor axis kinematics of 22 ellipticals. *ApJ*, **344**, 613–636.
- Jesseit, R., Cappellari, M., Naab, T., Emsellem, E., and Burkert, A. (2009). Specific angular momentum of disc merger remnants and the  $\lambda_R$ -parameter. *MNRAS*, **397**, 1202–1214.
- Khochfar, S. and Burkert, A. (2003). The Importance of Spheroidal and Mixed Mergers for Early-Type Galaxy Formation. *ApJ*, **597**, L117–L120.
- Khochfar, S. and Silk, J. (2006a). A Simple Model for the Size Evolution of Elliptical Galaxies. *ApJ*, **648**, L21–L24.
- Khochfar, S. and Silk, J. (2006b). On the origin of stars in bulges and elliptical galaxies. *MNRAS*, **370**, 902–910.
- Khochfar, S. and Silk, J. (2009). Dry mergers: a crucial test for galaxy formation. *MNRAS*, **397**, 506–510.
- Khochfar, S., Emsellem, E., Serra, P., Bois, M., Alatalo, K., Bacon, R., Blitz, L., Bournaud, F., Bureau, M., Cappellari, M., Davies, R. L., Davis, T. A., de Zeeuw, P. T., Duc, P.-A., Krajnović, D., Kuntschner, H., Lablanche, P.-Y., McDermid, R. M., Morganti, R., Naab, T., Oosterloo, T., Sarzi, M., Scott, N., Weijmans, A.-M., and Young, L. M. (2011). The ATLAS<sup>3D</sup> project - VIII. Modelling the formation and evolution of fast and slow rotator early-type galaxies within  $\Lambda$ CDM. *MNRAS*, **417**, 845–862.
- McDermid, R. M., Emsellem, E., Shapiro, K. L., Bacon, R., Bureau, M., Cappellari, M., Davies, R. L., de Zeeuw, T., Falcón-Barroso, J., Krajnović, D., Kuntschner, H., Peletier, R. F., and Sarzi, M. (2006). The SAURON project - VIII. OASIS/CFHT integral-field spectroscopy of elliptical and lenticular galaxy centres. *MNRAS*, **373**, 906–958.
- Scorza, C. and Bender, R. (1995). The internal structure of disk elliptical galaxies. *A&A*, **293**, 20–43.
- Young, L. M., Bureau, M., Davis, T. A., Combes, F., McDermid, R. M., Alatalo, K., Blitz, L., Bois, M., Bournaud, F., Cappellari, M., Davies, R. L., de Zeeuw, P. T., Emsellem, E., Khochfar, S., Krajnović, D., Kuntschner, H., Lablanche, P.-Y., Morganti, R., Naab, T., Oosterloo, T., Sarzi, M., Scott, N., Serra, P., and Weijmans, A.-M. (2011). The ATLAS<sup>3D</sup> project - IV. The molecular gas content of early-type galaxies. *MNRAS*, **414**, 940–967.